# Developing fast cryo-EM sample preparation for time-resolved structural studies

**David Paul Klebl**

University of Leeds

Astbury Centre for Structural and Molecular Biology

Submitted in accordance with the requirements for the degree of
*Doctor of Philosophy*

March 2022

## Declaration

The candidate confirms that the work submitted is his own, except where work which has formed part of jointly-authored publications has been included. The contribution of the candidate and the other authors to this work has been explicitly indicated overleaf. The candidate confirms that appropriate credit has been given within the thesis where reference has been made to the work of others. This copy has been supplied on the understanding that it is copyright material and that no quotation from the thesis may be published without proper acknowledgement.

II

# Jointly authored publications

The candidate confirms that the work submitted is his own, except where work which has formed part of jointly-authored publications has been included. The contribution of the candidate and the other authors to this work has been explicitly indicated below. The candidate confirms that appropriate credit has been given within the thesis where reference has been made to the work of others:

**Chapter 2:**

Dimitrios Kontziampasis*, David P. Klebl*, Matthew G. Iadanza, Charlotte A. Scarff, Florian Kopf, Frank Sobott, Diana C. F. Monteiro, Martin Trebbin, Stephen P. Muench, and Howard D. White. "A cryo-EM grid preparation device for time-resolved structural studies." IUCrJ 6, no. 6 (2019): 1024-1031.

* These authors contributed equally to this work.

For this publication, the author contribution statement reads:

D.K., D.P.K. and H.D.W. performed preliminary work and instrument setup; D.P.K. and D.K. performed cryo-EM experiments (grid preparation, data processing and analysis); M.G.I. and C.A.S. assisted with helical and single particle EM data processing; F.K., D.C.F and D.P.K. performed high speed imaging; F.S., M.T., S.P.M. and H.D.W. supervised the work; all authors contributed to the preparation of the manuscript.

**Chapter 3:**

David P. Klebl, Diana C. F. Monteiro, Dimitrios Kontziampasis, Florian Kopf, Frank Sobott, Howard D. White, Martin Trebbin, and Stephen P. Muench. "Sample deposition onto cryo-EM grids: from sprays to jets and back." Acta Crystallographica Section D: Structural Biology 76, no. 4 (2020): 340-349.

For this publication, the author contribution statement reads:

D.P.K. and D.K. performed cryo-EM experiments (grid preparation, data processing and analysis); D.C.F. designed the nozzles; D.C.F. and D.P.K. manufactured the nozzles; F.K., D.C.F and D.P.K. performed high speed imaging; F.S., M.T., S.P.M. and H.D.W. supervised the work; all authors contributed to the preparation of the manuscript.

**Chapter 4:**

David P. Klebl, Howard D. White, Frank Sobott, and Stephen P. Muench. "On-grid and in-flow mixing for time-resolved cryo-EM." Acta Crystallographica Section D: Structural Biology 77, no. 10 (2021).

For this publication, the author contribution statement reads:

D.P.K. performed cryo-EM experiments (grid preparation, data processing and analysis); F.S., S.P.M. and H.D.W. supervised the work; all authors contributed to the preparation of the manuscript.

**Chapter 5:**

David P. Klebl, Molly S. C. Gravett, Dimitrios Kontziampasis, David J. Wright, Robin S. Bon, Diana C. F. Monteiro, Martin Trebbin, Frank Sobott, Howard D. White, Michele C. Darrow, Rebecca F. Thompson and Stephen P. Muench. "Need for speed: examining protein behavior during CryoEM grid preparation at different timescales." Structure 28, no. 11 (2020): 1238-1248.

For this publication, the author contribution statement reads:

D.P.K. and M.S.C.G. performed cryo-EM experiments (grid preparation, data processing and analysis); D.J.W. and D.P.K. prepared the samples; D.C.F. manufactured the nozzles; M.C.D. did chameleon cryo-EM grid preparation; D.K., M.C.D. and R.F.T. assisted with data analysis; F.S., R.S.B., M.T., S.P.M., R.F.T. and H.D.W. supervised the work; all authors contributed to the preparation of the manuscript.

**Chapter 6 (in preparation):**

David P. Klebl, Charlotte A. Scarff, Cristina M. Risi, Betty Virok, Michele Stofella, Eva Forgacs, Donald A. Winkelmann, Frank Sobott, Vitold E. Galkin, Howard D. White and Stephen P. Muench. " Pre-power stroke structure of the Actomyosin Complex ".

For this publication, the author contribution statement reads:

D.P.K. performed cryo-EM experiments (grid preparation, data processing and analysis) and interpretation; C.A.S. assisted with data analysis and interpretation; C.M.R. performed preliminary atomic model building; B.V. and E.F. prepared protein samples; M.S. performed kinetic modelling; D.A.W. performed motility assays; F.S., V.E.G., H.D.W. and S.P.M. supervised the project; all authors contributed to the preparation of the manuscript.

## Acknowledgements

Most importantly, I would like to thank my supervisors, Dr Stephen Muench and Prof Frank Sobott, for their continued support, for all the time and effort that has gone into this project, and for always exploring new directions of the project with me. I could not have hoped for a better supervisory team. I would also like to thank Prof Howard White who taught me a great deal, has inspired with his knowledge and enthusiasm for the project and I really enjoyed staying with him in Norfolk for a few days.

I have been very lucky to be part of the excellent Wellcome Trust 4-year PhD program and I would like to acknowledge the University of Leeds for funding, Prof Alan Berry for directing the program and Prof Sheena Radford for encouraging me to apply. I am very grateful that I had the opportunity to come to Leeds and for the wonderful people that I have met through this program.

Thank you to all members of the Muench, EM and Sobott groups, past and present, for their help during the project and for creating a friendly and collaborative environment to work in. Special thanks goes to those who helped me get started and had to answer a lot of questions initially, Sophie Hesketh, Dimitrios Kontziampasis, Josh White, Rachel Johnson and Dave Nicholson, those who have worked together with me, Iso Hirst, Charlie Scarff, Alex Flynn and Molly Gravett as well as Master's students Matt Feasey and Kieran Wilde who have been very patient with me. Also, I very much enjoyed the occasional after work drinks with Seb Porav, the Radford group and other friends.

Further thanks goes to the electron microscopy and mass spectrometry facilities. It has been a joy working with Becky Thompson, Emma Hesketh, Martin Fuller, James Ault, Rachel George and everyone else who provided the amazing resources and all the support that have made this project possible.

Thank you also to all collaborators, Javier Lizarrondo and Dr Maria Garcia-Alai from EMBL Hamburg, Dr Diana Monteiro and Dr Martin Trebbin who invited me to visit DESY in Hamburg, Dr Andrew Scott and Dr Carlos Mata from the Stockley group in Leeds, Prof Nik Kapur and Dr Rob Kay from the engineering department in Leeds and all others.

Last but not least, I would like to thank my family. Moving to a new country is a big step and was only possible with their support, thank you to my mum and dad for always believing in me, Lenni and Clara for coming to visit, for skiing trips to the Cairngorms or to stay with us in Leeds. The biggest thank you goes

to Sabine, for going on this journey to Leeds with me, for many beautiful trips to Yorkshire and surroundings on the weekends and for always being the lovely, caring and wonderful person that you are.

# Abstract

Single particle cryo-electron microscopy (cryo-EM) has become one of the major techniques for protein structure determination, through advances in microscope hardware and image processing software. The resolution of cryo-EM and the speed of data collection are approaching those of X-ray crystallography, in addition cryo-EM allows determination of more dynamic and flexible structures. While computational methods that account for dynamics are being developed, the vast majority of cryo-EM structures is currently determined under equilibrium conditions.

In order to fulfil their functions, proteins partake in reactions and are usually in environments far from equilibrium. To determine the structural dynamics of proteins in non-equilibrium systems, a series of structural snapshots can be recorded over time after triggering the reaction of interest. In principle, this allows a ‘molecular movie’ to be assembled, which promises a much improved understanding of the relationship between protein structure, dynamics and function. However, recording such ‘molecular movies’ is experimentally challenging and requires the use of time-resolved structural techniques, such as time-resolved cryo-EM.

In time-resolved cryo-EM (TrEM) a reaction is initiated, often by rapid mixing, and quenched upon vitrification. The majority of biological reactions is faster than conventional cryo-EM grid preparation, so TrEM requires specialised instrumentation. In this thesis, methods for TrEM are presented, characterised and developed further. Different approaches for fast sample application and rapid mixing are compared and the effect of sample exposure to the air-water interface is analysed. Together, the thesis contributes to a better understanding of fast grid preparation for TrEM and aims to give directions for future TrEM studies. Using the methods established in this thesis, the structure of the pre-power stroke actomyosin complex is solved, demonstrating the power of TrEM and providing insight into the molecular mechanism of force generation by the actomyosin system.

# Table of Contents

# List of Figures

# List of Tables

# Abbreviations

| | |
|---|---|
| **2D** | Two dimensional |
| **3D** | Three dimensional |
| **A** | Filamentous actin |
| **ADP** | Adenosine diphosphate |
| **AM** (or **A-M**) | Actomyosin |
| **AMP-PNP** | Adenylyl-imidodiphosphate |
| **ATP** | Adenosine triphosphate |
| **AWI** | Air-water interface |
| **CM** | Cardiomyopathy |
| **CMOS** | Complementary metal-oxide-semiconductor |
| **cryo-EM** | Cryo-electron microscopy |
| **cryo-ET** | Cryo-electron tomography |
| **CTF** | Contrast transfer function |
| **DC** | Direct current |
| **dd$H_2O$** | Double-distilled water |
| **DTT** | Dithiothreitol |
| **E. coli** | Escherichia coli |
| **EGTA** | Ethylene glycol-bis(β-aminoethyl ether)-*N*,*N*,*N*′,*N*′-tetraacetic acid |
| **EM** | Electron microscopy |
| **EMDB** | Electron microscopy data bank |
| **F-actin** | Filamentous actin |
| **FEP** | Fluorinated ethylene propylene |
| **fps** | Frames per second |
| **FRET** | Förster resonance energy transfer |
| **FSC** | Fourier shell correlation |
| **G-actin** | Globular actin |
| **GDVN** | Gas-dynamic virtual nozzle |

| | |
|---|---|
| **HEPES** | 4-(2-hydroxyethyl)-1-piperazineethanesulfonic acid |
| **HLH** | Helix-loop-helix |
| **HSPD1** | Human mitochondrial heat shock protein family D member 1 |
| **ID** | Inner diameter |
| **IPTG** | Isopropyl β-D-1-thiogalactopyranoside |
| **IQ** | IQ calmodulin-binding motif |
| **KAc** | Potassium acetate |
| **L50** | Myosin lower 50 kDa subdomain |
| **LED** | Light-emitting diode |
| **M** | Myosin |
| **MD** | Molecular dynamics |
| **$MgAc_2$** | Magnesium acetate |
| **MOPS** | 3-(*N*-morpholino)propanesulfonic acid |
| **MW** | Molecular weight |
| **MWCO** | Molecular weight cut-off |
| **myo5** | Myosin V subfragment 1, $S^{217}A$ and $\Delta DDEK^{594-597}$ double mutant |
| **Ni-NTA** | Nickel nitrilotriacetic acid |
| **NMR** | Nuclear magnetic resonance |
| **OD** | Outer diameter |
| **$OD_{600}$** | Optical density at 600 nm |
| **PDB** | Protein data bank |
| **PDF** | Probability density function |
| **PDMS** | Polydimethylsiloxane |
| **$P_i$** | Inorganic phosphate |
| **PMSF** | Phenylmethylsulfonyl fluoride |
| **postPS** | Post-power stroke |
| **prePS** | Pre-power stroke |
| **PV-TF** | Porcine ventricular thin filaments |

| | |
|---|---|
| **RH** | Relative humidity |
| **RMS** | Root-mean-square |
| **RMSD** | Root-mean-square deviation |
| **rpm** | Revolutions per minute |
| **S1** | (Myosin) subfragment 1 |
| **SARS-CoV-2** | Severe acute respiratory syndrome coronavirus 2 |
| **SCCM** | Standard cubic centimetres per minute |
| **SD** | Standard deviation |
| **SDS-PAGE** | Sodium dodecyl sulfate-polyacrylamide gel electrophoresis |
| **SPA** | Single-particle analysis |
| **TB** | Terrific broth |
| **TED** | Time-resolved cryo-electron microscopy grid preparation device; Time-resolved EM device |
| **TEV** | Tobacco etch virus |
| **TrEM** | Time-resolved cryo-electron microscopy |
| **Tris** | Tris(hydroxymethyl)aminomethane |
| **TRP** | Transient receptor potential |
| **U50** | Myosin upper 50 kDa subdomain |
| **XFEL** | X-ray free electron laser |

# Chapter 1 Introduction

## 1.1 A History of Electron Microscopy

### 1.1.1 Early electron microscopy

In 1926, Hans Busch laid the foundation for electron microscopy by showing that the effect of certain magnetic fields on electron beams was analogous to how glass lenses can affect light [1]. The first electron microscope was then reported in 1931 by Ernst Ruska, proving that electron beams and electromagnetic lenses could be used for microscopy in practice [2]. At the time, it was already known that the resolution of conventional light microscopy was limited by Abbe's diffraction limit [3] and the small wavelength of electrons promised a much higher resolution limit for electron microscopes [4]. Using these early electron microscopes brought the realisation that very thin specimen produced images by electron scattering, rather than electron absorption which reduced heating of the samples. Despite the challenges of charging and damage by the electron beam, the electron microscope was quickly adopted for imaging biological samples, including eukaryotic cells, bacteria and viruses, with the smallest resolved features between 35-100 Å in 1937 [5]. Around this time, based on Ruska's work, Manfred von Ardenne developed the scanning electron microscope which allowed imaging of the surface of thicker samples [6, 7].

From 1939, Siemens produced the first commercial transmission electron microscopes, designed by Ruska and Bodo von Borries [8]. These instruments proved useful in studying the morphology of bacteria and viruses, but only sufficiently thin specimen could be imaged [9]. Subsequent electron microscopes used higher voltages and allowed exposure of only a small field on the sample, reducing exposure to the electron beam. It had been discovered early that heavy metal salts were well suited to (negatively) stain small particles like bacteria [5, 10]. With improved microscopes, better images of small, stained particles could be obtained [11], reaching resolutions between 15-25 Å [12]. It also became clear that applying a small defocus improved contrast in electron micrographs, which confirmed that phase contrast made a major contribution to the final image [13, 14]. Later, Friedrich Thon provided a more formal description of the modulation of images by defocus, and visualised the effect using power spectra of images of carbon film [15]. At this time, microscope performance had improved significantly: For inorganic samples that withstood high vacuum and beam exposure, resolutions

of 1-2 Å were achieved in the 1960's [16]. However, for biological samples, resolution was dictated by sample preparation and sensitivity to the electron beam [17].

### 1.1.2 Biological structure determination by electron microscopy

Although resolution was limited, de Rosier and Klug adapted methods from X-ray crystallography to obtain the first three-dimensional structures of a helical specimen from electron micrographs [18]. It became clear that a method to image hydrated biomolecules could be the key to achieving higher resolutions [19]. Using crystals of catalase, much improved diffraction patterns with diffraction spots to 2 Å resolution were obtained from hydrated crystals on special hydration stages [20]. Freezing of catalase crystals in liquid nitrogen after sandwiching between two thin hydrophilic support films also produced samples that diffracted to high resolutions in the electron microscope [21, 22]. Unwin and Henderson found that, alternatively, crystals could be preserved in the high vacuum of the microscope by addition of glucose, followed by drying [23]. The sample was still easily damaged by the beam, so images had to be recorded with very low exposure. As a result, a large number of repeating units had to be averaged in order to improve the signal to noise ratio [24]. The approach resulted in a 7 Å structure of bacteriorhodopsin from the purple membrane and was the first structure to show how transmembrane $\alpha$-helices span the lipid bilayer [25].

In parallel with the work on crystals and highly symmetrical samples, efforts were ongoing to obtain structural information from single protein molecules and complexes [26]. One of these approaches was to collect images of individual molecules at different tilt angles (tomography) to reconstruct a three dimensional model, but this method used very high total electron exposures [27]. A different approach was put forward by Joachim Frank, proposing that individual molecules could be imaged in random orientations and then averaged computationally to improve the signal to noise ratio, ultimately to reach higher resolutions [28]. The single-particle averaging method was successfully applied to a range of biological macromolecules, such as the eukaryotic 40S ribosome [29], but limited to negatively stained samples at the time.

### 1.1.3 The dawn of cryo-electron microscopy

When Jacques Dubochet started to work on preparing hydrated biological samples for electron microscopy (EM) there had already been a number of studies on EM of frozen specimens [30, 31]. However, it was thought that pure water could not be directly frozen to produce vitreous ice, it would crystallise instead [32]. Initially, a

nebuliser was used by Dubochet and McDowall to spray micrometre-sized droplets onto an EM grid, which were then frozen in liquid nitrogen, but this resulted in droplets of crystalline ice. The breakthrough was the use of liquid ethane as a coolant (with a temperature slightly above the freezing point, > 90 K), because it produced vitreous ice [33, 34][1]. Around the same time, an independent study confirmed that formation of vitreous ice was indeed possible by rapid cooling [37]. The vitrification method was refined by the use of blotting (see 1.2 Cryo-EM grid preparation). The procedure was simple, and resulted in thin layers of vitrified specimen, freely suspended over the holes in the grid foil [38]. Since then, the blotting method has remained the most popular method to prepare cryo-electron microscopy (cryo-EM) samples.

Preserving biological samples in vitreous ice gave unprecedented images of molecules in the electron microscope [39]. Images from vitrified samples were promptly used to obtain 3D reconstructions, exemplified by the 35 Å structure of Semliki Forest virus, but were still limited in resolution [40]. In contrast, crystal diffraction in the electron microscope had demonstrated that resolutions in the range of 3.5 Å could be attained [41]. Cryo-EM imaging of bacteriorhodopsin crystals showed that information up to 3.5 Å could be recovered by means of correcting for image distortions, for example caused by beam tilt [42]. Ultimately, these efforts led to a 3.5 Å resolution structure of bacteriorhodopsin, allowing atomic model building [43].

At this time, methods for computational processing of single particle images (single particle analysis, SPA) had been developed further, based on negatively stained samples. It was shown that images could not only be averaged in 2D to improve the signal to noise ratio, but also classified to distinguish different conformations [44]. The transition from 2D images to 3D structures was made a few years later, providing a structure of the 50S bacterial ribosome at 20-30 Å resolution [45, 46]. From 1990, the first 3D reconstructions of molecules embedded in vitreous ice (prepared by the blotting method) were obtained from large single particles like the 70S bacterial ribosome [47], octopus hemocyanin [48] and the ryanodine receptor [49]. To some, single-particle cryo-EM became known as ‘blobology’ because of the modest resolution which showed few features compared to data from X-ray

[1] Liquid nitrogen was thought to be unsuitable as a cryogen for vitrification due to the Leidenfrost effect [35], where the formation of a protective gas layer slows cooling. Liquid ethane has a larger difference between melting and boiling temperature, so it shows less or no Leidenfrost effect. A recent study has questioned this view and has shown that liquid nitrogen can be used for vitrification and that the layer of cold gas above the cryogen plays a key role [36].

crystallography. Results from cryo-EM of 2D crystals proved that higher resolutions were possible [50, 51] and it was predicted that by averaging a large number of single particles, side chain resolution should be achievable by SPA [52].

Around 2000, more stable stages and brighter sources (field emission guns) in the microscope had brought significant improvements for single-particle cryo-EM [53], as evidenced by two high-resolution (7.4 Å and 9 Å) reconstructions of the icosahedral hepatitis B virus capsid or the structure of the bacterial 70S ribosome at 11.5 Å [54-56]. It was found that in theory and in practice, there is an approximately linear relationship between the logarithm of particle number and resolution [57]. This meant that the quality of the images could be estimated with a single number, called B-factor[2], and that lower B-factors would be required to achieve higher resolution.

### 1.1.4 The resolution revolution

Until around 2010, cryo-EM images were collected on photographic film, and digitised on a scanner which limited speed of data collection and data quality. Significant improvement in electron detectors came through the use of complementary metal oxide semiconductor (CMOS) technology [60]. At higher voltages (300 kV), these detectors showed good detection efficiency, particularly at high spatial frequencies [61]. It was demonstrated that further improvements could be achieved by 'counting' individual electron events [62]. High-framerate detectors also allowed correcting for beam-induced motion by recording movies rather than individual images [63]. Commercially available versions of these detectors, which became available around 2013, had significantly improved performance over photographic film [64]. Single-particle image processing methods had also improved over the years. It had become possible to separate different 3D conformational states which allowed whole conformational ensembles to be studied [65]. Along with improved algorithms for 3D structure refinement, this formed the basis for modern single-particle cryo-EM [66].

---

[2] The B-factor was derived based on X-ray crystallography work, in particular Wilson statistics [58]. These predict a flat power spectrum of proteins at high resolutions (higher than ~ 10 Å) [59]. However, experimental cryo-EM data suffer from a loss of contrast at high resolutions during imaging and processing. The B-factor was therefore introduced as an empirical constant that describes the loss of contrast compared to flat Wilson statistics. As a result, the B-factor also determines when the signal amplitude reaches the noise level, where the noise level is a function of particle number. When plotting the logarithm of particle number against the inverse square of resolution, the B-factor determines the slope of the line [57].

There was a ‘resolution revolution’ in the following years [67, 68], with a number of remarkable structures solved at resolutions which allowed accurate atomic model fitting. In particular, the structures of large complexes that had resisted crystallisation efforts could now be determined: For example, the first structure of a transient receptor potential (TRP) channel, TRPV1, was described in 2013 at 3.4 Å resolution [69]. The large subunit of the yeast mitochondrial ribosome, which could not be purified in sufficient amounts for crystallography, was solved to 3.2 Å resolution in 2014 [70]. Also in 2014, a 5 Å cryo-EM structure revealed the architecture of bovine respiratory complex I, one of the largest and most complicated enzymes in the cell [71].

Since the ‘resolution revolution’, microscope hardware and data processing has improved further. In 2020, the first atomic resolution cryo-EM structures (better than 1.5 Å) were reported [72, 73]. Current direct electron detectors are faster and B-factors (as a measure of image quality) have improved from around 1000 $Å^2$ in 2003 to 36 $Å^2$ in 2020. Gold grids have been shown to minimise beam-induced movement in the specimen [74], to a point where structures can be extrapolated to zero electron exposure [75]. High resolution structures have also been obtained using microscopes operating at 200 kV or 100 kV, which are more affordable [76, 77]. Great advances have also been made in the field of cryo-electron tomography, averaging of sub-tomograms has made it possible to resolve amino acid side chains and bound small molecules inside the cell [78].

## 1.2 Cryo-EM grid preparation

### 1.2.1 Cryo-EM grid preparation by blotting

The vitrification method described by Jacques Dubochet and colleagues in the mid 1980s has been used to prepare the vast majority of samples for high-resolution single particle cryo-EM to date. Vitrification accomplishes two things, it preserves hydrated samples in the high vacuum of the electron microscope, and the low temperature in the electron microscope reduces beam-induced damage to the sample [30].

The anatomy of a typical cryo-EM grid is shown in Figure 1-1. It consists of a ~ 3 mm diameter metal rim (usually copper or gold), and a fine mesh of metal bars. The spacing of the grid bars determines the square size, which is typically on the order of 100 µm. The top of the grid is covered by a thin foil (usually carbon or gold), the foil typically has a thickness of around 100 nm or less and contains regularly spaced holes of constant size [79], or randomly distributed holes of variable size. After sample preparation, there should be a thin film of vitrified

sample, freely suspended over the foil holes. Cryo-EM images are then collected of the unsupported thin film of vitrified sample in the foil holes. Some cryo-EM grids have an additional ultrathin layer of carbon, graphene oxide, graphene, or other material which supports the thin sample film [80, 81][3].

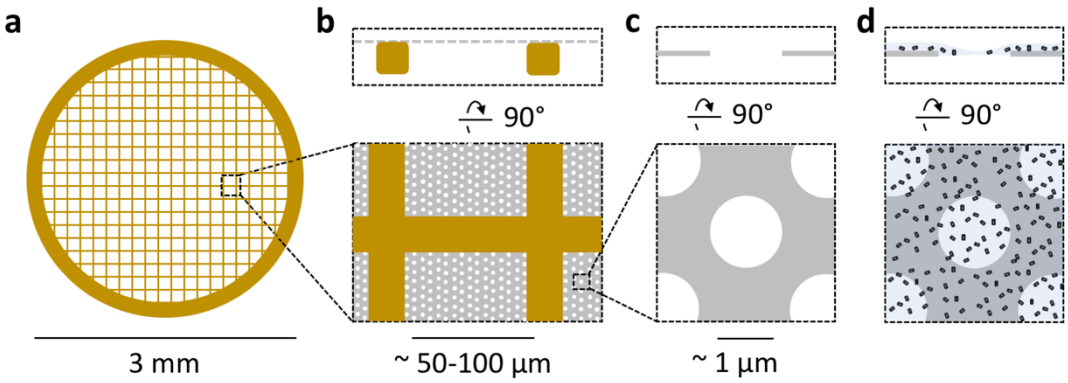


**Figure 1-1: Anatomy of a cryo-EM grid.**

(a) A cryo-EM grid is 3 mm in diameter, typically made of copper or gold and contains a fine mesh of grid bars. (b) On top of the grid, there is a thin film (around 100 nm thick), typically made of carbon or gold. (c) The foil contains regular or irregular spaced and sized holes. (d) After sample preparation, there is a thin film of vitrified specimen, suspended across the foil hole. Cryo-EM images are collected in the foil holes, where the sample film is unsupported.

Dubochet's blotting methods works as follows (Figure 1-2): The EM grid is held by tweezers in the vitrification instrument. A small amount of sample (typically 3 µL) is manually applied to the EM grid. With blotting paper, the excess of sample is removed from the EM grid, leaving only a very thin film of sample on the grid (10-100's of nm). The blotting step can be done manually or is automated as in commercial grid preparation instruments. The blotting paper is retracted, and the grid is then plunged into liquid ethane or another suitable cryogen [82]. The thickness of the vitrified sample layer is crucial and can decide over success or failure of the cryo-EM experiment: The ice (or sample layer) should be thinner than ~ 100 nm, to avoid multiple or inelastic electron scattering events [83]. In an ideal scenario, the ice layer is just thick enough to accommodate the particles of interest (often 20-30 nm), this will give the optimal signal to noise ratio and allow the most accurate determination of the contrast transfer function (CTF) [84].

[3] Grids with ultrathin support films are typically used to prevent interactions between the sample and the air-water interface (see below), or to increase particle concentration on the grid by binding of the particles to the support material.

Vitrification of the thin film is rapid, cooling rates need to be in the range of $10^5$-$10^6$ K/s for pure water to vitrify [36, 85]. This means it takes ~ 1 ms or less for the sample to cool down from room temperature (~ 293 K) to the glass transition temperature of water (~ 136 K). However, the entire cryo-EM grid preparation process takes about 10 s, manual sample application and blotting are the slowest steps, taking a few seconds each.

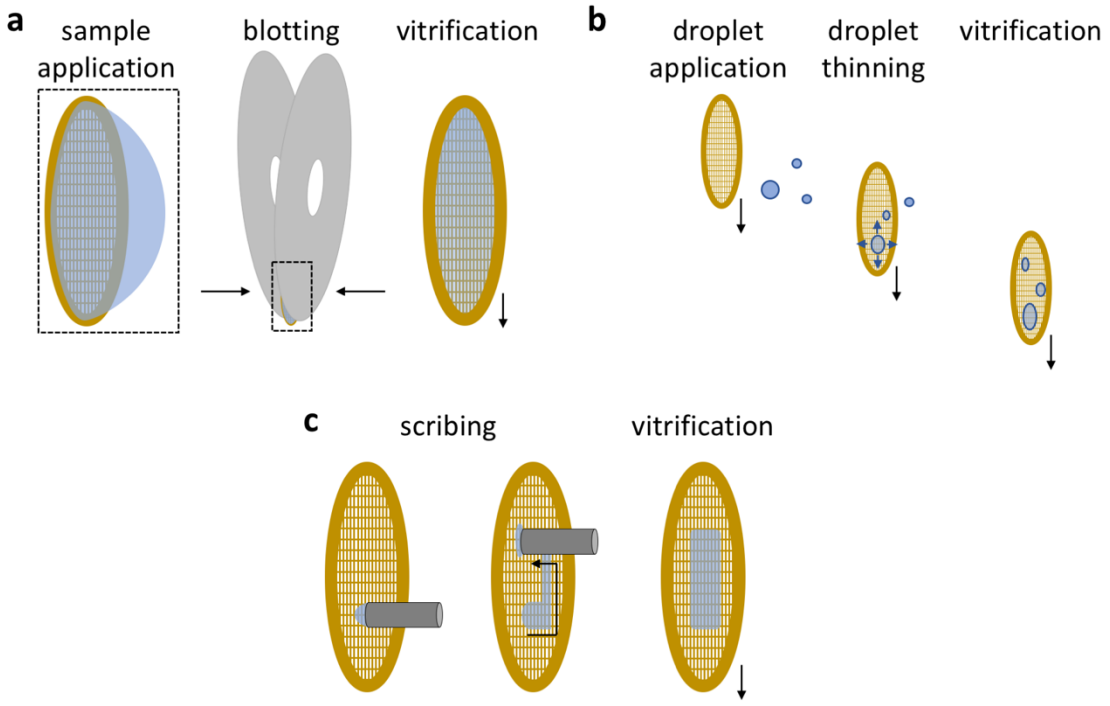


**Figure 1-2: Different cryo-EM grid preparation methods.**

(a) In the blotting method an excess of sample is applied (manually) to the grid. Most of the liquid is blotted off with filter paper and only a thin film remains which is then vitrified by plunging into liquid ethane. (b) In droplet-based sample preparation, the sample is applied as droplets. On the grid, the droplets spread or are thinned and the sample is then vitrified. (c) In the scribing approach, the sample is applied with a pin or capillary in close proximity to the grid. After the area of interest has been covered, the sample is vitrified. Adapted from [86].

### 1.2.2 Limitations of the blotting method

The first limitation that comes with the conventional slow blotting method is that fast reactions cannot be studied because they will have completed at the point of vitrification. This does not play a role when studying equilibrium systems, but is of great importance for time-resolved cryo-EM, as further discussed in section 1.4 Time-resolved cryo-EM.

A second limitation of the blotting method is the exposure of the sample to the air-water interface (AWI). The very thin liquid film needed for cryo-EM has a large surface/volume ratio. It has been known since the establishment of the blotting method that this can cause the particles to interact with the AWI [39], and the problem has regained attention since the 'resolution revolution'. When using unsupported vitreous ice for cryo-EM, about 90% of particles have been shown to interact with one or both air-water interfaces [87]. Binding of proteins to the AWI can cause preferential orientation in the cryo-EM images [88]. Such preferred orientation can lead to difficulties and even artefacts in 3D reconstruction [89]. A simple solution is tilting of the grid for cryo-EM data collection, at the cost of increased ice thickness [90]. There is also evidence that particles can denature at the AWI on the timescale of grid preparation [91]. Ultrathin support films, such as graphene or graphene oxide, have been used to prevent particles interacting with the AWI, and to avoid denaturation or change particle orientation [92]. Alternatively, detergents can reduce the interactions between particles and the AWI, and improve particle behaviour on cryo-EM grids [93, 94].

A third limitation is the blotting step itself: It has been shown that the interplay between grid, sample and filter paper is more complex than one may expect, explaining inconsistent ice thickness between replicate grids [95]. In addition, the blotting step wastes 99.9% of the sample volume applied to the grid, so sample consumption is unnecessarily high [96].

### 1.2.3 Alternative approaches to cryo-EM grid preparation

Alternative cryo-EM grid preparation methods have shown promising results and address some of the limitations of the blotting method outlined above. The alternative approaches to blotting can be divided into droplet-based methods and scribing-based methods (Figure 1-2) [86].

In the droplet-based approach, the sample is applied to the grid as small droplets (around 1-100 µm diameter). The original work by Dubochet and McDowall made use of droplet-based sample application, where droplets of water were sprayed onto a grid and then vitrified [33]. Microfluidic devices were used later to generate sprays, with conceptually similar gas driven nebulisers (or atomisers), and have shown success for single-particle cryo-EM of biological samples [97, 98]. Alternatively, spray droplets smaller than 10 µm have been generated with ultrasonic atomisers and have been used for grid preparation [99]. Piezo-electric dispensers (inkjet technology) offer the advantage of delivering droplets of constant size and on demand [100]. With conventional cryo-EM grids it was found that the larger droplets from piezo dispensers (~ 20 µm) did not form a suitably thin film,

but the use of more hydrophilic ‘self-wicking’ grids has solved this problem [101, 102]. Based on piezo dispensing and ‘self-wicking’ grids, a commercial grid preparation device has been developed that offers lower sample consumption and improved reproducibility as well as more rapid grid preparation compared to the blotting method [103]. Ultrasonic spray based sample application has also been used in combination with ‘self-wicking’ grids [104] or with ‘through-grid wicking’ with glass fibre filters [105], with promising results in terms of ice thickness and grid coverage. A common advantage of the droplet-based methods is the relatively short exposure of the sample to the AWI (around 100 ms or less from sample application to vitrification), which has been shown to reduce particle interaction with the AWI and lead to improved particle orientations [106].

In the scribing approach, the ‘scribing element’ (a pin or capillary) that holds the sample is brought in close proximity to the grid, and the sample forms a liquid bridge between element and grid. Moving the ‘scribing element’ above the grid surface leaves a thin line of sample behind on the grid [86]. The film thickness may be adjusted, for example, by controlled evaporation of the sample or scribing speed [107]. The first scribing-based grid preparation approach used a capillary and demonstrated grid preparation with volumes of less than 20 nL, allowing EM of a single cell lysate [96]. Coupled with a microfluidic purification stage, the low sample volume requirement has allowed purification and structure determination from less than 1 µL of cell lysate [108]. A commercial instrument for cryo-EM grid preparation by scribing uses a pin instead of a capillary, and the sample is vitrified by liquid ethane jets rather than plunging the grid into a liquid ethane reservoir [107].

A summary of current cryo-EM grid preparation methods is given in Table 1-1. Particularly relevant for this work is droplet-based grid preparation, which is well suited for time-resolved studies due to the short delay between sample application and vitrification. However, before discussing time-resolved cryo-EM, it is appropriate to give a short overview of protein structure and dynamics.

**Table 1-1: Overview of grid preparation methods.**

Listed are the method of sample preparation, the minimum sample volume required, the time delay between sample application and vitrification and the respective references. Note that the minimum sample volume listed includes the dead volume of the system, when preparing multiple grids the sample volume per grid may be lower. For droplet-based methods, only the shortest possible time delays are given, longer delays (typically up to ~ 1 s) are possible as well. Adapted from [86].

| sample application | minimum sample volume | time delay (application to vitrification) | references |
|---|---|---|---|
| **blotting** | | | |
| manual (pipette) | 3 µL | ~ 10 s | [38] |
| **droplet-based** | | | |
| gas driven atomiser | 30 µL | min. 10 ms | [97, 98] |
| ultrasonic atomiser | 1 µL | min. 10 ms | [99, 104] |
| piezo dispenser | 3-5 µL | min. 50 ms | [100, 101, 103] |
| **scribing** | | | |
| capillary | 20 nL | 1-3 s | [96, 108] |
| pin printing | 0.5 µL | 1-5 s | [107] |

## 1.3 Protein structure and dynamics

### 1.3.1 Protein structure, from past to present

One of the pioneers of structural biology was William Astbury who worked on the X-ray diffraction of keratin fibres from wool. Based on diffraction patterns, he proposed that the protein polypeptide backbone can adopt a compact $\alpha$-form and an elongated $\beta$-form [109]. These models were later corrected by Pauling [110, 111] and are known today as $\alpha$-helix and $\beta$-sheet, the most common secondary structures in proteins. At the end of the 1950s, the first high resolution protein structures from protein X-ray crystallography directly visualised these secondary

structures and their higher order arrangement (the tertiary structure) [112, 113]. This ground-breaking work by Kendrew and Perutz, paved the way for many other protein structures to be determined by X-ray crystallography. In 1971, the protein data bank (PDB) was established as an online archive for protein structures, with open access [114]. Today, there are more than 185000 structures deposited in the PDB, and X-ray crystallography remains the largest contributor, closely followed by EM (Figure 1-3).

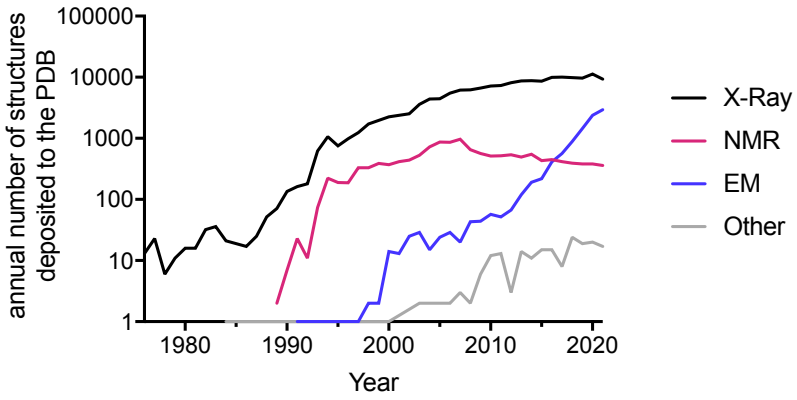


**Figure 1-3: Number of protein structures solved by year and method.**

Shown is the annual number of structures that were deposited to the PDB, separated by experimental method (X-ray crystallography, nuclear magnetic resonance (NMR), EM or other) from 1976 to 2021 (https://www.rcsb.org/stats).

Around the time of the first X-ray crystallographic protein structures, Anfinsen and co-workers proposed that the protein sequence contains the required information for the polypeptide chain to fold into the native protein structure [115]. This link between sequence and structure, later known as 'Anfinsen's dogma', should allow prediction of protein structures based on sequence, in principle. Such predictions were relatively unreliable in the past, unless there was a known structure with high sequence similarity. Recently, there has been a marked improvement in protein structure prediction, with near-experimental accuracy [116]. The improvement comes from the use of machine learning and makes use of existing structural data from the PDB in the training and prediction steps. *In silico* structure prediction can now be done for whole proteomes [117], but is not perfect and the need for experimental validation remains [118].

What does the structure of a protein reveal about its function? Richard Feynman stated, provocatively, that many fundamental biological questions could be answered if "you just look at the thing!" [119]. However, it is not that simple in the

case of protein structures, there is simply too much information in the entire structure so that a full picture may be overwhelming [120]. Additionally, conventional structural biology only depicts snapshots of proteins. Yet, proteins are not static, as shown for example by molecular dynamics simulations, and dynamics can be important for function [121, 122]. Understanding protein function from static structure may therefore be difficult, as “studying the photograph of a racehorse cannot tell you how fast it can run” [123].

### 1.3.2 Proteins are dynamic

How proteins ‘move’ was studied in some detail by Frauenfelder and colleagues, on the example of carbon monoxide binding to myoglobin in the 1970’s [124]. On the basis of distinct CO binding kinetics at different temperatures, they concluded that a number of successive energy barriers must be overcome for binding [125]. Generalisation of this model resulted in the use of energy landscapes with different tiers to describe protein dynamics (Figure 1-4) [126].

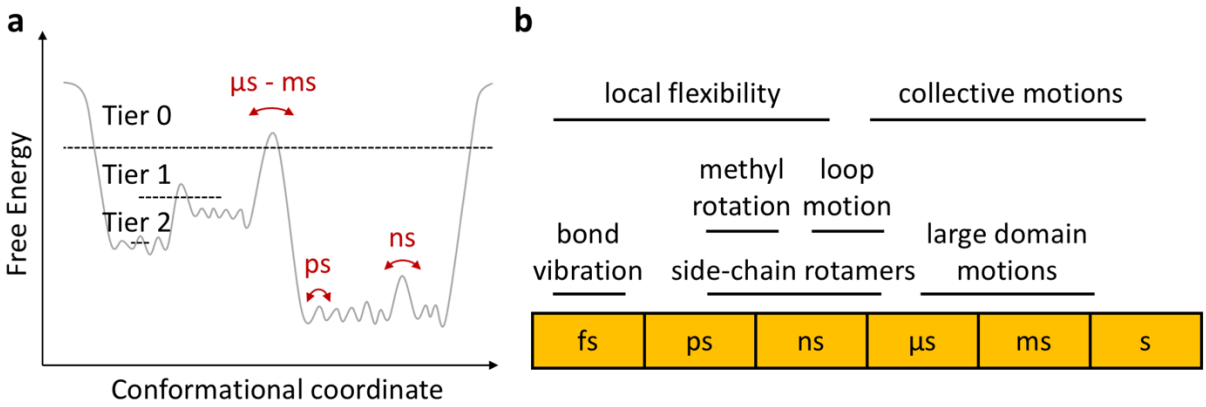


**Figure 1-4: Energy landscape and protein motions.**

(a) Schematic depiction of a protein energy landscape in one dimension. Indicated are the different tiers of protein motion and approximate timescales for the transitions between them in red. Note that the number of states for Tier 1 and Tier 2 is expected to be much higher than shown. (b) Timescale of protein motions, from fs to s. Adapted from [129].

For the example of myoglobin, the protein was considered in two states, CO-bound and CO-unbound. The CO-bound state could be further divided into a small number of Tier 0 substates. The Tier 0-substates are functionally relevant, because each of them is formed at a different rate [127]. From the non-exponential kinetics of CO-rebinding, it could be deduced that each Tier 0 substate can be further divided into Tier 1 substates, and the number of Tier 1 substates is expected to be

large [126]. Finally, evidence for a further division into Tier 2 substates came from measurements at very low temperatures, revealing very small structural changes which occur very rapidly at ambient temperature [126, 128].

The height of the energy barriers between different states or substates determines how quickly these can interconvert, according to the Arrhenius equation:

$$k(H) = A\, e^{\frac{-H}{RT}}$$

Where k is the reaction rate constant, A is the preexponential factor, H is the energy barrier height, R is the gas constant and T is the temperature. The Arrhenius equation is usually adequate, but in some cases variations of it need to be used [126]. It means that larger motions separated by higher energy barriers will occur more slowly, while smaller transitions with lower energy barriers happen more quickly (Figure 1-4). At equilibrium, a protein will likely populate different substates of Tier 0, and will continuously sample the lower tier substates.

### 1.3.3 Reactions of dynamic proteins

However, proteins do not function at equilibrium, they participate in reactions or catalyse them as part of their function. When a single transition state governs the transition between two states, the reaction rate can be described by the Eyring equation, analogous to the empirical Arrhenius equation [130, 131]. Relaxation towards equilibrium then usually follows a simple exponential function, or variations thereof in more complex cases [126, 132]. For bimolecular reactions, a reaction will also depend on formation of an initial protein-substrate complex by diffusion (in the case of an enzymatic reaction). This limits the rate to a maximum of $10^8$-$10^{10}$ $M^{-1}s^{-1}$ [133]. Indeed, there are ‘ideal’ enzymes that achieve such high rates and some proteins may have evolved to optimise the diffusion-limited association step [134, 135].

But how can reactions be pictured in terms of the energy landscape? A surprisingly simple way is to think about reactions as vertical transitions between energy landscapes of different states [136]. The approach is shown in Figure 1-5 and has been successfully applied to cryo-EM data of ligand binding to the large ryanodine receptor [137].

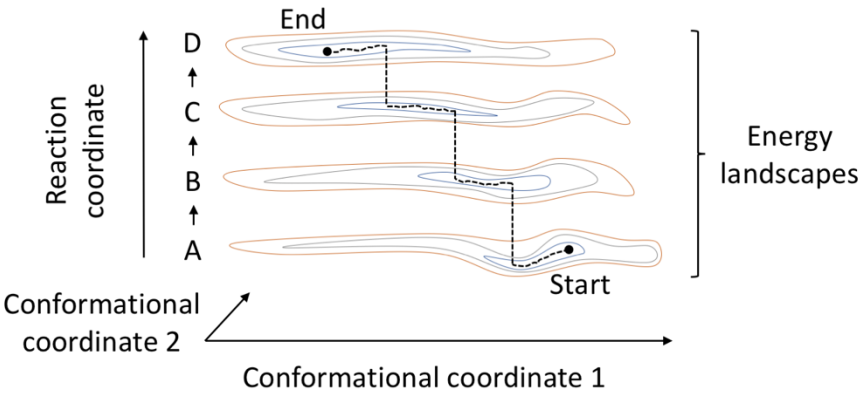


**Figure 1-5: Energy landscapes of reactions.**

Energy landscapes are shown along two conformational coordinates, as coloured contour maps. The reaction starts at state A, where the protein (or system) explores its energy landscape until it transitions, vertically, to state B of the reaction. This is repeated until the reaction is complete and the protein has adopted its final state D. While dividing the reaction into a small number of states may be artificial, it makes the process conceptually simpler and experimentally more feasible. Adapted from [136].

Returning to the analogy of the racehorse, a single snapshot was not sufficient to understand the mechanics of the horse. The solution is to collect a time series of photographs, famously done for the running horse by Eadweard Muybridge and others in the late 1800's [138, 139]. Analogously, collecting a time series of protein structures may help to understand the relation between structure and function and reveal functionally important dynamics. This is what time-resolved structural biology techniques are trying to achieve, among them time-resolved cryo-EM.

## 1.4 Time-resolved cryo-EM

### 1.4.1 General considerations for time-resolved cryo-EM

A definition of time-resolved cryo-EM (TrEM) has been given by Frank [140]:

"Time-resolved […] cryo-EM addresses the need for obtaining information about systems that are not in equilibrium but change over time, until equilibrium is reached"

The structural transitions of interest are therefore not equilibrium fluctuations, but the changes of protein structure during reactions. Because most structural changes are frozen upon vitrification, it is the time from reaction initiation to vitrification that determines how far the reaction has proceeded and what state(s) the protein is in [141]. A small limitation is imposed by the speed of cooling: Energy barriers of 8-10 kJ/mol can be overcome during vitrification, which is on the order of one or

two hydrogen bonds [142, 143]. As a result, most conformations will be kinetically trapped by cooling, but the observed conformational ensemble is slightly biased towards lower energy states [144].

If the reaction is slow and the time delay between reaction initiation and vitrification can be longer than ~20 s, TrEM does not require special instrumentation. The reaction can be initiated manually by mixing, and cryo-EM grids prepared with the conventional blotting technique. This has been used, for example, to study pH-induced conformational transitions of the influenza virus spike protein hemagglutinin [145]. TrEM by blotting has also resolved a number of ribosome translocation intermediates, where the bacterial ribosome is in complex with the GTPase elongation factor G [146]. Systems in a steady state may be studied with this approach as well, provided that the reaction proceeds for long enough [147].

Most enzymatic reactions and protein motions occur faster than seconds [148], and TrEM of these processes requires dedicated instruments for fast reaction initiation and vitrification. The first such instrument was reported in 1991 by Ménétret and colleagues, who triggered the reaction with light [149]. They applied mixture of photocaged AMP-PNP (an ATP analogue) and actomyosin complex to a grid and generated a thin film by blotting. Only 10s of milliseconds before vitrification the AMP-PNP was released from the ‘cage’ by flash illumination, causing rapid dissociation of the actomyosin complex. A similar approach was used to trap crystals of bacteriorhodopsin within 10-20 ms after light-activation, and later with a shorter time delay of only 1 ms [150, 151]. These experiments contributed to an atomic model of the light-driven proton transport and helped to understand how bacteriorhodopsin functions [152]. In a more recent study a similar instrument for light triggered TrEM using a high-power LED has been reported [153].

### 1.4.2 Time-resolved cryo-EM by rapid mixing

While light can be used to trigger reactions with highly accurate timing, relatively few biological reactions are light-dependent. The most versatile method for reaction initiation is probably mixing, and the use of rapid mixing for TrEM was pioneered by Berriman and Unwin. They achieved short delay times of 1-100 ms by preparing a thin film of one reactant by blotting and spraying fine droplets of the second reactant onto the thin film [154]. After landing on the thin film, the droplets spread and mixing occurred by diffusion from the droplet. The sample was vitrified shortly after the spray droplets had impacted the grid. This ‘blot-and-spray’ method was then used to spray acetylcholine onto acetylcholine receptor ‘tubes’ to trap the channel in an open state [155]. Further work allowed the gating mechanism to be described in some detail, with atomic models for the closed and open states [156].

Blotting and spraying also revealed the initial conformational changes of a virus upon being exposed to a change in pH [157]. A similar instrument to that used by Unwin was further developed by White and colleagues from 1995 [158]. They used it to spray ATP onto blotted actomyosin, and follow the rapid dissociation of the actomyosin complex. In subsequent work, formation of the actomyosin complex was studied by spraying myosin onto blotted filamentous actin [159] and the use of electrospray was investigated to generate fine spray droplets [160].

An alternative method was introduced in 2009, where the two reactants are first mixed and then the mixture is sprayed onto an EM-grid and vitrified [97]. Essential to this approach is the thinning of the spray droplets after impacting on the cryo-EM grid and before vitrification (see 1.2 Cryo-EM grid preparation). Applying the 'mix-and-spray' method it was shown that the small and large subunits of the bacterial ribosome can form initial interactions in less than 10 ms [161]. Similar experiments using a modified instrument for the 'mix-and-spray' method were done later by the Frank group [162]. At progressively higher resolutions, Frank and colleagues were able to trap intermediates with 'mix-and-spray' TrEM, first of the ribosome recycling process [163] and then of translation initiation [164] and translation termination [165].

There has been growing interest in TrEM recently, fuelled by the 'resolution revolution', improved classification algorithms and methods to account for continuous protein motions [166, 167]. This has become apparent by an increasing number of instruments being developed for TrEM, making use of variations of the 'mix-and-spray' method [168, 169]. A summary of the current methods is given in Table 1-2.

**Table 1-2: Overview of current TrEM methods**

Listed are the method of reaction initiation, the method of sample application and the approximate minimum time delay and the respective references.

| reaction initiation | sample application | minimum time delay | references |
|---|---|---|---|
| **TrEM by conventional blotting** | | | |
| mixing | blotting | ~ 20 s | [145-147] |
| **Light-triggered TrEM** | | | |
| light | blotting | 1 ms | [149, 150, 153] |
| **'Blot-and-spray'** | | | |
| on-grid mixing | blotting and droplet-based | 1 ms | [154, 158, 160] |
| **'Mix-and-spray'** | | | |
| microfluidic mixer | droplet-based | ~ 10 ms | [97, 162, 169] |
| on-grid mixing | droplet-based | ~ 50 ms | [168] |

### 1.4.3 Promising developments and limitations of time-resolved EM

There have been other interesting instances of time-resolved EM that are beyond classical biological single-particle cryo-EM but may serve as an inspiration for future developments. Zewail and colleagues used methods from ultrafast spectroscopy to image materials with femtosecond time resolution in a modified electron microscope [170]. They also applied this principle to electron tomography, and studied physical properties of biological materials such as amyloid fibrils [171, 172]. Recently, it has been shown that specimen can be melted within the electron microscope by laser irradiation and samples cool sufficiently fast to re-vitrify after irradiation [173]. In the future, this may allow *in situ* time-resolved cryo-EM with microsecond time-resolution [174]. Time-resolved EM can also be done in a more native context: A combination of optogenetics and rapid high-pressure freezing allowed mouse neuron ultrastructure to be trapped at timepoints between 15 ms to 10 s after stimulation. Freeze substitution and electron tomography has given an unprecedented insight into ultrafast endocytosis at the synapse and the role of clathrin in this process [175, 176].

Current single-particle TrEM, with the fastest possible time delays of around 1 ms (Table 1-2), can resolve the large collective protein motions that occur on the millisecond or second timescale. Therefore, it has been used mostly to trap highly distinct structural states, or biochemical states. Smaller motions such as the transitions between Tier 0 and Tier 1 substates (see 1.3 Protein structure and dynamics) will mostly be preserved in the vitrification process, and may be structurally resolved if high resolution is achieved. However, these more subtle and faster protein dynamics will not be temporally resolved, they will have to be separated computationally and their order of appearance, or role in the reaction may remain unclear. While future TrEM methods with improved time resolution may solve this problem, there is also a suite of alternative techniques, some of which have higher temporal resolution that can complement TrEM and can address the microsecond timescale and beyond (see below).

## 1.5 Other time-resolved structural techniques

Historically, time-resolved techniques have used fast detection methods, allowing measurement of the reaction *in situ*. In the 1920's, fast chemical reactions were first studied using the continuous flow method where the reaction is initiated by mixing, and optical measurements are taken through a capillary downstream [177]. Later, the stopped flow technique allowed experiments with much reduced sample volumes and instrument dead times of about 1 ms [178, 179]. The measurement is usually optical, such as fluorescence, absorbance, light scattering or another spectroscopic technique. Stopped flow has been used extensively to characterise the reactions and catalytic cycles of molecular machines, such as the actomyosin ATPase [180-182]. The timescale usually allows successive biochemical steps to be distinguished and can also give insight into millisecond timescale dynamics. While the spatial resolution of classical optical techniques is low, some of them can be very sensitive to the local protein environment. Modern continuous flow devices can achieve dead times as low as a few microseconds, used for example to study fast protein folding reactions [183], and covering the entire timescale of Tier 0 protein dynamics.

Higher resolution insight into Tier 0 protein dynamics requires different techniques. Nuclear magnetic resonance (NMR) has played an important role in resolving microsecond to millisecond dynamics (Tier 0), as it allows different structural states to be distinguished from steady state reactions, and the determination of their interconversion rates [184]. In some cases, NMR has also been used to quantify the faster Tier 1-2 dynamics and draw conclusions about the entropic contributions of the Tier 1-2 states [185]. Single molecule fluorescence methods can reveal

structural heterogeneity and rare events which remain hidden in ensemble techniques [129]. Coupled with Förster resonance energy transfer (FRET), inter-residue distances can be measured in single molecules with high accuracy and sub millisecond time resolution. Using FRET measurements, for example, the rotation of the $F_0F_1$-ATP Synthase was resolved in single molecules, showing that transitions between rotational states are rare and rapid (dwell times > 10 ms and transitions < 1 ms), the different rotational states are thus separated by relatively large energy barriers [186].

Molecular dynamics simulations have played an important role in understanding of protein dynamics, and are capable of providing the most 'complete' picture. In simulations, it is possible to follow how small local structural changes propagate and translate into larger scale motions ('protein quakes') [187, 188]. However, the timescale of molecular simulations is limited by computational power, large systems are typically limited to the microsecond timescale, and even with the fastest computers, simulations remain in the sub millisecond range [189]. Coarse-graining to various levels of detail can speed up simulations and make longer timescales accessible, but at the cost of spatial resolution [190, 191].

Experimentally probing the fast Tier 1-2 protein dynamics requires very high time-resolution. Ultrafast spectroscopic methods can serve this purpose, they use a 'clocking' light pulse to initiate the reaction and a delayed 'probe' pulse to probe the state of the system [192, 193]. In a similar manner, Laue X-ray diffraction has been used to visualise picosecond conformational changes in myoglobin after laser induced photolysis of bound CO [194, 195].

Around 2010, the advent of serial X-ray crystallography marked a paradigm shift in time-resolved crystallography [196]. Originally developed for the use with X-ray free electron lasers (XFELs), the serial crystallography approach was subsequently also used at synchrotron X-ray sources [197, 198]. The X-ray pulses from XFELs are sufficiently bright and short to obtain a diffraction pattern before radiation damage affects the exposed crystal [199]. For reaction initiation with laser pulses, XFEL serial crystallography has been used to study photoinduced processes with a time resolution up to a few femtoseconds [200, 201]. Slower light triggered reactions on the microsecond or millisecond timescale have been studied as well, with XFEL or synchrotron sources [202, 203]. Serial crystallography has also been used with rapid mixing, but the conformational changes must be accommodated by the crystal lattice and the relatively large size of the crystals may limit mixing speeds [204, 205].

For most biological reactions, a combination of methods will be required to describe the underlying protein dynamics, from small side chain motions (Tier 2 states) to collective, large scale conformational changes between biochemical states. A recent demonstration of integrating structural techniques is the visualisation of protein 'breathing motions' that allow aromatic side chains to flip [206]. Cryo-EM, and TrEM in particular, are certainly a valuable addition to the toolbox for investigating protein dynamics, especially for larger molecular machines. But as most experimental methods, TrEM will give an incomplete picture, so that a combination of experiments and computational methods will be needed to understand in detail how protein structure and dynamics contribute to function.

## 1.6 Aim of this Thesis

The 'resolution revolution' in cryo-EM has dramatically changed the field and its role in structural biology. The recent improvements in microscope hardware and image processing software make time-resolved single particle cryo-EM possible at high resolutions, and promise new insights into the large-scale conformational changes of proteins and protein complexes. The aim of this work is the development of fast droplet-based cryo-EM grid preparation methods, their characterisation and application to TrEM.

In Chapter 2, 'A cryo-EM grid preparation device for time-resolved structural studies', an updated custom built device for fast grid preparation is presented and characterised. A voltage-assisted spraying approach is used to atomise the sample, and droplets show sufficient thinning on conventional cryo-EM grids to obtain high-resolution structures. This study served as a starting point for further optimisation and development of the time-resolved EM device (TED).

Chapter 3, 'Sample deposition onto cryo-EM grids: from sprays to jets and back', compares different droplet deposition methods for fast grid preparation. The relation between droplet size and thinning is discussed, and microfluidic gas-dynamic virtual nozzles (GDVNs) are introduced for cryo-EM grid preparation. GDVNs can reduce sample consumption and improve reproducibility compared to the voltage-assisted method from Chapter 2.

Chapter 4, 'On-grid and in-flow mixing for time-resolved cryo-EM', shows how an exemplary reaction, the ATP-induced dissociation of actomyosin, can be visualised by TrEM with the methods introduced in Chapters 2-3. With two different methods for mixing, a range of time delays from ~10 ms to several seconds can be achieved.

The advantages and limitations of the two different approaches are pointed out. This chapter provides some guidelines for the design of TrEM experiments.

In Chapter 5, 'Need for speed: examining protein behaviour during cryo-EM grid preparation at different timescales', droplet-based fast grid preparation is studied in more detail. The interactions between different samples and the AWI are characterised by SPA and cryo-electron tomography. It is found that even the fastest current grid preparation does not eliminate interactions with the AWI, but reduces some of the problems associated with the AWI, such as partial protein denaturation. The in-depth characterisation of droplet-based grid preparation is also relevant for time-resolved experiments.

In Chapter 6, 'Pre-power stroke structure of the Actomyosin Complex', the structure of the actomyosin complex in the pre-power stroke state is presented, solved by TrEM. This chapter serves as a demonstration of the capabilities of current TrEM methods, making use of the methods developed in Chapters 2-5. The pre-power stroke state structure also solves long standing questions about the structural details of the actomyosin catalytic cycle.

The thesis will be concluded with a discussion in Chapter 7, summarising the findings of this work and giving a future perspective for TrEM, its application in structural biology and its role in resolving the relation between protein structure, dynamics and function.

## 1.7 References


1. Busch, H., *Berechnung der Bahn von Kathodenstrahlen im axialsymmetrischen elektromagnetischen Felde.* Annalen der Physik, 1926. **386**(25): p. 974-993.
2. Ruska, E., *The development of the electron microscope and of electron microscopy (Nobel Lecture).* Angewandte Chemie International Edition in English, 1987. **26**(7): p. 595-605.
3. Abbe, E., *Beiträge zur Theorie des Mikroskops und der mikroskopischen Wahrnehmung.* Archiv für mikroskopische Anatomie, 1873. **9**(1): p. 413-468.
4. Knoll, M. and E. Ruska, *Das Elektronenmikroskop.* Zeitschrift für Physik, 1932. **78**(5): p. 318-339.
5. Krause, F., *Das magnetische Elektronenmikroskop und seine Anwendung in der Biologie.* Naturwissenschaften, 1937. **25**(51): p. 817-825.
6. Von Ardenne, M., *Das Elektronen-Rastermikroskop.* Zeitschrift für Physik, 1938. **109**(9): p. 553-572.

7. McMullan, D., *Scanning electron microscopy 1928–1965.* Scanning, 1995. **17**(3): p. 175-185.
8. Ruska, E., *Ein Übermikroskop für Forschungsinstitute.* Naturwissenschaften, 1939. **27**(34): p. 577-582.
9. Von Borries, B., E. Ruska, and H. Ruska, *Bakterien und Virus in übermikroskopischer Aufnahme.* Klinische Wochenschrift, 1938. **17**(27): p. 921-925.
10. Marton, L., *Quelques considérations concernant le pouvoir séparateur en microscopie électronique.* Physica, 1936. **3**(9): p. 959-967.
11. Hall, C.E., *Electron densitometry of stained virus particles.* The Journal of biophysical and biochemical cytology, 1955. **1**(1): p. 1.
12. Brenner, S. and R. Horne, *A negative staining method for high resolution electron microscopy of viruses.* Biochimica et biophysica acta, 1959. **34**: p. 103-110.
13. Gansler, H. and T. Nemetschek, *Phasenkontrast bei der Abbildung biologischer Objekte.* Zeitschrift für Naturforschung B, 1958. **13**(3): p. 190-192.
14. Lenz, F. and W. Scheffels, *Das Zusammenwirken von Phasen-und Amplitudenkontrast in der elektronenmikroskopischen Abbildung.* Zeitschrift für Naturforschung A, 1958. **13**(3): p. 226-230b.
15. Thon, F., *Zur Defokussierungsabhängigkeit des Phasenkontrastes bei der elektronenmikroskopischen Abbildung.* Zeitschrift für Naturforschung A, 1966. **21**(4): p. 476-478.
16. Heidenreich, R.D., W. Hess, and L. Ban, *A test object and criteria for high resolution electron microscopy.* Journal of Applied Crystallography, 1968. **1**(1): p. 1-19.
17. Erickson, H. and A. Klug, *Measurement and compensation of defocusing and aberrations by Fourier processing of electron micrographs.* Philosophical Transactions of the Royal Society of London. B, Biological Sciences, 1971. **261**(837): p. 105-118.
18. De Rosier, D. and A. Klug, *Reconstruction of three dimensional structures from electron micrographs.* Nature, 1968. **217**(5124): p. 130-134.
19. Beer, M., et al., *The possibilities and prospects of obtaining high-resolution information (below 30 Å) on biological material using the electron microscope: Some comments and reports inspired by an EMBO workshop held at Gais, Switzerland, October 1973.* Quarterly Reviews of Biophysics, 1974. **7**(2): p. 211-238.

20. Matricardi, V.R., R.C. Moretz, and D.F. Parsons, *Electron diffraction of wet proteins: catalase.* Science, 1972. **177**(4045): p. 268-270.
21. Taylor, K.A. and R.M. Glaeser, *Electron diffraction of frozen, hydrated protein crystals.* Science, 1974. **186**(4168): p. 1036-1037.
22. Taylor, K.A. and R.M. Glaeser, *Hydrophilic support films of controlled thickness and composition.* Review of Scientific Instruments, 1973. **44**(10): p. 1546-1547.
23. Unwin, P.N.T. and R. Henderson, *Molecular structure determination by electron microscopy of unstained crystalline specimens.* Journal of molecular biology, 1975. **94**(3): p. 425-440.
24. McLachlan Jr, D., *Crystal structure and information theory.* Proceedings of the National Academy of Sciences of the United States of America, 1958. **44**(9): p. 948.
25. Henderson, R. and P.N.T. Unwin, *Three-dimensional model of purple membrane obtained by electron microscopy.* Nature, 1975. **257**(5521): p. 28-32.
26. Frank, J., *Single‐Particle Reconstruction of Biological Molecules—Story in a Sample (Nobel Lecture).* Angewandte Chemie International Edition, 2018. **57**(34): p. 10826-10841.
27. Hoppe, W., *Three-dimensional reconstruction of individual negatively stained yeast fatty-acid synthetase molecules from tilt series in the electron microscope.* Hoppe-Seyler's Z. Physiol. Chem., 1974. **355**: p. 1483-1487.
28. Frank, J., *Averaging of low exposure electron micrographs of non-periodic objects*, in *Single-Particle Cryo-Electron Microscopy: The Path Toward Atomic Resolution: Selected Papers of Joachim Frank with Commentaries*. 1975, World Scientific. p. 69-72.
29. Frank, J., A. Verschoor, and M. Boublik, *Computer averaging of electron micrographs of 40 S ribosomal subunits.* Science, 1981. **214**(4527): p. 1353-1355.
30. Taylor, K.A. and R.M. Glaeser, *Electron microscopy of frozen hydrated biological specimens.* Journal of ultrastructure research, 1976. **55**(3): p. 448-456.
31. Fernández-Morán, H., *Low temperature preparation techniques for electron microscopy of biological specimens based on rapid freezing with liquid helium II.* Annals of the New York Academy of Sciences (US), 1960. **85**.
32. Dubochet, J., *Cryo‐EM—the first thirty years.* Journal of microscopy, 2012. **245**(3): p. 221-224.

33. Dubochet, J. and A. McDowall, *Vitrification of pure water for electron microscopy.* Journal of Microscopy, 1981. **124**(3): p. 3-4.
34. Dubochet, J., *On the Development of Electron Cryo-Microscopy (Nobel Lecture).* Angewandte Chemie International Edition, 2018. **57**(34): p. 10842-10846.
35. Leidenfrost, J.G., *De aquae communis nonnullis qualitatibus tractatus*. 1756: Ovenius.
36. Engstrom, T., et al., *High-resolution single-particle cryo-EM of samples vitrified in boiling nitrogen.* IUCrJ, 2021. **8**(6).
37. Brüggeller, P. and E. Mayer, *Complete vitrification in pure liquid water and dilute aqueous solutions.* Nature, 1980. **288**(5791): p. 569-571.
38. Adrian, M., et al., *Cryo-electron microscopy of viruses.* Nature, 1984. **308**(5954): p. 32-36.
39. Dubochet, J., et al., *Cryo-electron microscopy of vitrified specimens.* Quarterly reviews of biophysics, 1988. **21**(2): p. 129-228.
40. Vogel, R., et al., *Envelope structure of Semliki Forest virus reconstructed from cryo-electron micrographs.* Nature, 1986. **320**(6062): p. 533-535.
41. Jeng, T.-W., et al., *Electron imaging of crotoxin complex thin crystal at 3.5 Å.* Journal of molecular biology, 1984. **175**(1): p. 93-97.
42. Henderson, R., et al., *Structure of purple membrane from Halobacterium halobium: recording, measurement and evaluation of electron micrographs at 3.5 Å resolution.* Ultramicroscopy, 1986. **19**(2): p. 147-178.
43. Henderson, R., et al., *Model for the structure of bacteriorhodopsin based on high-resolution electron cryo-microscopy.* Journal of molecular biology, 1990. **213**(4): p. 899-929.
44. Van Heel, M. and J. Frank, *Use of multivariates statistics in analysing the images of biological macromolecules.* Ultramicroscopy, 1981. **6**(1): p. 187-194.
45. Van Heel, M., *Angular reconstitution: a posteriori assignment of projection directions for 3D reconstruction.* Ultramicroscopy, 1987. **21**(2): p. 111-123.
46. Radermacher, M., et al., *Three-dimensional reconstruction from a single-exposure, random conical tilt series applied to the 50S ribosomal subunit of Escherichia coli.* Journal of microscopy, 1987. **146**(2): p. 113-136.
47. Frank, J., et al., *Three-dimensional reconstruction of the 70S Escherichia coli ribosome in ice: the distribution of ribosomal RNA.* The Journal of cell biology, 1991. **115**(3): p. 597-605.
48. Lambert, O., et al., *Quaternary structure of Octopus vulgaris hemocyanin: three-dimensional reconstruction from frozen-hydrated specimens and*

*intramolecular location of functional units Ove and Ovb.* Journal of molecular biology, 1994. **238**(1): p. 75-87.

49. Radermacher, M., et al., *Cryo-EM of the native structure of the calcium release channel/ryanodine receptor from sarcoplasmic reticulum.* Biophysical journal, 1992. **61**(4): p. 936-940.
50. Kühlbrandt, W., D.N. Wang, and Y. Fujiyoshi, *Atomic model of plant light-harvesting complex by electron crystallography.* Nature, 1994. **367**(6464): p. 614-621.
51. Nogales, E., S. Wolf, and K. Downing, *Structure of the alpha beta tubulin dimer by electron crystallography.* Nature, 1998. **391**(6663): p. 199-203.
52. Henderson, R., *The potential and limitations of neutrons, electrons and X-rays for atomic resolution microscopy of unstained biological molecules.* Quarterly reviews of biophysics, 1995. **28**(2): p. 171-193.
53. Henderson, R., *From electron crystallography to single particle cryoEM (Nobel Lecture).* Angewandte Chemie International Edition, 2018. **57**(34): p. 10804-10825.
54. Böttcher, B., S. Wynne, and R. Crowther, *Determination of the fold of the core protein of hepatitis B virus by electron cryomicroscopy.* Nature, 1997. **386**(6620): p. 88-91.
55. Gabashvili, I.S., et al., *Solution Structure of the E. coli 70S Ribosome at 11.5 Å Resolution.* Cell, 2000. **100**(5): p. 537-549.
56. Conway, J.F., et al., *Visualization of a 4-helix bundle in the hepatitis B virus capsid by cryo-electron microscopy.* Nature, 1997. **386**(6620): p. 91-94.
57. Rosenthal, P.B. and R. Henderson, *Optimal determination of particle orientation, absolute hand, and contrast loss in single-particle electron cryomicroscopy.* Journal of molecular biology, 2003. **333**(4): p. 721-745.
58. Wilson, A., *Determination of Absolute from Relative X-Ray Intensity Data.* Nature, 1942. **150**(3796): p. 152-152.
59. Singer, A., *Wilson statistics: derivation, generalization and applications to electron cryomicroscopy.* Acta Crystallographica Section A: Foundations and Advances, 2021. **77**(5).
60. Xuong, N.-H., et al. *First use of a high-sensitivity active pixel sensor array as a detector for electron microscopy*. in *Sensors and Camera Systems for Scientific, Industrial, and Digital Photography Applications V*. 2004. International Society for Optics and Photonics.
61. McMullan, G., et al., *Detective quantum efficiency of electron area detectors in electron microscopy.* Ultramicroscopy, 2009. **109**(9): p. 1126-1143.

62. McMullan, G., et al., *Enhanced imaging in low dose electron microscopy using electron counting.* Ultramicroscopy, 2009. **109**(12): p. 1411-1416.
63. Li, X., et al., *Electron counting and beam-induced motion correction enable near-atomic-resolution single-particle cryo-EM.* Nature methods, 2013. **10**(6): p. 584-590.
64. McMullan, G., et al., *Comparison of optimal performance at 300 keV of three direct electron detectors for use in low dose electron microscopy.* Ultramicroscopy, 2014. **147**: p. 156-163.
65. Scheres, S.H., et al., *Disentangling conformational states of macromolecules in 3D-EM through likelihood optimization.* Nature Methods, 2007. **4**(1): p. 27-29.
66. Scheres, S.H., *A Bayesian view on cryo-EM structure determination.* Journal of molecular biology, 2012. **415**(2): p. 406-418.
67. Kühlbrandt, W., *The resolution revolution.* Science, 2014. **343**(6178): p. 1443-1444.
68. Callaway, E., *The revolution will not be crystallized: a new method sweeps through structural biology.* Nature News, 2015. **525**(7568): p. 172.
69. Liao, M., et al., *Structure of the TRPV1 ion channel determined by electron cryo-microscopy.* Nature, 2013. **504**(7478): p. 107-112.
70. Amunts, A., et al., *Structure of the yeast mitochondrial large ribosomal subunit.* Science, 2014. **343**(6178): p. 1485-1489.
71. Vinothkumar, K.R., J. Zhu, and J. Hirst, *Architecture of mammalian respiratory complex I.* Nature, 2014. **515**(7525): p. 80-84.
72. Nakane, T., et al., *Single-particle cryo-EM at atomic resolution.* Nature, 2020. **587**(7832): p. 152-156.
73. Yip, K.M., et al., *Atomic-resolution protein structure determination by cryo-EM.* Nature, 2020. **587**(7832): p. 157-161.
74. Russo, C.J. and L.A. Passmore, *Ultrastable gold substrates for electron cryomicroscopy.* Science, 2014. **346**(6215): p. 1377-1380.
75. Naydenova, K., P. Jia, and C.J. Russo, *Cryo-EM with sub–1 Å specimen movement.* Science, 2020. **370**(6513): p. 223-226.
76. Wu, M., G.C. Lander, and M.A. Herzik Jr, *Sub-2 Angstrom resolution structure determination using single-particle cryo-EM at 200 keV.* Journal of structural biology: X, 2020. **4**: p. 100020.
77. Naydenova, K., et al., *CryoEM at 100 keV: a demonstration and prospects.* IUCrJ, 2019. **6**(6): p. 1086-1098.

78. Tegunov, D., et al., *Multi-particle cryo-EM refinement with M visualizes ribosome-antibiotic complex at 3.5 Å in cells.* Nature Methods, 2021. **18**(2): p. 186-193.
79. Marr, C.R., S. Benlekbir, and J.L. Rubinstein, *Fabrication of carbon films with∼ 500 nm holes for cryo-EM with a direct detector device.* Journal of Structural Biology, 2014. **185**(1): p. 42-47.
80. Naydenova, K., M.J. Peet, and C.J. Russo, *Multifunctional graphene supports for electron cryomicroscopy.* Proceedings of the National Academy of Sciences, 2019. **116**(24): p. 11718-11724.
81. Wang, F., et al., *General and robust covalently linked graphene oxide affinity grids for high-resolution cryo-EM.* Proceedings of the National Academy of Sciences, 2020. **117**(39): p. 24269-24273.
82. Tivol, W.F., A. Briegel, and G.J. Jensen, *An improved cryogen for plunge freezing.* Microscopy and Microanalysis, 2008. **14**(5): p. 375-379.
83. Glaeser, R.M., *How good can cryo-EM become?* Nature methods, 2016. **13**(1): p. 28-32.
84. Wu, S., J.-P. Armache, and Y. Cheng, *Single-particle cryo-EM data acquisition by using direct electron detection camera.* Journal of Electron Microscopy, 2015. **65**(1): p. 35-41.
85. Warkentin, M., J.P. Sethna, and R.E. Thorne, *Critical droplet theory explains the glass formability of aqueous solutions.* Physical review letters, 2013. **110**(1): p. 015703.
86. Weissenberger, G., R.J. Henderikx, and P.J. Peters, *Understanding the invisible hands of sample preparation for cryo-EM.* Nature Methods, 2021. **18**(5): p. 463-471.
87. Noble, A.J., et al., *Routine single particle CryoEM sample and grid characterization by tomography.* Elife, 2018. **7**: p. e34257.
88. Taylor, K.A. and R.M. Glaeser, *Retrospective on the early development of cryoelectron microscopy of macromolecules and a prospective on opportunities for the future.* Journal of structural biology, 2008. **163**(3): p. 214-223.
89. Naydenova, K. and C.J. Russo, *Measuring the effects of particle orientation to improve the efficiency of electron cryomicroscopy.* Nature communications, 2017. **8**(1): p. 1-5.
90. Tan, Y.Z., et al., *Addressing preferred specimen orientation in single-particle cryo-EM through tilting.* Nature methods, 2017. **14**(8): p. 793-796.
91. D'Imprima, E., et al., *Protein denaturation at the air-water interface and how to prevent it.* Elife, 2019. **8**: p. e42747.

92. Naydenova, K., et al., *Structure of the SARS-CoV-2 RNA-dependent RNA polymerase in the presence of favipiravir-RTP.* Proceedings of the National Academy of Sciences, 2021. **118**(7).
93. Chen, J., et al., *Eliminating effects of particle adsorption to the air/water interface in single-particle cryo-electron microscopy: Bacterial RNA polymerase and CHAPSO.* Journal of structural biology: X, 2019. **1**: p. 100005.
94. Li, B., et al., *Effect of charge on protein preferred orientation at the air–water interface in cryo-electron microscopy.* Journal of Structural Biology, 2021. **213**(4): p. 107783.
95. Armstrong, M., et al., *Microscale fluid behavior during cryo-EM sample blotting.* Biophysical journal, 2020. **118**(3): p. 708-719.
96. Arnold, S.A., et al., *Blotting-free and lossless cryo-electron microscopy grid preparation from nanoliter-sized protein samples and single-cell extracts.* Journal of structural biology, 2017. **197**(3): p. 220-226.
97. Lu, Z., et al., *Monolithic microfluidic mixing–spraying devices for time-resolved cryo-electron microscopy.* Journal of structural biology, 2009. **168**(3): p. 388-395.
98. Feng, X., et al., *A fast and effective microfluidic spraying-plunging method for high-resolution single-particle cryo-EM.* Structure, 2017. **25**(4): p. 663-670. e3.
99. Ashtiani, D., et al., *Delivery of femtolitre droplets using surface acoustic wave based atomisation for cryo-EM grid preparation.* Journal of structural biology, 2018. **203**(2): p. 94-101.
100. Jain, T., et al., *Spotiton: a prototype for an integrated inkjet dispense and vitrification system for cryo-TEM.* Journal of structural biology, 2012. **179**(1): p. 68-75.
101. Dandey, V.P., et al., *Spotiton: New features and applications.* Journal of structural biology, 2018. **202**(2): p. 161-169.
102. Wei, H., et al., *Optimizing "self-wicking" nanowire grids.* Journal of structural biology, 2018. **202**(2): p. 170-174.
103. Darrow, M.C., et al., *Chameleon: next generation sample preparation for cryoEM based on spotiton.* Microscopy and Microanalysis, 2019. **25**(S2): p. 994-995.
104. Rubinstein, J.L., et al., *Shake-it-off: a simple ultrasonic cryo-EM specimen-preparation device.* Acta Crystallographica Section D: Structural Biology, 2019. **75**(12).

105. Tan, Y.Z. and J.L. Rubinstein, *Through-grid wicking enables high-speed cryoEM specimen preparation.* Acta Crystallographica Section D: Structural Biology, 2020. **76**(11).
106. Noble, A.J., et al., *Reducing effects of particle adsorption to the air–water interface in cryo-EM.* Nature methods, 2018. **15**(10): p. 793-795.
107. Ravelli, R.B., et al., *Cryo-EM structures from sub-nl volumes using pin-printing and jet vitrification.* Nature communications, 2020. **11**(1): p. 1-9.
108. Schmidli, C., et al., *Microfluidic protein isolation and sample preparation for high-resolution cryo-EM.* Proceedings of the National Academy of Sciences, 2019. **116**(30): p. 15007-15012.
109. Astbury, W.T. and A. Street, *X-ray studies of the structure of hair, wool, and related fibres.-I. General.* Philosophical Transactions of the Royal Society of London. Series A, Containing Papers of a Mathematical or Physical Character, 1931. **230**(681-693): p. 75-101.
110. Pauling, L., R.B. Corey, and H.R. Branson, *The structure of proteins: two hydrogen-bonded helical configurations of the polypeptide chain.* Proceedings of the National Academy of Sciences, 1951. **37**(4): p. 205-211.
111. Pauling, L. and R.B. Corey, *The pleated sheet, a new layer configuration of polypeptide chains.* Proceedings of the National Academy of Sciences of the United States of America, 1951. **37**(5): p. 251.
112. Kendrew, J.C., et al., *A three-dimensional model of the myoglobin molecule obtained by x-ray analysis.* Nature, 1958. **181**(4610): p. 662-666.
113. Perutz, M.F., et al., *Structure of hæmoglobin: a three-dimensional Fourier synthesis at 5.5-Å. resolution, obtained by X-ray analysis.* Nature, 1960. **185**(4711): p. 416-422.
114. Berman, H.M., et al., *The protein data bank.* Nucleic acids research, 2000. **28**(1): p. 235-242.
115. Anfinsen, C.B., et al., *The kinetics of formation of native ribonuclease during oxidation of the reduced polypeptide chain.* Proceedings of the National Academy of Sciences of the United States of America, 1961. **47**(9): p. 1309.
116. Jumper, J., et al., *Highly accurate protein structure prediction with AlphaFold.* Nature, 2021. **596**(7873): p. 583-589.
117. Tunyasuvunakool, K., et al., *Highly accurate protein structure prediction for the human proteome.* Nature, 2021. **596**(7873): p. 590-596.
118. Moore, P.B., et al., *The protein-folding problem: Not yet solved.* Science, 2022. **375**(6580): p. 507-507.
119. Feynman, R., *There's plenty of room at the bottom.* Engineering and science, 1959. **23**(5): p. 22-36.

120. Perutz, M., et al., *Three-dimensional Fourier synthesis of horse oxyhaemoglobin at 2.8 Å resolution: the atomic model.* Nature, 1968. **219**(5150): p. 131-139.
121. McCammon, J.A., et al., *The hinge-bending mode in lysozyme.* Nature, 1976. **262**(5566): p. 325-326.
122. McCammon, J.A., B.R. Gelin, and M. Karplus, *Dynamics of folded proteins.* Nature, 1977. **267**(5612): p. 585-590.
123. Engen, J.R. and E.A. Komives, *Complementarity of hydrogen/deuterium exchange mass spectrometry and cryo-electron microscopy.* Trends in Biochemical Sciences, 2020. **45**(10): p. 906-918.
124. Austin, R., et al., *Dynamics of carbon monoxide binding by heme proteins.* Science, 1973. **181**(4099): p. 541-543.
125. Austin, R.H., et al., *Dynamics of ligand binding to myoglobin.* Biochemistry, 1975. **14**(24): p. 5355-5373.
126. Frauenfelder, H., S.G. Sligar, and P.G. Wolynes, *The energy landscapes and motions of proteins.* Science, 1991. **254**(5038): p. 1598-1603.
127. Ansari, A., et al., *Rebinding and relaxation in the myoglobin pocket.* Biophysical chemistry, 1987. **26**(2-3): p. 337-355.
128. Köhler, W. and J. Friedrich, *Probing of conformational relaxation processes of proteins by frequency labeling of optical states.* The Journal of Chemical Physics, 1989. **90**(2): p. 1270-1273.
129. Henzler-Wildman, K. and D. Kern, *Dynamic personalities of proteins.* Nature, 2007. **450**(7172): p. 964-972.
130. Eyring, H., *The activated complex in chemical reactions.* The Journal of Chemical Physics, 1935. **3**(2): p. 107-115.
131. Evans, M.G. and M. Polanyi, *Some applications of the transition state method to the calculation of reaction velocities, especially in solution.* Transactions of the Faraday Society, 1935. **31**: p. 875-894.
132. Petrich, J.W., et al., *Ligand binding and protein relaxation in heme proteins: A room temperature analysis of nitric oxide geminate recombination.* Biochemistry, 1991. **30**(16): p. 3975-3987.
133. Alberty, R.A. and G.G. Hammes, *Application of the theory of diffusion-controlled reactions to enzyme kinetics.* The Journal of Physical Chemistry, 1958. **62**(2): p. 154-159.
134. Koenig, S.H. and R.D. Brown, *H2CO3 as substrate for carbonic anhydrase in the dehydration of HCO3.* Proceedings of the National Academy of Sciences, 1972. **69**(9): p. 2422-2425.

135. Payens, T., *Why are enzymes so large?* Trends in Biochemical Sciences, 1983. **8**(2): p. 46.
136. Ourmazd, A., K. Moffat, and E.E. Lattman, *Structural biology is solved—now what?* Nature methods, 2022. **19**(1): p. 24-26.
137. Dashti, A., et al., *Retrieving functional pathways of biomolecules from single-particle snapshots.* Nature communications, 2020. **11**(1): p. 1-14.
138. Muybridge, E., *The science of the horse's motions.* Scientific American, 1882. **14**(346).
139. Marey, E., *Méchanique animale.* Nature, 1894. **1119**: p. 569-570.
140. Frank, J., *Time-resolved cryo-electron microscopy: Recent progress.* Journal of structural biology, 2017. **200**(3): p. 303-306.
141. Moffat, K. and R. Henderson, *Freeze trapping of reaction intermediates.* Current opinion in structural biology, 1995. **5**(5): p. 656-663.
142. Kabsch, W. and C. Sander, *Dictionary of protein secondary structure: pattern recognition of hydrogen-bonded and geometrical features.* Biopolymers: Original Research on Biomolecules, 1983. **22**(12): p. 2577-2637.
143. Preißner, R., U. Egner, and W. Saenger, *Occurrence of bifurcated three-center hydrogen bonds in protpins.* FEBS letters, 1991. **288**(1-2): p. 192-196.
144. Bock, L.V. and H. Grubmüller, *Effects of cryo-EM cooling on structural ensembles.* bioRxiv, 2021.
145. Benton, D.J., et al., *Structural transitions in influenza haemagglutinin at membrane fusion pH.* Nature, 2020. **583**(7814): p. 150-153.
146. Carbone, C.E., et al., *Time-resolved cryo-EM visualizes ribosomal translocation with EF-G and GTP.* Nature communications, 2021. **12**(1): p. 1-13.
147. Walker, M., et al., *Electron cryomicroscopy of acto-myosin-S1 during steady-state ATP hydrolysis.* Biophysical journal, 1994. **66**(5): p. 1563-1572.
148. Bar-Even, A., et al., *The moderately efficient enzyme: evolutionary and physicochemical trends shaping enzyme parameters.* Biochemistry, 2011. **50**(21): p. 4402-4410.
149. Ménétret, J.-F., et al., *Time-resolved cryo-electron microscopic study of the dissociation of actomyosin induced by photolysis of photolabile nucleotides.* Journal of molecular biology, 1991. **219**(2): p. 139-144.

150. Subramaniam, S., et al., *Electron diffraction analysis of structural changes in the photocycle of bacteriorhodopsin.* The EMBO journal, 1993. **12**(1): p. 1-8.
151. Subramaniam, S. and R. Henderson, *Electron crystallography of bacteriorhodopsin with millisecond time resolution.* Journal of structural biology, 1999. **128**(1): p. 19-25.
152. Subramaniam, S. and R. Henderson, *Molecular mechanism of vectorial proton translocation by bacteriorhodopsin.* Nature, 2000. **406**(6796): p. 653-657.
153. Yoder, N., et al., *Light-coupled cryo-plunger for time-resolved cryo-EM.* Journal of structural biology, 2020. **212**(3): p. 107624.
154. Berriman, J. and N. Unwin, *Analysis of transient structures by cryo-microscopy combined with rapid mixing of spray droplets.* Ultramicroscopy, 1994. **56**(4): p. 241-252.
155. Unwin, N., *Acetylcholine receptor channel imaged in the open state.* Nature, 1995. **373**(6509): p. 37-43.
156. Unwin, N. and Y. Fujiyoshi, *Gating movement of acetylcholine receptor caught by plunge-freezing.* Journal of molecular biology, 2012. **422**(5): p. 617-634.
157. Fuller, S.D., et al., *Low pH induces swiveling of the glycoprotein heterodimers in the Semliki Forest virus spike complex.* Cell, 1995. **81**(5): p. 715-725.
158. Walker, M., J. Trinick, and H. White, *Millisecond time resolution electron cryo-microscopy of the M-ATP transient kinetic state of the acto-myosin ATPase.* Biophysical journal, 1995. **68**(4 Suppl): p. 87S.
159. Walker, M., et al., *Observation of transient disorder during myosin subfragment-1 binding to actin by stopped-flow fluorescence and millisecond time resolution electron cryomicroscopy: evidence that the start of the crossbridge power stroke in muscle has variable geometry.* Proceedings of the National Academy of Sciences, 1999. **96**(2): p. 465-470.
160. White, H., et al., *A second generation apparatus for time-resolved electron cryo-microscopy using stepper motors and electrospray.* Journal of structural biology, 2003. **144**(1-2): p. 246-252.
161. Shaikh, T.R., et al., *Initial bridges between two ribosomal subunits are formed within 9.4 milliseconds, as studied by time-resolved cryo-EM.* Proceedings of the National Academy of Sciences, 2014. **111**(27): p. 9822-9827.

162. Chen, B., et al., *Structural dynamics of ribosome subunit association studied by mixing-spraying time-resolved cryogenic electron microscopy.* Structure, 2015. **23**(6): p. 1097-1105.
163. Fu, Z., et al., *Key Intermediates in Ribosome Recycling Visualized by Time-Resolved Cryoelectron Microscopy.* Structure, 2016. **24**(12): p. 2092-2101.
164. Kaledhonkar, S., et al., *Late steps in bacterial translation initiation visualized using time-resolved cryo-EM.* Nature, 2019. **570**(7761): p. 400.
165. Fu, Z., et al., *The structural basis for release-factor activation during translation termination revealed by time-resolved cryogenic electron microscopy.* Nature communications, 2019. **10**(1): p. 1-7.
166. Dance, A., *Molecular motion on ice.* Nature Methods, 2020: p. 1-5.
167. Nakane, T., et al., *Characterisation of molecular motions in cryo-EM single-particle data by multi-body refinement in RELION.* Elife, 2018. **7**: p. e36861.
168. Dandey, V.P., et al., *Time-resolved cryo-EM using Spotiton.* Nature Methods, 2020. **17**(9): p. 897-900.
169. Mäeots, M.-E., et al., *Modular microfluidics enables kinetic insight from time-resolved cryo-EM.* Nature communications, 2020. **11**(1): p. 1-14.
170. Barwick, B., et al., *4D imaging of transient structures and morphologies in ultrafast electron microscopy.* Science, 2008. **322**(5905): p. 1227-1231.
171. Kwon, O.-H. and A.H. Zewail, *4D electron tomography.* Science, 2010. **328**(5986): p. 1668-1673.
172. Fitzpatrick, A.W., G.M. Vanacore, and A.H. Zewail, *Nanomechanics and intermolecular forces of amyloid revealed by four-dimensional electron microscopy.* Proceedings of the National Academy of Sciences, 2015. **112**(11): p. 3380-3385.
173. Voss, J.M., et al., *Microsecond melting and revitrification of cryo samples.* Structural Dynamics, 2021. **8**(5): p. 054302.
174. Voss, J.M., et al., *Rapid melting and revitrification as an approach to microsecond time-resolved cryo-electron microscopy.* Chemical Physics Letters, 2021. **778**: p. 138812.
175. Watanabe, S., et al., *Ultrafast endocytosis at mouse hippocampal synapses.* Nature, 2013. **504**(7479): p. 242-247.
176. Watanabe, S., et al., *Clathrin regenerates synaptic vesicles from endosomes.* Nature, 2014. **515**(7526): p. 228-233.
177. Hartridge, H. and F.J.W. Roughton, *A method of measuring the velocity of very rapid chemical reactions.* Proceedings of the Royal Society of London. Series A, Containing Papers of a Mathematical and Physical Character, 1923. **104**(726): p. 376-394.

178. Chance, B., *Rapid and sensitive spectrophotometry. I. The accelerated and stopped-flow methods for the measurement of the reaction kinetics and spectra of unstable compounds in the visible region of the spectrum.* Review of Scientific Instruments, 1951. **22**(8): p. 619-627.
179. Gibson, Q., *Stopped-flow apparatus for the study of rapid reactions.* Discussions of the Faraday Society, 1954. **17**: p. 137-139.
180. Lymn, R. and E.W. Taylor, *Mechanism of adenosine triphosphate hydrolysis by actomyosin.* Biochemistry, 1971. **10**(25): p. 4617-4624.
181. Siemankowski, R.F. and H.D. White, *Kinetics of the interaction between actin, ADP, and cardiac myosin-S1.* Journal of Biological Chemistry, 1984. **259**(8): p. 5045-5053.
182. Liu, Y., et al., *Omecamtiv Mecarbil modulates the kinetic and motile properties of porcine β-cardiac myosin.* Biochemistry, 2015. **54**(10): p. 1963-1975.
183. Mitić, S., et al., *Microsecond time-scale kinetics of transient biochemical reactions.* PloS one, 2017. **12**(10): p. e0185888.
184. Kern, D., E.Z. Eisenmesser, and M. Wolf-Watz, *Enzyme dynamics during catalysis measured by NMR spectroscopy*, in *Methods in enzymology*. 2005, Elsevier. p. 507-524.
185. Frederick, K.K., et al., *Conformational entropy in molecular recognition by proteins.* Nature, 2007. **448**(7151): p. 325-329.
186. Diez, M., et al., *Proton-powered subunit rotation in single membrane-bound F0F1-ATP synthase.* Nature structural & molecular biology, 2004. **11**(2): p. 135-141.
187. Henzler-Wildman, K.A., et al., *A hierarchy of timescales in protein dynamics is linked to enzyme catalysis.* Nature, 2007. **450**(7171): p. 913-916.
188. Ansari, A., et al., *Protein states and proteinquakes.* Proceedings of the National Academy of Sciences, 1985. **82**(15): p. 5000-5004.
189. Shaw, D.E., et al. *Anton 3: twenty microseconds of molecular dynamics simulation before lunch*. in *Proceedings of the International Conference for High Performance Computing, Networking, Storage and Analysis*. 2021.
190. Souza, P.C., et al., *Martini 3: a general purpose force field for coarse-grained molecular dynamics.* Nature methods, 2021. **18**(4): p. 382-388.
191. Solernou, A., et al., *Fluctuating Finite Element Analysis (FFEA): A continuum mechanics software tool for mesoscale simulation of biomolecules.* PLoS computational biology, 2018. **14**(3): p. e1005897.
192. Zewail, A.H., *Femtochemistry: Atomic-scale dynamics of the chemical bond.* The Journal of Physical Chemistry A, 2000. **104**(24): p. 5660-5694.

193. Fröbel, S., et al., *Photoinduced electron transfer between psoralens and DNA: Influence of DNA sequence and substitution.* ChemPhysChem, 2016. **17**(9): p. 1377-1386.
194. Schotte, F., et al., *Picosecond time-resolved X-ray crystallography: probing protein function in real time.* Journal of structural biology, 2004. **147**(3): p. 235-246.
195. Moffat, K., *Laue diffraction and time-resolved crystallography: a personal history.* Philosophical Transactions of the Royal Society A, 2019. **377**(2147): p. 20180243.
196. Schlichting, I., *Serial femtosecond crystallography: the first five years.* IUCrJ, 2015. **2**(2): p. 246-255.
197. Chapman, H.N., et al., *Femtosecond X-ray protein nanocrystallography.* Nature, 2011. **470**(7332): p. 73.
198. Stellato, F., et al., *Room-temperature macromolecular serial crystallography using synchrotron radiation.* IUCrJ, 2014. **1**(4): p. 204-212.
199. Neutze, R., et al., *Potential for biomolecular imaging with femtosecond X-ray pulses.* Nature, 2000. **406**(6797): p. 752-757.
200. Pande, K., et al., *Femtosecond structural dynamics drives the trans/cis isomerization in photoactive yellow protein.* Science, 2016. **352**(6286): p. 725-729.
201. Hosseinizadeh, A., et al., *Few-fs resolution of a photoactive protein traversing a conical intersection.* Nature, 2021. **599**(7886): p. 697-701.
202. Suga, M., et al., *Light-induced structural changes and the site of O= O bond formation in PSII caught by XFEL.* Nature, 2017. **543**(7643): p. 131-135.
203. Weinert, T., et al., *Proton uptake mechanism in bacteriorhodopsin captured by serial synchrotron crystallography.* Science, 2019. **365**(6448): p. 61-65.
204. Stagno, J., et al., *Structures of riboswitch RNA reaction states by mix-and-inject XFEL serial crystallography.* Nature, 2017. **541**(7636): p. 242-246.
205. Levantino, M., et al., *Using synchrotrons and XFELs for time-resolved X-ray crystallography and solution scattering experiments on biomolecules.* Current opinion in structural biology, 2015. **35**: p. 41-48.
206. Mariño Pérez, L., et al., *Visualizing protein breathing motions associated with aromatic ring flipping.* Nature, 2022: p. 1-6.

# Chapter 2 A cryo-EM grid preparation device for time-resolved structural studies

Published in edited form as: Dimitrios Kontziampasis, David P. Klebl, Matthew G. Iadanza, Charlotte A. Scarff, Florian Kopf, Frank Sobott, Diana C. F. Monteiro, Martin Trebbin, Stephen P. Muench, and Howard D. White. "A cryo-EM grid preparation device for time-resolved structural studies." IUCrJ 6, no. 6 (2019): 1024-1031.

## 2.1 Abstract

Structural biology generally provides static snapshots of protein conformations that can provide information on the functional mechanisms of biological systems. Time-resolved structural biology provides a means to visualize, at near-atomic resolution, the dynamic conformational changes that macromolecules undergo as they function. X-ray free-electron-laser technology has provided a powerful tool to study enzyme mechanisms at atomic resolution, typically in the femtosecond to picosecond timeframe. Complementary to this, recent advances in the resolution obtainable by electron microscopy and the broad range of samples that can be studied make it ideally suited to time-resolved approaches in the microsecond to millisecond timeframe to study large loop and domain motions in biomolecules. Here we describe a cryo-EM grid preparation device that permits rapid mixing, voltage-assisted spraying and vitrification of samples. It is shown that the device produces grids of sufficient ice quality to enable data collection from single grids that results in a sub-4 Å reconstruction. Rapid mixing can be achieved by blot-and-spray or mix-and-spray approaches with a delay of ∼10 ms, providing greater temporal resolution than previously reported mix-and-spray approaches.

## 2.2 Introduction

Our fundamental understanding of biological processes is often underpinned by structural biology, which ultimately may assist our ability to design tailored medicines through structure-based drug design [1]. Advances in technology are allowing us to determine the structure of more complicated and challenging systems. Yet, these methods typically yield structural snapshots of single states of otherwise dynamic protein systems. Better understanding of molecular mechanisms in biology requires time resolution, which is restricted by current technology. X-ray free-electron-laser technology can resolve side-chain movements during catalysis on the picosecond to minute timescale, but its use is limited to samples that form ordered micro-crystals [2, 3]. Cryo-electron-

microscopy (cryo-EM) is not constrained by the crystal lattice and allows for structure determination of large non-symmetric macromolecular complex structures in solution, to near-atomic resolution [4]. Cryo-EM has been used to visualize large structural changes in proteins and protein complexes on the millisecond timescale [5] and used to determine the structure of multiple conformational states exhibited by numerous macromolecular systems, such as the ribosome and rotary F-ATPase [6, 7]. However, it has proven difficult to trap different kinetic sub-states and, although computational sorting can provide different conformations, it does not provide information on the order of catalysis, or the lifetime of the intermediates [8].

The recent renaissance in cryo-EM has been fuelled by rapid developments in microscopes, direct electron detectors and ever more sophisticated data-processing algorithms, but a current bottleneck still resides within the sample-preparation procedure, which has changed little over the last 30 years. There have been recent advances in grid-production technology such as Spotiton and VitroJet, which show great promise in producing high-quality and consistent ice but they are not currently capable of time-resolved applications [9, 10].

Time-resolved cryo-EM (TrEM) is an ideal method to study conformational changes occurring on the microsecond to millisecond timescale [11, 12], providing snapshots of conformational states at sub-nanometre resolutions that can be put in order to understand mechanisms on a broad range of specimens. TrEM experiments have previously been demonstrated using a blot-and-spray approach; applying the protein of interest to an EM grid and pre-blotting before spraying substrate to initiate a reaction, followed by rapid plunging into liquid ethane to vitrify and stop the reaction after a specific time delay. This was demonstrated by the ground-breaking work on the acetylcholine receptor [13]. Through spraying of substrate mixed with a fiducial marker (ferritin) upon a pre-blotted EM grid, and taking account of the diffusion edge of the substrate, it was possible to achieve time-resolutions as low as 2 ms for the mixing of acetylcholine with the acetyl-choline receptor [14]. This approach can be challenging because of difficulties in getting consistent mixing across an EM grid, and requires high substrate concentrations and fiducial markers. An alternative is the mix-and-spray approach where substrate and protein can be pre-mixed before directly spraying onto a fast-moving EM grid, which is plunged into liquid ethane [15]. This technique has shown considerable success for studies of ribosome mechanics [16].

Here we report a significantly improved device which provides greater reproducibility and more detailed characterization than previous designs. This is

the first apparatus that permits both blotting and spraying of EM grids, as well as rapid mixing, and that takes advantage of the benefits of voltage-assisted spraying (typically 5 kV). The resulting grids are of sufficient quality for sub-4 Å resolution structure determination and allow rapid mixing and freezing in the millisecond time frames (>10 ms). These capabilities will allow us to determine different conformational states of protein complexes with a time resolution not accessible through conventional EM-grid preparation methods.

## 2.3 Materials and methods

### 2.3.1 Sample preparation

Apoferritin from equine spleen was obtained from Sigma–Aldrich (A3660), and dialysed into the target buffer {20 m*M* HEPES [4-(2-hydroxyethyl)-1-piperazineethanesulfonic acid], 150 m*M* NaCl pH 7}. *Escherichia coli* ribosomes were prepared in 50 m*M* HEPES pH 7.5, 100 m*M* KAc (potassium acetate) and 8 m*M* $MgAc_2$ (magnesium acetate). Porcine ventricular thin filaments were prepared as previously described [17] and diluted to 10 µ*M* in 10 m*M* MOPS [3-(*N*-morpholino)propanesulfonic acid] pH 7, 50 m*M* KAc, 3 m*M* $MgCl_2$ and 1 m*M* EGTA prior to use. G-actin used for the blot/spray experiment was polymerized according to a protocol by Professor Peter Knight (personal communication). For the blotting/spraying experiment, 30 µ*M* apoferritin (24-mer) was sprayed onto a grid which was pre-blotted with 2 µ*M* F-actin (3 µl, 4 s blot time). For the mixing/spraying experiment with apoferritin and thin filaments, 30 µ*M* apoferritin and 10 µ*M* thin filaments were used and mixed in a 1:1 ratio. For the actomyosin dissociation experiment, a solution of 20 µ*M* thin filaments with 24 µ*M* myosin Va(1IQ)S1 in 10 m*M* MOPS pH 7, 50 m*M* KAc, 3 m*M* $MgCl_2$ and 1 m*M* EGTA was rapidly mixed (1:1) with buffer containing 0, 0.016, 0.16 or 1.6 m*M* ATP (making final ATP concentrations of 0, 8, 80 and 800 µ*M*, respectively).

### 2.3.2 Grid preparation

Before spraying/plunge freezing grids, all syringe pumps were initialized and the generated spray was examined visually. Compressed $N_2$ gas was bubbled through water to increase humidity in the spraying chamber to avoid possible evaporation of the spray in flight. The position of the sprayer was adjusted, using a trial grid to ensure it was aligned. A Styrofoam system from a Mark IV Vitrobot was used to provide a reservoir of liquid nitrogen and to house the liquid ethane. Valves controlling plunger speed and $N_2$ flow were adjusted to provide the desired flow rate through the nozzle and the desired plunger speed. The tubing and syringes of

the plunge freezing apparatus was washed with 3 × 50 µl dd$H_2O$ (purified water), followed by 3 × 50 µl of the respective buffer and loaded with 33 µl protein solution (the dead volume between the valves and the sprayer is 25–35 µl). Cryo-EM grids (Quantifoil R2/1 Cu mesh 200–300 or Quantifoil R1.2/1.3 Cu mesh 300) were glow discharged with air plasma in a Cressington 208 carbon coater with a glow-discharge unit for 90 s (10 mA/0.1 mbar air pressure) and used within 30 min to avoid hydrophilic recovery of the grids. For grid preparation, negative-pressure tweezers holding a grid were mounted into the plunging arm of the instrument, and the environmental chamber of the instrument was closed allowing the humidity to reach ≥80–90%. Then, 33 µl of protein solution was loaded into a 100 µl glass syringe (Kloehn). The ethane cup was placed in the target position and the high voltage was turned on. A software-controlled system was used to control the flow rates and timing. Typically, the solution was sprayed at 8.3 µl $s^{-1}$ for 3.5 s (to stabilize the spray) before plunging through the spray. A pressure of 0.5–2.5 bar was applied to the piston causing the grid to accelerate and reach the spray in less than 0.1 s (distance: 4 cm). The grid passed through the spray, accelerated further over the remaining 3 cm to the ethane surface and terminated by a mechanical stop leaving the grid ~1 cm below the surface of the liquid ethane.

The grid was then transferred into liquid $N_2$ and stored until screening. For the mix/spray technique, two syringes were used, one with each reactant, and the flow rate was reduced accordingly to 4.2 µl $s^{-1}$ for each syringe, resulting in the same overall flow rate. For the blot-and-spray technique, 3 µl of the first protein sample was placed onto the grid, which was subsequently blotted with two strips of Whatman 43 filter paper for 4 s. After blotting, the blotter was retracted and the grid plunged through the spray (which had been initiated during the blotting step to ensure stabilization) into the liquid ethane. Upon completion of all the experiments the syringes and tubing were washed with buffer and water.

### 2.3.3 Data collection and processing

All cryo-EM imaging was done on an FEI Titan Krios microscope equipped with a Falcon III direct electron detector operating in integrating mode (Astbury BioStructure Laboratory). The main data acquisition and processing parameters are listed in Table 2-S1. All processing was done using *RELION*2.1 [18] and *RELION*3 beta [19]. For all three datasets, the processing was done as follows: micrographs were motion corrected with the *RELION*3 implementation of *MotionCor2* [20] and then the contrast transfer function (CTF) for each micrograph was estimated using *Gctf* [21]. For apoferritin and ribosome, references for automated particle picking were generated from class averages obtained from a

small number of manually selected particles. The results of the template-based automated picking were manually inspected. Then, 2D classification was used to select particles with high-resolution information, which were taken forward to generate an initial 3D reconstruction. After two rounds of CTF refinement and Bayesian particle polishing the final reconstruction was obtained. The presented structures were filtered by local resolution.

For the ribosome dataset, 3D classification with six classes was used to sort out 50S subunits reducing the particle number from 47 866 to 34 010. For the thin-filament dataset, the *RELION* tools for helical processing were employed [22]. All filaments were manually picked. As an initial model, either a 60 Å low-pass filtered structure of actin (PDB entry 5mvy; [23]) or a featureless cylinder were used. Both gave nearly identical results with the low-pass filtered PDB model leading to slightly higher resolution. CTF refinement was not found to be beneficial in this case. The final reconstruction was subjected to 3D classification with eight classes to extract a tropomyosin-containing structure (9 496 particles) which after 3D refinement had a resolution of 10.4 Å. Helical symmetry for both structures was applied using the refined values for twist and rise with the *relion_helix_toolbox* program. Fourier shell correlation was determined by the two half-map gold-standard method for which curves are shown in Figure 2-S1.

### 2.3.4 Mixer design

The mixer/sprayer was constructed from standard high-performance liquid chromatography fittings and tubing, and the air tip from a 10 µl Gilson pipette tip (Figure 2-S2). The spray tip (Figure 2-S2 a) was constructed from a 2–3 mm length of 150/40 µm polyimide-coated quartz tubing (Molex) glued into 360/180 µm tubing with polyacrylate glue. The 360 tubing was sealed into 1/16″ outer diameter (OD) fluorinated ethylene propylene (FEP) tubing (Upchurch) with a 0.015″ inner diameter (ID). The spray tip was positioned 0–0.5 mm past the end of the air tip. Connection to the high voltage was via a short piece of 0.007″ platinum wire used to make contact with the solution via a `T' connector with 1/16″ OD, 0.01″ ID FEP tubing. The voltage of the high-voltage supply could be varied from 2 to 10 kV by varying the input from a low-voltage DC power supply (Celex BPS1510) to an EMCO Q101N-5 high-voltage converter. The high voltage was measured from the voltage across the 100 KΩ section of a 100 MΩ–100 KΩ voltage-divider circuit using a digital voltmeter (Radio Shack). The valves and pistons of the syringe pumps and forceps holding the EM grid were all grounded to prevent possible damage from stray high voltage.

For the mixing units (Figure 2-S2 b), two concentric tubes (360/200 µm and 165/100 µm) (Molex) were used so that mixing of the two solutions would not occur until just prior to spraying. FEP tubing (0.007″ ID 1/16″ OD) was used to seal the inner 165 µm capillary. The interior tubing was positioned 100–200 µm from the beginning of the spray tip to minimize the dead time. The mixer's geometry approximates that of a double back-to-back `T' mixer.

## 2.4 Results

### 2.4.1 Optimization of the setup

The modified setup described in this work (Figure 2-1) is based on a previous design [24], to which a number of significant adaptations have been applied, a humidity chamber has been added and the sprayer design optimized to provide efficient mixing and droplet sizes. These improvements have been made possible through better characterization of droplet speed and size, and the ability to collect Atlas low magnification views of each grid to better assess ice thickness and consistency. To improve spray distribution and produce a fine aerosol of droplets, a 5 kV potential is used for voltage-assisted spraying, which has significant advantages over standard spraying using only air pressure (see Appendix B for the rationale behind the term ‘voltage-assisted spraying’). With this approach, the behaviour of the spray can be more stringently controlled so as to obtain optimal ice thickness whilst requiring less sample. Droplets produced by voltage-assisted spraying are highly charged, promoting their self-dispersion and preventing coalescence [25]. Additionally, a humidity-controlled chamber is used to provide reproducible conditions and ensure that the micro-droplet spray does not evaporate en-route to the EM grid. The system is operated through computer-controlled syringe drivers (Kloehn 50300 series) that control the timing of and flow of the spraying, and additionally provide software control of sample blotting and plunging. The basic design has been described in detail in a previous review [12].

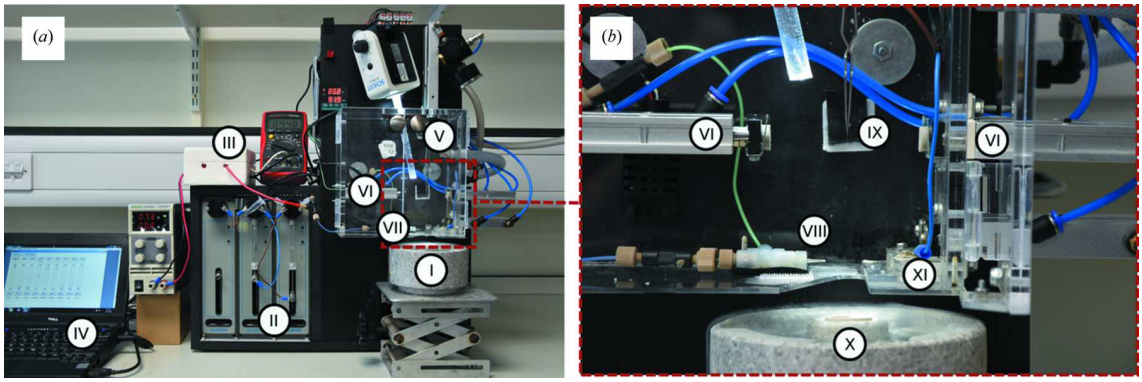


**Figure 2-1: Current setup of the TrEM apparatus.**

(*a*) Overview of the complete apparatus showing the Styrofoam freezing cup which houses the liquid ethane (I), syringe pumps (II), high-tension voltage module (III), computer controller (IV), forceps on plunger (V), blotting arms (VI) and sprayer (VII). (*b*) Zoomed-in view of the spray chamber showing the spray nozzle (VIII), blotting arms (VI), forceps with grid (IX), ethane cup within the Styrofoam liquid nitrogen holder (X), and a port that opens just prior to the grid plunge and limits the exposure of the liquid ethane to the humid air in the chamber (XI).

As in the case of traditional blotting, plasma treatment of the grid's surface is an essential step in reducing the inherent hydrophobicity of the carbon coated grids; otherwise very few, if any, droplets adhere to the grid. In addition to the time of mixing, the plunge speed of the grid was used to alter the delay time and time resolution of the experiments. In our apparatus, we use dual chamber air pistons (Figure 2-1) to blot the grids (VI), accelerate the grid into the liquid ethane (I), and open and close the port opening (XI). To better define the parameters and speeds at which grids could be plunged, a range of air pressures (0.5–2.5 bar) were used, producing plunge velocities between 1 and 3 m $s^{-1}$ (see Movie 2-S1).

We initially investigated the ability of the TrEM set-up to produce grids with ice of sufficient quality and to collect cryo-EM data capable of generating high-resolution structures. Three different model systems (apoferritin, ribosome, and thin filaments) were used to investigate the ability to spray protein samples onto a fast-moving glow-discharged EM grid. Data for each system were collected from single grids, using a Falcon 3 detector running in integrating mode on an overnight run (~12 h). From overview images, we observed ~20–50% of the grids' surface area covered with droplets. Although many droplets produced ice too thick for data collection, the grids showed many areas of ice that were suitable for imaging and subsequent high-resolution structure determination (Figure 2-S3). For each sample, this resulted in ~1 800 holes with suitable ice for imaging with the ability to take multiple exposures per hole permitting a maximum of 6 000 micrographs per grid (see Table 2-S2). For apoferritin, a total of 1 772 micrographs were

collected, with the resulting reconstruction producing a global resolution of 3.6 Å (Figure 2-2 b and e). For the *E. coli* ribosome, 1 494 micrographs were collected, with 34 010 particles contributing to a final reconstruction that had a global resolution of 4.3 Å (Figure 2-2 a and d) and showed a wide sampling of angular orientations (Figure 2-S1 c). Porcine cardiac thin filaments were studied to investigate the applicability of the apparatus on long thin filamentous particles. The resulting grids showed good distribution of the specimen within the holes, with no signs of damage in terms of filament length (Figure 2-2 c). The resulting reconstruction of the actin core of the thin filaments was resolved to 5.6 Å with the entire thin filament having a lower resolution (10.4 Å, Figure 2-S1 b) because of the heterogeneity of the attached tropomyosin. Of the micrographs collected a significant number went into the final reconstruction, demonstrating the consistency in the ice with ~86%, 97% and 100% of the collected micrographs containing particles that went into the final reconstruction of the apoferritin, ribosome and F-actin, respectively (Figure 2-S4 a). Tomographic analysis of the ice shows that it varies between 80 and 125 nm, which is thicker than ideal and limits the resolution of the data (data not shown). Moreover, Thon ring analysis of all collected micrographs shows the maximum resolution lies between 3 and 5 Å (Figure 2-S4 b). Since the resolution of the apoferritin dataset is not particle-number limited (>800 000 asymmetric units), ice thickness is the main determinant of resolution and we conclude that thinner ice will be required to obtain resolutions better than 3.5 Å. However, it should be noted that the ability to rapidly mix and spray even at resolutions below 3.5 Å can provide new insights into protein mechanism and cycling.

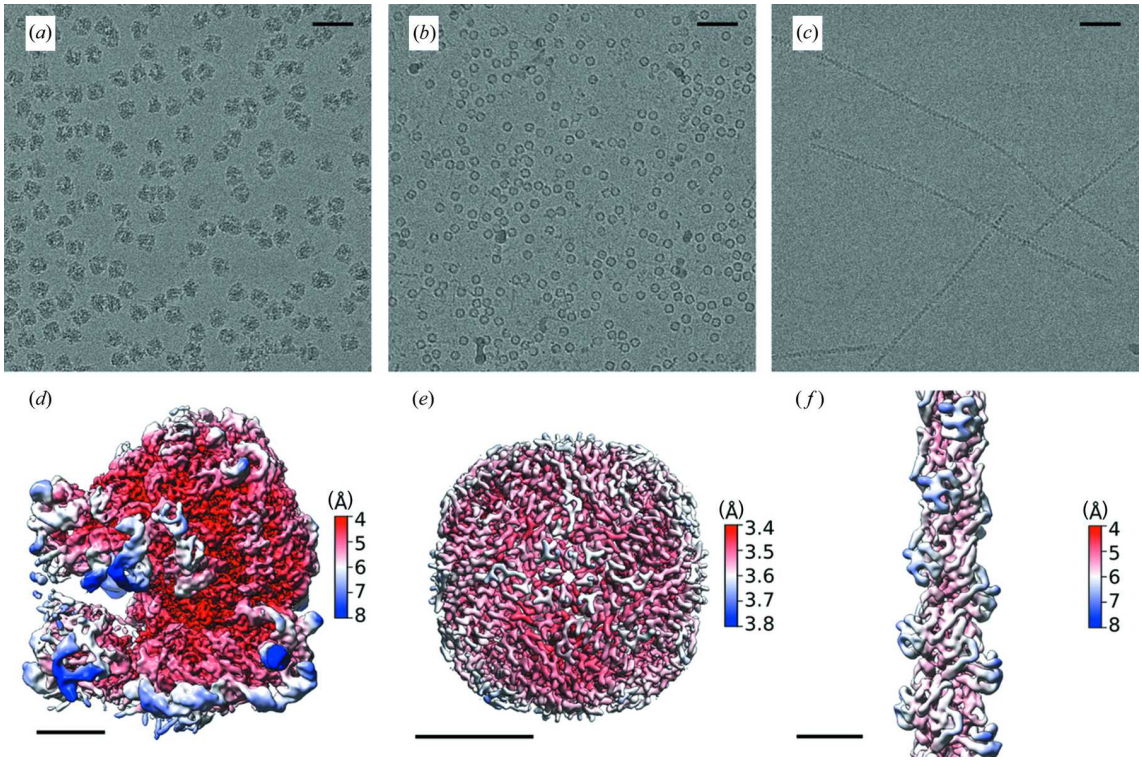


**Figure 2-2: Structures of the three model systems from grids prepared on the TrEM setup.**

To test our ability to make high-quality EM grids by spraying proteins on a fast-moving plunging grid, three samples were tested and data are shown with representative micrographs and 3D reconstructions: (*a*, *d*) *E. coli* ribosome (0.72 µ*M* in 50 m*M* HEPES pH 7.5, 100 m*M* KAc, 8 m*M* $MgAc_2$), (*b*, *e*) apoferritin [30 µ*M* (24-mer) in 20 m*M* HEPES pH 7.5, 150 m*M* NaCl], and (*c*, *f*) porcine thin filaments [5 µ*M* (actin monomer) in 10 m*M* MOPS pH 7, 50 m*M* KAc, 3 m*M* $MgCl_2$, 1 m*M* EGTA]. The scale bars in (*a*), (*b*) and (*c*) represents 50 nm. The scale bars in (*d*), (*e*) and (*f*) represents 5 nm.

### 2.4.2 Estimation of plunging and droplet speed

In a mix-and-spray type of experiment, the total amount of time that the mixed substrates interact can be calculated if we know the speed of the plunger arm, the distance travelled and the speed of the droplets after leaving the mixer/sprayer. The speed of the pneumatic plunging arm was determined using a linear potentiometer. Although, it should be noted that the plunger continuously accelerates as the grid moves towards the ethane container but reaches near maximal velocity at the point of the spray. Therefore, the measurement is a single measure of velocity at the position of the spraying nozzle and it will only slightly underestimate the overall plunging speed. With a constant distance of 3 cm between the central point of the spray cone and the ethane surface, we calculate a time between 30 and 10 ms (for a pressure range of 0.5–2.5 bar) for the grid to reach the ethane once the sample has been applied (Figure 2-3 a). Droplet speeds

were calculated based on high-speed video recordings of sprayed droplets at the tip of the nozzle, as well as at a distance of 4 mm from the nozzle (green/blue square in Figure 2-3 b).

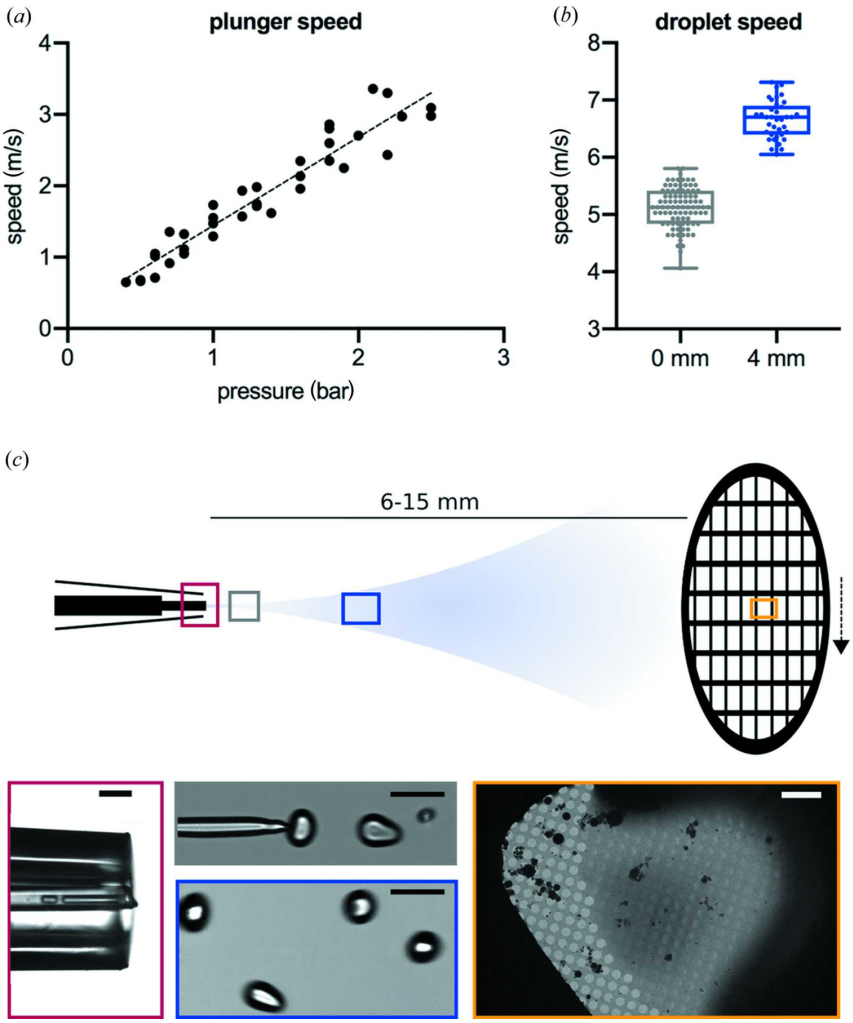


**Figure 2-3: Measuring plunger and droplet speeds.**

(*a*) The relationship between pressure and plunger speed, linear fit: speed (m $s^{-1}$) = ~1.5 × pressure (bar). (*b*) A boxplot of droplet speeds with ten different droplets tracked over at least three frames for each position, measured at the spray tip (0 mm) and at a distance of 4 mm. (*c*) Microscopic images of the spray tip (red, scale bar 200 µm), the breakup point of the liquid jet (grey, scale bar 100 µm), 4 mm away from the capillary tip (blue, scale bar 100 µm) and a grid square of a vitrified grid in the electron microscope (yellow, scale bar 10 µm).

Both yield droplet speeds of greater than 4 m $s^{-1}$ (Figure 2-3 c). We also observed acceleration of the droplets as they moved away from the sprayer. With a tip/grid distance of 6–15 mm, this equates to a time of flight of ≤4 ms for the slowest droplets and the longest distance. Higher plunge speeds result in fewer droplets

adhering to the grid, with the shortest possible delay on the current setup equating to ~11 ms from the time the droplet leaves the spray nozzle to it being vitrified on the grid (with a typical drop speed of 6 m $s^{-1}$, a sprayer-to-grid distance of 6 mm and a spray-to-ethane distance of 3 cm). Analysis of the droplets on the high-speed videos shows an approximate diameter of 75 µm (Figure 2-3 c). This is considerably larger than previously reported (1 µm), which used electrospray [24] rather than voltage-assisted spraying, but produces ice suitable for high-resolution data collection.

In order to examine the applicability of the new apparatus for the preparation of time-resolved samples, we validated the mixing capability using several different approaches. The first was to conventionally blot the grid containing the first protein and subsequently pass the blotted grid through a voltage-assisted spray containing the second protein (Movie 2-S2). By removing the dead time associated with the mixing chamber and the in-flight time of the droplets, the time delay between protein deposition on the grid and freezing is ~10 ms, and is dependent only on the distance between the sprayer and the liquid ethane (3 cm), and the plunge speed (≤3 m $s^{-1}$). Actin filaments were pre-blotted on the grid (blot time 4 s) and then passed through a voltage-assisted spray of apoferritin. Good quality and clear co-localization could be detected for the samples (Figure 2-4 a). The second approach was to mix apoferritin and thin filaments within the capillary tube just prior to voltage-assisted spraying with the resulting ice showing clear mixing of both samples in all areas studied (Movie 2-S3 and Figure 2-4 b). The added delay time, resulting from the additional volume prior to spraying is 1–2 ms, and the time of flight from the spray trip to the grid was measured to be less than 4 ms resulting in an overall time delay of ~15 ms. Although both of these approaches provided promising results and showed clear co-localization, the next step was to provide clear evidence of mixing. To achieve this, we rapidly mixed and vitrified two samples by mixing actomyosin-S1 with varying concentrations of MgATP, which dissociates the myosin-S1 from the actin with a second-order rate constant of $10^6$ $M^{-1}$ $s^{-1}$ [17]. The extent of dissociation of S1 from actin after ~15 ms of mixing of 0, 8, 80 and 800 µ*M* MgATP is predicted to be 0, 10, 70 and >99%, respectively. By maintaining the plunger speed in a way that the TrEM setup was working with an ~15 ms delay, the resulting filament decoration seen in the microscope was consistent with that expected, demonstrating that the two solutions were mixed for ~15 ms, prior to freezing (Figure 2-4 c). Investigations are currently ongoing to determine the degree of mixing within the chamber, with provisional modelling suggesting most of the mixing may occur within the droplets in-flight. With the increased time of mixing and time of flight for the sample, the approximate resulting

time resolution of this approach is in the range of 10–15 ms. Using refined microfluidic mixers, it may be possible to achieve more complete mixing before spraying the mixed sample.

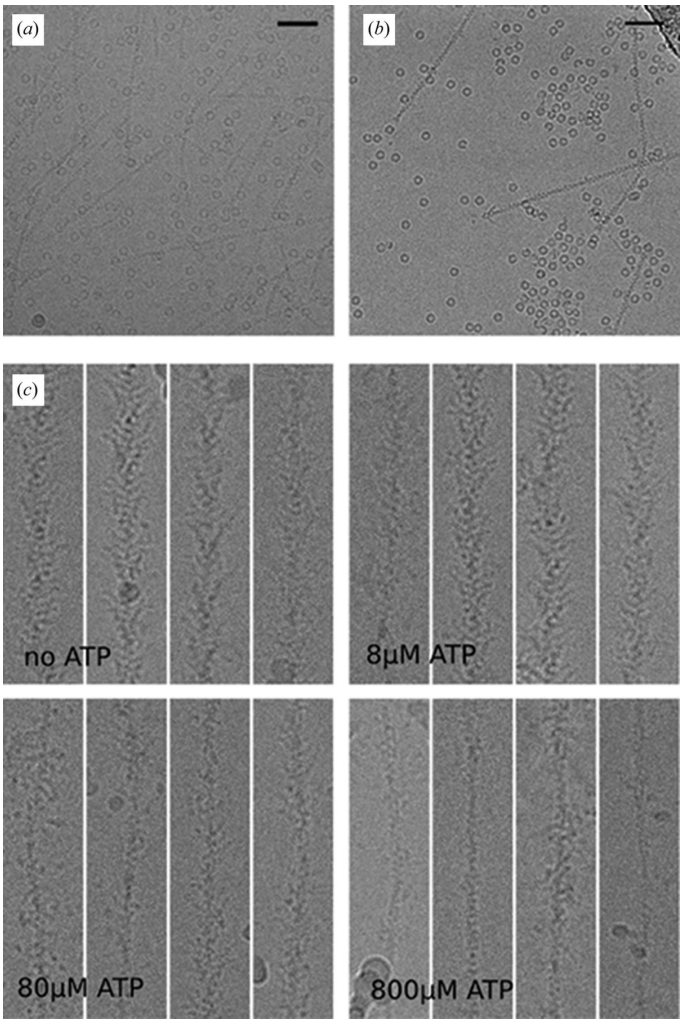


**Figure 2-4: Rapid mixing of samples on the TrEM setup.**

(*a*) Representative micrograph with thin filaments blotted and apoferritin sprayed on the subsequent plunged grid. (*b*) Representative micrograph from the rapid mixing of apoferritin and thin filaments, and direct spraying onto the EM grid. (*c*) Four representative images of myosin S1 decorated filaments after the rapid mixing (~15 ms) of 0, 8, 80 and 800 μ*M* MgATP showing decoration consistent with that predicted by kinetic modelling (0, 10, 70 and 99%, respectively).

## 2.5 Discussion

Electron microscopy has seen significant developments over the last ten years with numerous high-resolution structures of previously intractable protein systems. However, despite the first reported TrEM experiment being conducted in 1994 by

the pioneering work of Nigel Unwin, progress has been slow [26]. With the recent developments in cryo-EM hardware and software, developing a reliable TrEM setup is becoming a reality. In this work, we reported a system which can produce cryo-EM grids with a minimum time delay between mixing and freezing of 10 ms, faster than the previously reported fastest speed of 24 ms for a mix-and-spray device [27]. Through three model systems we have shown the capability of producing high-quality EM data at a resolution sufficient for resolving side-chain density. By using either a blot-and-spray or a direct mixing and spraying approach we can produce grids that display clear mixing of the samples, as demonstrated by the dissociation of myosin-S1 from the actin filaments.

Recent studies have suggested that rapid vitrification of grids can minimize the interactions with the air–water interface, which is detrimental to the biological sample [28, 29]. The methodology reported here is capable of vitrifying grids rapidly and reproducibly, which may alleviate some of the problems associated with interactions at the air–water interface, as well as other problems in conventional blotting systems [30, 31]. Ribosome data collected from sprayed grids suggest a broad distribution of views (Figure 2-S1 c). This is consistent with the particles making fewer interactions with the air–water interface; however, a full systematic study of this is beyond the scope of this work.

The grid preparation procedure is still a significant bottleneck in cryo-EM and has plenty of room for improvement both in terms of reproducibility and in the development of TrEM applications. A number of new approaches have emerged which aim to produce more consistent and reproducible high-quality ice, for example Spotiton and VitroJet systems [9, 10]. Here we report a system that addresses a different problem, that of the rapid mixing and trapping of different conformational states to produce cryo-EM grids sufficient for high-resolution EM structure determination. By using a voltage-assisted spray and a rapid mixing unit we can directly spray onto rapidly plunging EM grids or mix and freeze grids with an $\sim$10 ms time delay. This integrated apparatus may allow us to open up new opportunities in understanding the mechanisms of different protein systems

## 2.6 Supporting information

**Table 2-S1: Data collection statistics for the three reported datasets, Apoferritin, ribosome and PV-TF.**

| | **Apoferritin** | **Ribosome** | **PV-TF** |
|---|---|---|---|
| **Data collection** | | | |
| Magnification | 75000 | 75000 | 75000 |
| Voltage (kV) | 300 | 300 | 300 |
| Electron dose ($e^-$ /Å$^2$) | 91 | 66 | 65 |
| Defocus range (μm) | -1.5 to -3.4 | -0.8 to -2.9 | -1.3 to -4 |
| Pixel size (Å) | 1.07 | 1.07 | 1.07 |
| **Processing** | | | |
| Initial number of particles | 225,604 | 47,866 | 107,121 segments (3316 filaments) |
| Final number of particles | 34,170 | 34,010 | 93,468 |
| Symmetry | O | C1 | H<br>Twist: -166.33°<br>Rise: 27.65 Å |
| Pre-polishing global resolution (FSC = 0.143) | 3.9 | 5.2 | 8.0 |
| Global resolution (FSC = 0.143) | 3.6 | 4.3 | 5.6 |

**Table 2-S2: Analysis of the ice quality on the sprayed grids for the apoferritin, ribosome and thin filament data.**

| | thick ice | thin ice |
|---|---|---|
| Apoferritin | 51 % | 0.6 % |
| Ribosome | 29 % | 0.5 % |
| Thin filaments | 20 % | 0.5 % |
| **Mean** | **33 %** | **0.5 %** |

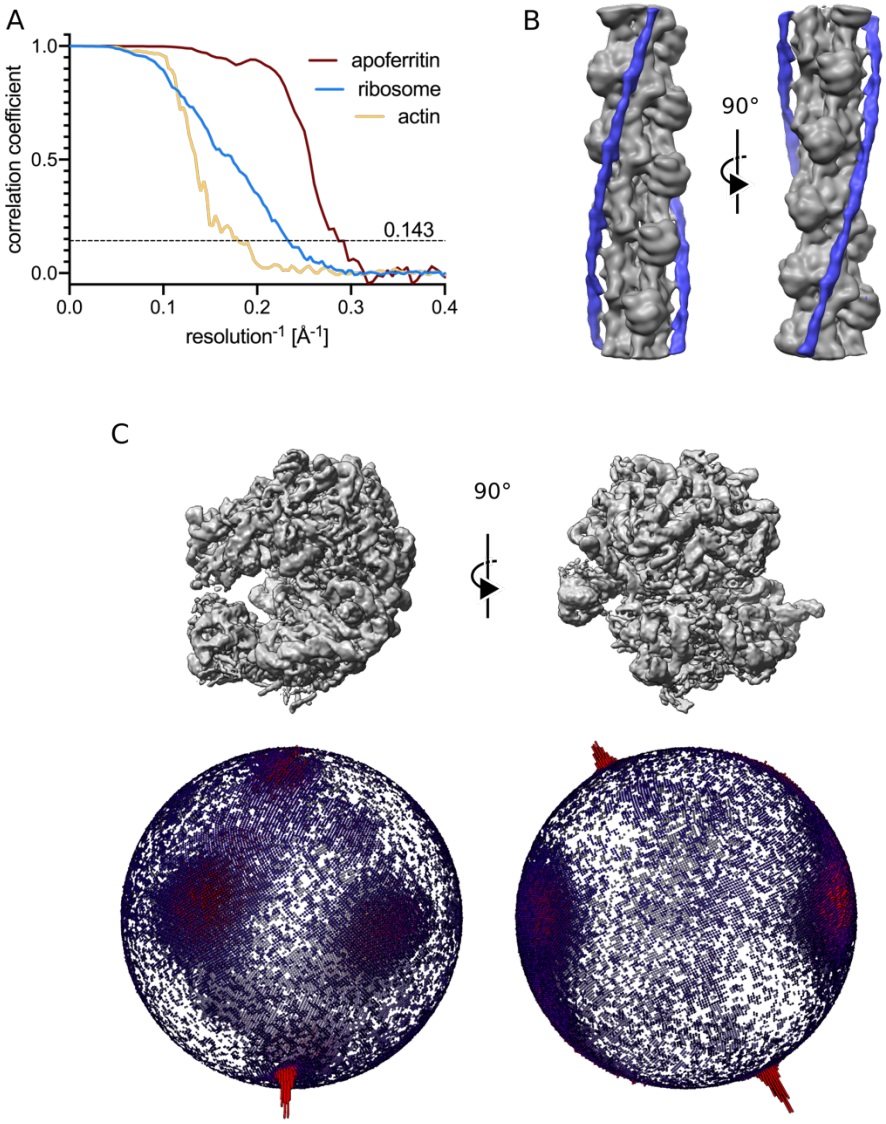


**Figure 2-S1: Processing data from sprayed grids.**

(A) Corrected FSC curves for the final masked maps of apoferritin, actin and ribosome. The dashed line represents the 0.143 cut-off. (B) Tropomyosin-containing sub-class (9496 particles) from the PV-TF dataset at 10.4 Å resolution, the actin backbone is colored in grey and tropomyosin in blue. (C) Spread of angular orientation for the ribosome dataset.

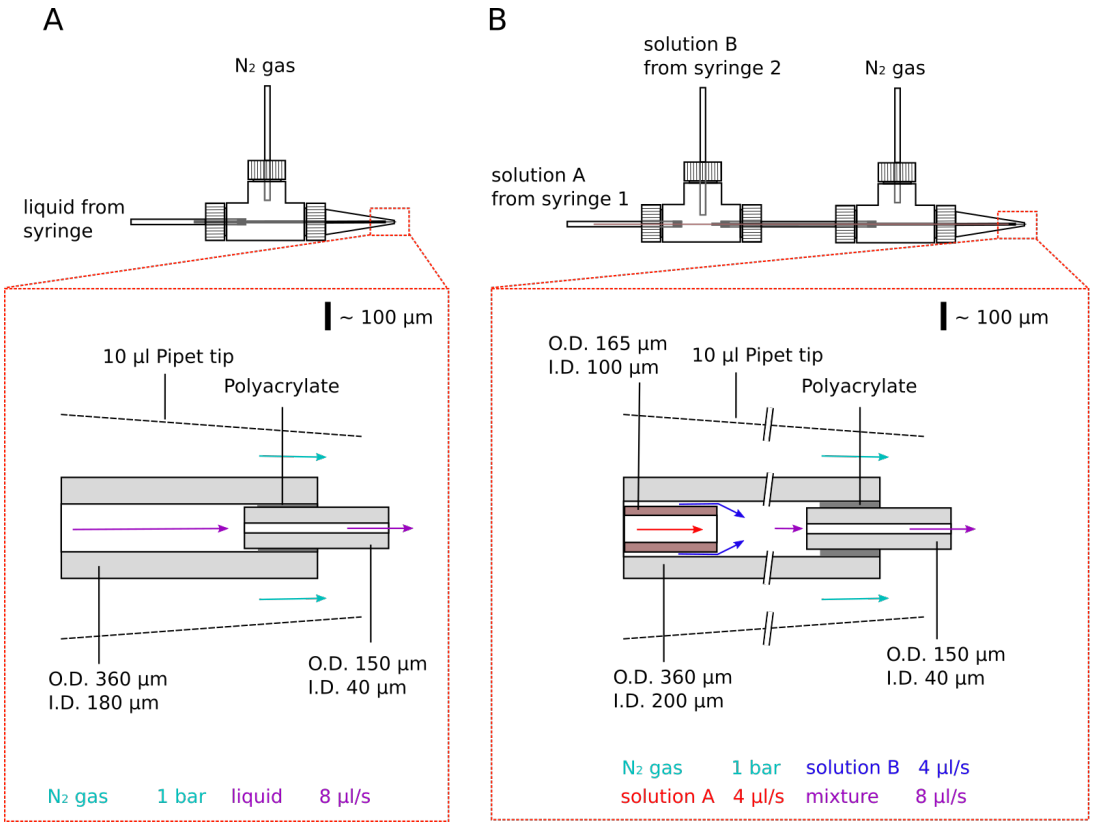


**Figure 2-S2: Spraying nozzle schematics.**

Schematic of the standard spraying unit (A) and the mixing/spraying unit (B) with an overview at the top and magnified view of the spray tip below.

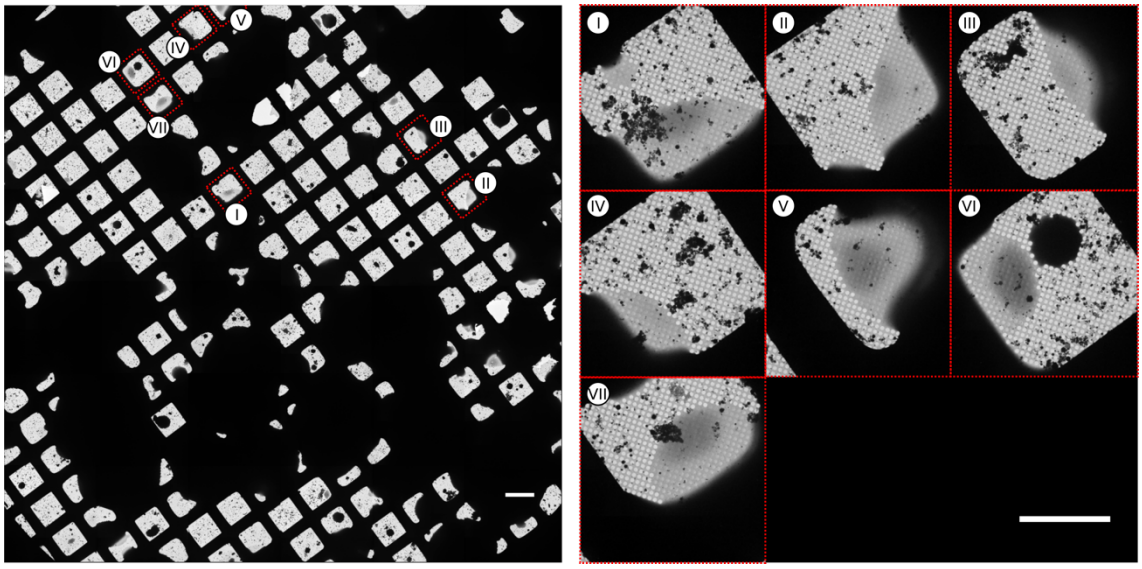


**Figure 2-S3: Selection of grid squares for data collection (exemplified for the apoferritin dataset).**

The image on the left shows a low magnification montage (atlas view) of grid with areas used in data collection highlighted in red (scale bar: 100 µm). The image on the right shows higher magnification micrographs of the selected grid squares with the numbers highlighting the position on the atlas (scale bar: 50 µm).

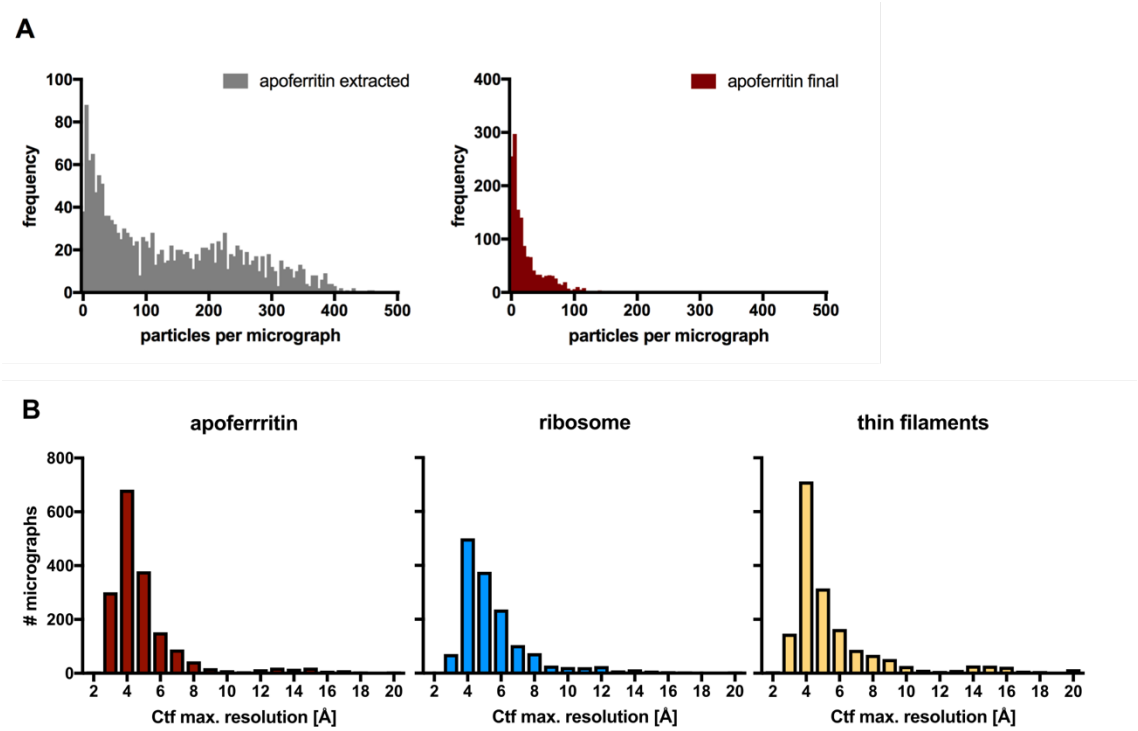


**Figure 2-S4: Particle number per micrograph and resolution from CTF fits.**

(A) Histograms showing the distribution of particle number per micrograph in the apoferritin dataset. Before any classification, micrographs contributed between 1 and 460 particles to the dataset, after curation of the dataset through 2D classification and selection for particles in high resolution classes, micrographs contributed mainly low particle numbers, between 1 and 175 particles, showing that 'good' particles are spread throughout the dataset. (B) Thon ring analysis for all micrographs in the apoferritin, ribosome and thin filament datasets, estimated by Gctf [21] showing the main peak lying between 3-5 Å.

DOI: https://doi.org//10.1107/S2052252519011345/pw5007sup1.mov

**Movie 2-S1**

Real time movie of the TrEM setup operating in the basic spray mode to generate grids with no pre-mixing or blotting. Note that the voltmeter is resting upon the high tension voltage module (III in Figure 2-1) rather than standing at the side.

DOI: https://doi.org//10.1107/S2052252519011345/pw5007sup2.mov

**Movie 2-S2**

Real time movie of the TrEM setup operating in 'blot and spray' mode. The setup is the same as in Movie 2-S1 with the sprayer as shown in Figure 2-S2 a.

DOI: https://doi.org//10.1107/S2052252519011345/pw5007sup3.mov

**Movie 2-S3**

Real time movie of the TrEM setup operating in 'mix and spray' mode with the sprayer design as shown in Figure 2-S2 b.

## 2.7 References


1. Blundell, T.L., *Protein crystallography and drug discovery: recollections of knowledge exchange between academia and industry.* IUCrJ, 2017. **4**(4): p. 308-321.
2. Suga, M., et al., *Light-induced structural changes and the site of O= O bond formation in PSII caught by XFEL.* Nature, 2017. **543**(7643): p. 131-135.
3. Stagno, J., et al., *Structures of riboswitch RNA reaction states by mix-and-inject XFEL serial crystallography.* Nature, 2017. **541**(7636): p. 242-246.
4. Smith, M.T. and J.L. Rubinstein, *Beyond blob-ology.* Science, 2014. **345**(6197): p. 617-619.
5. Frank, J., *Time-resolved cryo-electron microscopy: Recent progress.* Journal of structural biology, 2017. **200**(3): p. 303-306.
6. Fernández, I.S., et al., *Molecular architecture of a eukaryotic translational initiation complex.* Science, 2013. **342**(6160).
7. Zhou, A., et al., *Structure and conformational states of the bovine mitochondrial ATP synthase by cryo-EM.* elife, 2015. **4**: p. e10180.
8. Nakane, T., et al., *Characterisation of molecular motions in cryo-EM single-particle data by multi-body refinement in RELION.* Elife, 2018. **7**: p. e36861.
9. Dandey, V.P., et al., *Spotiton: New features and applications.* Journal of structural biology, 2018. **202**(2): p. 161-169.
10. Ravelli, R.B., et al., *Cryo-EM structures from sub-nl volumes using pin-printing and jet vitrification.* Nature communications, 2020. **11**(1): p. 1-9.
11. Subramaniam, S. and R. Henderson, *Electron crystallography of bacteriorhodopsin with millisecond time resolution.* Journal of structural biology, 1999. **128**(1): p. 19-25.
12. Kaledhonkar, S., et al., *Time-resolved cryo-electron microscopy using a microfluidic chip*, in *Protein Complex Assembly*. 2018, Springer. p. 59-71.
13. Unwin, N., *Acetylcholine receptor channel imaged in the open state.* Nature, 1995. **373**(6509): p. 37-43.

14. Unwin, N. and Y. Fujiyoshi, *Gating movement of acetylcholine receptor caught by plunge-freezing.* Journal of molecular biology, 2012. **422**(5): p. 617-634.
15. Feng, X., et al., *A fast and effective microfluidic spraying-plunging method for high-resolution single-particle cryo-EM.* Structure, 2017. **25**(4): p. 663-670. e3.
16. Kaledhonkar, S., et al., *Late steps in bacterial translation initiation visualized using time-resolved cryo-EM.* Nature, 2019. **570**(7761): p. 400.
17. Siemankowski, R.F. and H.D. White, *Kinetics of the interaction between actin, ADP, and cardiac myosin-S1.* Journal of Biological Chemistry, 1984. **259**(8): p. 5045-5053.
18. Kimanius, D., et al., *Accelerated cryo-EM structure determination with parallelisation using GPUs in RELION-2.* elife, 2016. **5**: p. e18722.
19. Zivanov, J., et al., *New tools for automated high-resolution cryo-EM structure determination in RELION-3.* Elife, 2018. **7**: p. e42166.
20. Zheng, S.Q., et al., *MotionCor2: anisotropic correction of beam-induced motion for improved cryo-electron microscopy.* Nature methods, 2017. **14**(4): p. 331.
21. Zhang, K., *Gctf: Real-time CTF determination and correction.* Journal of structural biology, 2016. **193**(1): p. 1-12.
22. He, S. and S.H. Scheres, *Helical reconstruction in RELION.* Journal of structural biology, 2017. **198**(3): p. 163-176.
23. Paul, D.M., J.M. Squire, and E.P. Morris, *Relaxed and active thin filament structures; a new structural basis for the regulatory mechanism.* Journal of structural biology, 2017. **197**(3): p. 365-371.
24. White, H., et al., *A second generation apparatus for time-resolved electron cryo-microscopy using stepper motors and electrospray.* Journal of structural biology, 2003. **144**(1-2): p. 246-252.
25. Jadhav, A., et al. *Study of electrospraying characteristics of polymer solution coating on textile substrate*. in *Advanced Materials Research*. 2011. Trans Tech Publ.
26. Berriman, J. and N. Unwin, *Analysis of transient structures by cryo-microscopy combined with rapid mixing of spray droplets.* Ultramicroscopy, 1994. **56**(4): p. 241-252.
27. Fu, Z., et al., *The structural basis for release-factor activation during translation termination revealed by time-resolved cryogenic electron microscopy.* Nature communications, 2019. **10**(1): p. 1-7.

28. Noble, A.J., et al., *Reducing effects of particle adsorption to the air–water interface in cryo-EM.* Nature methods, 2018. **15**(10): p. 793-795.
29. D'Imprima, E., et al., *Protein denaturation at the air-water interface and how to prevent it.* Elife, 2019. **8**: p. e42747.
30. Glaeser, R.M., et al., *Factors that influence the formation and stability of thin, cryo-EM specimens.* Biophysical Journal, 2016. **110**(4): p. 749-755.
31. Glaeser, R.M., *Proteins, interfaces, and cryo-EM grids.* Current opinion in colloid & interface science, 2018. **34**: p. 1-8.

# Chapter 3 Sample deposition onto cryo-EM grids: from sprays to jets and back

Published in edited form as: David P. Klebl, Diana C. F. Monteiro, Dimitrios Kontziampasis, Florian Kopf, Frank Sobott, Howard D. White, Martin Trebbin, and Stephen P. Muench. "Sample deposition onto cryo-EM grids: from sprays to jets and back." Acta Crystallographica Section D: Structural Biology 76, no. 4 (2020): 340-349.

## 3.1 Abstract

Despite the great strides made in the field of single-particle cryogenic electron microscopy (cryo-EM) in microscope design, direct electron detectors and new processing suites, the area of sample preparation is still far from ideal. Traditionally, sample preparation involves blotting, which has been used to achieve high resolution, particularly for well-behaved samples such as apoferritin. However, this approach is flawed since the blotting process can have adverse effects on some proteins and protein complexes, and the long blot time increases exposure to the damaging air–water interface. To overcome these problems, new blotless approaches have been designed for the direct deposition of the sample on the grid. Here, different methods of producing droplets for sample deposition are compared. Using gas dynamic virtual nozzles, small and high-velocity droplets were deposited on cryo-EM grids, which spread sufficiently for high-resolution cryo-EM imaging. For those wishing to pursue a similar approach, an overview is given of the current use of spray technology for cryo-EM grid preparation and areas for enhancement are pointed out. It is further shown how the broad aspects of sprayer design and operation conditions can be utilized to improve grid quality reproducibly.

## 3.2 Introduction

Over the last decade, cryo-electron microscopy (cryo-EM) has emerged as a major technique for the high-resolution structure determination of proteins and protein complexes [1, 2]. However, sample preparation is regarded as one of the main bottlenecks in cryo-EM, and research into novel grid-preparation methods has gained much attention. The traditional blotting technique was introduced in the 1980s by Dubochet and coworkers [3]. In the blotting approach, typically 3 µl of protein solution is applied to a cryo-EM grid, with subsequent blotting leaving only a thin liquid film on the grid (≤100–200 nm thick). The thin film is then vitrified, typically by plunging into liquid ethane, and can be transferred for imaging in the electron microscope. While the blotting method has undoubtedly been very

successful in producing high-resolution sub-2 Å resolution structures [4], its widespread use, and the increasing popularity of cryo-EM in general, have revealed its shortcomings. A large amount of sample is wasted through blotting, with 99.9% of the sample being removed by the blotting paper [5]. The interactions between the filter paper and the sample are not yet fully understood, but a recent study suggests that the process is much less controlled than one might expect [6]. In addition, contaminants such as divalent cations may leach from the filter paper, which can be detrimental to the sample [7]. The blotting step is typically conducted in between 2 and 10 s, a period of time that allows the sample to adhere to surfaces such as the air–water interface, adopt a preferred orientation or even denature, which can hinder high-resolution structure determination [8, 9]. Moreover, this (relatively) long time of blotting does not allow the trapping of reaction intermediates on the millisecond timescale.

Consequently, a whole new generation of freezing techniques is currently under development. Many of these techniques apply much lower sample volumes directly onto the grid. There are well understood ways to generate small liquid droplets that were developed for various applications such as combustion, drug inhalation or surface coating [10]. The cryo-EM field has turned to these approaches and reported their use for the preparation of cryo-EM grids. The Spotiton system employs piezo-electric dispensers (such as those used in inkjet printers) to deliver small amounts of liquid in a highly controlled manner [11, 12]. The VitroJet uses pin-printing technology to remove blotting and reduce sample volume to the nanolitre scale [13]. The Frank group has used direct-pressure atomizers for rapid sample delivery onto cryo-EM grids, which allowed capture of the ribosome in transient conformational states at near-atomic resolution [14]. The use of ultrasonic nozzles for spraying has been independently described by two groups and has proven to be capable of producing grids for high-resolution structure determination [15, 16].

However, the major prerequisite for cryo-EM imaging, and a significant challenge when spraying a sample, is the thinning of the droplets on the grid to ≤100–200 nm prior to vitrification. Droplet thinning is a function of the surface properties of the grid, as discussed by Jain *et al.* [11]. The success of self-wicking grids for Spotiton [17] and Shake-it-off [16] demonstrates the importance of the grid surface properties for thinning. In contrast, gas-assisted and ultrasonic sprays can also produce thin liquid films using regular grid types. Therefore, spray characteristics also play an important role in droplet thinning on grids, alongside the surface properties of the grid. This is further underpinned by work from Frank and coworkers who, in their spraying approach, show a correlation between droplet

size and ice thickness [18]. However, to date there are no publications that describe the spray behaviour for these devices in detail, which limits the development of this approach by other groups.

We have previously reported the use of another variation of cryo-EM grid preparation, voltage-assisted spraying, to enable rapid mixing and freezing for time-resolved cryo-EM studies (TrEM) [19]. In the voltage-assisted spraying approach, the sample is applied onto a fast-moving (1 m $s^{-1}$ to 3 m $s^{-1}$) cryo-EM grid. Between the droplets landing on the grid and freezing in liquid ethane, the liquid forms a thin film, allowing high-resolution imaging. In this work, we set out to deepen our understanding of the parameters that control droplet spreading when using standard cryo-EM grids. We hypothesize that droplet size and droplet speed play important roles in sufficiently thinning the droplets prior to freezing. Based on these findings, we compare different methods for depositing droplets with different sizes and speeds onto EM grids to produce grids for biological structure determination by cryo-EM.

## 3.3 Materials and methods

Cryo-EM grid-preparation experiments were performed using the previously described setup for voltage-assisted spraying [19]. The only significant modification to the setup was the new nozzles, which are described below. Quantifoil 200 mesh Cu R2/1 or 300 mesh Cu R1.2/1.3 grids were glow-discharged in air for 99 s at 10 mA and 0.1 mbar using a Cressington 208 carbon coater with a glow-discharge unit and were used within 30 min after glow discharge. No voltage was applied to the liquid/nozzle when preparing grids using capillaries for Rayleigh jets or gas dynamic virtual nozzles (GDVNs).

Analysis of the voltage-assisted spraying approach was conducted on the previously presented grids of equine apoferritin, *Escherichia coli* ribosome and porcine thin filaments [19]. To estimate the relation between droplet diameter in-flight and on-grid the contact-angle estimation of Jain *et al.* [11] was used (θ = 10 - 15°). The height and radius of the spread droplet were estimated using the following equations [11],

$$h = \left( \sqrt[3]{\frac{3V}{\pi}} \right) * (1 - \sin(\phi)) * (2 - 3 * \sin(\phi) + sin^3(\phi))^{-\frac{1}{3}}$$

$$r = \left(\sqrt[3]{\frac{3V}{\pi}}\right) * \cos(\phi) * (2 - 3 * \sin(\phi) + sin^3(\phi))^{-\frac{1}{3}}$$

where φ = (π/2) − θ, *V* is the droplet volume, *h* is the height and *r* is the radius of the spread droplet. We note that while this model seems to hold true for large droplets from voltage-assisted spray and Rayleigh jets, it cannot explain the larger spread areas of thin ice produced by droplets from GDVNs or by the smaller droplets in the voltage-assisted approach.

For all grids prepared using Rayleigh jets, apoferritin from equine spleen (Sigma–Aldrich, catalogue No. A3660) was used as a test sample at 10 µ*M* (24-mer) in 30 m*M* HEPES, 150 m*M* NaCl pH 7.5. For the generation of Rayleigh jets, either a 10 or 50 µm internal diameter (ID) capillary was used (PicoTip SilicaTip emitter with 10 µm ID or TaperTip emitter with 50 µm ID). The capillaries were connected to the computer-controlled syringe pumps using fluorinated ethylene propylene (FEP) tubing with appropriate IDs (Upchurch, 1/16″ outer diameter). Grid speeds were between 0.7 and 1.4 m $s^{-1}$, the capillary tip was positioned 7 mm from the grid trajectory and the vertical distance between the capillary and liquid ethane was 3 cm. The liquid flow rates were 1 and 8 µl $s^{-1}$ for the 10 and 50 µm capillaries, respectively.

Microfluidic GDVN devices were produced as described previously [20]. In short, the liquid-jet geometries were designed in *AutoCAD* (Autodesk) in a three-layer design. The first layer determined the main fluid inlet and the nozzle gas-flow focusing geometry, the second layer introduced the 3D gas-flow focusing with gas. The third layer contained the remaining necessary structural features for correct alignment during fabrication. The nozzle parameters are listed in Table 3-S1.

The *AutoCAD* structures were transferred to a chromium photolithographic mask (MB Whitaker, 4 × 4 × 0.09″ soda lime glass coated with AZ1518 photoresist) using laser lithography. The designs were transferred to a layered SU8-3025 (negative photoresist, Michrochem) using UV photolithography with an MJB4 mask aligner (SUSS Microtec). The photoresist was spin-coated to the desired layer heights and baked, exposed and developed following the manufacturers' guidelines. These steps were repeated to build a multi-layered structure. After development, the SU8 master was used to produce the microfluidic nozzles using soft lithography techniques using polydimethylsiloxane (PDMS) as described previously [20]. 10:1 PDMS:curing agent mixtures were used for fabrication of the final GDVN devices.

High-speed imaging of the jets/sprays was performed using a Photron SA-Z at a recording rate of 200 000 frames per second (fps). While the electronic shutter time was 159 ns, the actual exposure of the frame was determined by the 10 ns pulses of the illumination laser (640 nm; Cavilux Smart UHS, Cavitar). The high-speed camera and illumination laser were connected to an IX73 microscope (Olympus). The flow tests were performed using neMESYS high-precision syringe pumps (Cetoni).

Grids for cryo-EM data collection were prepared using 20 µ*M* apoferritin (Sigma–Aldrich, catalogue No. A3660) in 30 m*M* HEPES, 150 m*M* NaCl pH 7.5. The grid speed was 0.7 m $s^{-1}$, the capillary tip was positioned 7 mm from the grid trajectory and the vertical distance between the capillary and liquid ethane was 2.5 cm, resulting in a time delay of 36 ms between spraying and freezing.

All cryo-EM was performed on FEI Titan Krios microscopes at the Astbury Biostructure Laboratory in Leeds. The apoferritin data set was collected on Titan Krios 2 equipped with a Gatan Bioquantum energy filter (20 eV slit) and a Gatan K2 Summit direct electron detector operated in counting mode. Briefly, 690 micrographs were collected and corrected for beam-induced motion with *MotionCor2* [21], and the contrast transfer function was estimated using *Gctf* [22] in *RELION*-3 [4]. Particles were picked with *crYOLO* 1.3 using the general model [23]. All further processing was performed in *RELION*-3. After one round of 2D and 3D classification, good particles were taken forward to refinement (with octahedral symmetry), Bayesian polishing [24], per-particle CTF and beam-tilt estimation. The final resolution was 3.5 Å according to the FSC = 0.143 criterion [25]. A summary of the data-collection and processing parameters is given in Table 3-S2. A schematic overview of the processing is given in Figure 3-S1. The apoferritin map has been deposited in the EMDB (EMD-10533).

## 3.4 Results

### 3.4.1 Droplet sizes in the voltage-assisted spraying approach

In an attempt to improve our new rapid mixing and spraying setup [19], we dissected the voltage-assisted spraying approach to better quantify the relationship of voltage, drop size and speed to droplet spreading on the grid. To generate the spray in the voltage-assisted approach, three main mechanisms are used. (i) Liquid exits the nozzle at a high flow rate, leading to the formation of a liquid jet which eventually breaks up into droplets, (ii) a sheath of $N_2$ gas flow is used to aid the breakup of the liquid jet and accelerate the droplets and (iii) an electric potential of 5 kV is applied to the liquid, destabilizing the jet and dispersing the droplets. As

previously described, the latter produces a spray consisting mainly of large droplets (~70 µm diameter) with moderate speed (4–8 m $s^{-1}$) [19]. Using the voltage-assisted spraying approach, we successfully produced a number of grids using a variety of samples including apoferritin, thin filaments and ribosomes. With this method, a range of spread droplet sizes was found, with an average diameter of ~200 µm (Figure 3-1 a). Assuming a contact angle of 10–15° [11], spherical droplets of 70 µm in diameter would be expected to spread over a circular area of ~200 µm in diameter, covering multiple grid squares. The low-magnification `Atlas' views collected for the sprayed grids were consistent with large spread droplets being most abundant on the grids after spraying (Figure 3-1 a and b). However, thinning of the ice suitable for data collection was more frequently observed for smaller droplets with a <100 µm spread diameter (Figure 3-1 c). As in previous studies, we noticed the presence of background contamination (dark regions on the grid). These are also present when only buffer components are sprayed, suggesting that these are not aggregated protein but ice contamination.

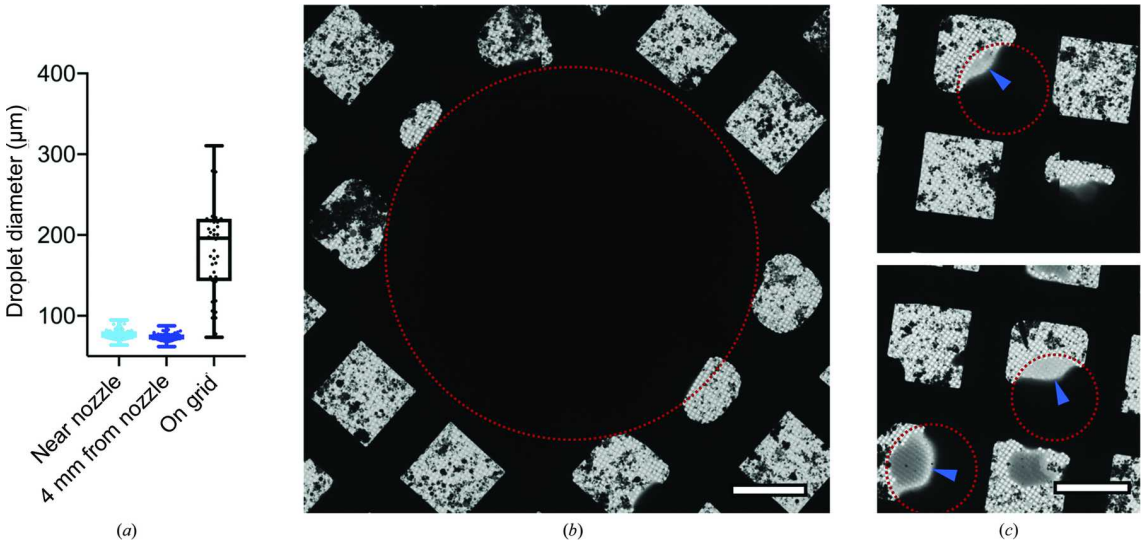


**Figure 3-1: Characterization of droplet spreading after voltage-assisted spraying and freezing.**

(a) The average diameter of spread droplets on the grid is ~200 µm, which is far in excess of the droplet size generated by the spray. The data are based on 50 observations in-flight and 48 droplets on three grids. (*b*) A large droplet which has not formed a thin film around the periphery of the drop. (*c*) Smaller spread droplets which produce areas suitable for imaging, highlighted with the blue arrows. The red dotted line shows the approximate droplet outline. The scale bar denotes 50 µm.

### 3.4.2 Liquid jets for the deposition of droplets with constant size

If the thinning of the droplet on the grid is solely dependent on droplet size, then an approach which produces smaller droplets should be better suited for cryo-EM grid preparation. To study the relationship between droplet size and thin-film formation in more detail, we required a method for the reliable production of droplets that were both smaller and more consistent in size. To this end, we adopted the use of Rayleigh jets, where liquid is pushed through an open capillary to form a liquid jet, the diameter of which typically adopts that of the inner diameter (ID) of the capillary. As the jet travels away from the nozzle, it accumulates instabilities (Rayleigh instabilities) and eventually breaks up into droplets. The droplet size after jet breakup is primarily dependent on the jet diameter and therefore on the ID of the nozzle [26, 27].

To investigate the effect of droplet size on the resulting ice quality, we used two different nozzles with 50 or 10 µm ID (Figure 3-2 a). Stable jetting could be observed at flow rates of ≥8 and ≥1 µl $s^{-1}$ for the 50 and 10 µm nozzles, respectively. Cryo-EM grids were prepared under these conditions, and low-magnification images of the grids showed a stripe of ice with consistent width across the grid, but no droplet thinning was observed (Figure 3-2 b). The nozzle–grid distance was 7 mm, which may provide a sufficient distance for the jet to break up into droplets. Consequently, higher grid speeds led to separated droplets on the surface of the grid for the 10 µm capillary rather than a continuous stripe, but did not promote droplet thinning (Figure 3-S2).

The width of the stripe of thick ice (Figure 3-2 c) is consistent with droplet radii of approximately 35 and 10 µm pre-spreading on the grid, assuming a contact angle of 12.5°. This is in agreement with the droplets being larger in diameter than the jet that they originate from [26]. Additionally, droplet coalescence occurs on the grids, which will lead to a wider stripe and an overestimated droplet size.

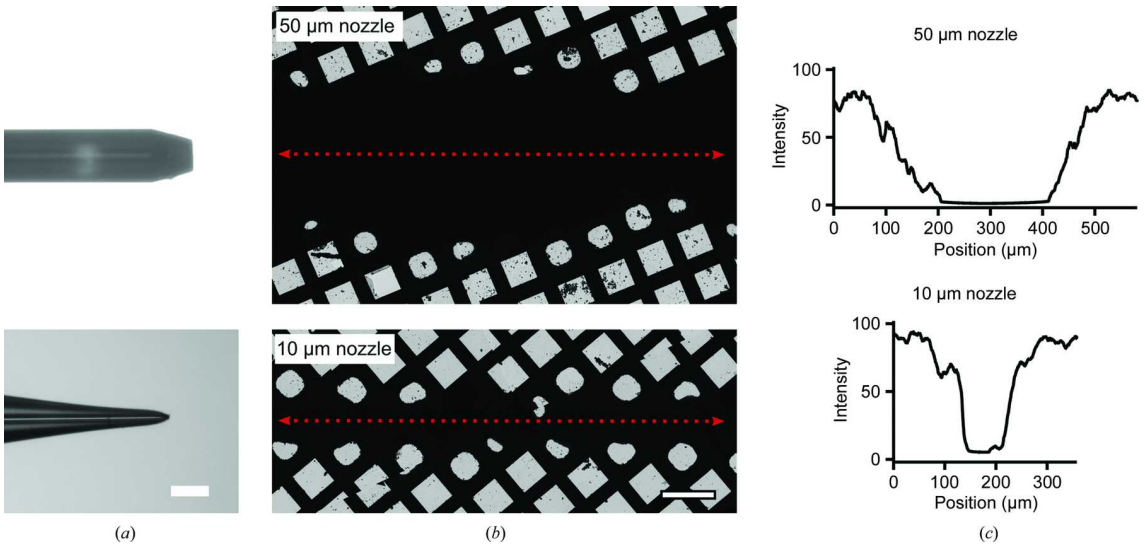


**Figure 3-2: Deposition of droplets from Rayleigh jets.**

(a) Capillaries used for the generation of Rayleigh jets. (*b*) Frozen grids at low magnification in the electron microscope showing a clear strip but no droplet spreading. (*c*) The widths of the ice strips were approximately 200 and 60 µm for the 50 and 10 µm capillaries, respectively. All scale bars correspond to 100 µm.

Notably, the droplet sizes (on the frozen grid) stemming from the 10 µm ID capillary are close to the sizes of thinned droplets in voltage-assisted spraying. However, no spreading is observed for these droplets with useable ice at the rims. The difference in spreading implies that the contact angles are different, so droplets covering similar areas on the grid may have different volumes. A possible reason is that droplet speed and spreading upon impact are different, with droplets in the voltage-assisted approach being accelerated through an $N_2$ gas flow. The very high backpressure created by the 10 µm ID capillary imposed a limit on the maximum flow rate in our setup and prohibited the use of even smaller capillaries, and therefore limited the attainable droplet speed and size. Blocking of the capillary was also a problem; this was not restricted to a particular protein sample or buffer, but was an inherent drawback of the design. In order to reduce the clogging effect and create smaller or faster droplets, we turned to gas dynamic virtual nozzles (GDVNs) [28].

### 3.4.3 GDVNs to produce small droplets which form thin films on cryo-EM grids

The GDVN design was introduced over two decades ago [10] and has been used for a number of applications, including sample delivery for X-ray free-electron lasers [29, 30]. GDVNs are made of two key components: (i) a liquid capillary through which the sample exits at a defined flow rate and (ii) an aperture at a

distance from this liquid channel. A pressure drop at this aperture causes gas to flow through it, thereby focusing the liquid into a thin jet and accelerating it. The jet diameter for a given sample is governed by the liquid flow rate and pressure drop in the nozzle, and is typically much smaller than the inner diameter of the liquid inlet [10]. Like the Rayleigh jets described above, the gas-focused liquid jet breaks up into droplets through accumulating instabilities, and the droplet diameter depends on the jet diameter. The GDVN design allows small droplets to be produced with relatively large ID liquid capillaries, which makes this approach less prone to blocking and importantly produces lower backpressure [20]. The main design used in this work (Figure 3-3 a and b) was based on a previous geometry which is capable of producing liquid jets with sub-micrometre diameters or, when operated at higher gas flows, fine sprays [20].

Using the GDVN nozzle to deliver sample onto a moving EM grid, we found a large number of droplets spreading at significantly reduced liquid flow rates (Figure 3-3 c). As expected, the droplets are distributed as a stripe on the grid, since they originate from a narrow jet and the distance between the nozzle and grid is low (7–15 mm). At the lowest flow rate tested (0.2 µl $s^{-1}$) and a low applied $N_2$ gas pressure (0.5 bar), the deposited liquid volume is sufficiently low to avoid the formation of a thick ice layer. Importantly, the droplets instead spread out and produce areas with ice of appropriate thickness for cryo-EM imaging (left panel in Figure 3-3 c). Increasing the $N_2$ gas flow leads to a thinner liquid jet and smaller droplets, which lead to a large number of areas with thin ice (middle panel in Figure 3-3 c). If the liquid flow rate is increased to ≥1 µl $s^{-1}$ (at 1 bar applied sheath-gas pressure), the amount of liquid becomes too high in the centre of the deposited stripe, resulting in very thick, crystalline ice that is unsuitable for imaging (right panel in Figure 3-3 c). Droplets at a distance from the central stripe, however, show spreading and produce areas that are suitable for imaging. This can be accounted for in part by changing the speed at which the grid passes in front of the spray, but in our current setup this can only be altered within a relatively narrow range. At even higher liquid flow rates (≥2 µl $s^{-1}$) we were not able to produce sufficiently small droplets running the GDVN nozzle in jetting mode, resulting in grids similar to that shown in Figure 3-2 b (bottom panel).

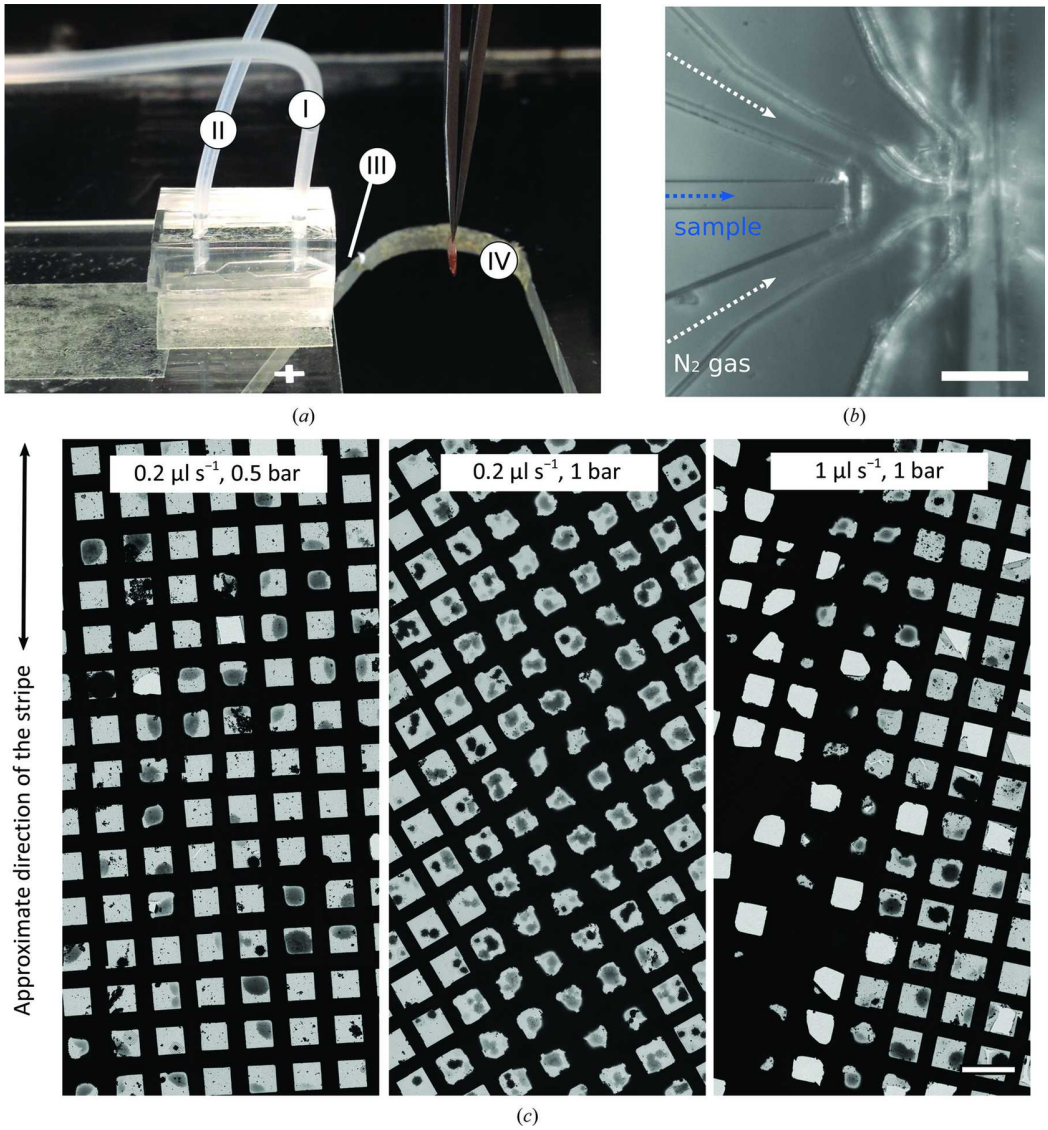


**Figure 3-3: GDVN used for cryo-EM grid preparation.**

(a) The GDVN device fitted within the current setup showing (I) the liquid inlet tubing, (II) the $N_2$ gas inlet tubing, (III) the position of the nozzle and (IV) the grid in the target position for spraying. (*b*) Microscopic image of the internal GDVN geometry used in this work with the sample and gas channels labelled. The scale bar denotes 100 µm. (*c*) Typical grids generated with the microfluidic GDVN device under three different conditions. On all three grids, liquid was deposited approximately as a stripe across the grid. The scale bar denotes 100 µm.

### 3.4.4 From liquid jets to sprays

Using the same GDVN geometry, we explored the use of higher $N_2$ flow rates (1–2 bar) at high liquid flow rates (≥2 µl $s^{-1}$). Using high-speed imaging, we found a transition from well-defined jets to more chaotic sprays at $N_2$ gas-flow rates of ~200 standard cubic centimetres per minute (SCCM) (approximately 2 bar pressure) for liquid flow rates of up to 8 µl $s^{-1}$ (Figure 3-4 a). The formation of these sprays is

quite different from the gas-focused jets described earlier. Owing to the high gas and liquid flow rates, high turbulence at the liquid surface leads to faster and more chaotic jet breakup, which occurs at the orifice of the nozzle.

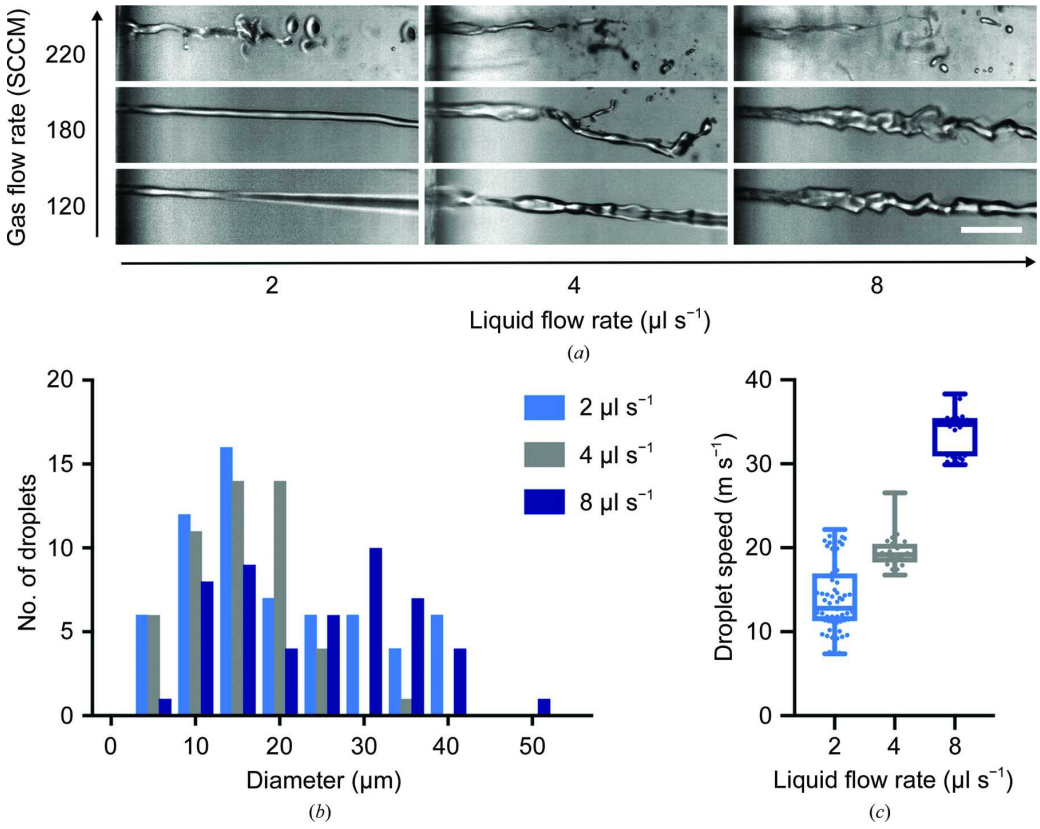


**Figure 3-4: Sprays from GDVNs**

(a) High-speed imaging at the GDVN orifice of the jet/spray transition resulting from increasing gas and liquid flow rates. Bursts of 3000 consecutive frames were collected at 200 000 frames per second (fps) with an exposure time of 10 ns (pulsed laser illumination). The scale bar is 100 µm. (*b*) Droplet diameter distribution for a 220 SCCM $N_2$ flow. (*c*) Droplet-speed distribution at 220 SCCM.

At these increased gas and liquid flow rates, we observed a wider spray cone of smaller and faster droplets covering a larger area on the grid compared with the gas-focused jetting mode. We found a bimodal distribution of droplet sizes of between 5 and 40 µm in diameter (Figure 3-4 b) when running at the highest tested liquid flow rate (8 µl s$^{-1}$) and at 220 SCCM $N_2$, but this trend was not evident at lower liquid flow rates, where most droplets had a size of <20 µm. The droplet speed depended mostly on the liquid flow rate, with the fastest droplets reaching a speed of 35 m s$^{-1}$ (Figure 3-4 c). With our grid-preparation setup, we also found the spraying mode to be a more robust approach than the jetting mode and to

tolerate imperfections in the nozzle much more, for example from manufacturing errors or contamination from the sample.

Based on the aforementioned results, these small and high-velocity droplets should be ideally suited for deposition and thinning liquid samples on cryo-EM grids. To verify this, we chose apoferritin as a specimen and prepared cryo-EM grids for data collection operating the GDVN nozzle in spraying mode. We used a 4 µl $s^{-1}$ liquid flow rate and a high $N_2$ gas pressure (2 bar); under these conditions the spray consists of very small droplets compared with the voltage-assisted approach (compare Figure 3-4 b and Figure 3-1 a) and the droplets are significantly faster ($\sim$20 m $s^{-1}$ versus $\sim$6 m $s^{-1}$). Using equine apoferritin as a sample, 690 micrographs were collected from a grid prepared with a time delay of 36 ms between spraying and freezing. The resultant apoferritin structure was determined to 3.5 Å resolution (Figure 3-5), which is consistent with the resolution achieved using the voltage-assisted approach [19]. The preparation of this grid was reproducible and more efficient compared with the voltage-assisted approach: only 4 µl of sample was used per grid, as the spray from the GDVN nozzle stabilizes more quickly (0.5 s) and was operated at a lower liquid flow rate.

## 3.5 Discussion

The grid-preparation stage of single-particle cryo-EM is still an area for development, with problems in grid quality, consistency and interactions with the air–water interface. The traditional blotting method has been highly successful for many samples, but does not come without its limitations, such as sample loss and protein instability for various systems. Alternatively, one can spray or deposit the sample directly onto the grid to eliminate interactions with the filter paper and often reduce the time that the protein resides within a thin film before plunging and freezing. The direct spraying approach for cryo-EM grid preparation (introduced in the early days of cryo-EM) [31] has not been extensively used, as generating a film that is thin enough for single-particle imaging presents a significant challenge. However, one major advantage of sample spraying is the possibility of introducing a mixing step for time-resolved cryo-EM experiments [32-34].

More recently, there have been a handful of reports on direct spray devices within the literature for cryo-EM. The voltage-assisted approach discussed in this work uses a nozzle where the capillary ends flush with the nozzle or protrudes beyond the gas outlet. A similar design, without the use of high voltage, has been described by Wagenknecht and coworkers [35, 36]. In that device, the breakup of the liquid stream into droplet occurs outside the injector geometry and is purely driven by the

gas stream. In GDVN nozzles under spraying conditions (high liquid and gas flows), the gas and the liquid come into contact within the nozzle. At the nozzle orifice, the expansion of the gas and the fast velocity of both fluids leads to chaotic instabilities, resulting in more efficient atomization and a fine spray. This is similar to the `internal-atomization' sprayer developed by Frank and coworkers, in which atomization occurs within the nozzle, allowing a degree of control over the resulting droplet size [18]. Additionally, GDVNs can be used in jetting mode at low liquid and gas flow rates, where the liquid stream is focused to low diameters by a coaxial gas flow. Breakup of the jet (outside the device) then produces a narrow range of droplet sizes downstream.

In this work, we wanted to provide a better understanding of the droplet behaviour on a commercially available EM grid that had not been modified other than by glow-discharge treatment, using the direct spraying approach. We observed broken areas on the grid to varying extents (Figure 3-3 and Figure 3-5), depending on the grid foil and mesh type and spray conditions (liquid and gas flow). Using 300 mesh grids and R1.2/1.3 foil, however, the number of intact grid squares is high and sufficient for the collection of >1000 micrographs. Our initial results suggest that droplet size is an important parameter in forming a suitable film on a fast-moving cryo-EM grid but may not be the sole determinant. We hypothesize that droplet speed could play an important role in overcoming the challenge of appropriate surface wetting in forming a very thin film. The GDVNs presented in this work can produce small and high-velocity droplets over a wide range of liquid flow rates, operating in jetting (low liquid flow rates of <2 µl $s^{-1}$, medium gas pressures of ~1 bar) or spraying mode (high liquid flow rates of ≥2 µl $s^{-1}$, high gas pressures of ≥2 bar). The jetting mode allows grid preparation with much lower sample consumption per grid than previous spraying approaches (~1 µl versus tens of microlitres), but still suffers from the large dead volume in our setup (~30 µl). However, the dead volume of this setup can be lowered significantly in future iterations by reducing the tubing ID and length of the liquid lines. The spraying approach allows higher liquid flow rates which might be needed upstream, in a mixing unit for example, or for generating faster droplets if the grid is moved at very high velocity. Our apoferritin reconstruction shows that these droplets are equally as suitable for cryo-EM data collection as those produced by the voltage-assisted approach. The benefits of the GDVN gas-flow focusing geometry could be combined with high voltage in the future to offer an additional parameter to control droplet size and behaviour in a voltage-assisted GDVN spraying device [37].

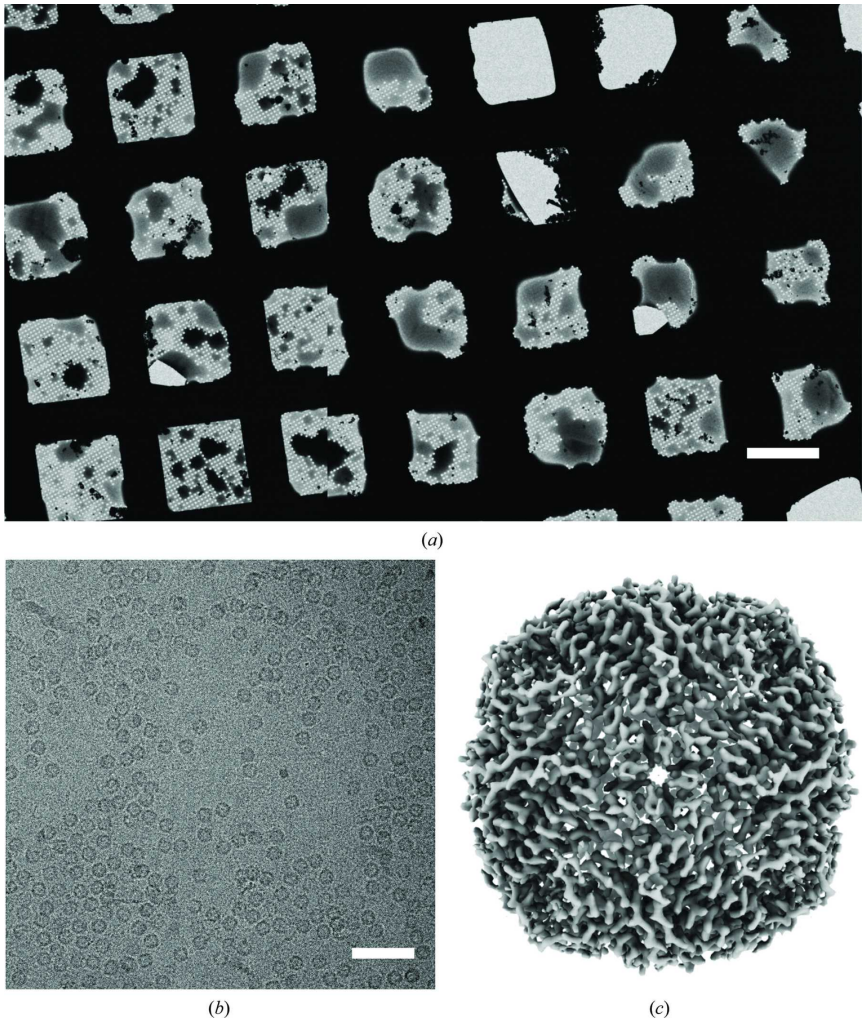


**Figure 3-5: Apoferritin structure from GDVN in spraying mode.**

(a) Low-magnification cryo-electron micrograph of a grid prepared using the microfluidic GDVN device in spraying mode (liquid at 4 µl $s^{-1}$, gas at 2 bar). The scale bar corresponds to 50 µm. (*b*) Representative high-magnification image of an area with thin ice used for data collection (the scale bar corresponds to 50 nm). (*c*) Single-particle reconstruction of apoferritin to 3.5 Å resolution with data collected from a single grid made using the GDVN nozzle under spraying conditions (liquid at 4 µl $s^{-1}$, gas at 2 bar).

Additionally, other solutions are available to control droplet spreading, one of which is the recent development of self-wicking grids by Wei *et al.* [17], which have proven to be successful not only for piezo-dispensing but also for use with ultrasonic sprayers [16]. This grid type is expected to also improve droplet spreading in the setup described in this work and can offer the potential for far more areas of thinner ice. We look forward to seeing how we can further increase the quality and consistency of the ice thickness through self-wicking grids in combination with changes in droplet size, droplet velocity and voltage, giving a choice of variables to modulate droplet behaviour depending on the experimental setup and sample properties.

The aim of the setup that we have designed is to study the rapid mixing of proteins and substrates in order to, for example, trap distinct states, rapidly change the pH or solute concentration and better understand protein-complex mechanisms [38]. Currently, the minimum time delay between sample exiting the nozzle and vitrification is ~5 ms, but one of the main limitations for going faster is the ice thickness at faster plunge speeds. We anticipate that optimization of the droplet size and velocity together with modification of the grid surface properties will help to achieve shorter time delays and ultimately allow grid preparation in a sub-millisecond timeframe. Although sub-4 Å resolution is sufficient to address many biological questions, by further understanding droplet thinning on the grid we aim to achieve sub-3 Å spatial resolution (through improved ice quality) in combination with faster grid preparation and shorter time delays. There is still work to be performed towards this goal but, as with many developments in the cryo-EM field, the future looks promising.

## 3.6 Supporting information

**Table 3-S1: Design parameters for the microfluidic GDVN devices used in this work.**

| | |
|---|---|
| Liquid inlet ID | 30 μm |
| Nozzle opening | 30 μm |
| Inlet to nozzle distance | 125 μm |

**Table 3-S2: Data collection and processing parameters for the apoferritin dataset.**

Data collection

| | |
|---|---|
| Magnification | 130,000 x |
| Voltage [kV] | 300 |
| Pixel size [Å] | 1.07 |
| Electron Dose [$e^-/Å^2$] | 60 |
| Defocus range [μm] | 0.8 - 2.8 |
| Number of micrographs | 690 |

Processing

| | |
|---|---|
| Initial particle number | 70,425 |
| Final particle number | 9,633 |
| Symmetry | O |
| Global resolution (FSC = 0.143) [Å] | 3.5 |

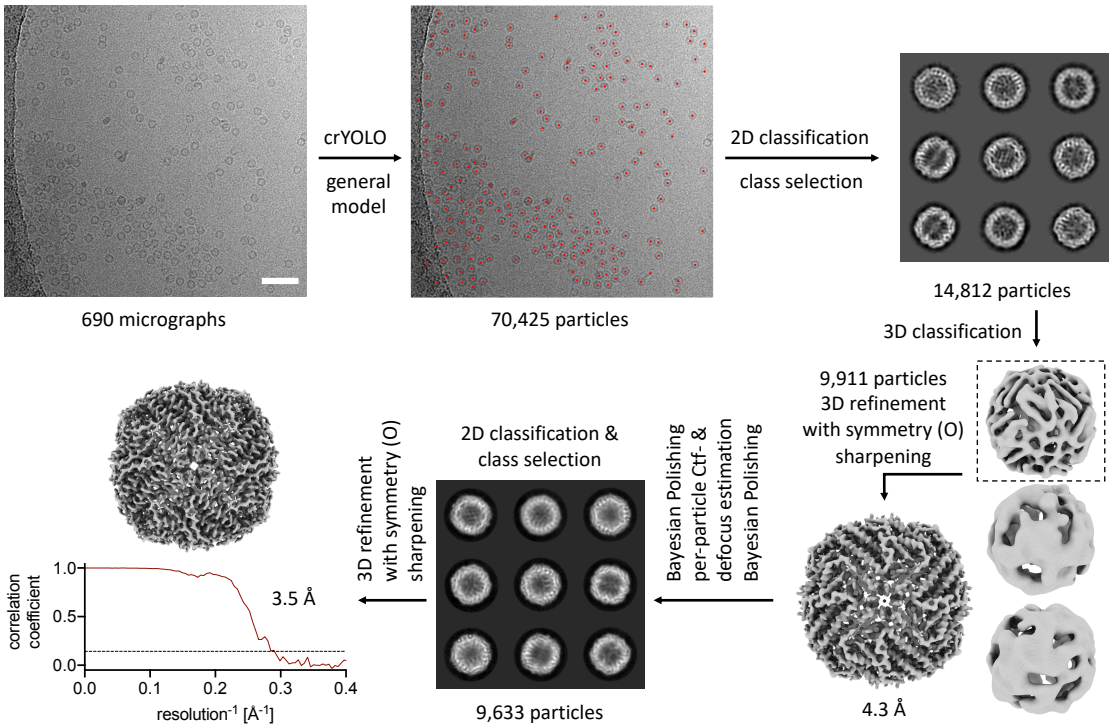


**Figure 3-S1: Processing flowchart for apoferritin dataset.**

The scale bar in the micrograph corresponds to 50 nm.

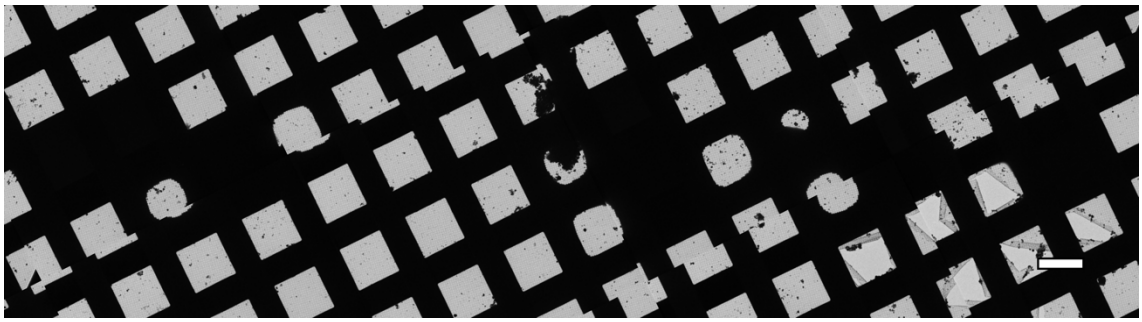

**Figure 3-S2: Sample deposition using a Rayleigh jet emitted from the 10 µm capillary at 1.4 m/s grid speed.**

Droplets show little or no coalescence on the grid and do not spread. Scale bar denotes 50 µm.

## 3.7 References


1. Callaway, E., *The revolution will not be crystallized: a new method sweeps through structural biology.* Nature News, 2015. **525**(7568): p. 172.
2. Cheng, Y., *Single-particle cryo-EM—how did it get here and where will it go.* Science, 2018. **361**(6405): p. 876-880.
3. Dubochet, J., et al., *Emerging techniques: Cryo-electron microscopy of vitrified biological specimens.* Trends in Biochemical Sciences, 1985. **10**(4): p. 143-146.
4. Zivanov, J., et al., *New tools for automated high-resolution cryo-EM structure determination in RELION-3.* Elife, 2018. **7**: p. e42166.
5. Arnold, S.A., et al., *Blotting-free and lossless cryo-electron microscopy grid preparation from nanoliter-sized protein samples and single-cell extracts.* Journal of structural biology, 2017. **197**(3): p. 220-226.
6. Armstrong, M., et al., *Microscale fluid behavior during cryo-EM sample blotting.* Biophysical journal, 2020. **118**(3): p. 708-719.
7. Walker, M., et al., *Electron cryomicroscopy of acto-myosin-S1 during steady-state ATP hydrolysis.* Biophysical journal, 1994. **66**(5): p. 1563-1572.
8. D'Imprima, E., et al., *Protein denaturation at the air-water interface and how to prevent it.* Elife, 2019. **8**: p. e42747.
9. Noble, A.J., et al., *Routine single particle CryoEM sample and grid characterization by tomography.* Elife, 2018. **7**: p. e34257.
10. Gañán-Calvo, A.M., *Generation of steady liquid microthreads and micron-sized monodisperse sprays in gas streams.* Physical Review Letters, 1998. **80**(2): p. 285.
11. Jain, T., et al., *Spotiton: a prototype for an integrated inkjet dispense and vitrification system for cryo-TEM.* Journal of structural biology, 2012. **179**(1): p. 68-75.
12. Dandey, V.P., et al., *Spotiton: New features and applications.* Journal of structural biology, 2018. **202**(2): p. 161-169.
13. Ravelli, R.B., et al., *Cryo-EM structures from sub-nl volumes using pin-printing and jet vitrification.* Nature communications, 2020. **11**(1): p. 1-9.
14. Kaledhonkar, S., et al., *Late steps in bacterial translation initiation visualized using time-resolved cryo-EM.* Nature, 2019. **570**(7761): p. 400.
15. Ashtiani, D., et al., *Delivery of femtolitre droplets using surface acoustic wave based atomisation for cryo-EM grid preparation.* Journal of structural biology, 2018. **203**(2): p. 94-101.

16. Rubinstein, J.L., et al., *Shake-it-off: a simple ultrasonic cryo-EM specimen-preparation device.* Acta Crystallographica Section D: Structural Biology, 2019. **75**(12).
17. Wei, H., et al., *Optimizing "self-wicking" nanowire grids.* Journal of structural biology, 2018. **202**(2): p. 170-174.
18. Feng, X., et al., *A fast and effective microfluidic spraying-plunging method for high-resolution single-particle cryo-EM.* Structure, 2017. **25**(4): p. 663-670. e3.
19. Kontziampasis, D., et al., *A cryo-EM grid preparation device for time-resolved structural studies.* IUCrJ, 2019. **6**(6).
20. Trebbin, M., et al., *Microfluidic liquid jet system with compatibility for atmospheric and high-vacuum conditions.* Lab on a Chip, 2014. **14**(10): p. 1733-1745.
21. Zheng, S.Q., et al., *MotionCor2: anisotropic correction of beam-induced motion for improved cryo-electron microscopy.* Nature methods, 2017. **14**(4): p. 331.
22. Zhang, K., *Gctf: Real-time CTF determination and correction.* Journal of structural biology, 2016. **193**(1): p. 1-12.
23. Wagner, T., et al., *SPHIRE-crYOLO is a fast and accurate fully automated particle picker for cryo-EM.* Communications Biology, 2019. **2**(1): p. 218.
24. Zivanov, J., T. Nakane, and S.H. Scheres, *A Bayesian approach to beam-induced motion correction in cryo-EM single-particle analysis.* IUCrJ, 2019. **6**(1).
25. Scheres, S.H. and S. Chen, *Prevention of overfitting in cryo-EM structure determination.* Nature methods, 2012. **9**(9): p. 853.
26. van Hoeve, W., et al., *Breakup of diminutive Rayleigh jets.* Physics of fluids, 2010. **22**(12): p. 122003.
27. Eggers, J. and E. Villermaux, *Physics of liquid jets.* Reports on progress in physics, 2008. **71**(3): p. 036601.
28. DePonte, D., et al., *Gas dynamic virtual nozzle for generation of microscopic droplet streams.* Journal of Physics D: Applied Physics, 2008. **41**(19): p. 195505.
29. Chapman, H.N., et al., *Femtosecond X-ray protein nanocrystallography.* Nature, 2011. **470**(7332): p. 73.
30. Wiedorn, M.O., et al., *Megahertz serial crystallography.* Nature communications, 2018. **9**(1): p. 4025.
31. Dubochet, J., et al., *Electron microscopy of frozen water and aqueous solutions.* Journal of Microscopy, 1982. **128**(3): p. 219-237.

32. Berriman, J. and N. Unwin, *Analysis of transient structures by cryo-microscopy combined with rapid mixing of spray droplets.* Ultramicroscopy, 1994. **56**(4): p. 241-252.
33. Walker, M., et al., *Observation of transient disorder during myosin subfragment-1 binding to actin by stopped-flow fluorescence and millisecond time resolution electron cryomicroscopy: evidence that the start of the crossbridge power stroke in muscle has variable geometry.* Proceedings of the National Academy of Sciences, 1999. **96**(2): p. 465-470.
34. Chen, B., et al., *Structural dynamics of ribosome subunit association studied by mixing-spraying time-resolved cryogenic electron microscopy.* Structure, 2015. **23**(6): p. 1097-1105.
35. Lu, Z., et al., *Gas-assisted annular microsprayer for sample preparation for time-resolved cryo-electron microscopy.* Journal of Micromechanics and Microengineering, 2014. **24**(11): p. 115001.
36. Lu, Z., et al., *Monolithic microfluidic mixing–spraying devices for time-resolved cryo-electron microscopy.* Journal of structural biology, 2009. **168**(3): p. 388-395.
37. Ganán-Calvo, A.M., *Electro-flow focusing: The high-conductivity low-viscosity limit.* Physical review letters, 2007. **98**(13): p. 134503.
38. Levantino, M., et al., *Using synchrotrons and XFELs for time-resolved X-ray crystallography and solution scattering experiments on biomolecules.* Current opinion in structural biology, 2015. **35**: p. 41-48.

# Chapter 4 On-grid and in-flow mixing for time-resolved cryo-EM

Published in edited form as: David P. Klebl, Howard D. White, Frank Sobott, and Stephen P. Muench. "On-grid and in-flow mixing for time-resolved cryo-EM." Acta Crystallographica Section D: Structural Biology 77, no. 10 (2021).

## 4.1 Abstract

Time-resolved cryo-electron microscopy (TrEM) allows the study of proteins under non-equilibrium conditions on the millisecond timescale, permitting the analysis of large-scale conformational changes or assembly and disassembly processes. However, the technique is developing and there have been few comparisons with other biochemical kinetic studies. Using current methods, the shortest time delay is on the millisecond timescale (~5–10 ms), given by the delay between sample application and vitrification, and generating longer time points requires additional approaches such as using a longer delay line between the mixing element and nozzle, or an incubation step on the grid. To compare approaches, the reaction of ATP with the skeletal actomyosin S1 complex was followed on grids prepared with a 7–700 ms delay between mixing and vitrification. Classification of the cryo-EM data allows kinetic information to be derived which agrees with previous biochemical measurements, showing fast dissociation, low occupancy during steady-state hydrolysis and rebinding once ATP has been hydrolysed. However, this rebinding effect is much less pronounced when on-grid mixing is used and may be influenced by interactions with the air–water interface. Moreover, in-flow mixing results in a broader distribution of reaction times due to the range of velocities in a laminar flow profile (temporal spread), especially for longer time delays. This work shows the potential of TrEM, but also highlights challenges and opportunities for further development.

## 4.2 Introduction

Motor proteins and many other biological macromolecules change conformations, form complexes or dissociate from their interaction partners as part of their functional cycle. Such reactions often involve a series of transient intermediate states which can be trapped and analysed if the system is studied with appropriate temporal resolution. Cryo-electron microscopy (cryo-EM) is well suited for such studies: conformations may be separated *in silico* if they are structurally different and present in sufficient number upon vitrification. In principle, conventional grid-making approaches allow time-resolved studies, but typical blotting is inherently slow because of the manual sample application and the relatively long blot times

(seconds). This typically limits the technique to time points longer than ~10 s. With fast grid-preparation methods, however, a reaction may be initiated and quenched with a very short and defined time delay (>5 ms). Unwin first demonstrated this approach of rapid mixing, freeze-quenching and EM image processing to study the active state of the acetylcholine receptor in the mid-1990s [1]. More recent advances in biological cryo-EM promise to make this method more broadly applicable. These include software developments to account for continuous flexibility [2], the improved signal to noise obtained with modern microscope hardware, and developments in fast cryo-EM grid preparation [3-5]. The reaction is typically initiated by rapid mixing at a defined time point before vitrification. Mixing can either be achieved within custom-built microfluidic devices [6, 7] or on the grid [8, 9]. The reaction then proceeds until it is stopped by vitrification of the sample.

While starting the reaction by rapid mixing is perhaps the most versatile method of reaction initiation, it comes with limitations. In a microfluidic setup the liquid flow within the channels is laminar, resulting in a spread of time points, which affects longer time delays more strongly [7]. If the reaction is incubated on the grid, more closely resembling a stopped-flow setup, this spread could be eliminated. On the grid, however, particles are confined within the support film and/or air–water interfaces. Interactions, especially with the air–water interface, can result in preferred particle orientation and particle denaturation [10, 11]. These effects of preferred orientation and particle denaturation can occur on a millisecond timescale [12, 13]. Especially time points with longer reaction times on-grid may therefore be affected by the air–water or water–support interfaces.

In this work, we compare on-grid and in-flow mixing by following the reaction of ATP and skeletal actomyosin S1 by TrEM to establish which may be most suitable for different time delays. We chose the actomyosin complex as a test system because it was among the first assemblies to be studied by time-resolved cryo-EM [14, 15]. Its kinetics are well understood from biochemical experiments, and equilibrium structures have been determined for a variety of different actomyosin complexes [16-18]. As part of its catalytic cycle, the myosin motor alternates between states of high and low affinity for filamentous actin (F-actin). This is necessary to allow the cycle of attachment, force generation and dissociation, for example to achieve stepwise movement in the `two-headed' myosin V [19]. In the absence of nucleotide, myosin motors bind F-actin filaments with high affinity. Mixing with ATP leads to ATP binding by the myosin motor, a reduction in affinity and dissociation of the motor from the filament [20]. Using fast on-grid mixing time points at 7 and 13 ms, we followed this initial dissociation reaction of skeletal actomyosin S1. The actomyosin system then hydrolyses ATP in the steady state.

When most ATP has been turned over, the actomyosin complex re-associates [21]. These steps were followed by slow on-grid mixing at 340 and 640 ms and in-flow mixing at 400 and 700 ms.

## 4.3 Materials and methods

### 4.3.1 Protein preparation

Monomeric rabbit G-actin was obtained as described previously [22]. For polymerization, G-actin was mixed with 10%(*v*/*v*) exchange buffer (3 m*M* $MgCl_2$, 11 m*M* EGTA) and incubated on ice for 5 min. 10%(*v*/*v*) polymerization buffer (120 m*M* MOPS, 300 m*M* KCl, 12 m*M* $MgCl_2$, 1 m*M* EGTA) was then added and the solution was incubated for at least 2 h on ice to allow polymerization. F-actin was then diluted to the target concentration in reaction buffer (10 m*M* MOPS, 2 m*M* $MgCl_2$, 0.1 m*M* EGTA, 50 m*M* potassium acetate pH 7). Rabbit skeletal myosin S1 (A1 fraction) was prepared as described previously [21]. The actomyosin complex was obtained by mixing F-actin and myosin S1 in a 1:1 molar ratio at final concentrations of 40 µ*M* in reaction buffer. Disodium ATP (Roche) was prepared as a 100 m*M* stock solution in water at pH 7, stored at −20°C and diluted in reaction buffer to 200 µ*M* before use

### 4.3.2 Time-resolved cryo-EM grid preparation

All grids were prepared using our in-house setup for time-resolved cryo-EM [23]. The key experimental conditions for TrEM grid-preparation experiments are listed in Table 4-1 and Table 4-2. In all TrEM experiments, 40 µ*M* actomyosin complex was mixed with 200 µ*M* ATP in a 1:1(*v*:*v*) ratio to give final concentrations of 20 µ*M* actomyosin and 100 µ*M* ATP. Sample application was performed using gas dynamic virtual nozzles in spraying mode, as described previously [24]. The spray gas pressure was 2 bar. All grids were prepared at ambient temperature (~20°C) and at a relative humidity of >60%. For on-grid mixing, three separate syringes were used (Table 4-1). The three liquid flows meet in the microfluidic mixer/sprayer just before exiting the spray nozzle. For in-flow mixing, an external T-mixer (Upchurch Micro Static Mixing Tee) was introduced upstream of the nozzle. After passing a delay line (Table 4-2), the reaction mixture was sprayed using the same nozzle design as used for on-grid mixing, but only making use of the central channel. Quantifoil 300-mesh Cu R1.2/1.3 grids were used after glow-discharge in air for 90 s at 10 mA and 0.1 mbar using a Cressington 208 carbon coater with a glow-discharge unit.

**Table 4-1: Conditions for actomyosin on-grid mixing experiments**

| time-delay (ms) | flowrate (µL/s) | | | spray/ethane distance (cm) | plunge speed (m/s) |
|---|---|---|---|---|---|
| | syringe 1 (AM) | syringe 2 (ATP) | syringe 3 (ATP) | | |
| 7 ms | 2.08 | 1.04 | 1.04 | 1.4 | 2.0 |
| 13 ms | 1.04 | 0.52 | 0.52 | 2.0 | 1.6 |
| 340 ms | 2.08 | 1.04 | 1.04 | 4.9 | N/A* |
| 640 ms | 2.08 | 1.04 | 1.04 | 4.9 | N/A* |

*En route to vitrification, the grid was stopped and incubated for an additional 300 or 600 ms.

**Table 4-2: Conditions for actomyosin in-flow mixing experiments**

| time-delay (ms) | flowrate (µL/s) | | delay-line ID (µm) | delay-line length (cm) |
|---|---|---|---|---|
| | syringe 1 (AM) | syringe 2 (ATP) | | |
| 400 ms | 2.08 | 2.08 | 150 | 2.0 |
| 700 ms | 2.08 | 2.08 | 360 | 2.0 |

### 4.3.3 Estimation of time delays

For on-grid mixing experiments, the time delay was estimated by measuring the plunge speeds with a linear potentiometer and oscilloscope (Hantek 6022BE) recording at 1 MHz or 500 kHz, as described previously [23]. With a total liquid flow rate of 2–4 µl $s^{-1}$, the dead time between the mixing element and spray nozzle was estimated to be less than 1 ms. Similarly, the delay between spray generation and spray application was less than 1 ms, given the high droplet speed of ≥10 m $s^{-1}$ [24]. Thus, only the plunge speed, the distance between the nozzle and ethane, and stop times (for 340 and 640 ms delays) were considered (Table 4-1). The spray cone was approximately 5 mm wide at the point of sample application, leading to an estimated error of 2–3 ms.

For in-flow mixing experiments, total flow rates of 4 µl $s^{-1}$ were used. The volume of the delay line was 0.35 or 2 µl, depending on the tube inner diameter (ID) used

(Table 4-2). At the given tube diameter and liquid flow rate, the estimated Reynolds number (Re) is between 14 and 34, well below the transition of laminar to turbulent flow at Re ≃ 2000 [25]. Thus, the flow is expected to be laminar in the delay line. The residence time distribution $E(t)$ for a laminar flow reactor, such as the delay line used here, is [26]

$$E(t)\begin{cases} 0 & t < \frac{\tau}{2} \\ \frac{\tau^2}{2t^3} & t \geq \frac{\tau}{2} \end{cases}$$

where τ is the mean residence time, given by the tube volume divided by the volumetric flow rate. Under the experimental conditions, diffusion should have a negligible effect on the residence time distribution. The mixer dead volume was 0.95 µl and the spray-nozzle dead volume was estimated as 0.3 µl. The time between sample application and vitrification was 19 and 23 ms, respectively, for these experiments (with plunge speeds of 1.2 and 1.0 m $s^{-1}$ and a nozzle–ethane distance of 2.3 cm). Thus, median residence times of 400 ms (394 ms) and 700 ms (696 ms) were calculated for the 150 and 360 µm ID delay lines, respectively. Considering laminar flow in the delay line, 95% of particles had calculated residence times of 376–622 ms and 593–2016 ms for the 150 and 360 µm ID delay lines, respectively.

### 4.3.4 Cryo-EM data collection and processing

All cryo-EM data, except for the 13 ms time point, were collected on a Titan Krios microscope equipped with a Falcon III detector in integrating mode. The 13 ms data were collected on a Titan Krios microscope equipped with a Gatan K2 detector in counting mode. Key data-collection parameters are listed in Table 4-3. All image processing was performed using helical and single-particle processing in *RELION* 3.0 [2, 27]. Micrographs were motion-corrected using *MotionCor*2 [28] and CTF estimation was performed with *Gctf* [29]. All filaments were manually picked, extracted and rescaled to a 200-pixel box with a nominal pixel size of 2.13 Å per pixel. For the two different detectors used (Table 4-3), the optimal pixel size ratio was determined by cross-correlation of maps and appropriate rescaling during extraction [30]. One round of 2D classification was used to exclude poor-quality particles; less than 15% of particles were excluded from each time point. A consensus helical reconstruction was then calculated for each time point. For further processing, all data sets were combined. The processing strategy for the combined data is shown in Figure 4-S1. Focused classification without alignment was used to identify myosin-bound and unbound actin subunits. Unbound actin

subunits were selected and used to generate a reconstruction by standard helical processing. For the myosin-bound subunits, signal for the actin filament was subtracted, leaving only a central actin trimer with one myosin molecule bound. These actomyosin particles were then refined as single particles. Finally, the particles were traced back to their original data set (time point) and the per-micrograph distribution was analysed with an in-house Python script. Fits to the data and statistical tests were performed with *GraphPad Prism* 7.

**Table 4-3: Data-collection and processing parameters**

| dataset | 7 ms (on-grid) | 13 ms (on-grid) | 340 ms (on-grid) | 640 ms (on-grid) | 400 ms (in-flow) | 700 ms (in-flow) |
|---|---|---|---|---|---|---|
| data collection parameters | | | | | | |
| detector | Falcon III | K2 | Falcon III | Falcon III | Falcon III | Falcon III |
| fluence ($e^-/Å^2$) | 72 | 52 | 72 | 62 | 62 | 62 |
| nominal pixel size (Å) | 1.065 | 1.07 | 1.065 | 1.065 | 1.065 | 1.065 |
| number of frames | 59 | 32 | 59 | 40 | 40 | 40 |
| processing parameters | | | | | | |
| number of micrographs | 306 | 123 | 120 | 330 | 184 | 176 |
| original boxsize (pixels) | 400 | 404 | 400 | 400 | 400 | 400 |
| initial number of segments | 89892 | 30070 | 46246 | 67198 | 20083 | 82353 |
| number of free actin segments (final) | 27886 | 16617 | 32899 | 46513 | 13745 | 39044 |
| number of actomyosin particles (final) | 31128 | 6495 | 5848 | 9686 | 2129 | 19270 |

## 4.4 Results

Two major steps determine the time delay between mixing and freeze-quenching with our custom-built time-resolved EM device (TED) and in most other time-resolved EM devices. These time delays are schematically shown in Figure 4-1 a. The first relevant time delay is the time from mixing to sample application. In our current nozzle design (Figure 4-1 b) this delay is minimal; we expect mixing to occur in the spray or on-grid. The second time delay is the time between sample application and vitrification. We prepared cryo-EM grids of the skeletal actomyosin complex mixed with ATP, varying the time between sample application and vitrification between 7 and 640 ms (corresponding to time delay 2 in Figure 4-1 a). Time delays of 340 and 640 ms were achieved by stopping the pneumatic plunger for a defined time after passing the spray before vitrification (Figure 4-1 c). This approach is preferable over a slow continuous motion, because slow immersion in liquid ethane at speeds significantly lower than 1 m $s^{-1}$ results in the formation of crystalline ice [31]. For the short time delays of 7 and 13 ms, grids were plunged without a stop step before final plunging at high speeds (Table 4-1).

The resulting cryo-EM images of the actomyosin complex after mixing with ATP show, as expected, time-dependent dissociation of myosin S1 from the filaments (Figure 4-1 d). A small cryo-EM data set was collected at each of the four time points (7, 13, 340 and 640 ms) and the images were processed. Like the raw images, the 3D reconstructions show most myosin S1 bound at 7 ms, less myosin bound after 13 ms and very weak myosin density, at thresholds below 3σ, at the 340 and 640 ms time points (Figure 4-1 e). While they indicate the course of the reaction, these consensus reconstructions only give limited insight because they are an average of all filaments from the respective data set containing both decorated and undecorated filaments. In order to quantify the particles, we performed focused 3D classification without alignment. Each particle contains one unique, central myosin-binding site because particles were extracted along the filament with an inter-box distance close or equal to the helical rise (27.5 Å). By using a mask for the central myosin site, the myosin occupancy at this site was probed. To impose the same classification criteria and allow better comparison, all data sets were combined for classification. We note that the classification outcome showed approximately 5% variability in relative particle number depending on the parameters used. We also found that the classification was biased towards more predominant states, leading to a similar variability in particle numbers. This provides an estimate of the uncertainty introduced by 3D classification, even with a relatively large difference (myosin S1 present or absent) between states.

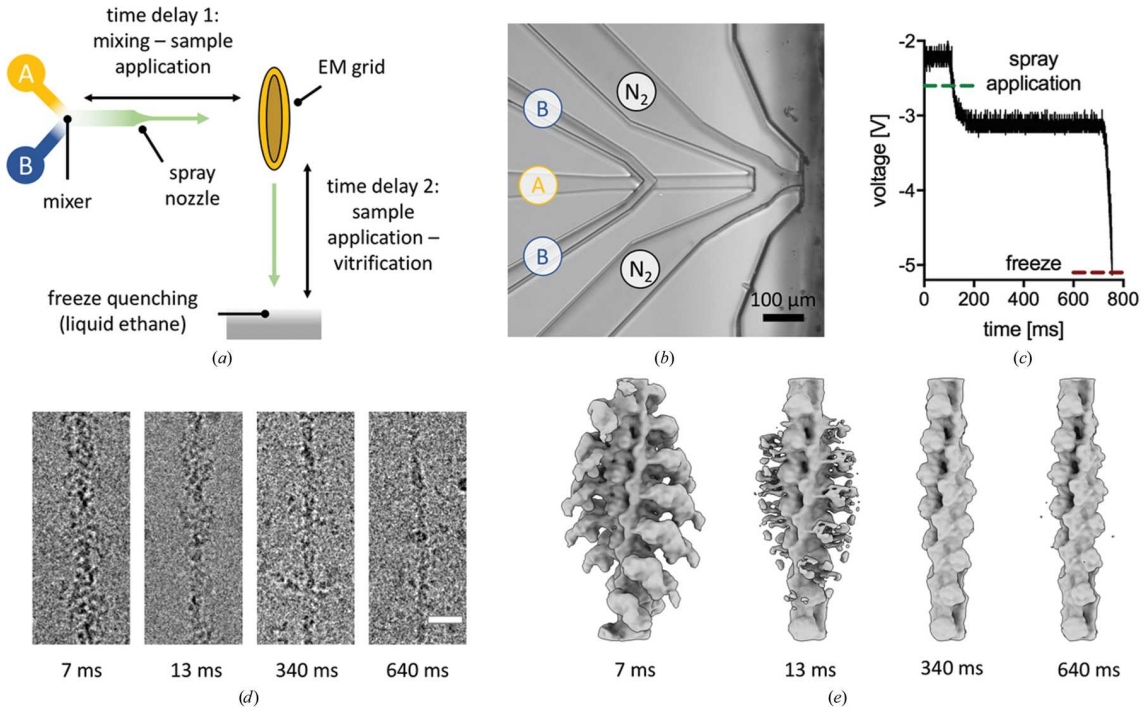


**Figure 4-1: TrEM of actomyosin dissociation.**

(a) Schematic of the TED with different delay times indicated. (*b*) Microscopic image of the microfluidic gas dynamic virtual nozzle with mixing element used in this work. (*c*) Oscilloscope recording for a grid prepared with a stop of 600 ms between spray application and vitrification. The measured voltage corresponds to the vertical position of the grid. (*d*) Raw cryo-EM images of the actomyosin complex mixed with ATP and vitrified after 7, 13, 340 and 640 ms. The scale bar corresponds to 20 nm. (*e*) Consensus reconstructions of the actomyosin complex 7, 13, 340 and 640 ms after on-grid mixing with ATP, all shown at a 3σ threshold.

From the combined data, we obtained a 4.8 Å resolution structure of F-actin and a 7.5 Å resolution structure of the skeletal actomyosin complex (Figure 4-2 a and b). While free F-actin was processed by the standard helical method, actomyosin particles were processed with a single-particle approach after subtracting signal for all but the central three actin subunits and the bound myosin. This gave improved density for the radially distant regions of the myosin motor, with only a few particles being misaligned in the absence of helical constraints (Figure 4-S2). The reconstructions (at 4.8 and 7.5 Å resolution, respectively) were the same as the published structures of F-actin and skeletal actomyosin in the rigor state, respectively [17, 32]. In the actomyosin reconstruction, the actin backbone and myosin motor have similarly strong density, suggesting that this set of particles has very high, or full, myosin occupancy. The data also contained a subset of particles which were not assigned to either class (Figure 4-S1). This population was probably a mixture of unbound and bound states, and potentially other weakly bound states.

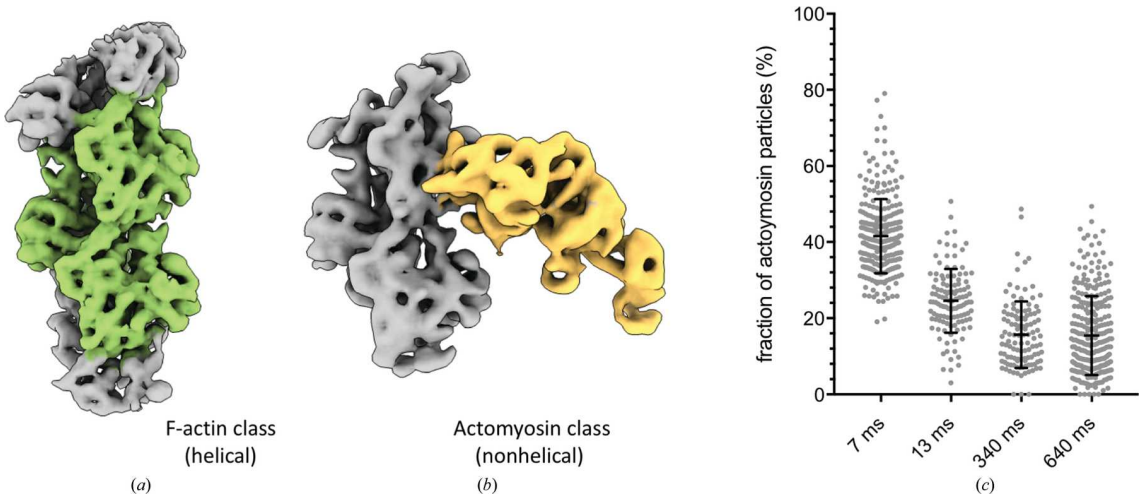


**Figure 4-2: TrEM data processing.**

Reconstructions of F-actin (*a*) and the actomyosin complex (*b*) from the combined data. The central three actin subunits are shown in green and myosin S1 is in yellow. (*c*) Relative particle numbers of the actomyosin complex traced back to individual time points. Shown is the percentage of actomyosin particles relative to the total number of myosin-binding sites (the number of actin subunits). For each time point, the mean and standard deviation are shown as black lines and per-micrograph particle numbers are shown as grey points.

We quantified the relative number of particles in the two identified states (bare actin and actomyosin) at each time point by tracing the particles back to their original data set. As expected, there is a decrease in the relative number of actomyosin particles over time, from ~42% occupancy at 7 ms to ~16% occupancy at 340 ms (Figure 4-2 c). Plotting the per-micrograph relative number of actomyosin particles showed a significant spread between micrographs from a single grid and time point. These results show that ATP-induced dissociation of the actomyosin complex can be quantitatively followed by varying the on-grid delay time. An exponential fit to the on-grid TrEM data gave a pseudo-first-order reaction rate of 177 $s^{-1}$, similar to published values for this reaction [21]. The fraction of actomyosin complex was not significantly different between the 340 and 640 ms time points ($p$ = 0.3, Mann–Whitney test), indicating that the reaction was completed or remained in a steady state.

The reaction cycle of the actomyosin complex is such that after dissociation, re-association should occur at longer time delays. However, no re-association was seen when the mixing occurred predominantly `on-grid'. In order to examine whether this may be a feature of on-grid mixing, a different experimental setup was used. An external mixing unit and delay line were introduced upstream of the nozzle (Figure 4-3 a). This corresponds to changing time delay 1 in Figure 4-1 a: the two reactants meet in a T-mixer, flow through the delay line, are sprayed onto

the EM grid and are then vitrified. Using this approach, we could minimize any interactions with the air–water interface which may occur during on-grid mixing due to the length of time that the protein resides on the grid. In this case the delay line ID and liquid flow rate, as well as the mixer and sprayer dead volumes, determined the total time delay. Grids were prepared at two different time points, with median time delays of 400 or 700 ms. We assumed laminar flow in the delay line. In this case the setup resembles a laminar flow reactor [26] and the time points are spread by the parabolic flow profile in the delay line; see Methods section for details. The 400 or 700 ms in-flow time points were analysed in the same way as the on-grid mixing data. Consensus reconstructions from each time point, at a threshold of 3σ, show that little myosin was bound at 400 ms (consistent with the on-grid mixing experiment) but an increase in myosin density for the later 700 ms time point was observed, in contrast to the on-grid mixing approach, where no re-association is observed at 640 ms (Figure 4-3 b).

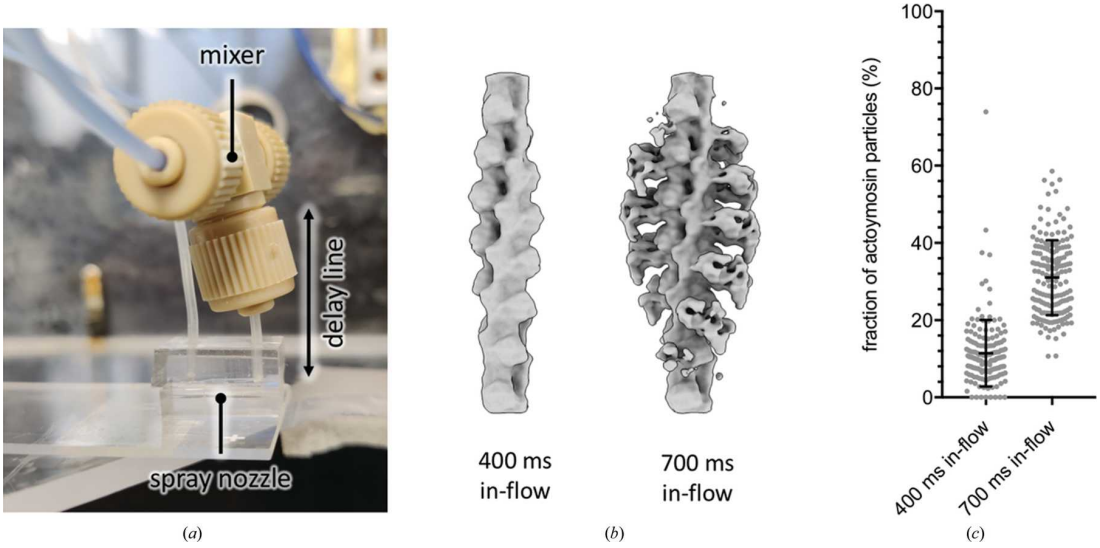


**Figure 4-3: Longer time delays by in-flow mixing.**

(*a*) Photograph of the experimental setup with T-mixer, delay line and spray nozzle. The delay line length is 2 cm. (*b*) Consensus reconstructions of the actomyosin complex 400 or 700 ms after mixing with ATP in-flow shown at 3σ. (*c*) Relative particle numbers of the actomyosin complex traced back to individual time points. Shown is the fraction of actomyosin particles relative to the total number of myosin-binding sites (the number of actin subunits). For each time point, the mean and standard deviation are shown as black lines and per-micrograph particle numbers are shown as grey points.

For classification, the 400 and 700 ms in-flow mixing data were processed with the on-grid data to allow a direct comparison. The 400 ms in-flow data showed the lowest fraction of myosin bound, 11%, and there was an increase in bound myosin

particles at the 700 ms time point (Figure 4-3 c). This was in contrast to the 640 ms on-grid time point. Such an increase in actin binding is expected when most of the available ATP has been hydrolysed.

## 4.5 Discussion

There have been some significant steps in recent years in the development of time-resolved cryo-EM methodologies, with a number of systems being reported, showing great promise in this area. However, although we and others have shown that TrEM can be used to follow biomolecular reactions at high resolution, there are limitations to the technique: only a limited range of concentrations are suitable for TrEM and a high particle number per micrograph is usually required to achieve high-resolution reconstruction. This is an important consideration because concentrations will affect reaction rates and TrEM requires relatively high concentrations compared with other biochemical methods. There is also a limited amount of data comparing TrEM experimental results with those from complementary techniques such as stopped-flow light-scattering measurements to date. Here, we chose the actomyosin system as a test system because its kinetics are well understood.

A graphical summary of the TrEM data is shown in Figure 4-S3. The on-grid TrEM kinetics of actomyosin dissociation (7–640 ms) are in agreement with stopped-flow measurements, although we note that the buffer composition has been shown to affect the actomyosin dissociation rate and is not matched exactly between studies [20, 21]. There is a small but significant difference between the 340 ms on-grid and 400 ms in-flow time points (16% and 11% myosin bound, respectively; $p < 0.0001$, Mann–Whitney test). This may indicate that there is a small difference in mixing efficiency, with the in-flow mixer being more efficient.

The rebinding of myosin to F-actin is expected after most ATP has been hydrolysed, and is also observed in stopped-flow light-scattering measurements [21]. Published steady-state ATP turnover rates for skeletal myosin S1 (A1) are in the range 5–10 $s^{-1}$, depending on the F-actin concentration and the buffer composition [33]. Given the fivefold excess of ATP in our TrEM experiments, our in-flow data agree well with previous studies. However, there is a substantial difference between the 640 ms on-grid and 700 ms in-flow time points (15% and 31% myosin bound, respectively; $p < 0.0001$, Mann–Whitney test). In part, this could be accounted for by laminar flow in the in-flow setup, with the in-flow reaction having a larger temporal spread, with residence times exceeding 2 s for ~2% of particles. Other factors may also contribute to the difference between the 640 ms

on-grid and 700 ms in-flow time points. For example, confinement of the reaction mixture on-grid could affect the reaction. The air–water interface has been shown to bind proteins quickly, so there is likely to be a competition between F-actin and the air–water interface for myosin binding. Moreover, binding to the air–water interface may cause protein unfolding and sequestering of the protein, creating an accumulation away from the bulk protein within the thin film layer on the grid.

From the data shown here, we conclude that there are important considerations when designing a TrEM experiment, which are summarized in Figure 4-4. On-grid TrEM has the advantage that the time delay is minimally influenced by laminar flow. It can also allow the mixing of very different components that may not be suitable for microfluidic channels. However, when using this approach one factor which may need to be considered depending on the type and time frame of the reaction are interactions with the air–water interface, which may sequester proteins away and therefore alter the relative concentrations on-grid, potentially affecting the kinetics of the reaction or shifting the equilibrium (Figure 4-4 a).

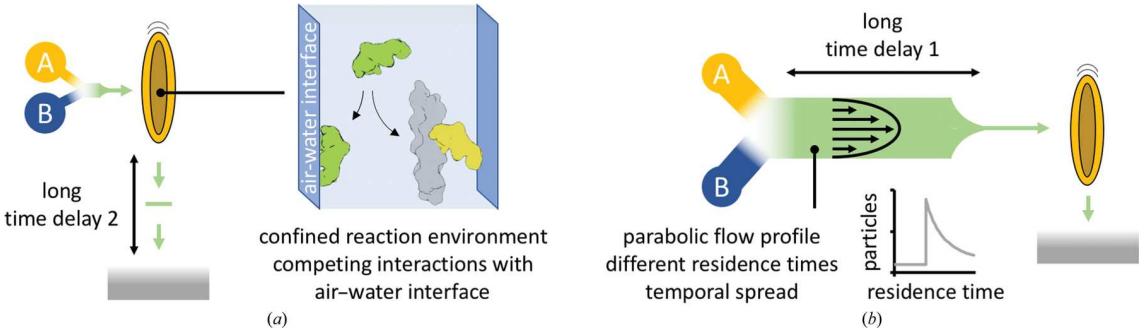


**Figure 4-4: Graphical summary of challenges in TrEM.**

Schematics are analogous to Figure 4-1 a. (*a*) The main time delay for on-grid mixing is the time between sample application and vitrification. During this time, especially for long time delays, the air–water interface can interfere with the reaction, for example by competing for binding. (*b*) For in-flow reactions, the main time delay is the time between mixing and sample application. In this case, the parabolic flow profile during laminar flow results in different residence times for individual molecules and a larger temporal spread.

This can be mitigated by the use of in-flow approaches, where mixing occurs away from the grid and therefore the time exposed to the grid and the air–water interface is low. A clear drawback of in-flow mixing is the temporal spread by laminar flow, which especially affects longer time delays (Figure 4-4 b and Figure 4-S3). However, it is preferable over on-grid mixing, particularly for even longer time delays than used in this study. On the time scale of seconds, evaporation,

interactions with the air–water interface and/or interactions with the grid support or foil will have an even greater influence for on-grid mixing.

## 4.6 Supporting information

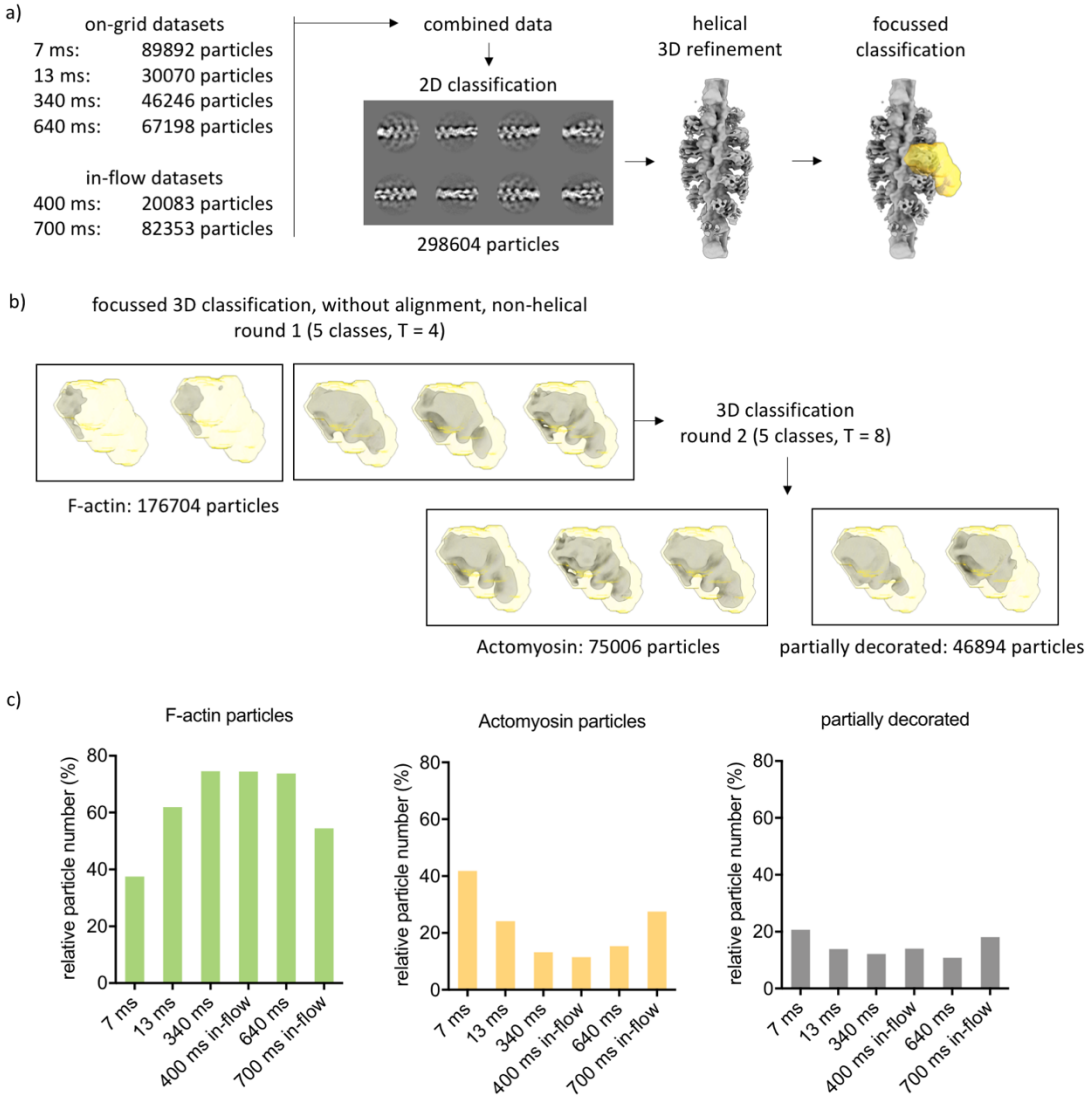


**Figure 4-S1: TrEM data processing.**

(a) All datasets were combined. One round of 2D classification was used to remove 'bad' particles. Helical refinement was then used to generate a consensus reconstruction with all 'good' particles from all timepoints. A myosin mask was generated that covered the central myosin binding site. (b) Focussed classification was used to separate F-actin and actomyosin particles. No helical constraints were used and particles were not aligned during classification. In two rounds of 3D classification, the dataset was split into F-actin, actomyosin and partially decorated particles. (c) Relative particle number for each class from each dataset. F-actin and actomyosin particles show a time-dependent change in particle number while partially decorated particles do not show as clear a trend.

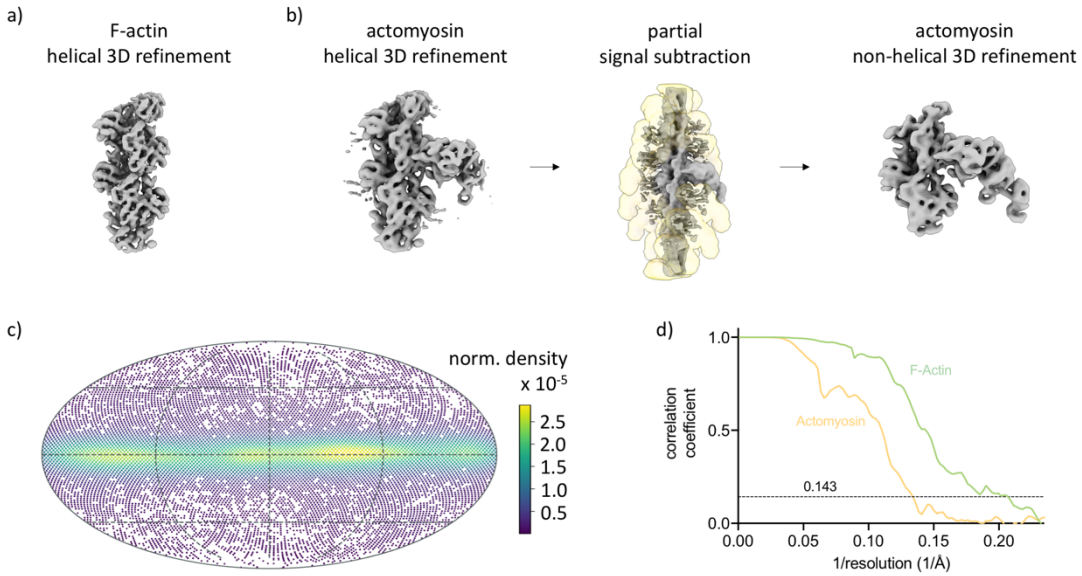


**Figure 4-S2: Further TrEM data processing.**

(a) Helical refinement of all F-actin subunits, shown is the sharpened final reconstruction. (b) Non-helical refinement used for actomyosin particles. A helical 3D reconstruction was made first, then a mask was created covering all but 3 central actin subunits and the central myosin binding site. After partial signal subtraction, a non-helical (single particle) reconstruction for the actomyosin particles was made. This shows improved density for the radially distant regions of the myosin. (c) Orientation distribution for the non-helical actomyosin reconstruction. Most particles show ~ 90° tilt angle (highest density along the equator), indicating that the angular assignment of most particles is sufficient without helical constraints. The colour indicates estimated normalised probability density. (d) Fourier shell correlation curves for the helical F-actin (green) and non-helical actomyosin (yellow) with the 0.143 threshold indicated as dashed line.

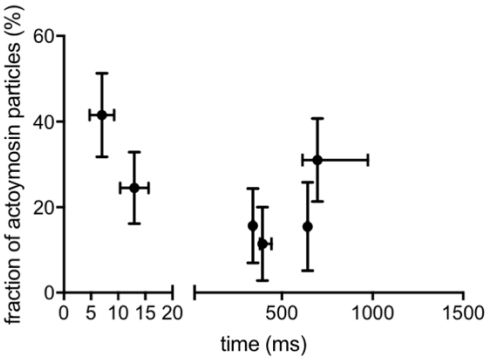


**Figure 4-S3: Summary of TrEM data.**

Plotted is the fraction of actomyosin particles determined by focussed 3D classification for each timepoint, shown are mean and standard deviation in y. For estimation of x error, see Methods section. For in-flow timepoints, the x value shown is the median and error bars in x represent 1 $\sigma$ deviation in either direction as this better represents the skewed distribution.

## 4.7 References


1. Unwin, N., *Acetylcholine receptor channel imaged in the open state.* Nature, 1995. **373**(6509): p. 37-43.
2. Zivanov, J., et al., *New tools for automated high-resolution cryo-EM structure determination in RELION-3.* Elife, 2018. **7**: p. e42166.
3. Feng, X., et al., *A fast and effective microfluidic spraying-plunging method for high-resolution single-particle cryo-EM.* Structure, 2017. **25**(4): p. 663-670. e3.
4. Rubinstein, J.L., et al., *Shake-it-off: a simple ultrasonic cryo-EM specimen-preparation device.* Acta Crystallographica Section D: Structural Biology, 2019. **75**(12).
5. Jain, T., et al., *Spotiton: a prototype for an integrated inkjet dispense and vitrification system for cryo-TEM.* Journal of structural biology, 2012. **179**(1): p. 68-75.
6. Kaledhonkar, S., et al., *Time-resolved cryo-electron microscopy using a microfluidic chip*, in *Protein Complex Assembly*. 2018, Springer. p. 59-71.
7. Mäeots, M.-E., et al., *Modular microfluidics enables kinetic insight from time-resolved cryo-EM.* Nature communications, 2020. **11**(1): p. 1-14.
8. Berriman, J. and N. Unwin, *Analysis of transient structures by cryo-microscopy combined with rapid mixing of spray droplets.* Ultramicroscopy, 1994. **56**(4): p. 241-252.
9. Dandey, V.P., et al., *Time-resolved cryo-EM using Spotiton.* Nature Methods, 2020. **17**(9): p. 897-900.

10. Noble, A.J., et al., *Routine single particle CryoEM sample and grid characterization by tomography.* Elife, 2018. **7**: p. e34257.
11. D'Imprima, E., et al., *Protein denaturation at the air-water interface and how to prevent it.* Elife, 2019. **8**: p. e42747.
12. Noble, A.J., et al., *Reducing effects of particle adsorption to the air–water interface in cryo-EM.* Nature methods, 2018. **15**(10): p. 793-795.
13. Klebl, D.P., et al., *Need for speed: Examining protein behaviour during cryoEM grid preparation at different timescales.* BioRxiv, 2020.
14. Walker, M., J. Trinick, and H. White, *Millisecond time resolution electron cryo-microscopy of the M-ATP transient kinetic state of the acto-myosin ATPase.* Biophysical journal, 1995. **68**(4 Suppl): p. 87S.
15. Walker, M., et al., *Observation of transient disorder during myosin subfragment-1 binding to actin by stopped-flow fluorescence and millisecond time resolution electron cryomicroscopy: evidence that the start of the crossbridge power stroke in muscle has variable geometry.* Proceedings of the National Academy of Sciences, 1999. **96**(2): p. 465-470.
16. von der Ecken, J., et al., *Cryo-EM structure of a human cytoplasmic actomyosin complex at near-atomic resolution.* Nature, 2016. **534**(7609): p. 724-728.
17. Fujii, T. and K. Namba, *Structure of actomyosin rigour complex at 5.2 Å resolution and insights into the ATPase cycle mechanism.* Nature communications, 2017. **8**(1): p. 1-11.
18. Risi, C., et al., *High-Resolution Cryo-EM Structure of the Cardiac Actomyosin Complex.* Structure, 2021. **29**(1): p. 50-60. e4.
19. Walker, M.L., et al., *Two-headed binding of a processive myosin to F-actin.* Nature, 2000. **405**(6788): p. 804-807.
20. Millar, N.C. and M.A. Geeves, *The limiting rate of the ATP-mediated dissociation of actin from rabbit skeletal muscle myosin subfragment 1.* FEBS letters, 1983. **160**(1-2): p. 141-148.
21. White, H. and E. Taylor, *Energetics and mechanism of actomyosin adenosine triphosphatase.* Biochemistry, 1976. **15**(26): p. 5818-5826.
22. Spudich, J.A. and S. Watt, *The regulation of rabbit skeletal muscle contraction I. Biochemical studies of the interaction of the tropomyosin-troponin complex with actin and the proteolytic fragments of myosin.* Journal of biological chemistry, 1971. **246**(15): p. 4866-4871.
23. Kontziampasis, D., et al., *A cryo-EM grid preparation device for time-resolved structural studies.* IUCrJ, 2019. **6**(6).

24. Klebl, D.P., et al., *Sample deposition onto cryo-EM grids: from sprays to jets and back.* Acta Crystallographica Section D: Structural Biology, 2020. **76**(4).
25. Avila, K., et al., *The onset of turbulence in pipe flow.* Science, 2011. **333**(6039): p. 192-196.
26. Fogler, H.S., *Essentials of Chemical Reaction Engineering: Essenti Chemica Reactio Engi*. 2010: Pearson Education.
27. He, S. and S.H. Scheres, *Helical reconstruction in RELION.* Journal of structural biology, 2017. **198**(3): p. 163-176.
28. Zheng, S.Q., et al., *MotionCor2: anisotropic correction of beam-induced motion for improved cryo-electron microscopy.* Nature methods, 2017. **14**(4): p. 331.
29. Zhang, K., *Gctf: Real-time CTF determination and correction.* Journal of structural biology, 2016. **193**(1): p. 1-12.
30. Wilkinson, M.E., A. Kumar, and A. Casañal, *Methods for merging data sets in electron cryo-microscopy.* Acta Crystallographica Section D: Structural Biology, 2019. **75**(9): p. 782-791.
31. Kasas, S., et al., *Vitrification of cryoelectron microscopy specimens revealed by high-speed photographic imaging.* Journal of microscopy, 2003. **211**(1): p. 48-53.
32. Merino, F., et al., *Structural transitions of F-actin upon ATP hydrolysis at near-atomic resolution revealed by cryo-EM.* Nature structural & molecular biology, 2018. **25**(6): p. 528-537.
33. Rosenfeld, S. and E. Taylor, *The ATPase mechanism of skeletal and smooth muscle acto-subfragment 1.* Journal of Biological Chemistry, 1984. **259**(19): p. 11908-11919.

# Chapter 5 Need for speed: examining protein behaviour during cryo-EM grid preparation at different timescales

Published in edited form as: David P. Klebl, Molly S. C. Gravett, Dimitrios Kontziampasis, David J. Wright, Robin S. Bon, Diana C. F. Monteiro, Martin Trebbin, Frank Sobott, Howard D. White, Michele C. Darrow, Rebecca F. Thompson and Stephen P. Muench. "Need for speed: examining protein behavior during CryoEM grid preparation at different timescales." Structure 28, no. 11 (2020): 1238-1248.

## 5.1 Abstract

A host of new technologies are under development to improve the quality and reproducibility of cryo-electron microscopy (cryo-EM) grid preparation. Here we have systematically investigated the preparation of three macromolecular complexes using three different vitrification devices (Vitrobot, chameleon, and a time-resolved cryo-EM device) on various timescales, including grids made within 6 ms (the fastest reported to date), to interrogate particle behaviour at the air-water interface for different timepoints. Results demonstrate that different macromolecular complexes can respond to the thin-film environment formed during cryo-EM sample preparation in highly variable ways, shedding light on why cryo-EM sample preparation can be difficult to optimize. We demonstrate that reducing time between sample application and vitrification is just one tool to improve cryo-EM grid quality, but that it is unlikely to be a generic “silver bullet” for improving the quality of every cryo-EM sample preparation.

## 5.2 Introduction

Single-particle cryo-electron microscopy (cryo-EM) has emerged as a major structural biology technique during the last decade [1]. While refined data processing software [2-4] and automated data acquisition [5] have streamlined the technique, sample preparation remains a major bottleneck for many projects. For single-particle cryo-EM sample preparation, the specimen is typically spread as liquid film as thinly as possible ($\gtrapprox$20 nm) [6] before being rapidly vitrified by plunging into a cryogenic liquid such as ethane [7]. The formation of this thin film has commonly been achieved by applying a relatively large sample volume (3–4 µL) to a cryo-EM grid and then blotting away excess liquid with filter paper. The cryo-EM grid, a 3 mm diameter metal (commonly copper) disk with square windows, has a support layer (typically amorphous carbon) with small, usually circular perforations (~1–2 µm diameter) in a regular array. The typical blotting

process removes almost all of the liquid applied to the grid, leaving a thin film of sample suspended across the holes in the support where imaging can occur. This procedure was pioneered over 30 years ago by Dubochet [7].

Formation of a thin film using blotting paper followed by vitrification can be achieved through manual and home-built devices, as well as using commercially available devices such as the Vitrobot (Thermo Fisher Scientific), EM GP (Leica Microsystems), and CP3 (Gatan), for which the general concept remains the same as when the method was first conceived. While there can be problems with reproducibility of thin-film formation through a blotting approach it is undeniably successful, resulting in its application to a broad range of specimens, and it has consequently come to underpin the vast majority of single-particle structures to date.

Over the years, and across different fields of research, it has been shown that the air-water interface (AWI) can be a hostile environment for proteins and macromolecular complexes [8-11]. In a typical cryo-EM grid preparation both sides of the thin film are exposed to the AWI, creating a very high surface-area-to-volume ratio. Blotting and plunging into cryogens usually takes seconds, during which time the sample can come into contact with the AWI hundreds to thousands of times. Macromolecular complexes and proteins can interact preferentially with and/or denature (either fully or partially) on exposure to the AWI [12, 13].

A recent systematic study of particle localization on cryo-EM grids prepared with traditional blotting methods by Noble et al. [14] has shown that ~90% of the 46 samples analysed associate with the AWI, demonstrating that the vast majority of specimens have the potential to be perturbed by the AWI. Recent advancements have led to a greater awareness of variables that can be changed to alter the distribution and behaviour of particles on a cryo-EM grid. These include the use of grid supports made of different materials such as carbon or gold [15], the use of continuous support films [16, 17], affinity grids [18], the addition of detergents or surfactants [19], or reducing the time between sample application and vitrification [20]. All of these approaches are linked by a common theme: they either sequester particles away from an AWI or they modulate the properties of the AWI by adjusting chemical properties and surface tension of the liquid film [8].

The grid-making process is currently a major focus in the cryo-EM field, with a number of approaches in various stages of development, all seeking to improve access, quality, and/or reproducibility of cryo-EM sample preparation. The Spotiton system uses an inkjet piezo dispenser to directly deposit samples onto self-wicking grids to create a thin film, and is currently undergoing commercialization

(chameleon; SPT Labtech, formerly TTP Labtech) [21-23]. An alternative open-source approach, the “Shake-it-off,” uses an off-the-shelf ultrasonic humidifier to spray small sample volumes onto an electron microscopy (EM) grid and offers a low-cost solution to grid preparation [24]. The cryoWriter system uses a microcapillary to deposit sample directly on the grid, enabling direct purification and vitrification from low volumes of lysate [25, 26]. The Vitrojet (CryoSol) uses a pin printing system to deposit small volumes of sample onto the surface of a grid to directly create a thin film in a controlled manner, followed by vitrification with jets of cryogen [27]. Finally, microfluidic spraying devices such as the time-resolved cryo-EM device (TED) enable fast dispense-to-plunge times [28] but require larger sample volumes. In this study we focus on the behaviour of particles prepared for cryo-EM using the Vitrobot Mk IV, TED, and chameleon. Since each of these sample preparation devices exposes particles to different environments, forces, and timescales, we will briefly describe the specifics of each device.

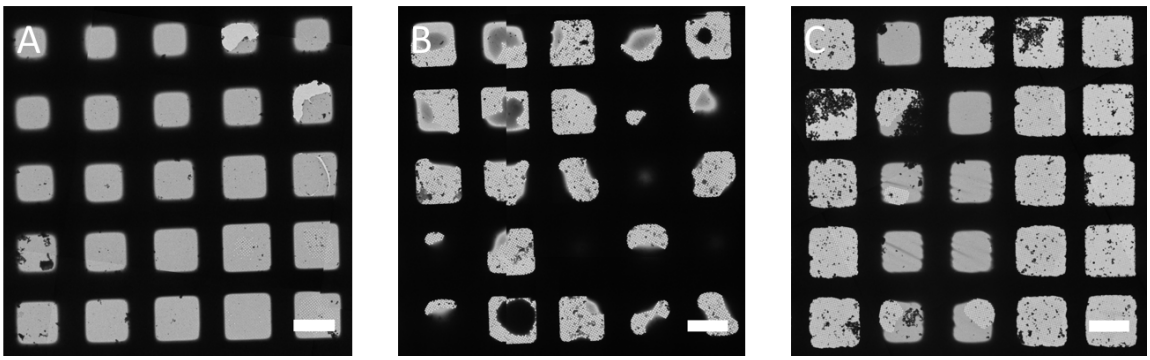


**Figure 5-1: Example low-magnification images of grids prepared using different vitrification devices.**

Comparison of typical results for (A) Vitrobot, (B) TED, and (C) chameleon (scale bar, 50 μm) as imaged by cryo-EM.

The Vitrobot involves the application of 3–4 μL of sample volume onto an EM grid held in a temperature- and humidity-controlled chamber. Subsequently it is blotted between two sheets of filter paper, for 3–10 s, removing the vast majority of the sample volume, before the blotting paper is withdrawn and the sample is plunged into the cryogen. Grids can be prepared on a timescale of 5–15 s from sample application, and typical grids will have a gradient containing some areas that are too thick and some that are too thin, with a large number of suitable grid squares for imaging (Figure 5-1 a) [5]. While this device has been used to successfully vitrify a wide range of specimens, there is evidence that the irregular pattern of fibres in the filter paper causes non-uniform alterations in surface-to-volume ratio across the grid, and this may be a root cause of the irreproducibility often reported for

blotting paper-based vitrification techniques, as well as being detrimental to samples [29].

The TED was primarily designed to perform time-resolved experiments by rapidly mixing constituents before vitrification on the millisecond timescale. However, in this study we only make use of its ability to deposit a single sample and vitrify it on a very fast timescale (≥6 ms) [28]. A conventional EM grid is placed on a plunging arm, which has an adjustable speed within a high-humidity chamber at room temperature. The liquid system (syringes, tubing, and nozzle) is then equilibrated with ~40 µL of sample, which is deposited by spraying directly onto the grid as it plunges into the cryogen. A typical experiment requires between 4 and 32 µL of sample volume per grid, depending mainly on the liquid flow rate. Exposure time to the AWI is determined by the time of flight for the spray droplets (from nozzle to grid) and the grid plunge time (from spray to ethane). A typical grid has a random droplet pattern, with some thick regions corresponding to the centre of a droplet, and thinner edges (which sometimes cover about half of a grid square) where the ice is sufficiently thin for imaging (Figure 5-1 b). With the current design, dispense-to-plunge times can be set from 6 ms to seconds.

The chameleon is a fully automated instrument that dispenses controlled droplets onto a self-wicking grid as it plunges into the cryogen. Self-wicking grids and 5 µL of sample are manually placed into the instrument as input. Workflows guide the user through system setup, preparation of grids, and system cleanup and reporting. Automated assessment of wicking and visual inspection together provides a quality control step prior to cryo-EM, allowing the routine preparation of grids with optimal ice thickness. Dispense-to-plunge times range from 54 ms to a few seconds with typical times in the range of 100–250 ms. A typical grid contains a stripe of approximately 20–40 grid squares with desired ice thickness (Figure 5-1 c).

For this study, we have examined the behaviour of three protein systems, apoferritin (480 kDa, O symmetry), mitochondrial chaperone heat-shock protein family D member 1 (HSPD1) (408 kDa, C7 symmetry), and *Escherichia coli* ribosome (30S, 50S, 70S, all C1 symmetry). Apoferritin was chosen because it is a common test specimen in cryo-EM, HSPD1 because when prepared using standard cryo-EM methods it adopts an extremely preferred orientation, and ribosomes because they are considered to be a very robust macromolecular complex and are also asymmetric, unlike the other two specimens.

## 5.3 Materials and methods

### 5.3.1 Sample preparation

Horse spleen apoferritin was purchased from Sigma Aldrich (A3660), and exchanged into 30 mM HEPES, 150 mM NaCl pH 7.5 by ultrafiltration using 100 kDa molecular weight cut-off (MWCO) spin concentrator tubes (Vivaspin, Sartorius). Protein concentration was then determined using absorbance at 280 nm ($\varepsilon_{280}$ = 14,565 $mol^{-1}cm^{-1}$, MW = 18.5 kDa and homo-24-mer stoichiometry). For grid preparation, apoferritin was diluted to the target concentration in 30 mM HEPES, 150 mM NaCl pH 7.5.

*E. coli* ribosome sample was purchased from New England Biolabs (P0763S), provided at a stock concentration of 33 mg/mL (= approx. 25 µM assuming an average molecular weight of 1.34 MDa [30]. For grid preparation, ribosomes were diluted to the target concentration using 50 mM HEPES, 8 mM $MgAc_2$, 100 mM KAc pH 7.5.

Mature human mitochondrial heat shock protein family D member 1 (HSPD1) was expressed in *E. coli* BL21 DE3 and purified based on a modified version previously described protocol [31]. The expression plasmid was kindly provided by Dr Hao Shao and Dr Jason Gestwicki (UCSF). Competent *E. coli* BL21 DE3 were transformed with the plasmid using the heat-shock method. Two flasks of 1 L TB media were inoculated with 2 x 20 mL overnight culture, incubated for 2.5 h at 37°C, 200 rpm until $OD_{600}$ reached 0.8. Expression was induced by adding 250 µM IPTG and cells were further incubated for 4 h at 37°C, 180 rpm, then cells were harvested by centrifugation (10 min, 4000 rpm) and stored at -80°C.

All purification steps until reconstitution were done on ice or at 4°C. The cell pellet was thawed on ice and resuspended in 40 mL lysis buffer (50 mM Tris, 500 mM NaCl, 10 mM imidazole pH 8), supplemented with 1 mM PMSF and protease inhibitor cocktail (set V, Calbiochem). The cells were further resuspended with 4 strokes in a dounce homogeniser and lysed with a sonicator (35% amplitude, 30 sec on/off, 10 min total). Cell debris was pelleted by centrifugation (30 min, 17,000 rpm) and the supernatant applied to 7 mL packed, equilibrated Ni-NTA resin. The protein-bound resin was washed with 200 mL lysis buffer and 200 mL wash buffer (50 mM Tris, 300 mM NaCl, 50 mM imidazole pH 8). The protein was eluted with 20 mL eluting buffer (50 mM Tris, 300 mM NaCl, 300 mM imidazole pH 8). To remove the His6-tag, DTT (final concentration 1 mM) and TEV protease (1.6 mg per 10 mL, 3.2 mg in total) were added and the mixture was incubated for 4 h at room temperature. The cleavage products were dialysed

against 4 L dialysis buffer (50 mM Tris, 150 mM NaCl pH 7.5) in a 10 kDa MWCO membrane overnight. TEV protease and His6-tag were removed by incubation with 3 mL of preequilibrated Ni-NTA resin for 1 h in lysis buffer. The flowthrough was collected, 10% (v/v) glycerol was added and the protein concentrated to 20 – 30 mg/mL in a 10 kDa MWCO spin concentrator (Vivaspin, Sartorius).

For reconstitution into its oligomeric form, 4 mL HSPD1 were mixed with 100 µL 1 M KCl, 100 µL 1 M $MgAc_2$ and 400 µL 50 mM Mg-ATP (pH 7). The reaction was incubated at 30°C for 60-90 min. All following steps were done at room temperature. Precipitate was removed by centrifugation at 13,000 rpm for 10 min and the soluble fraction was loaded onto a HiLoad 16/600 Superdex 200 gel filtration column (GE Healthcare). Size exclusion chromatography was done in 50 mM Tris, 150 mM NaCl, 10 mM $MgCl_2$ pH 7.7. The fractions corresponding to oligomeric HSPD1 (as determined by negative stain EM and SDS-PAGE) were collected, concentrated to 10-25 mg/mL with 10 kDa MWCO spin concentrators, supplemented with 5% (v/v) glycerol and frozen in liquid $N_2$.

Protein concentrations of HSPD1 was determined by measuring absorbance at 280 nm ($\varepsilon_{280}$ = 14,440 $mol^{-1}cm^{-1}$, MW = 58.2 kDa and homo-7mer stoichiometry). For grid preparation, HSPD1 was diluted to the target concentration in 50 mM Tris, 300 mM NaCl, 10 mM $MgCl_2$ pH 8.

### 5.3.2 Preparation of blotted grids

For specimens prepared by blotting, Quantifoil 300 mesh Cu R 1.2/1.3 holey carbon grids were glow-discharged in a Cressington 208 carbon coater with glow discharge unit at 10 mA and 0.1 mbar air pressure for 30 s. Grids were prepared using a Vitrobot™ mark IV (Thermo/FEI) with a blot force of 6 and a blot time of 6 s. The relative humidity (RH) was ≥90% and temperature 20°C for ribosome and 4°C for apoferritin and HSPD1. Concentrations for Vitrobot™ grid preparation were 20, 0.6 and 0.8 µM for apoferritin (24mer), HSPD1 (7mer) and ribosome, respectively. The applied sample volume was 3 µL for all blotted grids and the liquid ethane was used as cryogen in all cases.

### 5.3.3 Fast preparation of grids using the TED

Fast grid preparation using the TED was done as previously described, using gas-dynamic virtual nozzles in spraying mode [32]. Quantifoil 300 mesh Cu R 1.2/1.3 holey carbon grids were used after glow-discharge in a Cressington 208 carbon coater with glow discharge unit at 10 mA and 0.1 mbar air pressure for 99 s. In this TED setup, the droplets are small and fast and the delay between spray and

deposition short (≤1 ms). The spray parameters were held approximately constant for all grids, using a liquid flowrate of 8.3 µL/s and an atomizer gas pressure between 1.5 and 2.0 bar. The nozzle design used was slightly different from the one previously described with the distance between liquid channel and nozzle outlet being 95 µm instead of 125 µm. PDMS sprayers were manufactured as previously described. Droplet speeds are high under these conditions (>20 m/s) and the used nozzle-grid distance (during sample application) was low (7 - 10 mm). Therefore, to estimate exposure time of the thin film to the AWI, only the time between droplet impact on the grid and freezing was considered. Plunge speeds were measured using a linear potentiometer and the vertical distance between nozzle and liquid ethane surface was 1-3 cm and the plunge speed was ≤3 m/s. The humidity chamber was at ≥ 80% RH and ambient temperature for grid preparation. Concentrations for TED grid preparation were 20, 11 and 2.5 µM for apoferritin (24mer), HSPD1 (7mer) and ribosome, respectively.

### 5.3.4 Fast preparation of grids using the Chameleon

For specimens prepared on the chameleon system, SPT Labtech 300 mesh Cu R 1.2/0.8 holey carbon self-wicking nanowire grids were used. Variable amounts of glow discharge in a Pelco Easiglow at 12 mA, 0.39 mbar air pressure were used to activate and control the wicking speed. Samples were held at 4°C (apoferritin, ribosome) or 24°C (HSPD1) until aspiration into the dispenser. Grids were prepared at a RH between 75% and 85% at ambient temperature. The applied sample volume for each stripe is ~6 nL. Concentrations for chameleon grid preparation were 5.5 and 2.5 µM for HSPD1 (7mer) and ribosome, respectively.

### 5.3.5 Fiducial-less cryo-ET data collection and processing

All cryo-ET was collected in the Astbury Biostructure Laboratory in Leeds on Titan Krios II, using the Gatan K2 direct electron detector operated in counting mode and a Bioquantum energy filter. Data acquisition parameters are listed in Table 5-S2.

Frames were motion-corrected with MotionCor2 [33], stacked using an in-house script and tomograms were reconstructed using back projection in Imod after 4-fold binning to enhance the contrast [34, 35]. Particles were manually picked using EMAN2 [36]. Particle positions were then used to locate the AWI. In order to do this, the tomogram was divided into patches in the x/y-directions (4-16 patches depending on particle concentration). The particles at minimum and maximum Z-height were selected and used to fit a plane (first or second order polynomial, depending on the number of patches and visual inspection of the fit) which corresponds to the upper and lower AWI, respectively. Then, the closest distance

was determined between either of the AWIs and each particle. Particles which were at a distance ≤10 nm to an AWI were classed as 'bound' to the AWI. For the majority of tomograms collected, the 10 nm threshold adequately allowed characterisation of the data, but for tomograms on areas of thick ice (>80 nm)/where the AWI is not clearly defined, a threshold of 20 nm was more suitable. Ideal particle behaviour was modelled using the experimentally determined AWIs and randomly generating particle coordinates (number/volume corresponding to the respective concentration) in between the experimental ice layer. Then, distances between modelled particles and AWIs were determined.

### 5.3.6 Single particle cryo-EM data collection and processing

All single particle cryo-EM data was collected in the Astbury Biostructure Laboratory in Leeds on Titan Krios I, equipped with a FEI Falcon III detector and operated in integrating mode. Data collection parameters are listed in Table 5-S3 and Table 5-S4.

All single particle data processing was done in RELION 3 [37]. Micrographs were corrected for beam-induced motion with MotionCor2 and the CTF was estimated using GCTF [33, 38]. All further data processing was done as shown in Figure 5-S4 and Figure 5-S5 for HSPD1 and ribosome, respectively. Particles were picked using the general model in crYOLO [39].

All HSPD1 datasets were combined after particle extraction (rescaled to 2.13 Å pixel size). One round each of 2D- and 3D-classification were used to clean the dataset. Consensus reconstructions with particles from all datasets were generated in C1 and C7 symmetry and used to determine angular distributions. Finally, the dataset was split into its original subsets and each subset of particles and used to generate a reconstruction using the assigned angles from the C7 consensus reconstruction.

Similarly, all ribosome datasets were combined after extraction and subjected to one round of 2D classification to remove 'junk' particles. Then, 3D classification was performed to separate the combined datasets into 70S, 50S and 30S subsets. Those subsets were cleaned up by an additional round of 2D classification (2 rounds for 30S) and a consensus reconstruction was generated including data from all 4 datasets for the three species (70S, 50S and 30S). The subset for each species was then further split into the original datasets, resulting in reconstructions for 70S, 50S and 30S for each timepoint.

The maps were visualised using ChimeraX [40]. Orientation distributions were visualized using a script adapted from Naydenova et al. [41]. The probability

density function was estimated using kernel density estimation with a Gaussian kernel at a fixed bandwidth of 10°, wider than the estimated angular accuracy in all cases (to avoid overinterpretation of angular distribution maps).

## 5.4 Results

### 5.4.1 Partitioning of particles to the AWI

The speed of grid making has been reported to influence the particle distribution at the AWI, with ~100 ms showing a change in partitioning and angular orientation relative to slower speeds [20]. We used cryo-electron tomography (cryo-ET) to investigate differences in particle partitioning in the thin ice layer at different time points for various macromolecular complexes, using the Vitrobot, TED, and chameleon (Figure 5-2; Movie 5-S1, Movie 5-S2, Movie 5-S3, Movie 5-S4, Movie 5-S5, Movie 5-S6, Movie 5-S7, Movie 5-S8, Movie 5-S9). Areas for tomogram acquisition were selected without prior investigation of particle distribution in that area, and based upon ice thicknesses that would be deemed most suitable for data collection. We classified particles as partitioned to the AWI based on either a 10 nm or 20 nm distance from the AWI. For all three specimen types, on blotted Vitrobot grids (Figure 5-2 b) the majority of particles resided at the AWI, consistent with previous observations [14], with an average of 86%, 99%, and 80% of particles associated with the AWI across the apoferritin, HSPD1, and ribosome data, respectively (Figure 5-2 and Figure 5-S1; Table 5-S1).

To investigate trends in particle distribution on different timescales of vitrification, we used the TED to vitrify grids on “fast” timescales (6–13 ms), and used the TED and chameleon to vitrify grids on “intermediate” timescales (50–200 ms). The majority of the particles partitioned to the AWI on the TED “fast” timescale (apoferritin: 75% at 11 ms; HSPD1: 89% at 6 ms; ribosome: 96% at 13 ms), although it should be noted the TED data showed a greater variability compared with Vitrobot data (Figure 5-2 and Figure 5-S1). On the “intermediate” timescale, TED grids of apoferritin (50 ms) and HSPD1 (50 ms) displayed large variability across different tomograms of the same specimen, although the majority of particles interacted with the AWI (67% and 95% for apoferritin and HSPD1, respectively). “Intermediate” timescale chameleon grids of ribosome (200 ms) displayed 94% of sample interacting with the AWI.

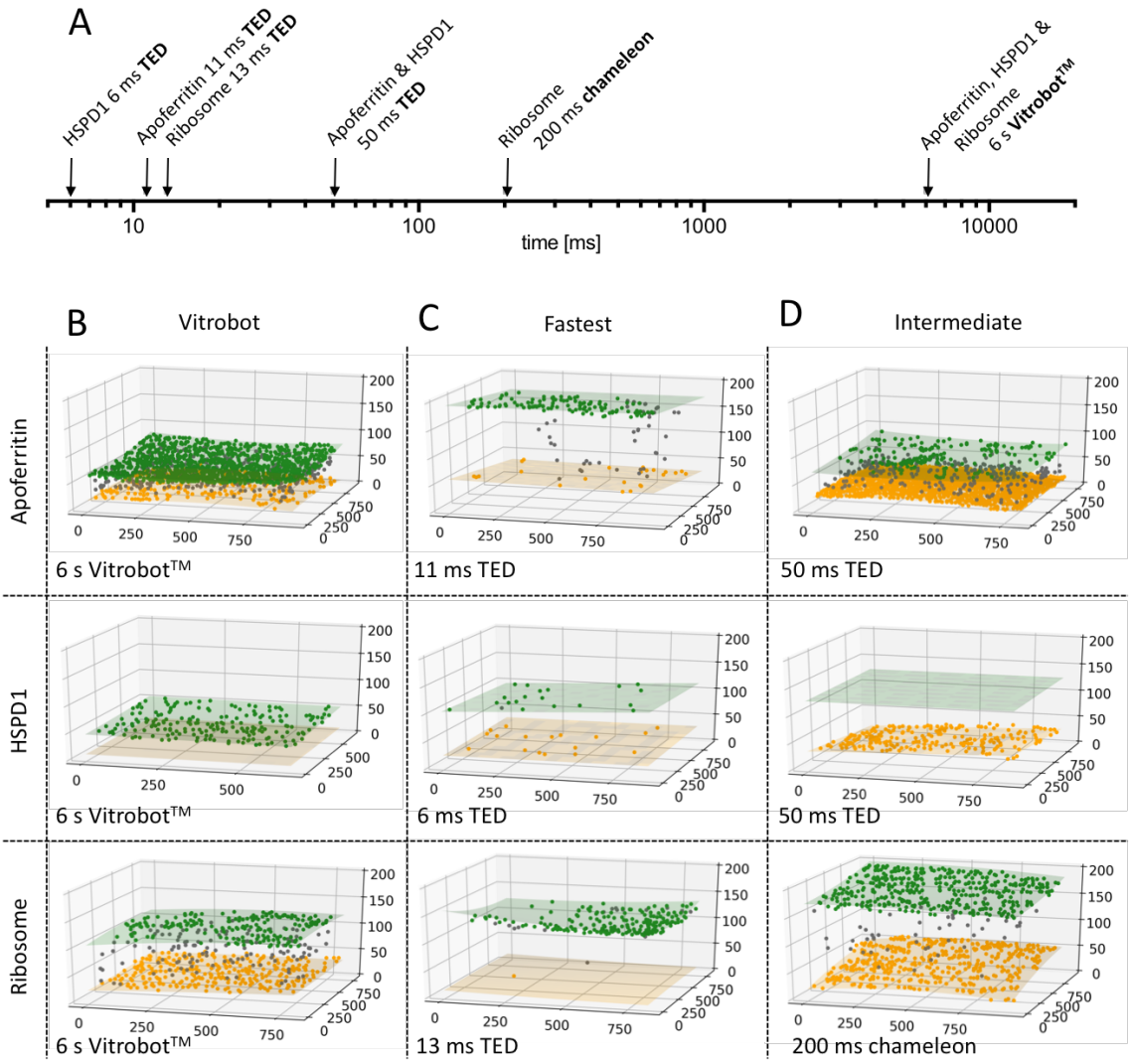


**Figure 5-2: Visualisation of particle partitioning at AWI using cryo-ET.**

(A) Timescale of grid preparation for tomography samples. (B–D) Representative tomograms of apoferritin, HSPD1, and ribosome grids prepared at standard blotting speed for Vitrobot (B; time given is Vitrobot "blot time"), (C) fastest time points (TED), and (D) intermediate time points. Green and yellow shaded areas indicate the top and bottom of the AWI, with yellow, grey, and green spheres representing the particle location at the top, middle, and bottom of the ice, respectively. The axis indicates coordinates of the particle location in ice in nanometres. Timescale from sample preparation to vitrification and sample preparation device is shown in the bottom of the box. Full raw data can be seen in Table 5-S1.

The "fast" TED data demonstrate that even on the fastest timescales we could investigate using this device and in thick ice (up to ~180 nm), the interaction with the AWI is not eliminated. This is perhaps unsurprising given that calculations suggest that particles will interact 10–100 times with the AWI within 1 ms, and for some proteins this interaction results in sequestering at the AWI [41]. It should be noted that TED generally produces thicker ice, especially at faster dispense-to-

plunge times, as the TED relies on droplet spreading upon contact with the grid to produce areas sufficiently thin to image (Table 5-S1). For the apoferritin grids prepared using the TED, we observed interesting trends in surface protein aggregates at 11 ms compared with 50 ms. At 11 ms, small aggregates of ~10–50 particles were observed, which appeared to be much larger at 50 ms where they consisted of hundreds of particles. Protein aggregates were only observed at the AWI (Figure 5-S2).

When considering the spraying devices across various timescales and Vitrobot blotting data together, the trend of a reduction in particles at the AWI at faster freezing times holds true for the apoferritin and HSPD1 samples (Figure 5-S1), although more variability is seen in the intermediate timepoints of grids made on the TED. Interestingly, the ribosome data show the opposite trend, with increased partitioning to the AWI at 13 ms compared with the blotted grid. A general observation across all sample preparation techniques (TED, chameleon, Vitrobot) was the presence of asymmetry in particle distribution in some tomograms, i.e., one AWI face was highly populated while the other was not (Figure 5-2), as previously reported for the Vitrobot and Spotiton [14].

### 5.4.2 Concentration of particles

Our experience with sample preparation has shown that there is a variation in the concentration of the necessary amount of sample required to achieve similar particle numbers in frozen grids when using the Vitrobot, TED, and chameleon. There have been previous studies which have shown that the blotting procedure can increase the apparent concentration of a protein, for example ATP synthase and O3-33, with multiple blotting and the use of detergents significantly affecting the resultant particle concentration on the grid [42, 43]. In addition to this we wanted to investigate the difference between the concentration of the protein solution used and the resultant concentration on the grid after preparation using the Vitrobot, TED, and chameleon and to compare this with previous estimations using a tomographic approach.

For Vitrobot blotted grids there was a large increase, or concentrating effect, with average 3-, 21-, and 24-fold increases in particle numbers for apoferritin, HSPD1, and ribosomes, respectively (Figure 5-3). This interesting result demonstrates a previously unreported advantageous sample concentration effect of blotting methods. To interrogate this further, we made a comparison between a theoretical model thin film and the observed data. A model thin film was generated by placing particles representing the actual concentration of sample applied to the grid with randomly generated coordinates (within the confines of the thin film, assuming no

concentration change and no affinity for the AWI) (Figure 5-S3). For apoferritin, the model data matched remarkably well the experimental data at distances away from the AWI (>10 nm), indicating that the concentration effect seen in Vitrobot blotted grids of apoferritin exclusively stems from particles bound to the AWI.

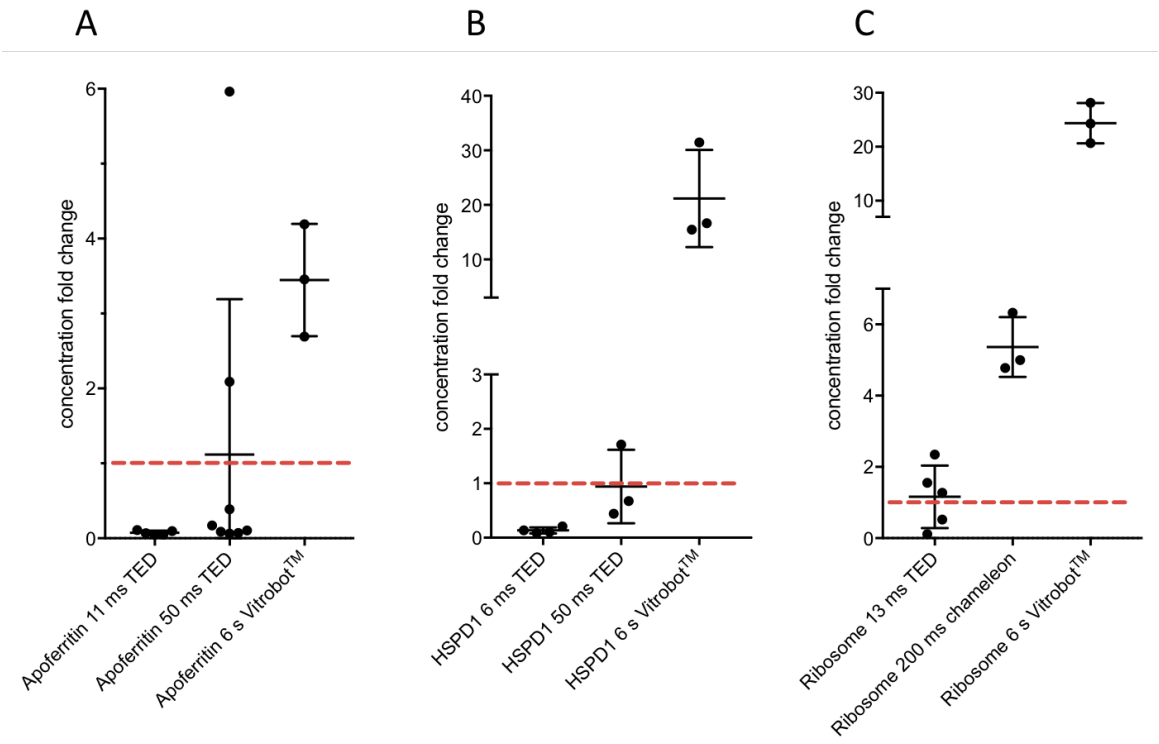


**Figure 5-3: Apparent change in protein concentrations in the thin film at varying timepoints and vitrification devices.**

Particle concentrations in thin film as determined from tomograms for (A) apoferritin, (B) HSPD1, and (C) ribosomes. The solid bars indicate mean ± SD and dots show individual values. Vitrification device and timescales are labelled. Red line indicates the concentration in solution (applied concentration).

For the TED, we hypothesized that there should be no particle concentration or dilution effects, as the droplets land on the grid without liquid being drawn away as in the case of both the Vitrobot (filter paper) and chameleon (self-wicking grids). Using the TED, at 50 ms for HSPD1 and apoferritin (and 13 ms for ribosome), we do indeed see, on average, the number of particles we would expect given the concentration of protein applied. This indicates that there are no significant concentrating effects for TED at these timepoints. However, there is large variability in the 50 ms apoferritin data compared with the 50 ms HSPD1 data. Interestingly, the “fast” apoferritin and HSPD1 data both show a large depletion of particles (14- and 7-fold, respectively). Data from the chameleon on the ribosome

sample at 200 ms show a substantial concentrating effect (5-fold), but much reduced compared with the Vitrobot data.

### 5.4.3 Orientation and angular distribution of HSPD1

HSPD1 is known to adopt strong preferred orientation when prepared using standard blot-freezing methods. We examined HSPD1 angular orientation using the TED at 6 and 50 ms, the chameleon at 54 ms, and the Vitrobot (Figure 5-4). Single-particle datasets for each timepoint and device were collected and combined after pre-processing. Two-dimensional (2D) and three-dimensional (3D) classifications were performed on the combined data to impose the same class selection criteria on all datasets, and the consensus structure was determined. From this, the angular assignments for particles that were frozen using each device at the specific timepoints were extracted to analyse trends in preferred orientation (Figure 5-4 c and Figure 5-S4).

As expected for HSPD1, strong preferred orientation was seen, with the “top” and “bottom” projections dominating the particle views present in all data collected. The quality of the consensus 3D reconstruction suffered from the anisotropy of views, as seen in the z-directional Fourier shell correlation (Figure 5-S4 b-d). The Vitrobot blotted sample (Figure 5-4 c) showed the strongest preferred orientation. By increasing the speed of grid making using either the chameleon or TED, broader angular distributions were obtained compared with the standard blotted grid. Reducing the time delay further, from 50 ms to 6 ms on the TED, provided further minor improvements in angular distribution, although the data were still dominated by preferred views.

Due to variations between datasets, such as ice thickness and particle number, it is not possible to draw comparisons between the freezing devices used and resolution outcomes. Instead we limit comparisons to the range of angular distributions. For example, the reconstruction from the 6-ms TED data, which had a greater angular distribution, is limited in resolution to approximately 7 Å. This is likely due to increased ice thickness compared with the other datasets (Table 5-S1); other reconstructions are likely resolution limited due to low particle numbers or ice thickness (Figure 5-S4).

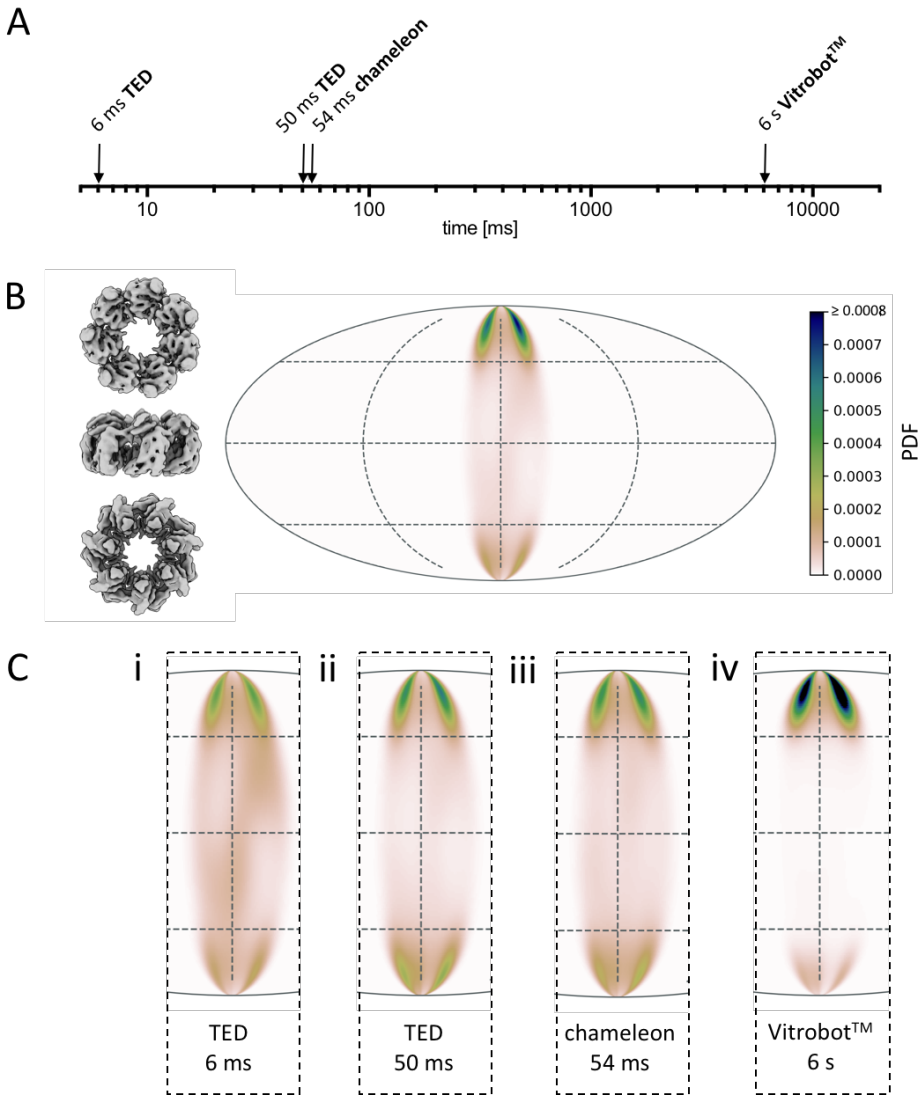


**Figure 5-4: Angular orientation of HSPD1 over varying timepoints and vitrification devices.**

(A) Timescale of grid preparation for HSPD1 samples analysed for angular distribution. (B) Preferred orientation of HSPD1 of the combined data, showing an angular orientation distribution map (Mollweide projection) of the C7 symmetric reconstruction so that only one-seventh of the area is occupied. Views of HSPD1 on the left show the approximate corresponding orientation, with these data dominated by the top view. (C) Orientation distribution maps for HSPD1 data collected from samples prepared with TED 6 ms (i), TED 50 ms (ii), chameleon 54 ms (iii), and Vitrobot 6 s (iv). The normalized probability density function (PDF) approximates the probability to find a particle in a certain orientation. The colour scale is the same in (B) and (C), with dark blue representing a high proportion of particles, through green, brown, and white representing no particles in a specific orientation.

### 5.4.4 Orientation and angular distribution of ribosomes

A sample containing the 30S, 50S, and 70S ribosomes was used to investigate the angular distributions of three related specimens in one dataset to keep as many parameters constant as possible (e.g., ice quality). Applying the same approach used to examine HSPD1 angular distribution, we collected single-particle datasets for ribosome samples prepared with TED (13 ms), chameleon (54 and 200 ms), and Vitrobot blotted samples (Figure 5-5 and Figure 5-S5).

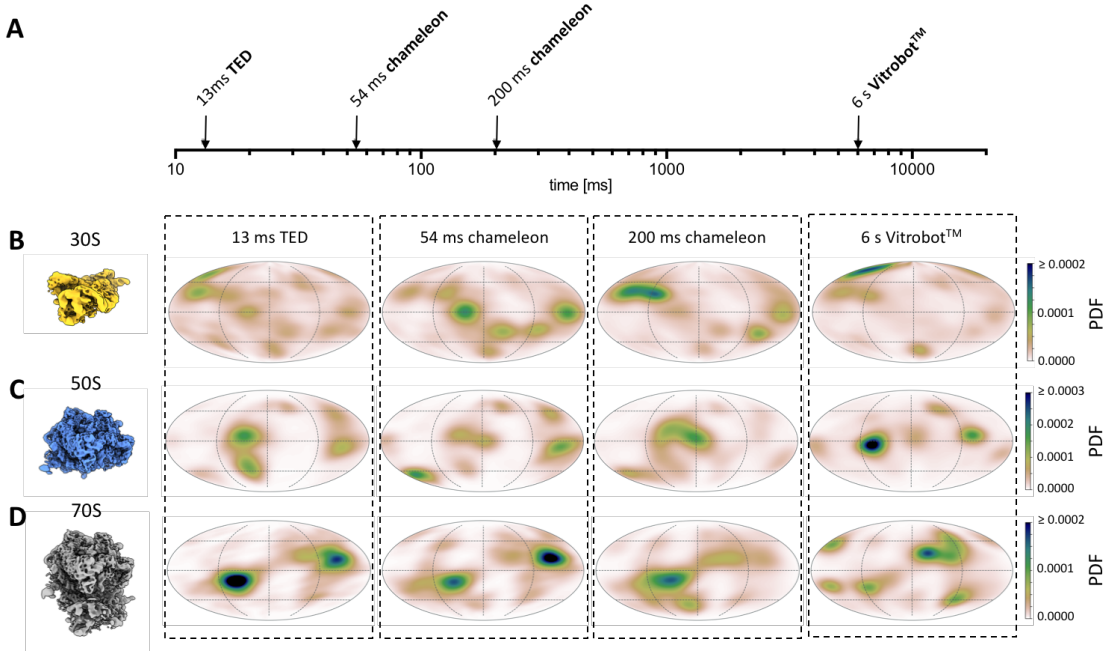


**Figure 5-5: Ribosome angular orientation over varying timepoints and vitrification devices.**

(A–D) (A) Timescale of grid preparation for ribosome angular single-particle analysis samples. Orientation distribution maps for (B) 30S, (C) 50S, and (D) 70S samples prepared using stated vitrification device and timescale. As in Figure 5-4, shown is the normalized probability density function (PDF) in Mollweide projection to approximate the probability to find a particle in a certain orientation.

The 30S subunit showed a clear correlation between speed of grid preparation and improved angular distribution (Figure 5-5 b). This trend was also present in the 50S subunit data, although not as pronounced (Figure 5-5 c). Interestingly, this trend is not present for the full ribosome; instead the greatest angular distribution was observed from grids prepared using the Vitrobot (Figure 5-5 d). Taking the datasets through the processing pipeline, none of the ribosome reconstructions appear to be limited in resolution by angular orientations, and the trends observed in

resolution for each of the sample preparation times and methods appear to link most closely to the particle number (Figure 5-S5 and Figure 5-S6).

Consistent with AWI interactions inducing complex dissociation, we observe a number of ribosomal subunits that are resolved at early but not later timepoints. Density for the 50S ribosomal protein L31 is lost in the 70S and 50S ribosome structures in a time-dependent manner (Figure 5-6 b and d). In the grids made in ≤54 ms using both TED and chameleon, the L31 subunit is clearly present. However, in those grids made at 200 ms and 6 s, the L31 subunit is absent within the EM maps when viewed at the same and lower threshold as the fast-plunge structures (Figure 5-6). During TED, chameleon, or Vitrobot grid preparation, shear forces acting on the sample may vary. Thus, exposure time to the AWI is not the only factor that could result in complex dissociation or protein unfolding. However, subunit L31 is absent in the 200 ms but present in the 54 ms timeframe grid, both made on the chameleon using the same protein sample. Dissociation of subunit L31 is therefore time dependent and likely through exposure to the AWI. The 30S and 70S reconstructions show that 30S ribosomal protein S2 also dissociates in a time-dependent manner. Interestingly, ribosomal protein S2 persists for a longer time frame than the L31 subunit, only disappearing in the Vitrobot prepared grids while present in the TED and chameleon datasets (Figure 5-6 f). The density for 50S ribosomal protein L9 behaves in a similar fashion; the difference is more pronounced in the 70S reconstructions, it is present at ≤200 ms but missing in the 6 s reconstruction. For the L9 and S2 subunits there is a possibility that dissociation is method dependent and not time dependent, as they are only absent in the blotted and not sprayed grids. It is interesting to note that the L31, L9, and S2 subunits all display a predominantly neutral/positive patch when compared with the negative charge of the ribosome. Moreover, L31, L9, and S2 also show a significantly reduced buried surface area, which may play a role in the relative ease with which these subunits dissociate compared with other subunits (Figure 5-S7).

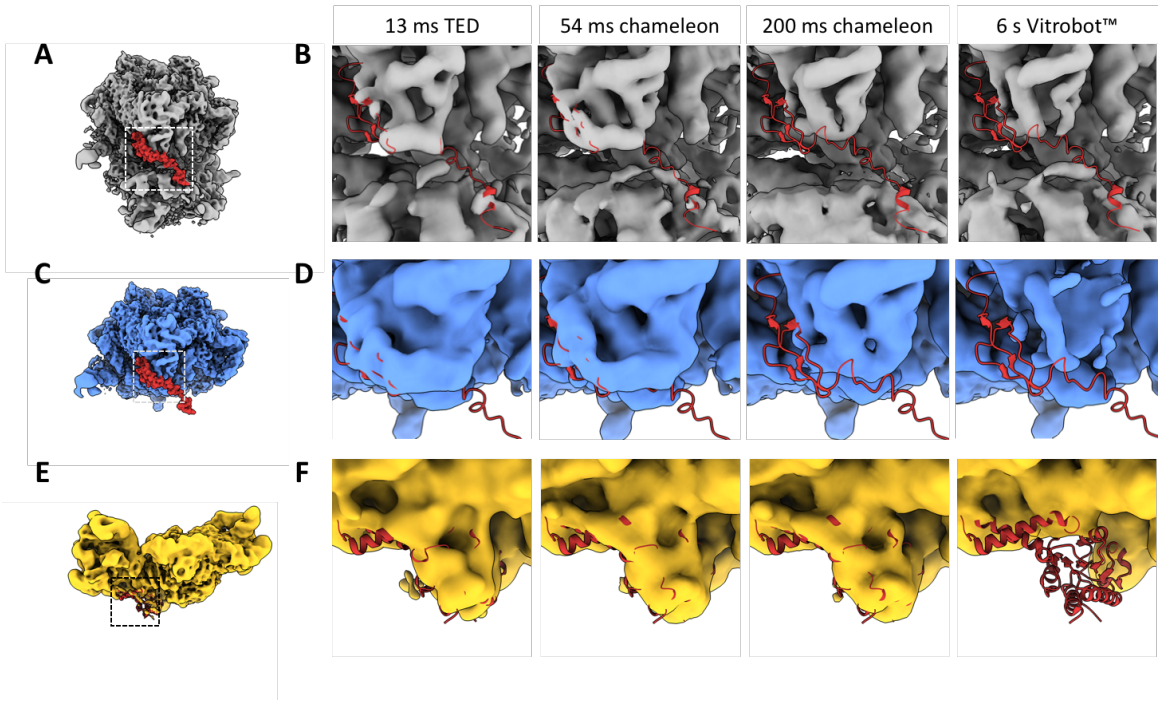


**Figure 5-6: Dissociation of ribosomal subunits over varying timepoints and vitrification devices.**

(A) Position of ribosomal protein L31 (from PDB: 6OSK) in the 70S ribosome. (B) Density for L31 in 70S reconstructions compared between all timepoints. While present in "fast" reconstructions, the density is absent in the 200 ms or Vitrobot reconstructions. (C) Position of ribosomal protein L31 (from PDB: 6OSK) in the 50S ribosome. (D) Density for L31 in 50S reconstructions compared between all timepoints showing the same trend as in (B). (E) Position of ribosomal protein S2 in the 30S subunit (from PDB: 6O7K). (F) Density for S2 in 30S reconstructions compared between all timepoints. The S2 density is missing in the Vitrobot but present in all other reconstructions. 70S in grey, 50S in blue, and 30S in yellow; all maps in (B), (D), and (F) are shown at threshold of 3σ.

## 5.5 Discussion

### 5.5.1 AWI partitioning

The physics of diffusion and AWI interactions cannot be outrun using technology currently available (to the best of our knowledge) for cryo-EM sample preparation. Even in the fastest cases of grid vitrification in our study (6 ms) and using different approaches (blotting versus spraying), the majority of particles still partitioned to the AWI. Considering AWI partitioning data from the three specimens we examined, apoferritin, HSPD1, and ribosomes, conflicting lessons can be learned from each. HSPD1 data suggest that the faster the grids are prepared, the fewer

particles partition to the AWI (Figure 5-2 and Figure 5-S1). The ribosome data suggest the precise opposite: the faster the grids are prepared, the more particles partition to the AWI (Figure 5-2 and Figure 5-S1). The apoferritin data are the most variable and provide the least clear picture across different timescales, which may be partially explained by the propensity of apoferritin to form “rafts” at the AWI (discussed below in Changes in Particle Concentration due to Speed of Grid Preparation).

Overall, altering speed of grid preparation could be one mechanism to influence AWI partitioning, but the effects of this are not linear and are difficult to predict across different specimens. A greater understanding of the factors that may influence partitioning, including specimen polarity, stability, and buffer composition, along with more information about how different specimens respond to the thin-film environment over time, may enable better predictions of specimen behaviour prior to freezing in the future.

### 5.5.2 Changes in angular distribution

Even though most particles could not be prevented from locating at the AWI, small (HSPD1) to very large (30S, 50S ribosome) changes in the angular distribution of particle over tens to hundreds of milliseconds were observed (Figure 5-4 and Figure 5-5). Previous work has shown that hemagglutinin from influenza A adopts preferred orientation on the ~100 ms timescale, slower than HSPD1 but also equilibrating in a single orientation [20, 44]. These data suggest that for a given specimen, there may be a fast (<10 ms) stage when the protein initially partitions to the AWI, followed by a slower stage when the particle explores its energy landscape before settling into a local energy minimum. For some specimens, there may be a distinct orientation (leading to preferred orientation), and for other specimens it may be a variety of orientations (Figure 5-7). The timescale in this second, slower stage is likely to vary from specimen to specimen.

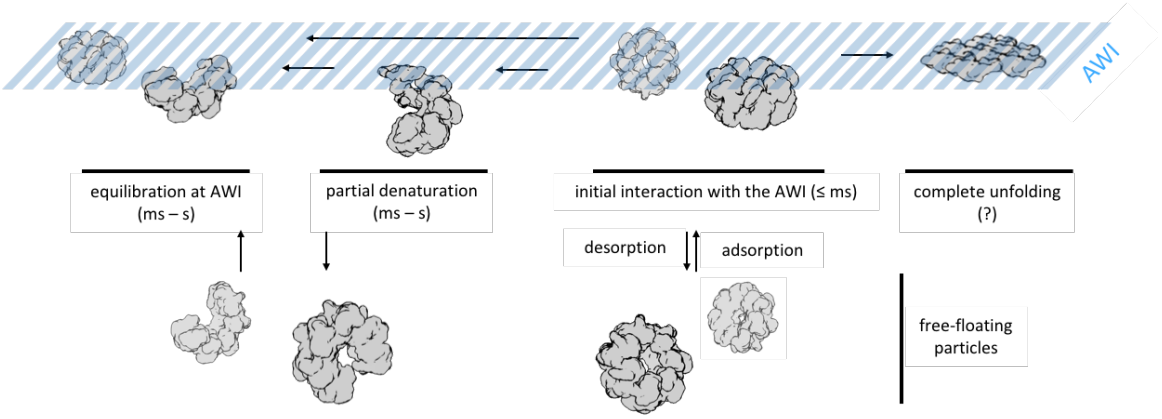


**Figure 5-7: Proposed model of protein-AWI interactions.**

The initial interaction with the AWI (adsorption) is fast. Equilibration of the protein-AWI system, however, is slower as it involves processes such as desorption, partial, or complete denaturation, which occur on various timescales (milliseconds to seconds) and are thought to be highly protein dependent (desorption from the AWI, rate of unfolding).

### 5.5.3 Particle damage over time

Another factor that must be considered at the AWI is the partial or full denaturation of protein specimens [13]. The time frame of such denaturation at the AWI is likely to depend on many factors. The ribosome data suggest that denaturation during sample preparation can occur on the timescale of hundreds to thousands of milliseconds. In 70S and 50S ribosomes, the L31 subunit is only present at timepoints <200 ms, while 30S ribosomal subunit S2 and 50S subunit L9 are still present at 200 ms (Figure 5-6). In agreement with our data, a recent study has shown that 30S ribosomal subunit S2 is present when grids have carbon support but is dissociated on unsupported grids [45]. These data suggest that the timescale of partial denaturation at the AWI is highly specimen dependent and extends into the timeframe accessible by various grid-preparation methods. This timescale suggests that partial denaturation may be an effect of the slower energy landscape exploration, helping to explain how particle orientation can change over longer timescales than partitioning to the AWI takes (Figure 5-7).

### 5.5.4 Concentrating effect of Vitrobot blotting

One of the most striking results was the change in concentration due to blotting as compared with spraying (Figure 5-3). These data clearly demonstrate that for the specimens we have examined, the Vitrobot blotting approach greatly enriches the thin film with particles, consistent with previous studies [42, 43], and indeed that the AWI may be responsible for the concentration of particles in the thin film, which in many systems is required to achieve a viable number of particles per

micrograph. It should also be noted that the degree of concentration is sample dependent. This may go some way toward explaining the experience of many cryo-EM researchers in ascertaining the “right” concentration of protein to use for their system. Adsorption to the grid support may also have a significant impact on apparent particle concentration in the imageable areas, which requires further investigation.

### 5.5.5 Changes in particle concentration due to speed of grid preparation

Across both TED and chameleon, higher concentrations of specimen were necessary at faster timepoints. However, specifically with TED at the “fast” timescales, a depletion of particles for apoferritin and HSPD1 was observed (Figure 5-3). The apoferritin data from TED display greater variability relative to the other samples, which could be linked to the formation of surface aggregates that were also observed in these data (Figure 5-S2). Surface aggregates, or particle “rafts,” may begin to form while the droplet is traveling from nozzle to grid in TED (~0.5 ms). The size of the aggregates may be time dependent with increases in size occurring at longer timescales. These rafts create locally high concentrations of particles on a single interface (Figure 5-S2 c). The reason for the preference for just one interface is currently unclear and requires further investigation. Occasionally, large rafts are found in the thin areas chosen for data collection, and are likely also present in the thick regions unsuitable for imaging by transmission EM. This rafting behaviour may explain why, on average, the expected number of particles are present in TED 50 ms apoferritin samples, but with large variability in concentration from area to area. A small number of examples of the “raft” effect were also observed for the 13 ms ribosome grids but not for HSPD1 data, indicating that the presence of rafts is sample dependent while its severity is time dependent. No “rafting” was seen in grids prepared using chameleon or the Vitrobot.

A major unexplained aspect of these data is that for HSPD1 and apoferritin at the “fast” TED time points (11 ms and 6 ms respectively), a large depletion in the concentration of particles compared with slower speeds was observed (Figure 5-3). We propose the following two hypotheses to explain these observations:

1. The first hypothesis relates to the variability of droplet size, a feature specific to the TED (Figure 5-1 b). The droplets have variable surface-to-volume ratios, so in smaller droplets particles would be more likely to interact with the AWI from the moment the droplet is formed and travels to the grid. If denaturation occurs at this interface, apparent protein concentration would decrease in this droplet and

become lower than what would have been observed in larger droplets where the surface-to-volume ratio would favour proportionally fewer AWI interactions. Once on the grid and frozen, smaller droplets are more likely to be imaged, especially at “fast” grid-preparation speeds, as they are more likely to result in thin ice. The larger droplets, which, according to this hypothesis, would contain closer to the expected number of particles, cannot be imaged at these “fast” timepoints because they will result in ice that is too thick. At intermediate grid-preparation timescales, the smaller droplets may have disappeared (due to film thinning) while the larger droplets have thinned to suitable thicknesses. This would explain the apparent depletion of particles observed at faster speeds and the “reappearance” of particles at intermediate timepoints.

2. Particle denaturation over time may also contribute to the observed concentration differences. On TED prepared grids, each frozen droplet has a thick central part that subsequently spreads out into a thin layer at the edge of the droplet. The apparent depletion of particles at the “fast” timepoints may be due to the loss of proteins in the formation of a sacrificial denatured protein layer. Particles could then diffuse from thicker areas in the droplet to repopulate thin, imageable areas, causing the “reappearance” of particles at intermediate timepoints. Theoretical calculations suggest that protein denaturation may occur on a sub-millisecond timescale [46] in addition to the longer timescales for partial denaturation seen here (Figure 5-7).

Formation of a sacrificial layer of denatured protein has been shown for apoferritin [47], but the timescale of complete particle denaturation on cryo-EM grids remains an open question. There may be alternative explanations for these data, and the hypotheses presented are not mutually exclusive. It is likely that there is interplay between multiple mechanisms on a specimen-dependent basis. It is only with additional information on these trends across many specimens, added to these initial data, that a better understanding of particle behaviour in thin films can be achieved.

In conclusion, these data go some way to offering an explanation to those cryo-EM researchers who have experienced huge variability in cryo-EM sample preparation between biological specimens. General trends indicate that speed may ameliorate some of the adverse effects of the AWI, thus providing a significant improvement in intact or non-preferentially oriented particles. However, this speed may come at the price of a higher required sample concentration, with data suggesting that the faster the grids are prepared, the higher the concentration of protein required. This

effect may seem exacerbated given the concentrating effect currently enjoyed when using Vitrobot blotting to prepare samples.

While much is still unknown about the behaviour of particle in thin films, a general model can be used to summarize the aforementioned ideas (Figure 5-7). First, diffusion dictates the rate at which a particle interacts with the AWI. This is an initial fast phase, occurring within ≤1 ms of the thin film forming. Each specimen will then have its own on-off rate and local energy minima at the AWI, determining how likely it is for the protein to disassociate back into bulk solution. Next, negative aspects of the AWI may take place with partial denaturation or dissociation of parts of the molecule, and/or adoption of preferred orientations. However, the timescales of this final equilibrium will likely be highly specimen specific. This model explains why no “silver bullet” has yet been developed to generically tackle cryo-EM sample preparation for every specimen. Speed of grid preparation, grid types, use of surfactants, continuous and engineered support, and new grid-making technologies will all have a role to play as the field moves toward the development of generically useful approaches for cryo-EM sample preparation, but in the meantime they can be used as individual tools along the research path toward an optimized cryo-EM grid.

## 5.6 Supporting information

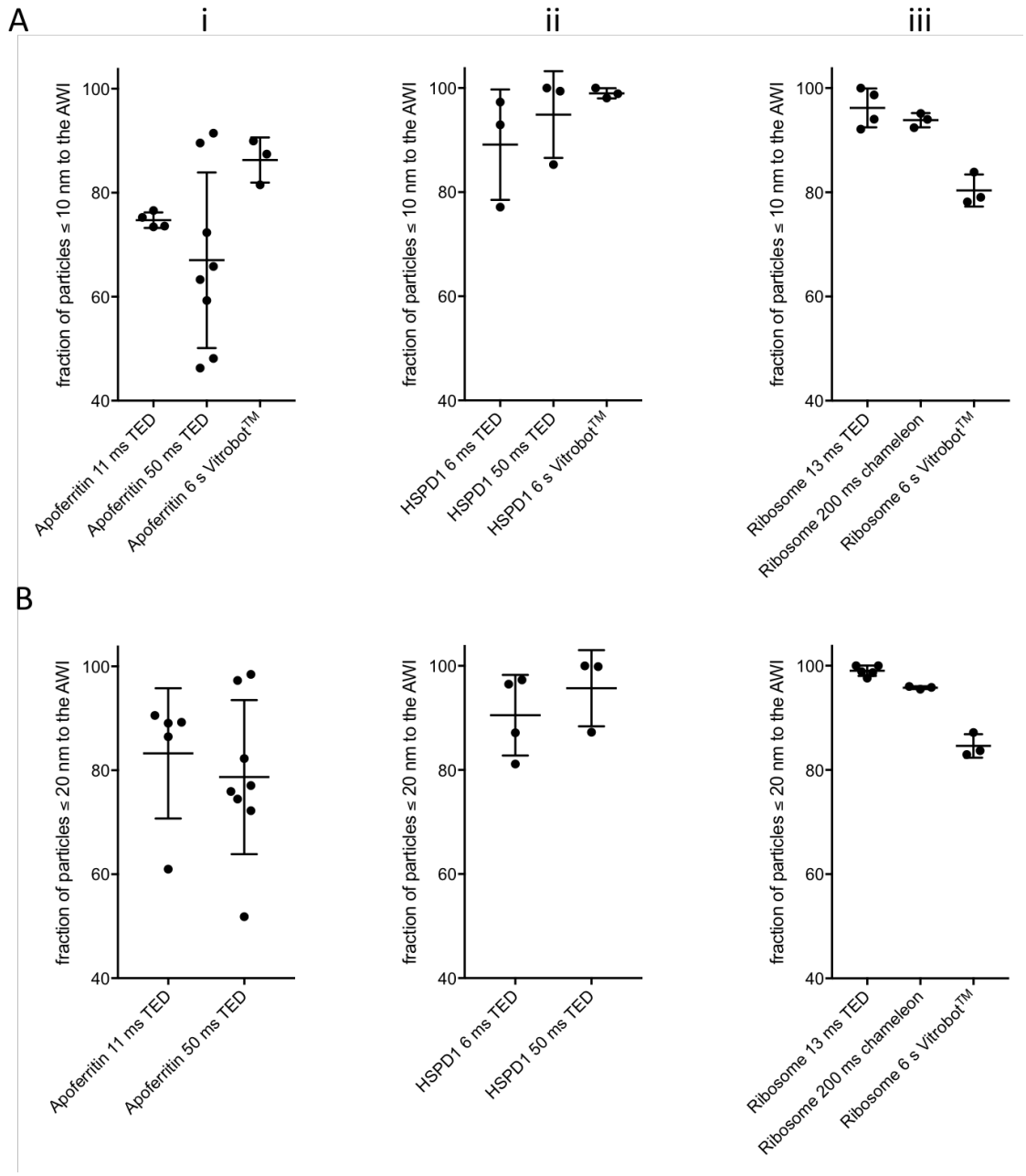


**Figure 5-S1: Partitioning of particles to the AWI.**

Fraction of particles partitioning to the AWI within 10 nm (A) or 20 nm (B) for apoferritin (i), HSPD1 (ii) and ribosomes (iii), with time and method of vitrification indicated. Some Vitrobot™ values were excluded from (B) because of low ice thickness. Shown are the individual data points, mean value and standard deviation.

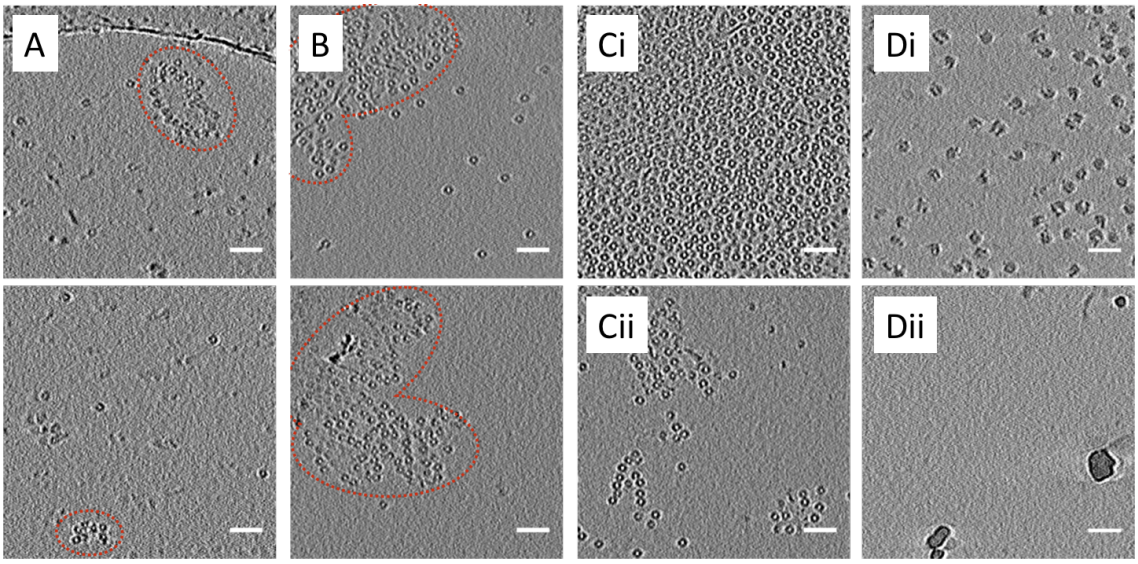


**Figure 5-S2: Surface aggregates at varying timepoints.**

Sections through reconstructed tomograms from TED grids, showing morphology of apoferritin aggregates at the AWI at (A) 11 ms or (B) 50 ms, outlined in red. Some tomograms showed highly asymmetric distributions of particles, with two interfaces from the same tomogram shown in (Ci) and (Cii) or (Di) and (Dii) for the apoferritin 50 ms and ribosome 13 ms sample, respectively. Scale bars 50 nm.

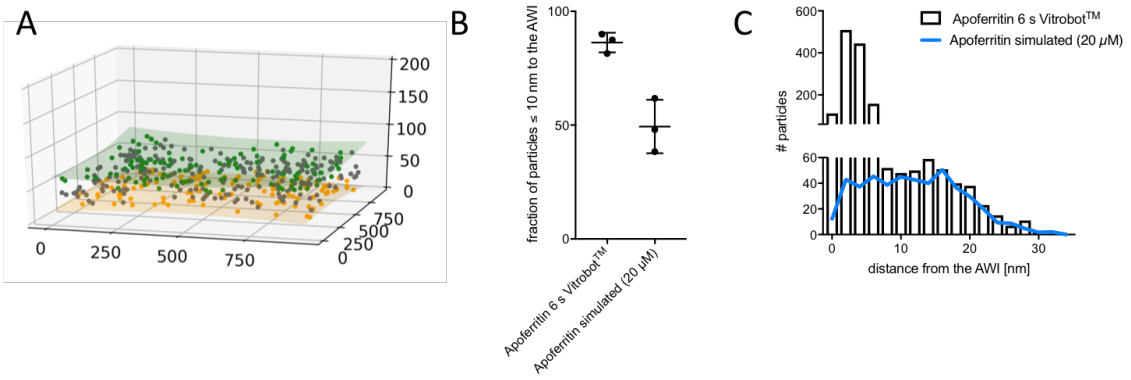


**Figure 5-S3: Comparing modelled data to experimental apoferritin partitioning.**

(A) Modelled distribution of particles (green, grey or yellow) in an ice layer (green and yellow surfaces), with coordinates indicated on axis (nm). AWIs were taken from an experimental tomogram and particle coordinates were randomly generated. This models a situation with no changes in concentration compared with sample applied, and no affinity for the AWI. (B) Comparison between modelled and experimental data for particle partitioning to the AWI. Particle concentration is 20 μM, P = 0.007. (C) Distributions of distances between particles and AWI for simulated (blue line) and experimental data (black bars) for apoferritin Vitrobot™ grids.

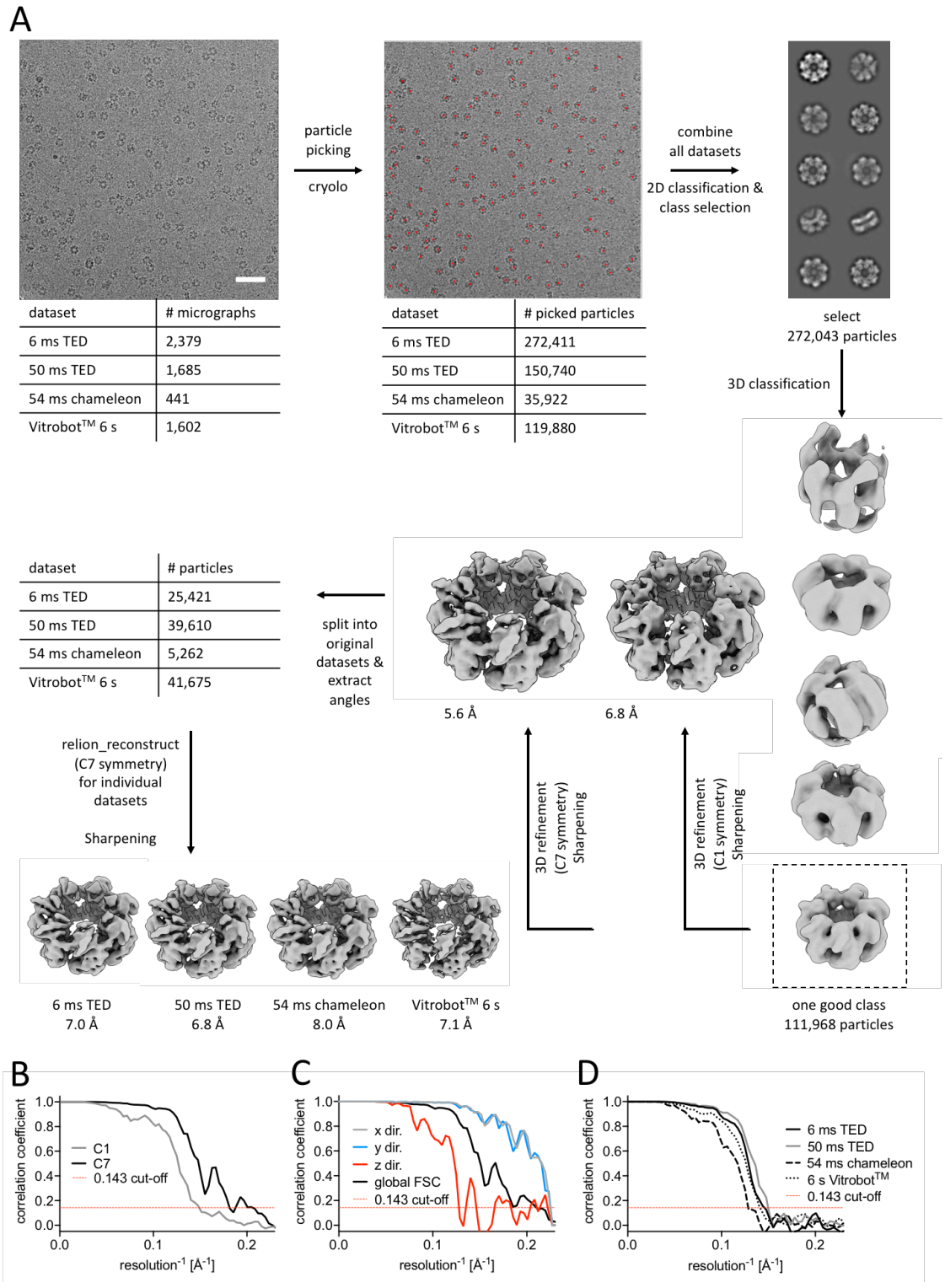


**Figure 5-S4: Cryo-EM image processing of HSPD1 data to yield angular distribution data and FSC curves for HSPD1 consensus structures.**

(Figure legend on the next page)

(A) Data processing pipelines for HSPD1 data showing particle numbers and corresponding 3D density maps and resolution for each sample preparation device and timescale analysed. Datasets have varying ice thicknesses, particle number and angular orientation and so resolutions cannot be directly compared. (B) FSC curves for masked maps of the consensus structure (all datasets combined) with and without symmetry. (C) 3D-FSC analysis of the same reconstruction, showing that resolution in the z-direction is limited through the lack of side views. Note that pixel size is 2.13 Å. (D) FSC curves for reconstructions for each individual dataset.

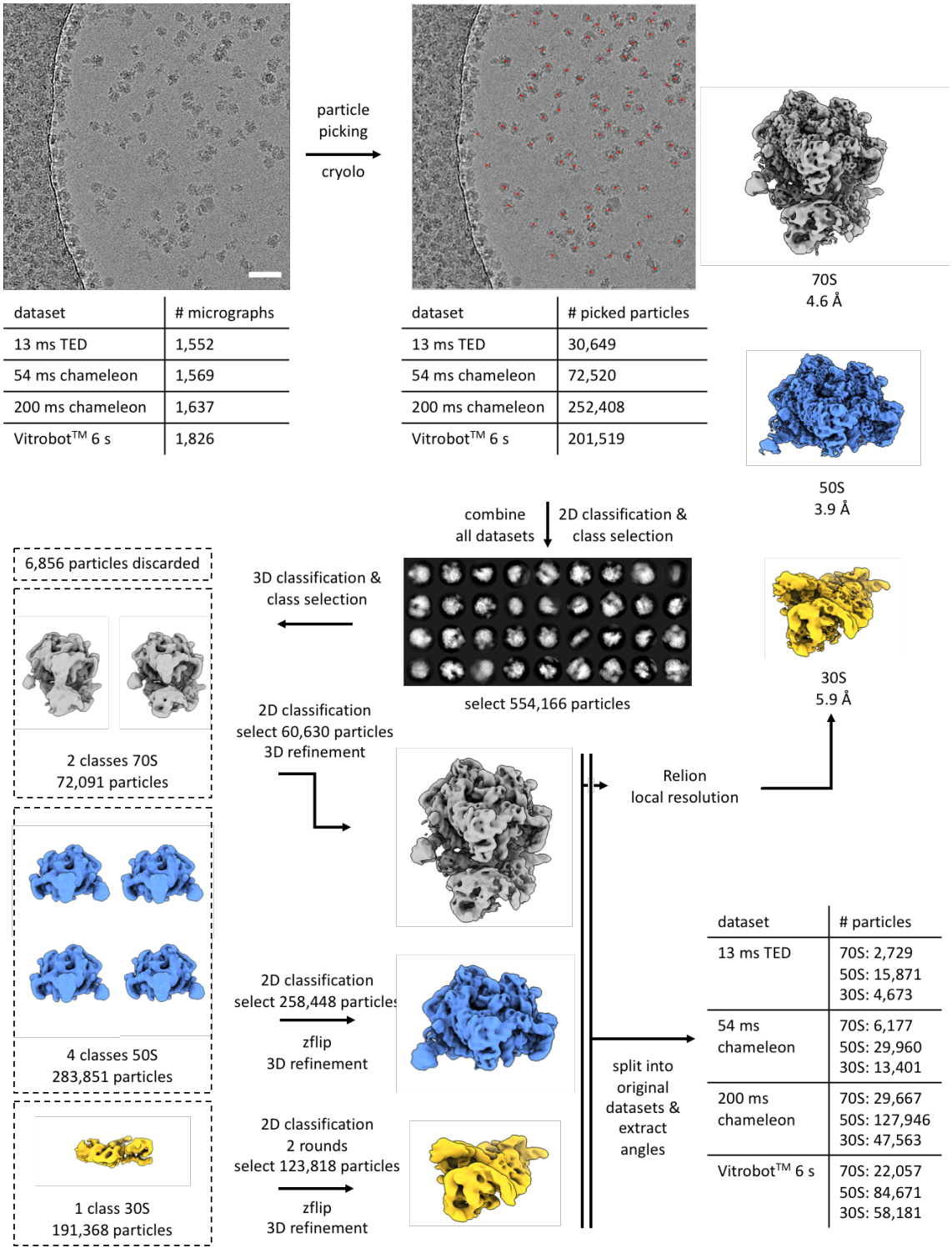


| dataset | # micrographs |
|---|---|
| 13 ms TED | 1,552 |
| 54 ms chameleon | 1,569 |
| 200 ms chameleon | 1,637 |
| Vitrobot™ 6 s | 1,826 |

| dataset | # picked particles |
|---|---|
| 13 ms TED | 30,649 |
| 54 ms chameleon | 72,520 |
| 200 ms chameleon | 252,408 |
| Vitrobot™ 6 s | 201,519 |

| dataset | # particles |
|---|---|
| 13 ms TED | 70S: 2,729<br>50S: 15,871<br>30S: 4,673 |
| 54 ms chameleon | 70S: 6,177<br>50S: 29,960<br>30S: 13,401 |
| 200 ms chameleon | 70S: 29,667<br>50S: 127,946<br>30S: 47,563 |
| Vitrobot™ 6 s | 70S: 22,057<br>50S: 84,671<br>30S: 58,181 |

**Figure 5-S5: Cryo-EM image processing of ribosome data to yield angular distribution data.**

Data processing pipelines for ribosome angular orientation maps. Micrographs shown are representative of the type of micrograph used.

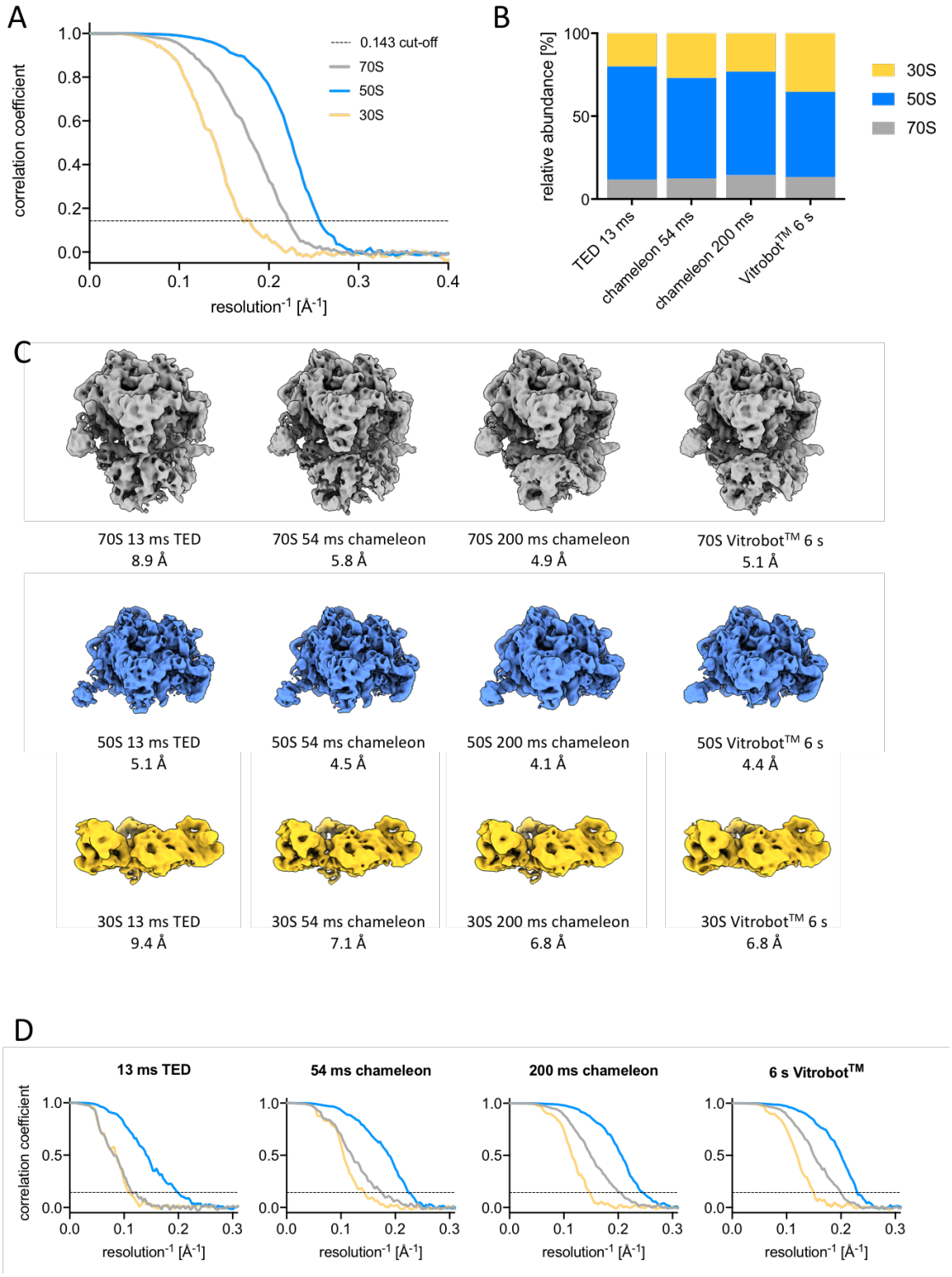


**Figure 5-S6: Cryo-EM reconstructions of ribosome data at different time points and vitrification devices.**

(A) FSC curves for masked, consensus reconstructions of 70S, 50S and 30S ribosome. (B) Relative particle numbers for 30S, 50S and 70S by individual dataset. (C) Individual reconstructed maps for 70S, 50S and 30S for all 4 subsets and corresponding FSC curves (D).

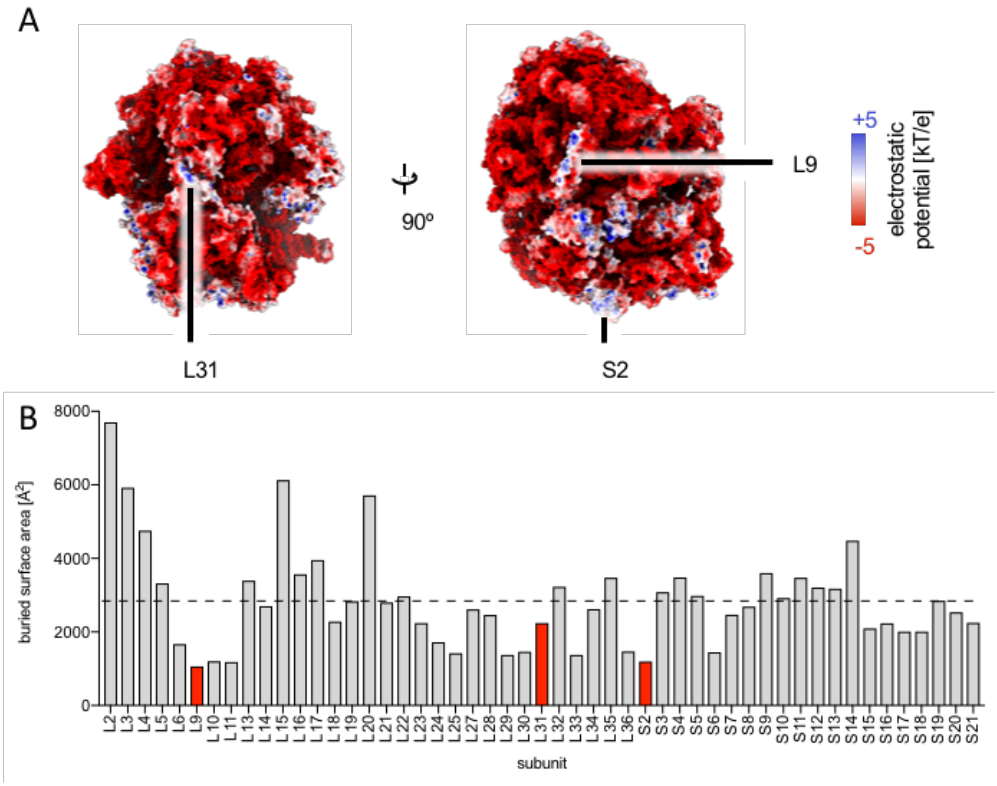


**Figure 5-S7: Analysis of the surface properties and buried surface area for the ribosomal proteins L9, L31 and S2.**

(A) Electrostatic surface potential of the ribosome with subunits L9, L31 and S2 highlighted showing their contrasting neutral/positive charge compared to the predominantly negative charge of the ribosome. (B) Buried surface are for the different ribosomal proteins with the average buried surface area indicated by a dashed line.

**Table 5-S1: Summary table of tomograms analysed to produce partitioning and particle concentration data.**

"Concentration" is the estimated concentration from the tomogram, "Applied concentration" is the concentration of the sample applied. "Relative particle #" is the percentage of particles within ≤ 10 or 20 nm of the AWI.

| | Time and vitrification device | Repeat | Concentration [µM] | Applied concentration [µM] | Ice thickness [nm] | # particles | relative particle # (≤ 10nm) | relative particle # (≤ 20nm) |
|---|---|---|---|---|---|---|---|---|
| Apoferritin | 11 ms TED | 1 | 1.0 | 20.0 | 168 | 100 | 21* | 61 |
| | | 2 | 1.9 | | 96 | 111 | 77 | 86 |
| | | 3 | 1.4 | | 78 | 64 | 73 | 89 |
| | | 4 | 0.9 | | 97 | 53 | 74 | 91 |
| | | 5 | 2.2 | | 139 | 186 | 75 | 89 |
| | 50 ms TED | 1 | 3.4 | 20.0 | 152 | 253 | 72 | 77 |
| | | 2 | 7.7 | | 135 | 509 | 66 | 74 |
| | | 3 | 2.1 | | 68 | 54 | 48 | 72 |
| | | 4 | 1.7 | | 76 | 79 | 63 | 82 |
| | | 5 | 1.4 | | 64 | 54 | 59 | 76 |
| | | 6 | 119.2 | | 47 | 2160 | 90 | 98 |
| | | 7 | 41.8 | | 90 | 1835 | 91 | 97 |
| | | 8 | 1.3 | | 88 | 54 | 46 | 52 |
| | 6 s Vitrobot™ | 1 | 53.9 | 20.0 | 54 | 1751 | 90 | 97** |
| | | 2 | 69.1 | | 43 | 1622 | 82 | 96** |
| | | 3 | 83.8 | | 34 | 1582 | 87 | 99** |
| HSPD1 | 6 ms TED | 1 | 1.5 | 11.0 | 95 | 70 | 77 | 87 |
| | | 2 | 1.2 | | 73 | 69 | 46* | 81 |
| | | 3 | 0.9 | | 82 | 37 | 97 | 97 |
| | | 4 | 2.3 | | 62 | 85 | 93 | 96 |
| | 50 ms TED | 1 | 18.8 | 11.0 | 60 | 680 | 99 | 100 |
| | | 2 | 4.9 | | 87 | 204 | 85 | 87 |
| | | 3 | 7.4 | | 73 | 325 | 100 | 100 |
| | 6 s Vitrobot™ | 1 | 18.9 | 0.6 | 39 | 193 | 100 | 100** |
| | | 2 | 10.0 | | 50 | 270 | 99 | 100** |
| | | 3 | 9.3 | | 64 | 156 | 98 | 100** |
| Ribosome | 13 ms TED | 1 | 1.3 | 2.5 | 113 | 57 | 19* | 100 |
| | | 2 | 0.3 | | 130 | 14 | 100 | 100 |
| | | 3 | 3.2 | | 151 | 84 | 94 | 98 |
| | | 4 | 3.9 | | 119 | 178 | 92 | 99 |
| | | 5 | 5.9 | | 67 | 152 | 99 | 99 |
| | 200 ms chameleon | 1 | 11.9 | 2.5 | 136 | 864 | 95 | 96 |
| | | 2 | 12.5 | | 137 | 934 | 94 | 96 |
| | | 3 | 15.8 | | 135 | 1235 | 92 | 96 |
| | 6 s Vitrobot™ | 1 | 17.0 | 0.8 | 92 | 601 | 79 | 84 |
| | | 2 | 23.5 | | 93 | 843 | 84 | 87 |
| | | 3 | 20.2 | | 97 | 787 | 78 | 83 |

* Values were excluded from analysis because of poor fitting of AWIs.

** Values were excluded from analysis because of low ice thickness.

**Table 5-S2: Microscope parameters for collection of cryo-ET data.**

| | |
|---|---|
| Microscope | Titan Krios II |
| Magnification | 42,000 |
| Voltage (kV) | 300 |
| Electron dose per image ($e^-/Å^2$) | 1.8 - 1.9 |
| Fractions per image | 3 |
| maximum/minimum tilt (increment) | -60°, +60° (2°) |
| Tilt scheme | bidirectional |
| Defocus range (μm) | -5 to -10 |
| Pixel size (Å) | 3.4 |

**Table 5-S3: Data collection parameters for SPA datasets of HSPD1.**

| | **HSPD1** | | | |
|---|---|---|---|---|
| | **6 ms TED** | **50 ms TED** | **54 ms chameleon** | **6 s Vitrobot™** |
| Microscope | Titan Krios I | | | |
| Magnification | 75,000 | | | |
| Voltage (kV) | 300 | | | |
| Total electron dose ($e^-/Å^2$) | 81 | 81 | 74 | 75 |
| Exposure time | 1.5 | 1.5 | 1.5 | 1.5 |
| Number of frames | 59 | 59 | 59 | 59 |
| Defocus range (μm) | -2 to -4 | -2 to -4.5 | -1.5 to -3.5 | -1.3 to -3.3 |
| Pixel size (Å) | 1.065 | | | |

**Table 5-S4: Data collection parameters for SPA datasets of the ribosome.**

| | **ribosome** | | | |
|---|---|---|---|---|
| | **13 ms TED** | **54 ms chameleon** | **200 ms chameleon** | **6 s Vitrobot™** |
| Microscope | Titan Krios I | | | |
| Magnification | 75,000 | | | |
| Voltage (kV) | 300 | | | |
| Total electron dose ($e^-/Å^2$) | 77 | 74 | 74 | 78 |
| Exposure time | 1.5 | 1.6 | 1.5 | 1.5 |
| Number of frames | 59 | 59 | 59 | 59 |
| Defocus range (μm) | -1.3 to -3.3 | -1.3 to -3.3 | -1.3 to -3.3 | -1.3 to -3.3 |
| Pixel size (Å) | 1.065 | | | |

https://ars.els-cdn.com/content/image/1-s2.0-S0969212620302823-mmc2.mp4

**Movie 5-S1**

Slice-Through of the Apoferritin Grid Prepared on the Vitrobot (6 s).

https://ars.els-cdn.com/content/image/1-s2.0-S0969212620302823-mmc3.mp4

**Movie 5-S2**

Slice-Through of the Apoferritin Grid Prepared on the TED in 11 ms.

https://ars.els-cdn.com/content/image/1-s2.0-S0969212620302823-mmc4.mp4

**Movie 5-S3**

Slice-Through of the Apoferritin Grid Prepared on the TED in 50 ms.

https://ars.els-cdn.com/content/image/1-s2.0-S0969212620302823-mmc5.mp4

**Movie 5-S4**

Slice-Through of the HSPD1 Grid Prepared on the Vitrobot (6 s).

https://ars.els-cdn.com/content/image/1-s2.0-S0969212620302823-mmc6.mp4

**Movie 5-S5**

Slice-Through of the HSPD1 Grid Prepared on the TED in 6 ms.

https://ars.els-cdn.com/content/image/1-s2.0-S0969212620302823-mmc7.mp4

**Movie 5-S6**

Slice-Through of the HSPD1 Grid Prepared on the TED in 50 ms.

https://ars.els-cdn.com/content/image/1-s2.0-S0969212620302823-mmc8.mp4

**Movie 5-S7**

Slice-Through of the Ribosome Grid Prepared on the Vitrobot (6 s).

https://ars.els-cdn.com/content/image/1-s2.0-S0969212620302823-mmc9.mp4

**Movie 5-S8**

Slice-Through of the Ribosome Grid Prepared on the TED in 13 ms.

https://ars.els-cdn.com/content/image/1-s2.0-S0969212620302823-mmc10.mp4

**Movie 5-S9**

Slice-Through of the Ribosome Grid Prepared on the Chameleon in 200 ms.

## 5.7 References

1. Kühlbrandt, W., *The resolution revolution.* Science, 2014. **343**(6178): p. 1443-1444.
2. Fernandez-Leiro, R. and S.H. Scheres, *A pipeline approach to single-particle processing in RELION.* Acta Crystallographica Section D: Structural Biology, 2017. **73**(6): p. 496-502.

3. Punjani, A., et al., *cryoSPARC: algorithms for rapid unsupervised cryo-EM structure determination.* Nature methods, 2017. **14**(3): p. 290-296.
4. De la Rosa-Trevín, J., et al., *Scipion: A software framework toward integration, reproducibility and validation in 3D electron microscopy.* Journal of structural biology, 2016. **195**(1): p. 93-99.
5. Thompson, R.F., et al., *Collection, pre-processing and on-the-fly analysis of data for high-resolution, single-particle cryo-electron microscopy.* Nature protocols, 2019. **14**(1): p. 100-118.
6. Rice, W.J., et al., *Routine determination of ice thickness for cryo-EM grids.* Journal of structural biology, 2018. **204**(1): p. 38-44.
7. Dubochet, J. and J. Lepault, *Cryo-electron microscopy of vitrified water.* J. Phys. Colloques, 1984. **45**(C7): p. C7-85-C7-94.
8. Glaeser, R.M. and B.-G. Han, *Opinion: hazards faced by macromolecules when confined to thin aqueous films.* Biophysics reports, 2017. **3**(1): p. 1-7.
9. Zhao, Y. and M. Cieplak, *Proteins at air–water and oil–water interfaces in an all-atom model.* Physical Chemistry Chemical Physics, 2017. **19**(36): p. 25197-25206.
10. Gerhardt, A., et al., *Protein aggregation and particle formation in prefilled glass syringes.* Journal of pharmaceutical sciences, 2014. **103**(6): p. 1601-1612.
11. Wiesbauer, J., R. Prassl, and B. Nidetzky, *Renewal of the air–water interface as a critical system parameter of protein stability: aggregation of the human growth hormone and its prevention by surface-active compounds.* Langmuir, 2013. **29**(49): p. 15240-15250.
12. Taylor, K.A. and R.M. Glaeser, *Retrospective on the early development of cryoelectron microscopy of macromolecules and a prospective on opportunities for the future.* Journal of structural biology, 2008. **163**(3): p. 214-223.
13. D'Imprima, E., et al., *Protein denaturation at the air-water interface and how to prevent it.* Elife, 2019. **8**: p. e42747.
14. Noble, A.J., et al., *Routine single particle CryoEM sample and grid characterization by tomography.* Elife, 2018. **7**: p. e34257.
15. Russo, C.J. and L.A. Passmore, *Ultrastable gold substrates: properties of a support for high-resolution electron cryomicroscopy of biological specimens.* Journal of structural biology, 2016. **193**(1): p. 33-44.
16. Hurdiss, D.L., et al., *New structural insights into the genome and minor capsid proteins of BK polyomavirus using cryo-electron microscopy.* Structure, 2016. **24**(4): p. 528-536.

17. Russo, C.J. and L.A. Passmore, *Controlling protein adsorption on graphene for cryo-EM using low-energy hydrogen plasmas.* Nature Methods, 2014. **11**(6): p. 649-652.
18. Han, B.-G., et al., *Electron microscopy of biotinylated protein complexes bound to streptavidin monolayer crystals.* Journal of structural biology, 2012. **180**(1): p. 249-253.
19. Chen, J., et al., *Eliminating effects of particle adsorption to the air/water interface in single-particle cryo-electron microscopy: Bacterial RNA polymerase and CHAPSO.* Journal of structural biology: X, 2019. **1**: p. 100005.
20. Noble, A.J., et al., *Reducing effects of particle adsorption to the air–water interface in cryo-EM.* Nature methods, 2018. **15**(10): p. 793-795.
21. Razinkov, I., et al., *A new method for vitrifying samples for cryoEM.* Journal of structural biology, 2016. **195**(2): p. 190-198.
22. Wei, H., et al., *Optimizing "self-wicking" nanowire grids.* Journal of structural biology, 2018. **202**(2): p. 170-174.
23. Dandey, V.P., et al., *Spotiton: New features and applications.* Journal of structural biology, 2018. **202**(2): p. 161-169.
24. Rubinstein, J.L., et al., *Shake-it-off: a simple ultrasonic cryo-EM specimen-preparation device.* Acta Crystallographica Section D: Structural Biology, 2019. **75**(12).
25. Arnold, S.A., et al., *Blotting-free and lossless cryo-electron microscopy grid preparation from nanoliter-sized protein samples and single-cell extracts.* Journal of structural biology, 2017. **197**(3): p. 220-226.
26. Schmidli, C., et al., *Microfluidic protein isolation and sample preparation for high-resolution cryo-EM.* Proceedings of the National Academy of Sciences, 2019. **116**(30): p. 15007-15012.
27. Ravelli, R.B., et al., *Cryo-EM structures from sub-nl volumes using pin-printing and jet vitrification.* Nature communications, 2020. **11**(1): p. 1-9.
28. Kontziampasis, D., et al., *A cryo-EM grid preparation device for time-resolved structural studies.* IUCrJ, 2019. **6**(6).
29. Armstrong, M., et al., *Microscale fluid behavior during cryo-EM sample blotting.* Biophysical journal, 2020. **118**(3): p. 708-719.
30. Van Holde, K. and W. Hill, *General physical properties of ribosomes*, in *Ribosomes*. 1974, Cold Spring Harbor Laboratory, Cold Spring Harbor, New York. p. 53-91.

31. Viitanen, P.V., et al., *[18] Purification of mammalian mitochondrial chaperonin 60 through in Vitro reconstitution of active oligomers.* Methods in enzymology, 1998. **290**: p. 203-217.
32. Klebl, D.P., et al., *Sample deposition onto cryo-EM grids: from sprays to jets and back.* Acta Crystallographica Section D: Structural Biology, 2020. **76**(4).
33. Zheng, S.Q., et al., *MotionCor2: anisotropic correction of beam-induced motion for improved cryo-electron microscopy.* Nature methods, 2017. **14**(4): p. 331.
34. Mastronarde, D.N., *Dual-axis tomography: an approach with alignment methods that preserve resolution.* Journal of structural biology, 1997. **120**(3): p. 343-352.
35. Kremer, J.R., D.N. Mastronarde, and J.R. McIntosh, *Computer visualization of three-dimensional image data using IMOD.* Journal of structural biology, 1996. **116**(1): p. 71-76.
36. Tang, G., et al., *EMAN2: an extensible image processing suite for electron microscopy.* Journal of structural biology, 2007. **157**(1): p. 38-46.
37. Zivanov, J., et al., *New tools for automated high-resolution cryo-EM structure determination in RELION-3.* Elife, 2018. **7**: p. e42166.
38. Zhang, K., *Gctf: Real-time CTF determination and correction.* Journal of structural biology, 2016. **193**(1): p. 1-12.
39. Wagner, T., et al., *SPHIRE-crYOLO is a fast and accurate fully automated particle picker for cryo-EM.* Communications Biology, 2019. **2**(1): p. 218.
40. Goddard, T.D., et al., *UCSF ChimeraX: Meeting modern challenges in visualization and analysis.* Protein Science, 2018. **27**(1): p. 14-25.
41. Naydenova, K. and C.J. Russo, *Measuring the effects of particle orientation to improve the efficiency of electron cryomicroscopy.* Nature communications, 2017. **8**(1): p. 1-5.
42. Snijder, J., et al., *Vitrification after multiple rounds of sample application and blotting improves particle density on cryo-electron microscopy grids.* Journal of structural biology, 2017. **198**(1): p. 38-42.
43. Rubinstein, J.L., *Structural analysis of membrane protein complexes by single particle electron microscopy.* Methods, 2007. **41**(4): p. 409-416.
44. Tan, Y.Z. and J.L. Rubinstein, *Through-grid wicking enables high-speed cryoEM specimen preparation.* Acta Crystallographica Section D: Structural Biology, 2020. **76**(11).
45. Jahagirdar, D., et al., *Alternative conformations and motions adopted by 30S ribosomal subunits visualized by cryo-electron microscopy.* RNA, 2020. **26**(12): p. 2017-2030.

46. Raffaini, G. and F. Ganazzoli, *Protein adsorption on biomaterial and nanomaterial surfaces: a molecular modeling approach to study non-covalent interactions.* Journal of Applied Biomaterials and Biomechanics, 2010. **8**(3): p. 135-145.
47. Yoshimura, H., et al., *Two-dimensional protein array growth in thin layers of protein solution on aqueous subphases.* Langmuir, 1994. **10**(9): p. 3290-3295.

# Chapter 6 Pre-power stroke structure of the actomyosin complex

To be published as: David P. Klebl, Charlotte A. Scarff, Cristina M. Risi, Betty Virok, Michele Stofella, Eva Forgacs, Donald A. Winkelmann, Frank Sobott, Vitold E. Galkin, Howard D. White and Stephen P. Muench. "Pre-power stroke structure of the Actomyosin Complex".

## 6.1 Abstract

The actomyosin complex is an archetypical molecular machine, which converts the chemical potential of ATP hydrolysis into mechanical energy allowing myosins to carry out their physiological functions such as muscle contraction and vesicular transport. High-resolution studies of actomyosin have been limited to equilibrium conditions and structures of important intermediate states in the catalytic cycle remain elusive. Here, we report the first structure of a pre-power stroke actomyosin complex, solved using time-resolved cryo-electron microscopy. In this pre-power stroke complex, the myosin motor has an open actin-binding cleft and a primed lever. It binds the actin filament through its lower 50 kDa subdomain only, with loop2 observed to reach out to the actin surface. In addition to the pre-power stroke actomyosin state, the time-resolved EM data contains one other conformational state, in which the actin-binding cleft is closed and the lever is in a post-power stroke position, similar to previous strongly-bound actomyosin structures. Together, the two states represent the start- and end-positions of the power stroke and allow us to assemble the most complete picture of the actomyosin catalytic cycle to date.

## 6.2 Introduction

Myosins perform a variety of functions in eukaryotes, ranging from muscle contraction to organelle transport. Mutations in myosins are linked to range of diseases in humans, including heart disease, deafness and cancer [1]. All myosins act as linear motors along filamentous actin (F-actin), fuelled by ATP hydrolysis. The myosin motor domain and its interaction with actin in the catalytic cycle are thought to be conserved across the > 70 myosin classes [2]. In the nucleotide-free state, the myosin motor is strongly bound to its F-actin track [3, 4]. ATP-binding to the motor reduces the affinity between myosin and F-actin, dissociating the complex and followed by a conformational change of the myosin lever arm (recovery stroke) [5]. Upon hydrolysis of ATP, myosin adopts a primed state with ADP and $P_i$ bound (pre-power stroke state). Binding of the primed state to F-actin track catalyses $P_i$-release, followed by a transition to stronger F-actin binding and

a major conformational change of the lever arm (power stroke), to produce force [6]. Release of ADP from the complex is coupled to a second, smaller swing of the lever arm, which completes the catalytic cycle [7, 8].

Although the actomyosin catalytic cycle is well understood, the mechanism by which myosin generates mechanical force remains controversial, with a paucity of structural information on how myosin initially interacts with actin in its primed state. Structurally, the myosin motor can be divided into 4 subdomains, N-terminal, upper 50 kDa (U50), lower 50 kDa (L50) and the converter domain which positions the lever arm [9]. The myosin motor alone has been trapped biochemically in the primed state, with ADP-$P_i$ or analogues, and the structure solved by X-ray crystallography. These structures of free myosin in the pre-power stroke state show an open cleft between the U50 and L50 subdomains, and a primed lever arm [8, 10]. Actomyosin complex structures in the ADP and nucleotide-free states have been obtained by cryo-electron microscopy (cryo-EM) and reveal the architecture of strongly-bound actomyosin complexes [8, 11, 12]. In the strongly bound states, the cleft between the U50 and L50 subdomains is closed, allowing interactions between F-actin and both U50 and L50, and the lever arm adopts a post-power stroke position.

However, it is currently unclear how myosin in the primed state binds F-actin, and how cleft closure between U50 and L50, the power stroke (lever arm movement) and phosphate release are coupled [9, 13]. Due to the fast conformational transition, traditional techniques have not been capable of determining an actomyosin-ADP-$P_i$ complex structure, to show how the myosin motor interacts with the actin filament prior to force generation. Therefore, we have employed, and show the power of, time-resolved cryo-EM to solve the structure of an actomyosin-5 complex in its pre-power stroke state (prePS).

## 6.3 Materials and methods

### 6.3.1 Sample preparation

Rabbit skeletal actin in monomeric form (G-Actin) was prepared as previously described [14]. Polymerisation to F-actin was done by mixing ~ 300 µM G-Actin with 10 % (v/v) exchange buffer (3 mM $MgCl_2$, 11 mM EGTA), incubating for 5 min on ice, adding 10 % (v/v) polymerization buffer (120 mM MOPS, 300 mM KCl, 12 mM $MgCl_2$, 1 mM EGTA) and incubating the mixture overnight on ice. Mouse PVL1392 myosin V subfragment 1 (S1), coding for amino acids 1–791 (1 IQ calmodulin-binding motif) and carrying the switch 1 $S^{217}A$ and loop 2 $\Delta DDEK^{594\text{-}597}$ modifications (myo5) was expressed and purified as previously described [15].

Disodium ATP was obtained from Roche and ADP was obtained from Sigma Aldrich.

### 6.3.2 Time-resolved cryo-EM grid preparation

Time-resolved cryo-EM experiments were done using a custom-built setup (TED) previously described [16] with modifications to allow for two mixing steps. A photo and schematic of the setup are shown in Figure 6-S1. The flowrates for each individual syringe were 2.1 µL/s. In the first mixing step, myo5 at 51 µM in 10 mM MOPS, 100 mM KCl, 3 mM $MgCl_2$, 0.1 mM EGTA pH 7 was mixed with 1 mM ATP in reaction buffer (10 mM MOPS, 50 mM KAc, 2 mM $MgCl_2$, 0.1 mM EGTA pH 7). The average time delay from the first mixing step to the spray nozzle was 2.2 s, given a flowrate of 4.2 µL/s, tube length of 7 cm, inner diameter (ID) of 0.38 mm and dead volumes of 1.0 and 0.3 µL for mixer and nozzle, respectively. The spray nozzles used here have been described and characterized previously [17, 18]. The myo5-nucleotide mixture 4.2 µL/s was met by two 2.1 µL/s flows of F-Actin at 25 µM (monomer concentration in reaction buffer) in the flow focussing region of the spray nozzle. This final mixture was sprayed onto an EM grid, moving at 1.8 m/s. The nozzle/grid distance at the point of sample application was 1.3 cm, resulting in a time-of-flight for the droplets of less than 1 ms. With a vertical distance of 1.7 cm between spray nozzle and liquid ethane surface, the time-delay was calculated to be 10 ms (10 ± 2 ms). The nozzle was operated in spraying mode with a spray gas pressure of 2 bar, the total flowrate was 8.4 µL/s.

A longer time-delay of 120 ms was obtained by increasing the vertical distance between nozzle and ethane surface to 5.2 cm and stopping the grid after passing the spray. In these experiments, the sample mixture was incubated for an additional ~100 ms on-grid, before plunging into liquid ethane for vitrification. The total time delay from droplet application to vitrification was 120 ms (122 ± 5 ms), including deceleration, 100 ms pause and acceleration. Otherwise, the conditions for grid preparation were the same as for the 10 ms timepoint.

All grids were prepared at room temperature (~ 20 °C) and at > 60 % relative humidity in the environmental chamber of the time-resolved EM device. Self-wicking grids were supplied by SPT Labtech and used after glow discharge in a Cressington 208 Carbon coater with glow-discharge unit for 60 s at 0.1 mbar air pressure and 10 mA. Four replicate grids were prepared for each timepoint, 3 of which were taken forward for data collection.

### 6.3.3 Conventional cryo-EM grid preparation

Cryo-EM grids of Acto-myo5 in the ADP-bound state were prepared by the conventional blotting method using a FEI/Thermo Vitrobot Mark IV. Myosin was prepared at 10 µM with 2 mM ADP in reaction buffer and mixed in a 1:1 ratio with 10 µM F-Actin (monomer concentration) to give 5 µM actomyosin complex. This was diluted to 2.5 µM prior to grid preparation. Quantifoil 300 mesh Cu R 2/2 grids were used after glow discharge in a Cressington 208 Carbon coater with glow-discharge unit for 30 s at 0.1 mbar air pressure and 10 mA. The chamber temperature was 4-6 °C, relative humidity was > 90 %, blot force was 6 and the blot time was 6 s.

### 6.3.4 Data processing and model building

Data were collected on a Titan Krios microscope equipped with a Gatan K2 direct electron detector operated in counting mode.

The main data collection and processing parameters for the time-resolved actomyosin data are listed in Table 6-1. A schematic overview of the processing pipeline is given in Figure 6-S2. Data from 3 grids was collected for each timepoint. All processing was done using RELION3.1 [19], unless otherwise mentioned. Micrographs were corrected for beam-induced motion using MotionCor2 and CTF estimation was done using gctf [20, 21]. Actin filaments were manually picked and processed using standard helical processing methods (Figure 6-S2 and Figure 6-S3 a-b) [22]. After CTF-refinement and Bayesian polishing, all 6 datasets were combined and a helical consensus structure calculated (Figure 6-S3 c). Using focussed 3D classification without alignment (non-helical) and a mask that covered the central myosin binding site (Figure 6-S3 d), particles were classified into prePS actomyosin, postPS actomyosin (Figure 6-S3 e), free actin and a small fraction of particles left unassigned. The final reconstruction of free actin was obtained by helical refinement. PrePS and postPS actomyosin were refined helically and after partial signal subtraction, as single particles (Figure 6-S3 f-i).

The main data collection and processing parameters for blotted Acto-myo5-ADP are listed in Table 6-2. Data for blotted Acto-myo5-ADP was processed analogous to the time-resolved actomyosin data (Figure 6-S4).

The main processing parameters for free myo5 are listed in Table 6-3, an overview of the processing is given in Figure 6-S5 a. Free myo5 particles were picked from a subset of micrographs of the 120 ms time-resolved data. Because of thicker ice, free myosin particles were not picked from the 10 ms data. After one round of 2D classification, good particles were used to train a crYOLO model [23]. With the

trained model, particles were picked from the entire 120 ms dataset, leading to a final selection of 23930 particles after one round of 2D and one round of 3D classification. The final 3D refinement after Bayesian polishing was done using non-uniform refinement in cryoSPARC [24].

**Table 6-1: Data collection, processing, model building and refinement statistics for time-resolved EM data.**

| | **10 ms TED** | **120 ms TED** | |
|---|---|---|---|
| **Data collection and processing** | | | |
| Magnification | 130,000 x | 130,000 x | |
| Voltage (kV) | 300 | 300 | |
| Nominal defocus range (μm) | -2 to -4.1 | -2 to -4.1 | |
| Pixel size (Å) | 1.07 | 1.07 | |
| Total fluence ($e^-/Å^2$) | 67.58 | 55.4 | |
| | 55.4 | 56.5 | |
| | 61.2 | 56.5 | |
| Number of fractions | 32 | 32 | |
| Exposure time (s) | 7 | 7 | |
| Number of micrographs | 3878 | 1020 | |
| | 3339 | 2602 | |
| | 2475 | 1354 | |
| Initial number of segments | 218602 | 122312 | |
| | 285704 | 198508 | |
| | 211425 | 111047 | |
| | **prePS** | **postPS** | **F-actin** |
| Final number of segments | 93374 | 94093 | 674122 |
| Resolution (FSC = 0.143) | 4.4 Å | 4.2 Å | 3.7 Å |

**Table 6-1 (continued): Data collection, processing, model building and refinement statistics for time-resolved EM data.**

| | prePS | postPS | F-actin |
|---|---|---|---|
| **Model Refinement** | | | |
| Initial Model used | pdb 4ZG4 (myosin)<br>pdb 5ONV (actin) | pdb 1W7I (myosin)<br>pdb 5ONV (actin) | pdb 5ONV |
| Map-model correlation (FSC = 0.5) | 4.5 Å | 4.1 Å | 3.6 Å |
| Map-sharpening B-factor (Å$^2$) | -119 | -84 | -81 |
| **Model composition** | | | |
| Non-hydrogen atoms | 14808 | 14765 | 8771 |
| Protein residues | 1853 | 1847 | 1112 |
| Ligands | ADP: 4 | ADP: 4 | ADP: 3 |
| **B factors (Å$^2$)** | | | |
| Protein | 180 | 134 | 79 |
| Ligand | 152 | 126 | 71 |
| **RMS deviations** | | | |
| Bond lengths (Å) | 0.005 | 0.008 | 0.005 |
| Bond angles ($^o$) | 0.887 | 0.945 | 0.785 |
| **Validation** | | | |
| MolProbity score | 2.32 | 2.26 | 1.95 |
| Clashscore | 19.87 | 19.11 | 9.76 |
| Poor rotamers (%) | 4.34 | 4.35 | 3.83 |
| **Ramachandran plot** | | | |
| Favoured (%) | 97.83 | 98.37 | 98.64 |
| Allowed (%) | 1.84 | 1.52 | 1.36 |
| Disallowed (%) | 0.33 | 0.11 | 0.00 |

**Table 6-2: Data collection and processing statistics for blotted Acto-myo5-ADP**

| | **ADP Vitrobot** |
|---|---|
| Magnification | 130,000 x |
| Voltage (kV) | 300 |
| Nominal defocus range (μm) | -0.8 to -2.3 |
| Pixel size (Å) | 1.07 |
| Total fluence ($e^-/Å^2$) | 67.58 |
| Number of fractions | 50 |
| Exposure time (s) | 7 |
| Number of micrographs | 1330 |
| Initial number of segments | 267519 |
| Final number of segments | 90220 |
| Resolution (FSC = 0.143) | 3.8 Å |

**Table 6-3: Processing, model building and refinement statistics for free myo5 from 120 ms time-resolved EM data**

| | **Free myo5** |
|---|---|
| **Data processing** | |
| Initial number of particles | 729596 |
| Final number of particles | 23930 |
| Resolution (FSC = 0.143) | 4.9 Å |
| **Model Refinement** | |
| Initial Model used | pdb 4ZG4 (myosin) |
| Map-model correlation (FSC = 0.5) | 5.1 Å |
| Map-sharpening B-factor (Å$^2$) | -233 |
| **Model composition** | |
| Non-hydrogen atoms | 5975 |
| Protein residues | 737 |
| **B factors (Å$^2$)** | |
| Protein | 305 |
| **RMS deviations** | |
| Bond lengths (Å) | 0.008 |
| Bond angles ($^o$) | 1.159 |
| **Validation** | |
| MolProbity score | 2.21 |
| Clashscore | 40.62 |
| Poor rotamers (%) | 1.09 |
| **Ramachandran plot** | |
| Favoured (%) | 97.54 |
| Allowed (%) | 2.05 |
| Disallowed (%) | 0.41 |

Homology models were generated using Modeller within Chimera [25, 26]. Model building was done using coot [27], small adjustments were also made in Isolde [28]. Real space refinement was performed using phenix [29]. Structures were visualised using Chimera. Lever arm rotation between prePS and postPS actomyosin was measured by aligning both structures on the $Actin_{+1}$ subunit and measuring the rotation of residues 751-763 in Chimera.

## 6.4 Results

### 6.4.1 Trapping pre-power stroke actomyosin by time-resolved cryo-EM

To trap the actomyosin prePS complex, we mixed myosin-5 S1, which had been pre-incubated with ATP to form the primed state, with F-actin and vitrified after 10 or 120 ms using our time-resolved cryo-EM device (see Methods and Figure 6-S1) [16]. We used the myosin-5 S1 mutant, $S^{217}A$, with a $DDEK^{594-597}$ deletion, to aid in trapping of the prePS state as $S^{217}A$ slows $P_i$ release (198 $s^{-1}$ to 16 $s^{-1}$) whilst the deletion in loop2 increases the affinity of the myosin-5 primed state for F-actin. This double mutant motor (myo5) remains fully functional in actin-motility assays and has a maximum actin-activated $P_i$-release rate of 7 $s^{-1}$ (Figure 6-S6 a,b). Within the time-resolved cryo-EM data, we observed two distinct classes of acto-myo5, which could be identified as the pre-power stroke (prePS) and post-power stroke (postPS) states, and we solved these states to global resolutions of 4.4 and 4.2 Å respectively. We observed no other intermediate states.

### 6.4.2 Pre-power stroke myosin binds actin with the L50 subdomain

The prePS state has an open cleft between L50 and U50, and a primed lever (Figure 6-1 a). The central actomyosin interface is formed between two neighbouring actin subunits ($Actin_{-1}$, $Actin_{+1}$) and the myosin helix-loop-helix (HLH) motif (Figure 6-1 b). The contacts are primarily of hydrophobic nature, including residues I345 and G146 on $Actin_{+1}$, M515 and P516 in the myosin HLH motif, and M47 in the D-loop of $Actin_{-1}$. A second interface is made by myosin loop3 and $Actin_{-1}$, bringing charged residues R542 (myosin) and E99 ($Actin_{-1}$) in close proximity, but also including hydrophobic V96, A97 ($Actin_{-1}$) and M542 (myosin) (Figure 6-1 c). As in other actomyosin structures, the flexible loop2 is poorly resolved in the prePS state. However, the density suggests that the N-terminal portion of loop2 adopts and elongated conformation, allowing positively charged K625 to interact with the acidic patch formed by D24 and D25 on the surface of $Actin_{+1}$ (Figure 6-1 d).

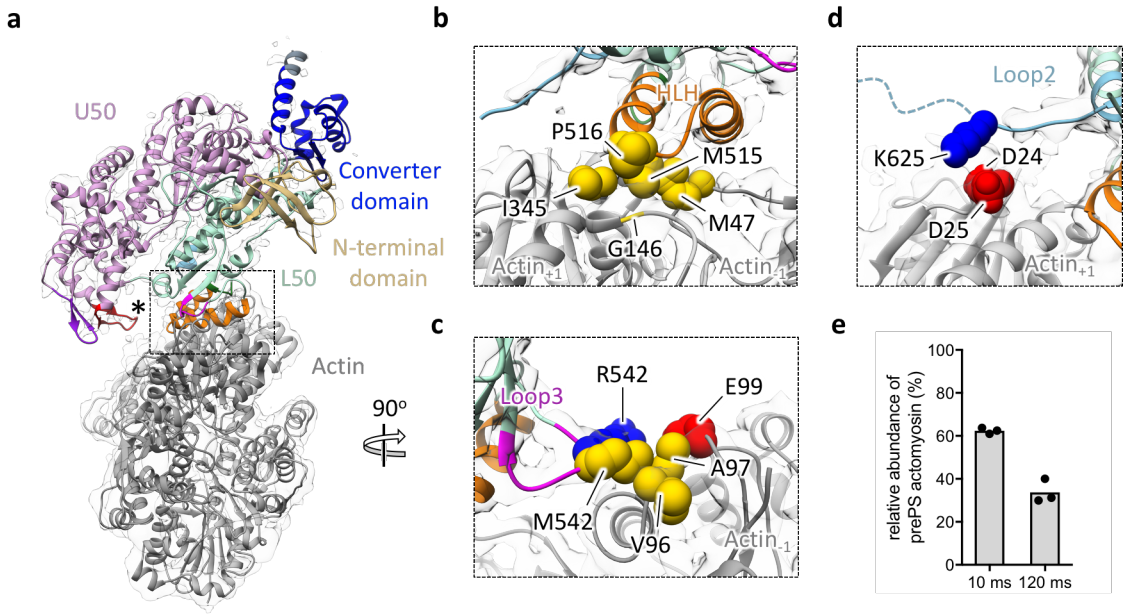


**Figure 6-1: Structure of the prePS actomyosin complex.**

(a) Model of the prePS actomyosin complex with actin in grey and myosin domains colored as indicated. EM density is shown as transparent isosurface. The open cleft is indicated with an asterisk. (b-d) Magnified image of the actomyosin interface, the major contacts are made by the myosin helix-loop-helix motif (b), loop3 (c) and loop2 (d). Relevant interacting residues are labelled and shown as van-der-Waals spheres. (e) Relative abundance of the prePS state at 10 ms or 120 ms. Shown is the mean as grey bars and replicates as black points.

The prePS state was the major population in the 10 ms data, comprising 62 % of actomyosin particles (Figure 6-1 e), in good agreement with a $P_i$-release rate of 7 $s^{-1}$ (Figure 6-S6 a) and kinetic modelling (Figure 6-S6 c,d). This confirmed that the prePS state was transient and turned over to a post-power stroke (postPS) state at the expected rate.

### 6.4.3 Structural changes during the power stroke

The observation of both the prePS and postPS states within our data allow us to describe the structural changes which occur during the power stroke. The most significant conformational change is the large-scale movement of the converter and light-chain binding domain (Figure 6-2 a), ultimately responsible for transmission of mechanical force. The ~93° lever rotation observed here (models aligned on $Actin_{+1}$) is similar to a previous estimate of 88° for the full power stroke [12]. As expected, the lever arm swing is accompanied by closure of the actin-binding cleft between the U50 and L50 subdomains (Figure 6-2 b). While the experimental density does not resolve the individual bound phosphate, cleft closure results in a

significant relative movement between switch-2 and switch-1/P-loop, indicating that phosphate has been released in the postPS structure (Figure 6-S7).

The interactions between actin and the myosin HLH motif and loop3 remain essentially unchanged between the prePS and postPS state. As a consequence of cleft closure, the postPS state shows a larger interface between myosin and $Actin_{+1}$ with a surface area of 375 $Å^2$ in the prePS and 729 $Å^2$ in the postPS state. The additional contacts are made by the myosin cardiomyopathy (CM) loop, mostly by uncharged or hydrophobic residues like the closely packed myosin Y387 and actin Y337 (Figure 6-2 c,d). Cleft closure also brings the negatively charged D344 and D346 of loop4 in close proximity to actin K328 (Figure 6-2 d). In the prePS state, CM loop and loop4 are less resolved, indicating flexibility in the region, and both loops are too distant to form stable contacts with the actin surface (Figure 6-2 c).

Our postPS acto-myo5 showed a closed actin-binding cleft and a post-power stroke lever (Figure 6-2 a) and had high similarity to previous structures of strongly-bound actomyosin complexes (ADP-bound or rigor states) [8, 12]. To confirm the identity of postPS actomyosin as ADP-bound, we collected cryo-EM data of ADP-bound acto-myo5 from a conventional blotted cryo-EM grid (Figure 6-S4). The resulting ADP-bound actomyosin-5 from conventional cryo-EM was nearly identical to the postPS state from the time-resolved data. Therefore, we assigned the postPS state to ADP-bound acto-myo5 but we note that it may in fact be a mixture of ADP-bound and nucleotide free particles, based on the kinetics of ADP-release (Figure 6-S6 d).

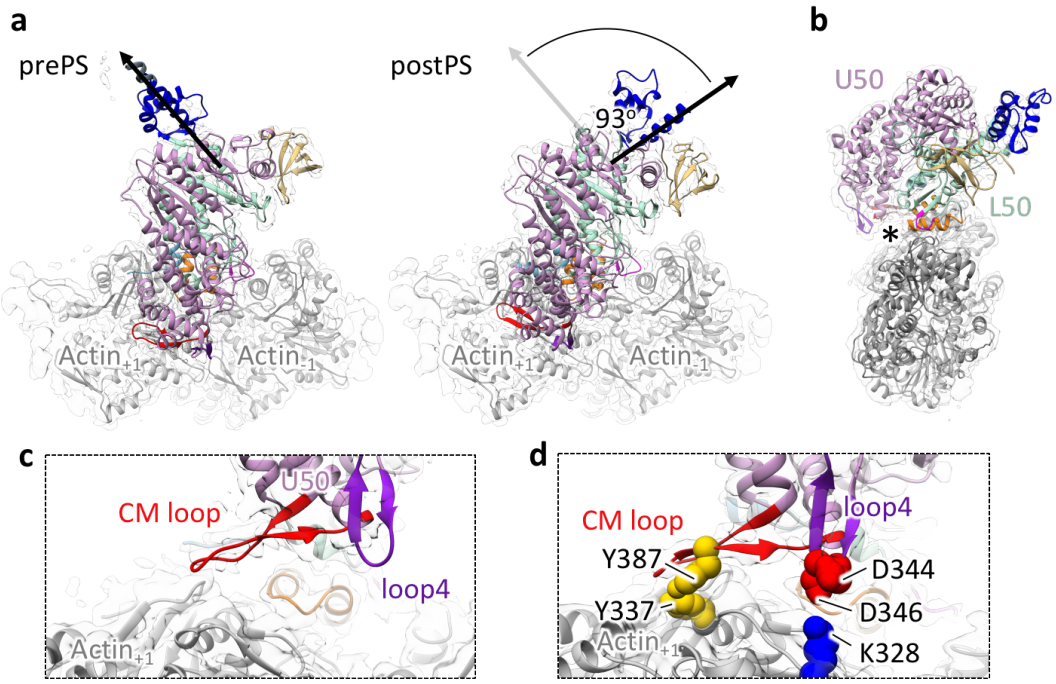


**Figure 6-2: Structural changes during the power stroke.**

(a) On the left, prePS actomyosin structure with lever arm position indicated by the black arrow. On the right postPS actomyosin structure with lever arm position indicated by the black arrow and prePS lever arm position indicated by the grey arrow. The lever arm swings approximately 93° between structures. (b) PostPS structure shows a closed cleft, indicated with an asterisk, between U50 and L50 subdomains. (c) In the prePS state, CM-loop and loop4 are distant from the actin surface due to the open cleft and poorly resolved. (d) In the postPS state the CM loop and loop4 form additional interfaces with the surface of $Actin_{+1}$. Relevant interacting residues are labelled and shown as van-der-Waals spheres. EM density is shown as transparent isosurface.

### 6.4.4 Conformational changes of the actin filament

The time-resolved data also contained a large number of non-myosin bound actin subunits (Figure 6-S2). The overall structure of F-actin remained the same between free actin, prePS and postPS actomyosin states (Figure 6-S8). The actin D-loop is in a 'closed' conformation in all cases, as previously described for ADP-bound actin [30], but is better resolved and therefore appears to be stabilised by myosin binding (Figure 6-S9 a-c). The N-terminal residues of $Actin_{+1}$ are also better resolved in the prePS and postPS complexes than in free actin (Figure 6-S9 d-f) [11]. However, at the present resolutions there is no clear conformational switch in the actin filament between prePS and postPS states, that would allow the actin filament to 'sense' the myosin conformational state [9].

### 6.4.5 Structural changes upon prePS complex formation

In addition to actomyosin complex, the time-resolved data also contained free myo5 particles. Processing of free myosin motors from the 120 ms data gave a 4.9 Å reconstruction (Figure 6-S5) and revealed that free myosin motors were in a pre-power stroke state, likely frozen prior to productive actin binding or alternatively after one cycle of actin-binding and dissociation. The cryo-EM density agreed well with a crystal structure of myosin Vc, biochemically trapped in the pre-power stroke state using ADP-vanadate (pdb: 4zg4) [8]. Comparison of prePS myosin to the prePS actomyosin complex showed no large structural changes occur upon actin binding, with the HLH-motif and loop3 adopting highly similar conformations in these two states (Figure 6-3 a). Closer inspection of loop2 revealed small differences between free pre-power stroke myosin, prePS and postPS actomyosin complexes (Figure 6-3 b). Upon actin binding, the resolved C-terminal end of loop2 switches its orientation to contact the actin surface (see also Figure 6-1 d). After the power stroke, this part of loop2 adopts a helical conformation, also observed in previous work [12].

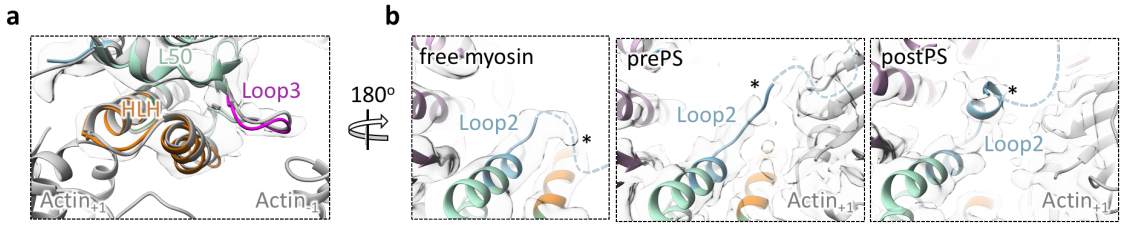


**Figure 6-3: Loop2 responds to prePS complex formation and the power stroke.**

(a) HLH motif and loop3 adopt highly similar conformations between free myosin (coloured) and prePS actomyosin complex (light grey). Density for free myosin is shown as transparent isosurface. (b) Loop2 changes conformation between free myosin (left), prePS actomyosin (centre) and postPS actomyosin (right). Unresolved residues are indicated by the dashed line, density for loop 2 is highlighted with asterisks.

## 6.5 Discussion

The time-resolved cryo-EM data only showed two distinct actomyosin conformations, the prePS and postPS state. The prePS state structure reveals how myosin interacts with actin before the power stroke and provides the final piece in the puzzle of the force-generation cycle, while the postPS state is similar to previously described strongly bound actomyosin structures.

Previous work has suggested that the initial contacts between myosin and F-actin are ionic interactions formed between positively-charged residues of myosin loop2

and negatively-charged residues on the actin surface [11, 31]. The small conformational change in loop2 between free pre-power stroke myosin and the prePS actomyosin complex could be reminiscent of this initial interaction. It has been hypothesized that these weak non-stereospecific interactions allow correct positioning of myosin on the F-actin track to enable formation of a force-bearing state, primed for the power stroke. The prePS state observed in this work, shows a stereospecific interaction between the L50 domain and the F-actin surface. The formation of the interface between HLH-motif/loop3 and F-actin requires little conformational change so we expect this state to be formed rapidly after the initial interaction. Single-molecule force-measurements have suggested that the force-bearing pre-power stroke state has an open cleft and is bound stereo-specifically [13]. The prePS state described in this work exhibits these features, we thus conclude that it resembles the force-bearing state.

High sequence and structural conservation of the HLH-motif across myosin classes and species [32] suggests that the structure of the prePS state is also conserved. This is in agreement with the HLH-motif forming the core of both the prePS and postPS interfaces with F-actin, and with a conserved mechanism of force production across myosins. The other interaction sites (loop2, loop3, CM loop, loop4 and activation loop) are more variable in sequence and structure, allowing fine-tuning of the motor properties of myosins [9], as shown for example for loop2 which controls the actin-activated ATPase rate [31, 33, 34].

Our observation of both pre- and post-PS conformations within the same dataset enable us to draw conclusions about the mechanism of force-generation: The time-resolved cryo-EM data did not reveal intermediate states between prePS and postPS, suggesting that the transition between prePS and postPS states is very rapid. This is in line with experimental rates for the power stroke on the order of 1000 $s^{-1}$ [35]. There is conflicting evidence on the exact sequence of $P_i$-release, cleft closure and lever arm swing [9, 13]. The open cleft and primed lever arm in the prePS state suggest that these two conformational changes are closely coupled, in agreement with previous work. Furthermore, the agreement between the rate of $P_i$-release (Figure 6-S6 a) and the relative abundance of the prePS state (Figure 6-1 e) suggests that the prePS state has ADP-$P_i$ bound. It has been suggested that $P_i$-release occurs from an intermediate state called the $P_i$-release (PiR) state, following the prePS state [10]. We hypothesize that the PiR state allows Pi-release while positioning the CM loop of the U50 subdomain close to the F-actin surface, committing the myosin motor to cleft closure. Once $P_i$ is released, the cleft between subdomains can close and the lever arm produces mechanical force (Figure 6-4) [9].

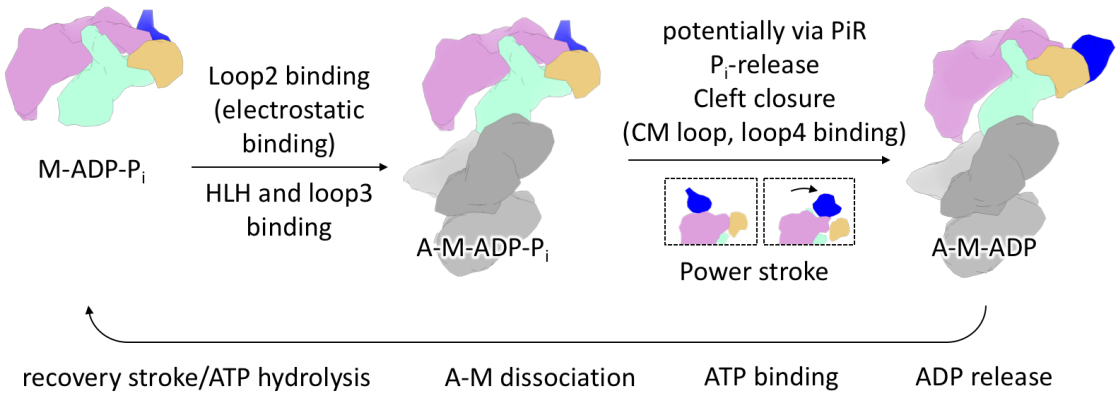


**Figure 6-4: Model of actomyosin catalytic cycle.**

First ADP-$P_i$ bound myosin in the pre-power stroke state (M-ADP-$P_i$) interacts weakly with F-actin through loop2. Then, HLH and loop3 bind the actin filament to form the stereospecific and force-bearing pre-power stroke actomyosin complex (A-M-ADP-$P_i$). Phosphate is released, potentially via a transient PiR state. Cleft closure results in CM loop and loop4 forming additional contacts with the actin filament. Concomitantly, the lever arm swings, producing mechanical force. This gives the post-power stroke A-M-ADP complex. In order to complete the catalytic cycle, ADP must be released and ATP must bind the complex, inducing actomyosin dissociation. After completing the recovery stroke and ATP-hydrolysis, free myosin is primed for the next cycle.

The myo5 system used in this work has a short lever arm in an unstrained conformation, without load. It seems plausible that the power stroke and $P_i$-release/cleft closure are not as tightly coupled in the presence of load or strain, for example in the case of processive full-length myosin V [36, 37]. In fact, it has been shown that under strain, the power stroke can be reversed to produce an ADP-bound state with a closed cleft and a primed lever arm [38].

In summary, we present the first structure of an actomyosin complex in the pre-power state. This represents one of the last unknown structural states of the actomyosin catalytic cycle, and gives the first high-resolution description for the starting point of the myosin power stroke on F-actin. Due to the high conservation of the HLH motif in the prePS actomyosin interface, the structure of this state is likely conserved across myosin classes. The prePS actomyosin structure is a significant step in understanding how myosin motors generate force and may aid in discerning how disease-associated mutations affect myosin function.

## 6.6 Supporting information

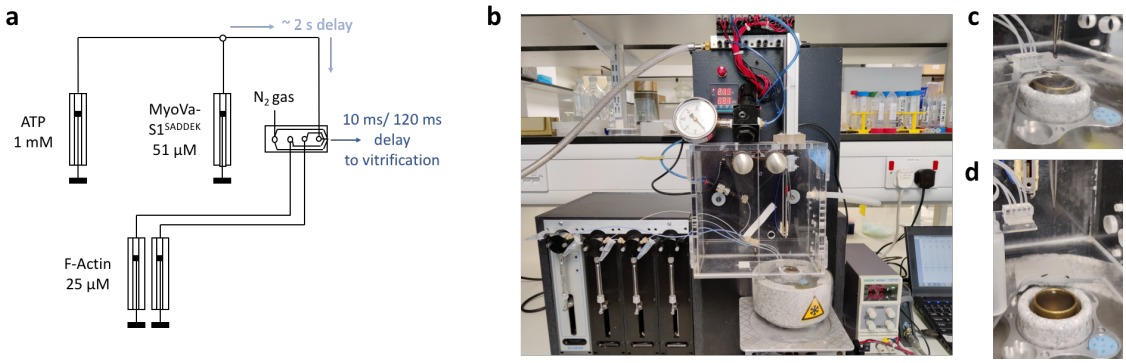


**Figure 6-S1: Experimental setup for time-resolved cryo-EM.**

(a) Schematic of experimental setup. (b) Photo of the experimental setup. Magnified of view of spray nozzle, grid in sample application positions and ethane cup for 10 ms time-delay (c) or 120 ms time-delay (d).

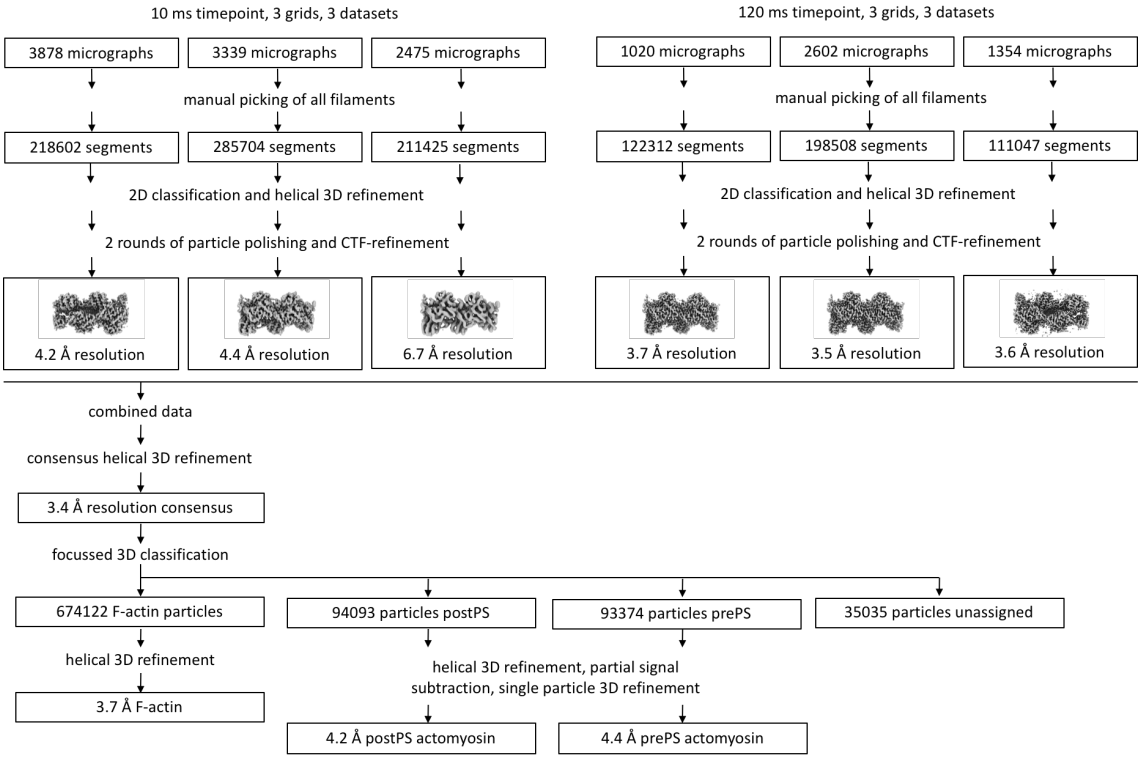


**Figure 6-S2: Processing pipeline for time-resolved cryo-EM data.**

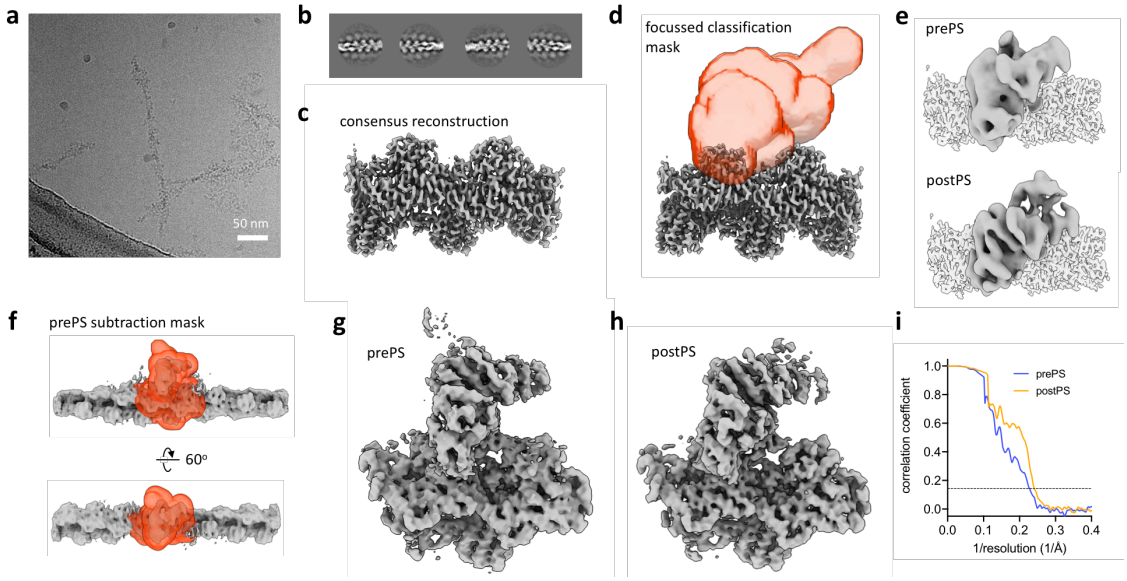


**Figure 6-S3: Time-resolved cryo-EM data processing.**

(a) Representative micrograph for the 10 ms timepoint. (b) Representative 2D classes for the 10 ms timepoint, bound myosin appears as a diffuse density along the actin filament. (c) Helical consensus reconstruction from all time-resolved datasets combined. (d) Mask used for focussed classification of myosin states. (e) Classes corresponding to prePS or postPS myosin from focussed classification. (f) Subtraction mask used for prePS processing. (g) Final prePS single particle reconstruction. (h) Final postPS single particle reconstruction. (i) Fourier shell correlation curves for prePS (blue) and postPS (yellow) with the 0.143 threshold indicated by a dotted line.

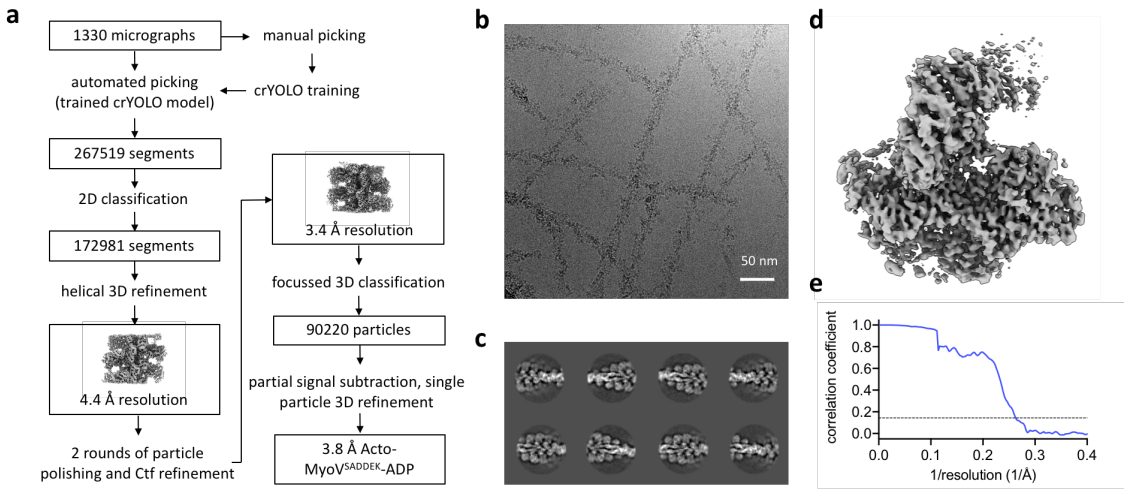


**Figure 6-S4: Blotted acto-myo5-ADP processing.**

(a) Processing pipeline. (b) Representative micrograph. (c) Representative 2D classes. (d) Final single-particle reconstruction. (e) Fourier shell correlation curve (blue) with the 0.143 threshold indicated by a dotted line.

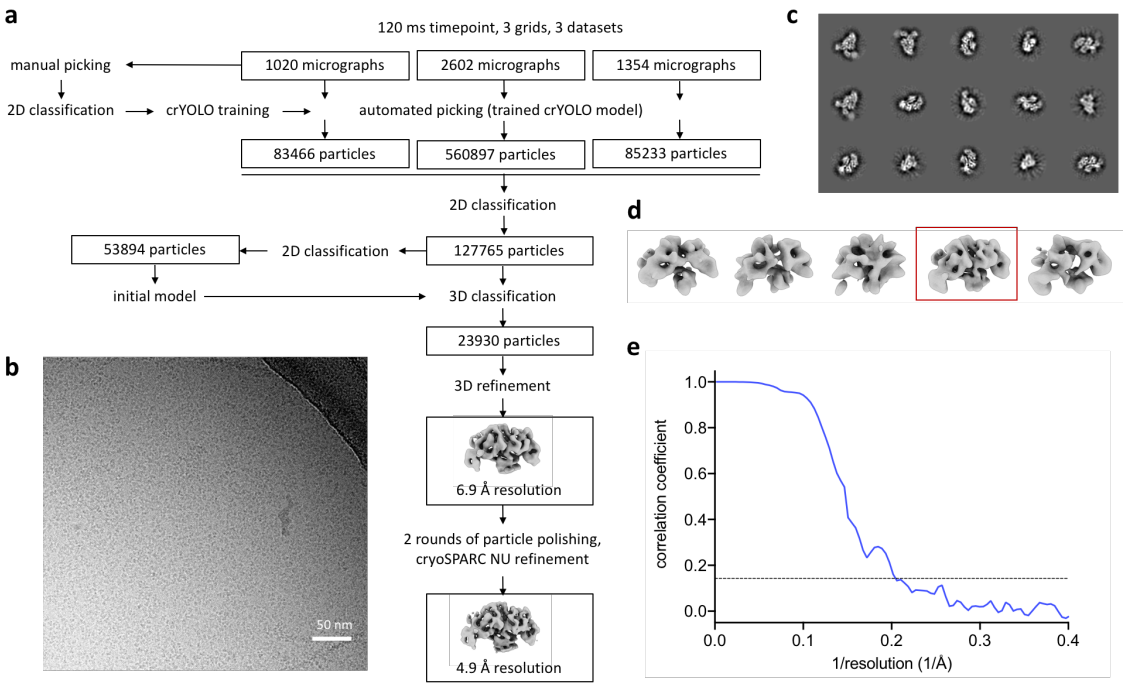


**Figure 6-S5: Free myo5 processing.**

(a) Processing pipeline. (b) Micrograph from the 120 ms time-resolved cryo-EM data with a large number of free myo5. (c) Representative 2D classes. (d) 3D classification with the selected class highlighted by the red box. (e) Fourier shell correlation curve (blue) with the 0.143 threshold indicated by a dotted line.

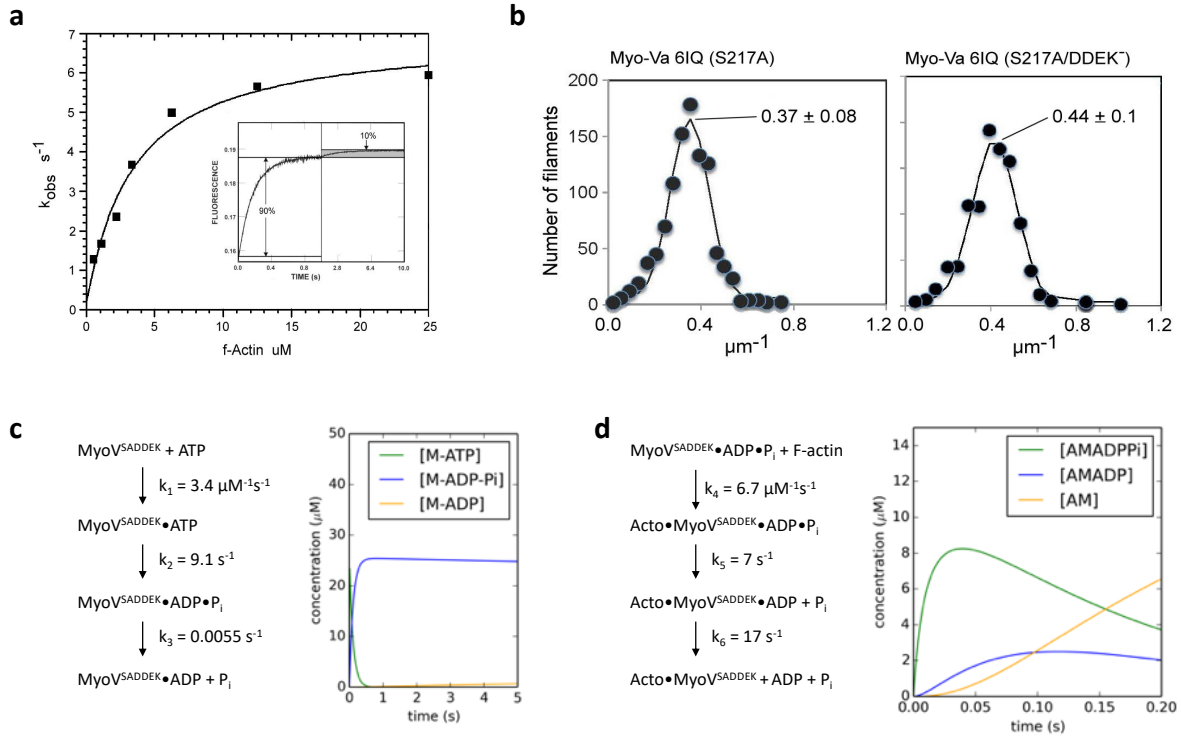


**Figure 6-S6: Biochemical kinetic measurements and kinetic modelling.**

(a) Dependence of the rate of phosphate dissociation from mouse acto-myo5-ADP-$P_i$ using double mixing stopped flow with fluorescent phosphate binding protein. Data are fit by $K_{actin}$ = 3 μM, $k_{Pi}$ = 7 $s^{-1}$. Insert: Double mixing in which 5 μM myo5 is mixed with 4 μM ATP, incubated for 20 s and then mixed 50 μM f-actin. All solutions contained 5 μM fluorescent phosphate binding protein. (b) In vitro motility assay of myosinVa $S^{217}A$ and $S^{217}A/\Delta DDEK^{594\text{-}597}$ constructs. (c) Simple kinetic modelling for the pre-mixing step of myo5 with ATP. All rates from ref. [15]. (d) Simple kinetic modelling for the fast mixing setup of myo5-ADP-$P_i$ with F-actin. Rate $k_4$ from ref. [35], $k_5$ from panel a, $k_6$ from ref. [15].

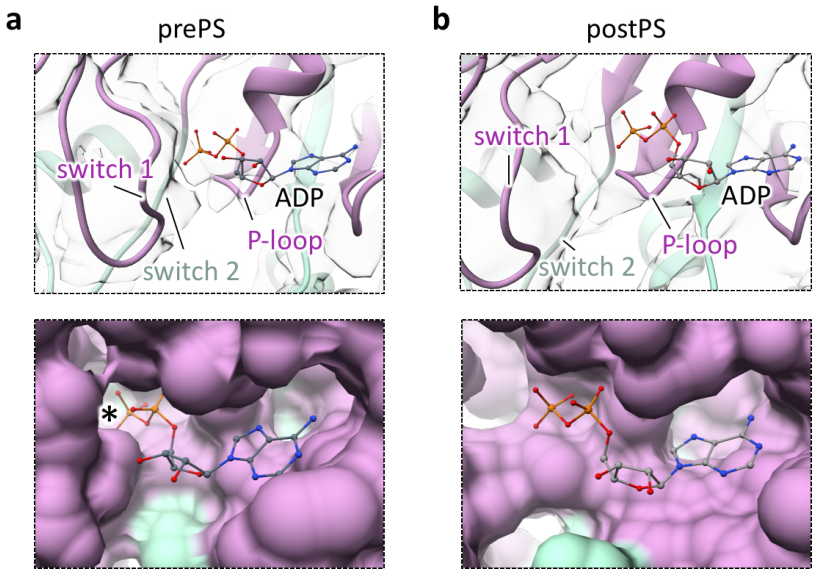


**Figure 6-S7: Myosin nucleotide binding site.**

(a) Nucleotide binding site for prePS actomyosin with switch1, switch2 and P-loop indicated and ADP modelled. The U50 subdomain is coloured in purple, the L50 in light green. The bottom panel shows the surface of the atomic model with the position of the putative phosphate indicated with an asterisk. EM density is shown as transparent isosurface. (b) PostPS actomyosin, with ADP modelled, shows a relative conformational change between switch2 and switch1/P-loop. The bottom panel shows a surface view with the more open binding site for ADP.

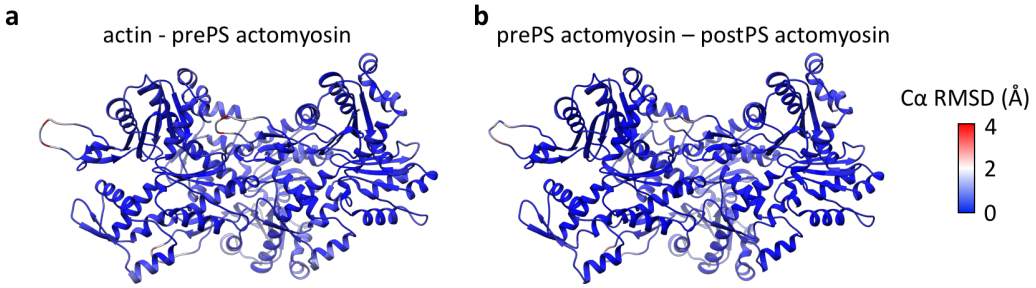


**Figure 6-S8: Actin structure remains largely unchanged.**

(a) Atomic model of free actin coloured by Cα RMSD between free actin and actin in the prePS complex. (b) Atomic model of actin in prePS complex coloured by Cα RMSD between actin in the prePS and the postPS complex.

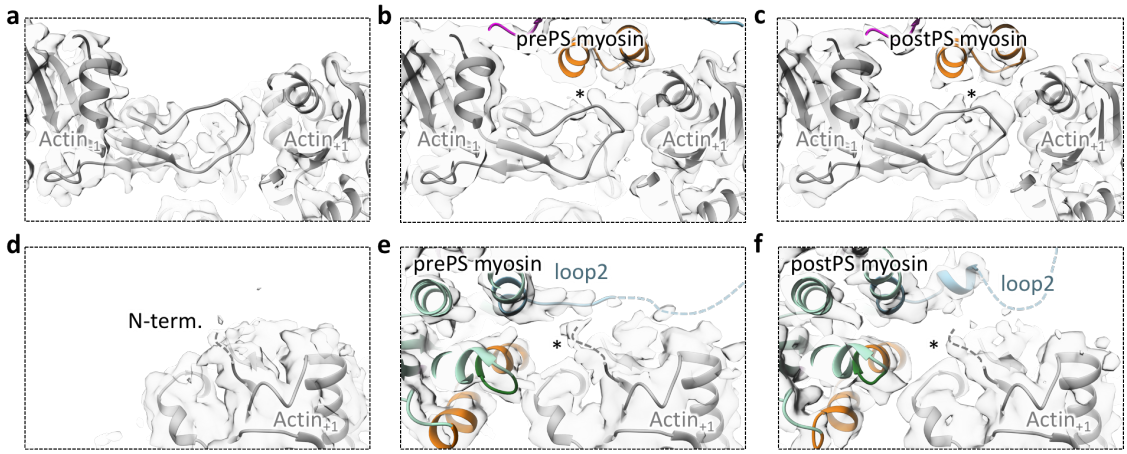


**Figure 6-S9: Structural changes in actin D-loop and N-terminus.**

(a) Free actin shows discontinuous density for the D-loop. (b-c) The actin$_{-1}$ D-loop is better resolved in the prePS and postPS complex structures, highlighted with asterisks. (d) The disordered N-terminus of free actin, poorly resolved N-terminal residues are indicated by the dashed line. (e-f) In the prePS and postPS complex structures there is additional density at high threshold for the actin N-terminus, highlighted by the asterisks. Missing residues in myosin loop2 are indicated with the light blue dashed line.

## 6.7 References


1. Hartman, M.A. and J.A. Spudich, *The myosin superfamily at a glance.* Journal of cell science, 2012. **125**(7): p. 1627-1632.
2. Kollmar, M. and S. Mühlhausen, *Myosin repertoire expansion coincides with eukaryotic diversification in the Mesoproterozoic era.* BMC evolutionary biology, 2017. **17**(1): p. 1-18.
3. Schröder, R.R., et al., *Three-dimensional atomic model of F-actin decorated with Dictyostelium myosin S1.* Nature, 1993. **364**(6433): p. 171-174.
4. Rayment, I., et al., *Structure of the actin-myosin complex and its implications for muscle contraction.* Science, 1993. **261**(5117): p. 58-65.
5. Trivedi, D.V., et al., *Direct measurements of the coordination of lever arm swing and the catalytic cycle in myosin V.* Proceedings of the National Academy of Sciences, 2015. **112**(47): p. 14593-14598.
6. Geeves, M.A. and K.C. Holmes, *Structural mechanism of muscle contraction.* Annual review of biochemistry, 1999. **68**(1): p. 687-728.
7. Volkmann, N., et al., *The structural basis of myosin V processive movement as revealed by electron cryomicroscopy.* Molecular cell, 2005. **19**(5): p. 595-605.

8. Wulf, S.F., et al., *Force-producing ADP state of myosin bound to actin.* Proceedings of the National Academy of Sciences, 2016. **113**(13): p. E1844-E1852.
9. Robert-Paganin, J., et al., *Force generation by myosin motors: a structural perspective.* Chemical Reviews, 2019. **120**(1): p. 5-35.
10. Llinas, P., et al., *How actin initiates the motor activity of Myosin.* Developmental cell, 2015. **33**(4): p. 401-412.
11. von der Ecken, J., et al., *Cryo-EM structure of a human cytoplasmic actomyosin complex at near-atomic resolution.* Nature, 2016. **534**(7609): p. 724-728.
12. Pospich, S., et al., *High-resolution structures of the actomyosin-V complex in three nucleotide states provide insights into the force generation mechanism.* eLife, 2021. **10**: p. e73724.
13. Woody, M.S., et al., *Single molecule mechanics resolves the earliest events in force generation by cardiac myosin.* Elife, 2019. **8**: p. e49266.
14. Spudich, J.A. and S. Watt, *The regulation of rabbit skeletal muscle contraction I. Biochemical studies of the interaction of the tropomyosin-troponin complex with actin and the proteolytic fragments of myosin.* Journal of biological chemistry, 1971. **246**(15): p. 4866-4871.
15. Forgacs, E., et al., *Switch 1 mutation S217A converts myosin V into a low duty ratio motor.* Journal of Biological Chemistry, 2009. **284**(4): p. 2138-2149.
16. Kontziampasis, D., et al., *A cryo-EM grid preparation device for time-resolved structural studies.* IUCrJ, 2019. **6**(6).
17. Klebl, D.P., et al., *Sample deposition onto cryo-EM grids: from sprays to jets and back.* Acta Crystallographica Section D: Structural Biology, 2020. **76**(4).
18. Klebl, D.P., et al., *On-grid and in-flow mixing for time-resolved Cryo-EM.* In press, 2021.
19. Zivanov, J., et al., *New tools for automated high-resolution cryo-EM structure determination in RELION-3.* Elife, 2018. **7**: p. e42166.
20. Zheng, S.Q., et al., *MotionCor2: anisotropic correction of beam-induced motion for improved cryo-electron microscopy.* Nature methods, 2017. **14**(4): p. 331.
21. Zhang, K., *Gctf: Real-time CTF determination and correction.* Journal of structural biology, 2016. **193**(1): p. 1-12.
22. He, S. and S.H. Scheres, *Helical reconstruction in RELION.* Journal of structural biology, 2017. **198**(3): p. 163-176.

23. Wagner, T., et al., *SPHIRE-crYOLO is a fast and accurate fully automated particle picker for cryo-EM.* Communications Biology, 2019. **2**(1): p. 218.
24. Punjani, A., H. Zhang, and D.J. Fleet, *Non-uniform refinement: adaptive regularization improves single-particle cryo-EM reconstruction.* Nature methods, 2020. **17**(12): p. 1214-1221.
25. Webb, B. and A. Sali, *Comparative protein structure modeling using MODELLER.* Current protocols in bioinformatics, 2016. **54**(1): p. 5.6. 1-5.6. 37.
26. Pettersen, E.F., et al., *UCSF Chimera—a visualization system for exploratory research and analysis.* Journal of computational chemistry, 2004. **25**(13): p. 1605-1612.
27. Casañal, A., B. Lohkamp, and P. Emsley, *Current developments in Coot for macromolecular model building of Electron Cryo-microscopy and Crystallographic Data.* Protein Science, 2020. **29**(4): p. 1055-1064.
28. Croll, T.I., *ISOLDE: a physically realistic environment for model building into low-resolution electron-density maps.* Acta Crystallographica Section D: Structural Biology, 2018. **74**(6): p. 519-530.
29. Afonine, P.V., et al., *Real-space refinement in PHENIX for cryo-EM and crystallography.* Acta Crystallographica Section D: Structural Biology, 2018. **74**(6): p. 531-544.
30. Merino, F., et al., *Structural transitions of F-actin upon ATP hydrolysis at near-atomic resolution revealed by cryo-EM.* Nature structural & molecular biology, 2018. **25**(6): p. 528-537.
31. Geeves, M.A., R. Fedorov, and D.J. Manstein, *Molecular mechanism of actomyosin-based motility.* Cellular and Molecular Life Sciences CMLS, 2005. **62**(13): p. 1462-1477.
32. Robert-Paganin, J., et al., *The actomyosin interface contains an evolutionary conserved core and an ancillary interface involved in specificity.* Nature communications, 2021. **12**(1): p. 1-11.
33. Rovner, A.S., Y. Freyzon, and K.M. Trybus, *Chimeric substitutions of the actin-binding loop activate dephosphorylated but not phosphorylated smooth muscle heavy meromyosin.* Journal of Biological Chemistry, 1995. **270**(51): p. 30260-30263.
34. Uyeda, T.Q., K.M. Ruppel, and J.A. Spudich, *Enzymatic activities correlate with chimaeric substitutions at the actin-binding face of myosin.* Nature, 1994. **368**(6471): p. 567-569.

35. Gunther, L.K., et al., *FRET and optical trapping reveal mechanisms of actin activation of the power stroke and phosphate release in myosin V.* Journal of Biological Chemistry, 2020. **295**(51): p. 17383-17397.
36. Walker, M.L., et al., *Two-headed binding of a processive myosin to F-actin.* Nature, 2000. **405**(6788): p. 804-807.
37. Burgess, S., et al., *The prepower stroke conformation of myosin V.* The Journal of Cell Biology, 2002. **159**(6): p. 983-991.
38. Sellers, J.R. and C. Veigel, *Direct observation of the myosin-Va power stroke and its reversal.* Nature structural & molecular biology, 2010. **17**(5): p. 590-595.

# Chapter 7 Concluding Remarks and Discussion

## 7.1 Development of time-resolved cryo-EM

Modern structural biology methods can solve protein structures at an unprecedented rate, one impressive example is the crystallographic fragment screen for inhibitors of the SARS-CoV-2 main protease [1, 2]. Structure-based drug design has benefited from the relative ease of structure determination, by X-ray crystallography and cryo-EM [3, 4]. Yet, structural biology typically provides static snapshots of protein structure, even though it has been established that protein structure is dynamic and that protein function requires dynamics [5, 6]. One plausible explanation is that time-resolved studies are experimentally more challenging, both in terms of sample preparation and structure determination (it is easier to determine a single structure than multiple structures in parallel). The aim of this work was to contribute new developments to sample preparation for TrEM and to characterise existing approaches in more detail. Ideally, this means that more challenging problems can be addressed by TrEM in the future, and that TrEM will become more accessible and widely used.

The characterisation and proof-of-principle in Chapter 2 ‘A cryo-EM grid preparation device for time-resolved structural studies’ provided a starting point for the work. A more detailed study of the sample deposition step was done in Chapter 3 ‘Sample deposition onto cryo-EM grids: from sprays to jets and back’. GVDNs, developed for sample delivery for XFEL crystallography, were found to reduce sample consumption and improve grid coverage compared with voltage-assisted spraying [7, 8]. In all subsequent work, the device described in Chapter 2 was used with the nozzles described in Chapter 3. In Chapter 4, ‘On-grid and in-flow mixing for time-resolved cryo-EM’, the ATP-induced dissociation of the actomyosin complex was studied by TrEM as a model system with known kinetics. This served as a further test of the experimental approach, and allowed characterisation of two different mixing approaches, which may prove useful in future TrEM work. In Chapter 5, ‘Need for speed: examining protein behaviour during cryo-EM grid preparation at different timescales’, the interactions between proteins and the AWI were analysed in detail, with a focus on their time dependence. The combined tomography and SPA results provided important insights into effective particle

concentration, and other parameters such as ice thickness and particle orientation, which may help to guide droplet based fast grid preparation efforts in the future. Finally, Chapter 6 'Pre-power stroke structure of the Actomyosin Complex' demonstrates the successful application of TrEM to a challenging biochemical question.

Below, the findings of this work will be discussed in a broader context, and possible future developments and applications of TrEM will be given.

## 7.2 Lessons from fast cryo-EM grid preparation and future directions

Previous work has shown that fast droplet based grid preparation reduces some of the effects of the AWI on proteins, in agreement with the results presented in Chapter 5 [9]. Common problems that have been associated with the AWI are particle denaturation, preferred orientation and aggregation [10-12]. A number of other reactions are catalysed significantly at the AWI, but their effects in cryo-EM grid preparation have not been reported. Among these reactions are spontaneous formation of hydrogen peroxide, presumably through hydroxyl radicals, and more complex processes, such as peptide bond formation and enzyme catalysed proteolysis [13-15]. Future comparisons of fast and slow cryo-EM grid preparation at higher resolutions could clarify whether there are additional effects of the AWI that have been overlooked so far.

While droplet based fast grid preparation may solve AWI-related problems in some cases, there are other limitations: There is less or no concentrating effect of the AWI, as a result higher protein concentrations are required to achieve the same particle density as conventional blotting. Droplet deposition onto conventional cryo-EM grids typically leads to less consistent and thicker layers of vitreous ice, limiting image quality[4]. However, ice thickness in droplet based grid preparation can be reduced by the use of self-wicking grids, both for sample application with piezo dispensers and spray droplets from GDVNs as done in Chapter 6 [16]. As pointed

[4] A systematic study to analyse ice thickness and its relation to various parameters such as droplet size, droplet speed, grid surface, surface tension or viscosity has not been done so far. However, such a systematic study would provide highly useful information on how to achieve thin ice and good-quality images reproducibly.

out in Chapter 5, droplet based fast grid preparation should probably be viewed as an addition to the toolbox for cryo-EM sample preparation, rather than a ‘silver bullet’ for AWI-induced problems. Because the timescale on the order of 10 ms for the fastest grid preparation is still relatively slow compared to particle diffusion in the thin film (1 ms or less) [11], further improvements may be achieved if cryo-EM grids are prepared on the sub-millisecond timescale.

Another development that may fuel the conception of novel grid preparation methods in the future, is the growing popularity of accessible electronic hardware and 3D printers. For example, this has resulted in the design and production of affordable optical microscopes for educational or research purposes, that can easily be customised [17, 18]. Other applications include liquid handling systems such as syringe pumps or sampling robots [19, 20]. Some of the recently developed grid preparation devices make use of the same open source design principles: They are controlled with affordable electronic hardware such as the raspberry pi computer or arduino microcontroller and are operated with freely available software [12, 21]. It seems likely that this will promote the adoption of these devices in other laboratories, and make further modifications more straightforward.

There is also scope for improvement of sample deposition methods: The use of techniques such as electrospray and its variations is probably worth revisiting [22, 23]. Direct deposition of very thin liquid sheets could also be an approach to produce the thin film required for cryo-EM [24]. In addition, manufacturing of the microfluidic components (mixers and nozzles) could be optimised: The PDMS-based nozzles introduced in Chapter 3 are produced in a multi-step process, where a template is fabricated by photolithography and then used for replica molding by soft lithography with PDMS. These PDMS-based nozzles are designed for single use and have a limited lifetime, so a more durable alternative may be desirable. Glass-based GDVNs have been used for sample delivery at XFELs but their preparation involves challenging manual production steps [25]. Alternatively, microfluidic devices can be made of borosilicate by photolithography, but devices with multiple layers are difficult to realise. More recently, two-photon stereolithography has emerged as an approach to produce microfluidic mixers and GDVNs, the method offers high resolution and can produce complex structures

[26]. In the future, such 3D printed microfluidics could serve as an alternative to PDMS-based nozzles.

## 7.3 Sub-millisecond time-resolved EM

As mentioned above, a method for preparing cryo-EM grids on the sub-millisecond timescale may prevent interactions between particles and the AWI more effectively. For TrEM applications it is worth noting that the fastest microfluidic mixers can achieve mixing times of a few microseconds, providing a limit for reaction initiation by mixing [27]. Shorter time delays can be achieved by triggering reactions with light, or temperature jumps [28]. However, the discussion here will focus on rapid mixing TrEM.

One may wonder if there is a need to improve the dead time of TrEM to less than one millisecond or if the capabilities of current methods are generally sufficient. Following on from the work in Chapter 4, this will be illustrated by the example of ATP-induced dissociation of the skeletal actomyosin complex. A simple kinetic model of the reaction is shown in Figure 7-1 a. As part of the catalytic cycle, actomyosin binds ATP and the complex dissociates into ATP-bound myosin and F-actin. The binding rate of ATP to actomyosin is assumed to be close to the diffusion limit. For simplicity, the reaction is modelled with a single intermediate ATP-bound actomyosin state, which dissociates in an irreversible manner. The resulting concentrations over time are given in Figure 7-1 b, c for two different initial concentrations of ATP.

At high ATP concentration (1 mM), the reaction proceeds quickly and almost all actomyosin has dissociated after 1 ms, which is beyond the reach of current TrEM methods. Lower ATP concentration slows down the overall reaction, as done in Chapter 4 where a pseudo-first order rate constant of about 150 $s^{-1}$ was obtained. However, at lower ATP concentration the intermediate state of interest (the ATP-bound state of actomyosin) is only populated at low levels. It becomes clear that very short delay times between mixing and freezing, and high ATP concentrations are required to trap this intermediate state. Under such conditions, the reaction is more ‘synchronised’ and enrichment of the intermediate is not limited by slow initial binding.

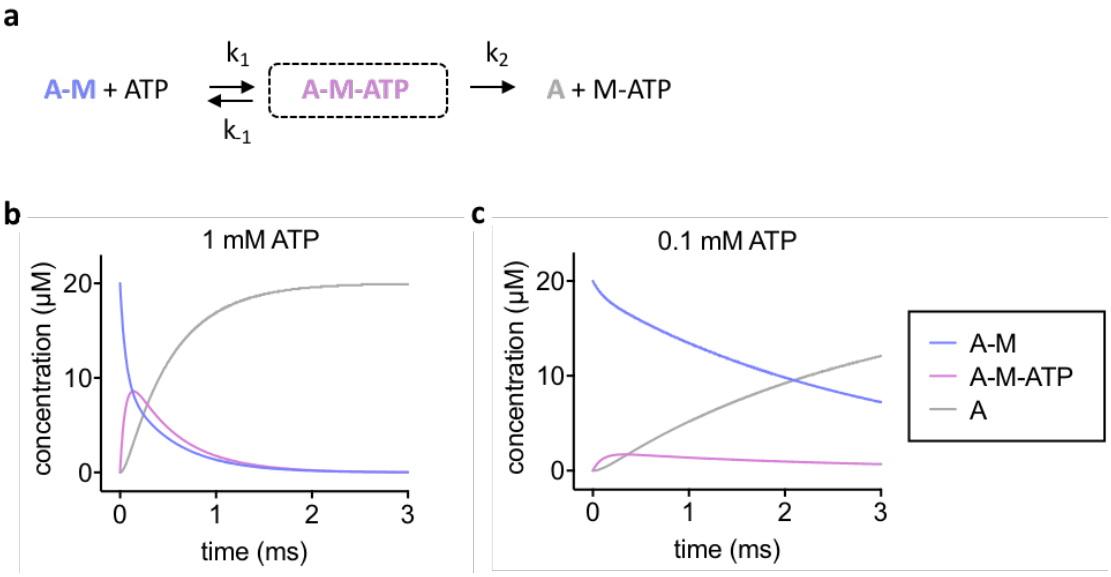


**Figure 7-1: Trapping a highly transient protein-ligand complex.**

(a) The reaction of actomyosin complex (A-M) with ATP. ATP binds A-M with a rate $k_1$, and dissociates from A-M with a rate of $k_{-1}$. In this simplified model, the intermediate A-M-ATP complex dissociates with a rate of $k_2$ to give free ATP-bound myosin (M-ATP) and F-actin (A). The rate constant of ATP binding was estimated as $k_1 = 10^7$ $M^{-1}s^{-1}$ [29]. The reverse reaction was estimated to have a rate constant of $k_{-1} = 6000$ $s^{-1}$ for ATP release from the actomyosin complex [30, 31]. The dissociation rate of A-M-ATP was estimated as $k_2 = 3500$ $s^{-1}$ [31]. (b) Kinetic modelling of the reaction at initial concentrations of 1 mM ATP and 20 μM A-M. (c) Kinetic modelling of the reaction at initial concentrations of 0.1 mM ATP and 20 μM A-M. Concentrations of A-M, A-M-ATP and A are shown by the purple, pink and grey lines, respectively.

ATP-induced actomyosin dissociation could be considered a case of the 'induced fit' model of ligand binding, where binding is followed by a ligand-induced conformational change [32]. Similarity to the Michaelis-Menten model of enzyme catalysis is also apparent [33]. Other reactions that follow this model should exhibit similar behaviour, as long as the rate constant of the conformational change ($k_2$ in Figure 7-1 a) is sufficiently slow, compared to the rate of ligand binding ($k_1$ in Figure 7-1 a). Thus, especially for bimolecular reactions and for trapping transient ligand-protein complexes, a method for sub-millisecond TrEM would be desirable. For current spray based TrEM approaches, sample application can be done in less

than 1 ms, but the challenge will be to achieve droplet thinning and subsequent vitrification on this timescale.

## 7.4 Biochemistry with the electron microscope

While shorter dead times and better time-resolution promise to increase the scope of TrEM in the future, there is a wide range of biological reactions that can be studied with current methods. Different types of experiments are discussed below, and an overview is given in Table 7-1.

The simplest case is presented in Chapter 4, where a reaction with known kinetics is visualised by TrEM without trapping any specific intermediate. Earlier work on dissociation of the actomyosin complex by TrEM could be classed as the same type of experiment. Even though there was evidence for a transient state, the intermediate was not structurally defined [34]. More recently, similar experiments have been done for bacterial ribosome subunit association and RecA filament growth [12, 35]. Such reactions serve as good test systems for TrEM method development. The prior information on the biochemical kinetics of the reaction is typically obtained by stopped-flow experiments. In the case of bimolecular association reactions, results from surface plasmon resonance may provide useful information because the technique allows direct measurement of association and dissociation rates.

In the most common type of TrEM experiment, one or a few intermediates are trapped, and the time delays in TrEM are chosen based on existing biochemical kinetic data. The work in Chapter 6 falls into this category. Earlier instances of this type of experiment used TrEM to trap the acetylcholine receptor in an open state, bacteriorhodopsin at various timepoints after flash illumination and a proposed intermediate during actomyosin complex formation [36-38]. More recent work includes the structure determination of ribosome intermediate states during translation initiation and translation termination [39, 40]. The complementary biochemical data usually come from a whole range of kinetic measurements, which have led to the identification of the intermediate state(s) of interest.

**Table 7-1: Different types of TrEM experiments**

Classification of TrEM experiments was done based on the prior biochemical kinetic information on the reaction, and the number of intermediate states of interest.

| prior kinetic information | intermediates of interest | experimental effort | example | references |
|---|---|---|---|---|
| yes | none | + | Chapter 4 | [12, 34, 35] |
| yes | one or a few | ++ | Chapter 6 | [36-40] |
| little to none | one or a few | +++ | Viral capsid conformations | - |
| little to none | many | +++ | Endocytosis | - |

Other types of TrEM experiments may become more relevant in the future, as access to cryo-EM instrumentation and the speed of data collection continue to improve. One could envision that reactions with one or a few discrete intermediate states could be studied by TrEM, even when there is no or little prior information on the reaction kinetics. This may be particularly interesting for systems that are difficult to deconvolute by other methods because of their size or relatively subtle conformational changes. One example is the conformational transition of viral capsids, such processes have been studied on long timescales with cryo-EM and typically exhibit a number of intermediate states [41]. Particle distributions from EM data could then be used to inform on the reaction kinetics, and give mechanistic insights.

TrEM may also become useful in understanding even more complex reactions with a large number of intermediate states, that may involve changes in the higher order structure of protein assemblies. Adapter proteins involved in endocytosis can serve as an example for this type of reaction: In clathrin-mediated endocytosis, a protein coat with many components assembles on the membrane within seconds, before membrane invagination [42]. Endocytosis adapter proteins have been shown to bind to membranes in a highly regular arrangement, and cause membrane bending in vitro [43]. Little is known about the details of how these adapter proteins assemble into a symmetrical lattice and how they induce membrane curvature.

Time-resolved EM could help to answer such questions, with single-particle or tomography approaches.

One technical difficulty, relevant especially for more challenging TrEM experiments, is the broad distribution of reactions times that results from laminar flow as discussed in Chapter 4 and described by others [12]. This problem could be solved by avoiding laminar flow, for example with droplet based methods or in devices with ‘fluid walls’ [44-46].

## 7.5 Time-resolved cryo-EM and its role in structural biology

The present work demonstrates what current TrEM methods are capable of, and discusses possible future developments. It also becomes clear that TrEM alone will not enable a complete description of the structural dynamics of biological systems, in the near future. Reaction initiation by rapid mixing is not sufficiently fast to resolve the lower tier protein dynamics in time (Tier 1-2). The continuous nature of these motions also makes it difficult to spatially resolve them with traditional cryo-EM classification methods. Recent image processing algorithms that account for continuous flexibility could help to overcome this problem [47-49]. There has also been progress in determining energy landscapes directly from 2D projection images by a promising approach called manifold embedding [50-52].

The minimum particle size for single-particle cryo-EM, currently around 40 to 60 kDa, also imposes limitations for TrEM studies [53, 54]. In addition, disordered regions usually remain unresolved by cryo-EM although they are functionally important, for example in amyloid fibril structures [55, 56]. Phase plates for cryo-EM may help with these challenges to some extent, by increasing contrast in the 2D projection images [57, 58]. However, other structural or biochemical techniques are better suited to deal with small or disordered proteins, including NMR, single-molecule fluorescence methods, cross-linking mass spectrometry or MD simulations.

The integration of MD simulations with TrEM data is particularly promising, because of the high spatial and temporal resolutions that simulations can provide. While current simulations are usually coarse-grained to achieve the timescale of experiments, an increase in computational power promises greater overlap of the techniques in the future [59]. The citizen science project ‘folding@home’, for

example, has mobilised unprecedented computational resources for the simulation of the SARS-CoV-2 proteome recently [60].

In summary, this thesis has characterised and developed new tools for TrEM and demonstrated their application. With protein structure determination becoming faster and more routine, it is an exciting time to focus on protein dynamics, in order to 'solve' protein mechanism and function [61].

## 7.6 References


1. Lynch, M.L., E.H. Snell, and S.E. Bowman, *Structural biology in the time of COVID-19: perspectives on methods and milestones.* IUCrJ, 2021. **8**(3).
2. Douangamath, A., et al., *Crystallographic and electrophilic fragment screening of the SARS-CoV-2 main protease.* Nature communications, 2020. **11**(1): p. 1-11.
3. Blundell, T.L., *Protein crystallography and drug discovery: recollections of knowledge exchange between academia and industry.* IUCrJ, 2017. **4**(4): p. 308-321.
4. Saur, M., et al., *Fragment-based drug discovery using cryo-EM.* Drug discovery today, 2020. **25**(3): p. 485-490.
5. Koshland Jr, D., *Enzyme flexibility and enzyme action.* Journal of cellular and comparative physiology, 1959. **54**(S1): p. 245-258.
6. Gurd, F.R. and T.M. Rothges, *Motions in proteins.* Advances in protein chemistry, 1979. **33**: p. 73-165.
7. Trebbin, M., et al., *Microfluidic liquid jet system with compatibility for atmospheric and high-vacuum conditions.* Lab on a Chip, 2014. **14**(10): p. 1733-1745.
8. DePonte, D., et al., *Gas dynamic virtual nozzle for generation of microscopic droplet streams.* Journal of Physics D: Applied Physics, 2008. **41**(19): p. 195505.
9. Noble, A.J., et al., *Reducing effects of particle adsorption to the air–water interface in cryo-EM.* Nature methods, 2018. **15**(10): p. 793-795.
10. D'Imprima, E., et al., *Protein denaturation at the air-water interface and how to prevent it.* Elife, 2019. **8**: p. e42747.
11. Naydenova, K. and C.J. Russo, *Measuring the effects of particle orientation to improve the efficiency of electron cryomicroscopy.* Nature communications, 2017. **8**(1): p. 1-5.
12. Mäeots, M.-E., et al., *Modular microfluidics enables kinetic insight from time-resolved cryo-EM.* Nature communications, 2020. **11**(1): p. 1-14.

13. Lee, J.K., et al., *Spontaneous generation of hydrogen peroxide from aqueous microdroplets.* Proceedings of the National Academy of Sciences, 2019. **116**(39): p. 19294-19298.
14. Griffith, E.C. and V. Vaida, *In situ observation of peptide bond formation at the water–air interface.* Proceedings of the National Academy of Sciences, 2012. **109**(39): p. 15697-15701.
15. Zhong, X., H. Chen, and R.N. Zare, *Ultrafast enzymatic digestion of proteins by microdroplet mass spectrometry.* Nature communications, 2020. **11**(1): p. 1-9.
16. Wei, H., et al., *Optimizing "self-wicking" nanowire grids.* Journal of structural biology, 2018. **202**(2): p. 170-174.
17. Diederich, B., et al., *A versatile and customizable low-cost 3D-printed open standard for microscopic imaging.* Nature communications, 2020. **11**(1): p. 1-9.
18. Collins, J.T., et al., *Robotic microscopy for everyone: the OpenFlexure microscope.* Biomedical Optics Express, 2020. **11**(5): p. 2447-2460.
19. Booeshaghi, A., et al., *Principles of open source bioinstrumentation applied to the poseidon syringe pump system.* Scientific reports, 2019. **9**(1): p. 1-8.
20. Carvalho, M.C. and R.H. Murray, *Osmar, the open-source microsyringe autosampler.* HardwareX, 2018. **3**: p. 10-38.
21. Rubinstein, J.L., et al., *Shake-it-off: a simple ultrasonic cryo-EM specimen-preparation device.* Acta Crystallographica Section D: Structural Biology, 2019. **75**(12).
22. White, H., et al., *A second generation apparatus for time-resolved electron cryo-microscopy using stepper motors and electrospray.* Journal of structural biology, 2003. **144**(1-2): p. 246-252.
23. Ganán-Calvo, A.M., *Electro-flow focusing: The high-conductivity low-viscosity limit.* Physical review letters, 2007. **98**(13): p. 134503.
24. Koralek, J.D., et al., *Generation and characterization of ultrathin free-flowing liquid sheets.* Nature communications, 2018. **9**(1): p. 1-8.
25. Weierstall, U., J. Spence, and R. Doak, *Injector for scattering measurements on fully solvated biospecies.* Review of Scientific Instruments, 2012. **83**(3): p. 035108.
26. Knoška, J., et al., *Ultracompact 3D microfluidics for time-resolved structural biology.* Nature communications, 2020. **11**(1): p. 1-12.
27. Knight, J.B., et al., *Hydrodynamic focusing on a silicon chip: mixing nanoliters in microseconds.* Physical review letters, 1998. **80**(17): p. 3863.

28. Levantino, M., et al., *Using synchrotrons and XFELs for time-resolved X-ray crystallography and solution scattering experiments on biomolecules.* Current opinion in structural biology, 2015. **35**: p. 41-48.
29. Trentham, D.R., J. Eccleston, and C.R. Bagshaw, *Kinetic analysis of ATPase mechanisms.* Quarterly reviews of biophysics, 1976. **9**(2): p. 217-281.
30. Millar, N.C. and M.A. Geeves, *The limiting rate of the ATP-mediated dissociation of actin from rabbit skeletal muscle myosin subfragment 1.* FEBS letters, 1983. **160**(1-2): p. 141-148.
31. Taylor, R.S. and A.G. Weeds, *The magnesium-ion-dependent adenosine triphosphatase of bovine cardiac myosin and its subfragment-1.* Biochemical Journal, 1976. **159**(2): p. 301-315.
32. Koshland Jr, D.E., *The key–lock theory and the induced fit theory.* Angewandte Chemie International Edition in English, 1995. **33**(23-24): p. 2375-2378.
33. Bar-Even, A., et al., *The moderately efficient enzyme: futile encounters and enzyme floppiness.* Biochemistry, 2015. **54**(32): p. 4969-4977.
34. Walker, M., J. Trinick, and H. White, *Millisecond time resolution electron cryo-microscopy of the M-ATP transient kinetic state of the acto-myosin ATPase.* Biophysical journal, 1995. **68**(4 Suppl): p. 87S.
35. Chen, B., et al., *Structural dynamics of ribosome subunit association studied by mixing-spraying time-resolved cryogenic electron microscopy.* Structure, 2015. **23**(6): p. 1097-1105.
36. Unwin, N., *Acetylcholine receptor channel imaged in the open state.* Nature, 1995. **373**(6509): p. 37-43.
37. Subramaniam, S. and R. Henderson, *Electron crystallography of bacteriorhodopsin with millisecond time resolution.* Journal of structural biology, 1999. **128**(1): p. 19-25.
38. Walker, M., et al., *Observation of transient disorder during myosin subfragment-1 binding to actin by stopped-flow fluorescence and millisecond time resolution electron cryomicroscopy: evidence that the start of the crossbridge power stroke in muscle has variable geometry.* Proceedings of the National Academy of Sciences, 1999. **96**(2): p. 465-470.
39. Kaledhonkar, S., et al., *Late steps in bacterial translation initiation visualized using time-resolved cryo-EM.* Nature, 2019. **570**(7761): p. 400.
40. Fu, Z., et al., *The structural basis for release-factor activation during translation termination revealed by time-resolved cryogenic electron microscopy.* Nature communications, 2019. **10**(1): p. 1-7.

41. Lata, R., et al., *Maturation dynamics of a viral capsid: visualization of transitional intermediate states.* Cell, 2000. **100**(2): p. 253-263.
42. Lu, R., D.G. Drubin, and Y. Sun, *Clathrin-mediated endocytosis in budding yeast at a glance.* Journal of Cell Science, 2016. **129**(8): p. 1531-1536.
43. Skruzny, M., et al., *An organized co-assembly of clathrin adaptors is essential for endocytosis.* Developmental cell, 2015. **33**(2): p. 150-162.
44. Graceffa, R., et al., *Probing ballistic microdrop coalescence by stroboscopic small-angle X-ray scattering.* Applied Physics Letters, 2012. **101**(25): p. 254101.
45. Song, H., D.L. Chen, and R.F. Ismagilov, *Reactions in droplets in microfluidic channels.* Angewandte chemie international edition, 2006. **45**(44): p. 7336-7356.
46. Dunne, P., et al., *Liquid flow and control without solid walls.* Nature, 2020. **581**(7806): p. 58-62.
47. Nakane, T., et al., *Characterisation of molecular motions in cryo-EM single-particle data by multi-body refinement in RELION.* Elife, 2018. **7**: p. e36861.
48. Zhong, E.D., et al., *CryoDRGN: reconstruction of heterogeneous cryo-EM structures using neural networks.* Nature methods, 2021. **18**(2): p. 176-185.
49. Punjani, A. and D.J. Fleet, *3D variability analysis: Resolving continuous flexibility and discrete heterogeneity from single particle cryo-EM.* Journal of Structural Biology, 2021. **213**(2): p. 107702.
50. Dashti, A., et al., *Trajectories of the ribosome as a Brownian nanomachine.* Proceedings of the National Academy of Sciences of the United States of America, 2014. **111**(49): p. 17492.
51. Maji, S., et al., *Propagation of conformational coordinates across angular space in mapping the continuum of states from cryo-EM data by manifold embedding.* Journal of chemical information and modeling, 2020. **60**(5): p. 2484-2491.
52. Dashti, A., et al., *Retrieving functional pathways of biomolecules from single-particle snapshots.* Nature communications, 2020. **11**(1): p. 1-14.
53. Wu, M. and G.C. Lander, *How low can we go? Structure determination of small biological complexes using single-particle cryo-EM.* Current opinion in structural biology, 2020. **64**: p. 9-16.
54. Khoshouei, M., et al., *Revisiting the structure of hemoglobin and myoglobin with cryo-electron microscopy.* Journal of molecular biology, 2017. **429**(17): p. 2611-2618.

55. Gallardo, R., N.A. Ranson, and S.E. Radford, *Amyloid structures: much more than just a cross-β fold.* Current opinion in structural biology, 2020. **60**: p. 7-16.
56. Ulamec, S.M., D.J. Brockwell, and S.E. Radford, *Looking beyond the core: The role of flanking regions in the aggregation of amyloidogenic peptides and proteins.* Frontiers in Neuroscience, 2020: p. 1216.
57. Khoshouei, M., et al., *Cryo-EM structure of haemoglobin at 3.2 Å determined with the Volta phase plate.* Nature communications, 2017. **8**(1): p. 1-6.
58. Schwartz, O., et al., *Laser phase plate for transmission electron microscopy.* Nature methods, 2019. **16**(10): p. 1016-1020.
59. Gravett, M.S., et al., *Moving in the mesoscale: Understanding the mechanics of cytoskeletal molecular motors by combining mesoscale simulations with imaging.* Wiley Interdisciplinary Reviews: Computational Molecular Science, 2021: p. e1570.
60. Zimmerman, M.I., et al., *SARS-CoV-2 simulations go exascale to predict dramatic spike opening and cryptic pockets across the proteome.* Nature chemistry, 2021. **13**(7): p. 651-659.
61. Ourmazd, A., K. Moffat, and E.E. Lattman, *Structural biology is solved—now what?* Nature methods, 2022. **19**(1): p. 24-26.

# Appendix A

## Publications which did not contribute to the thesis

David P. Klebl, Frank Sobott, Howard D. White, and Stephen P. Muench. "Fast Grid Preparation for Time-Resolved Cryo-Electron Microscopy." *Journal of visualized experiments: JoVE* 177 (2021).

For this publication, the author contribution statement reads:

D.P.K. recorded video and audio together with S.P.M; D.P.K. edited the video; D.P.K. and S.P.M. wrote the manuscript with input from all authors.

David P. Klebl, Matthew C. Feasey, Emma L. Hesketh, Neil A. Ranson, Heiko Wurdak, Frank Sobott, Robin S. Bon, and Stephen P. Muench. "Cryo-EM structure of human mitochondrial HSPD1." *Iscience* 24, no. 1 (2021): 102022.

For this publication, the author contribution statement reads:

D.P.K., M.C.F. and E.L.H. performed cryo-EM experiments; D.P.K and M.C.F. prepared samples, performed biophysical experiments and interpreted the data; N.A.R., F.S., R.S.B. and S.P.M. supervised the work; D.P.K., M.C.F., H.W., F.S., R.S.B., and S.P.M. contributed to the preparation of the manuscript.

Javier Lizarrondo*, David P. Klebl*, Stephan Niebling, Marc Abella, Martin A. Schroer, Haydyn D. T. Mertens, Katharina Veith, Roland Thuenauer, Dmitri I. Svergun, Michal Skruzny, Frank Sobott, Stephen P. Muench, and Maria M. Garcia-Alai. "Structure of the endocytic adaptor complex reveals the basis for efficient membrane anchoring during clathrin-mediated endocytosis." *Nature communications* 12, no. 1 (2021): 1-15.

* These authors contributed equally to this work.

For this publication, the author contribution statement reads:

J.L. and K.V. produced proteins and samples for cryo-EM, SAXS, and native Mass spectrometry; J.L. performed biophysical experiments and interpreted EM Data; D.P.K. performed cryo-EM experiments and determined the AENTH structures together with S.P.M.; D.P.K. performed mass spectrometry experiments and interpreted the data together with F.S.; D.P.K. performed LUV negative stain EM experiments; J.L. performed fluorescence light microscopy experiments with GUVs supervised by R.T.; M.A. and M.S. performed growth experiments in S. cerevisiae and interpreted data; M.A.S. and H.D.T.M. performed SAXS experiments and

interpreted the data together with D.I.S.; S.N. performed BLI experiments and SF-TR-SAXS data analysis with input from M.A.S.; M.G.A. conceived and supervised the project; J.L. and M.G.A. wrote the manuscript with input from all authors.

Dong Yang, David P. Klebl, Sheng Zeng, Frank Sobott, Martine Prévost, Patrice Soumillion, Guy Vandenbussche, and Véronique Fontaine. "Interplays between copper and Mycobacterium tuberculosis GroEL1." *Metallomics* 12, no. 8 (2020): 1267-1277.

For this publication, the contributions by D.P.K and F.S. are as follows:

D.P.K. performed native MS experiments and analysed the data; D.P.K. and F.S. interpreted the data; D.P.K. and F.S. contributed to the preparation of the manuscript.

# Appendix B

## Rationale behind the term ‘voltage-assisted spraying’

In a TrEM device previously described by White et al., electrospray was used to apply droplets to a blotted grid [1]. The grid preparation device in Chapter 2 makes use of high voltage (5 kV) to promote the formation of small droplets, but spray formation is mainly driven by a gas flow through the nozzle. The approach was therefore termed ‘voltage-assisted spraying’. In electrospray, the voltage alone is usually sufficient to produce a spray of very fine droplets. As a result, liquid flowrates can be much lower than the ~8 µL/s used in Chapter 2, and droplets form at the characteristic Taylor cone (Figure B-1) [2, 3]. The voltage-assisted spray does not exhibit a Taylor cone (Figure 2-3) and droplets are relatively large (Figure 3-1). However, high-speed imaging showed that there is repulsion between droplets, indicating that the charge is sufficient to affect droplet behaviour in the case of voltage-assisted spraying. Whether classical electrospray is suitable for direct droplet deposition onto cryo-EM grids remains unclear.

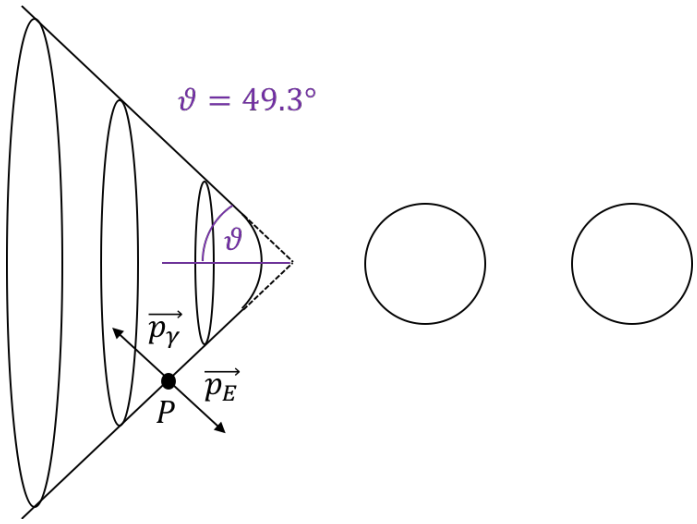


**Figure B-1: Schematic of a Taylor cone.**

The Taylor Cone forms because at any point P on the surface, the pressure due to electrostatic forces (E) and the pressure due to surface tension ($\gamma$) must be equal. This condition is fulfilled for a cone with an angle of $\vartheta$=49.3°, assuming a static cone. Either a jet, or droplets can be emitted from the tip of the cone (droplets shown here). The curvature at the tip of the (imperfect) cone determines the diameter of the emitted droplets. Adapted from [2].

## References

1. White, H., et al., *A second generation apparatus for time-resolved electron cryo-microscopy using stepper motors and electrospray.* Journal of structural biology, 2003. **144**(1-2): p. 246-252.
2. Wilm, M.S. and M. Mann, *Electrospray and Taylor-Cone theory, Dole's beam of macromolecules at last?* International Journal of Mass Spectrometry and Ion Processes, 1994. **136**(2-3): p. 167-180.
3. Taylor, G.I., *Disintegration of water drops in an electric field.* Proceedings of the Royal Society of London. Series A. Mathematical and Physical Sciences, 1964. **280**(1382): p. 383-397.